Energy Harvesting by Using Ferroelectric Switching



WENBIN KANG

Oriel College
Doctor of Philosophy in Engineering Science
University of Oxford

Michaelmas Term 2021

Energy harvesting by using ferroelectric switching

Wenbin Kang, Oriel College, University of Oxford
For the degree of D.Phil. in Engineering Science, Michaelmas Term 2021

Abstract

The aim of the current work is to develop a novel energy harvesting method by using ferroelectric/ferroelastic switching and to establish a practical prototype device with stability and robustness. The results are expected to provide a deep mechanistic understanding of the polarization state in ferroelectrics and assist in the improvement of transducers' performance in practical applications.

Ferroelectric/ferroelastic switching, which can generate greater energies and charge flows than those of piezoelectrics has attracted increased interest to improve transducers' performance in recent years. However, the challenges of nonlinearity, fatigue degradation and the difficulty of driving an electrical cycle by stress have limited ferroelectrics' use in energy harvesting applications. In the current work, by using a simple model of switching, a working cycle that could generate electrical energy from a harmonically varying source of stress is explored. The cycle uses depolarization by stress, followed by repolarization with combined electromechanical loading. A harvesting electric field and bias electric field are imposed to ensure a stable repeatable working cycle during the depolarization process and repolarization process, respectively. The bias electric field, which is much less than the coercive field, provides a preferred direction of repolarization. The conversion efficiency of this cycle is estimated and improvements to the cycle are explored by adjusting the electrical and mechanical field amplitudes.

The current work then explores a novel and robust ferroelectric energy harvester based on partial ferroelectric switching. The device is of simple construction and achieves a per-cycle energy density of about 1mJ/cm^3, orders of magnitude greater than that of typical piezoelectrics. Instead of using an external electrical bias field, the internal residual electric fields, generated during a partial depoling of an electroceramic, are adopted to provide 'memory' of a preferred direction for repolarizing it. A crucial feature is the control of residual stress by poling the active material in stages, first in a mechanically unconstrained state, then adhered to a substrate before completing the poling process. Then the method works by partially depolarizing a poled ferroelectric using a single application of tensile stress, and then using cycles of compression to vary the polarization state. It is shown that only periodic compressive stress is needed to induce the energy harvesting cycles, yielding unique and promising mechanical attributes that limit fatigue or fracture during cyclic loading. The results show this prototype device operating stably over 0.5×10^6 cycles at low frequency. The explorations of various polarization states and resistive electrical loads are also carried out to improve the performance for further practical applications.

Acknowledgements

I am immensely grateful to my supervisor, Professor John Huber, for his ubiquitous help and support in every aspect of my life at Oxford. His best guidance, genuine insights, enthusiasm for research and encouragement inspire me to pursue to solve more research questions in engineering. He is an excellent teacher and a great supervisor, and he is always encouraging me to learn new knowledge, experimental skills and improve my language proficiency, which helps me grow intellectually to conduct research individually. I would thank him for spending generous amounts of time in helping me turn our investigation in research into this thesis and several publications. I deeply appreciate his kind help and supervision without which I would never have completed these difficult tasks.

I would thank all the people who have inspired me to complete this work and continue my research – to Robert Paynter, Luke Blade and Lulu Chang (visiting student) in SMME group for helping me set up the experimental test platform and giving me solid support to solve the problems; to David (patent attorney), Marco, Rachel and Iraida in Oxford University Innovation, for their kindness to help me apply for a UK patent; to Professor Xi Wang in Shanghai Jiao Tong University, for introducing me to start my research about functional materials, which has been very important to my DPhil; to Jardine Foundation, for giving the precious opportunity to study at Oxford in which I had an invaluable experience over these four years.

I thank all the members in the SMME group for the help and support during my DPhil. I am very thankful to Professor Jin-Chong Tan and Professor Antoine Jérusalem for giving me the useful and valuable suggestions during my transfer viva. I am very thankful to Professor Laurence Brassart for offering me a great opportunity to work as a lab demonstrator, which helped me establish the finite element coding skills. I am very thankful to Kalin and Marzena for the training and instructions of LIMA laboratory. I am very thankful to Rima, Elsiddig, Nihal, Jure, Antonio, Majid and Guosheng for all the discussion towards academic and non-academic stuff. I am very grateful to Amanda, Suneeta and Sophie for the administrative support; to Richard, Andy and Simon for helping me prepare the specimens; to Hisham for IT support.

I really appreciate the friendships with Yuewen, Xin, Shaohong, Felix, Honglie, Odessa, George, Bingkun, Chao, Zhenhai, Keiin, Bob, Yutao, Zongyao and Jie etc, who have enriched my DPhil life with kebabs, beers and escape games. I am very lucky to have you all! Here, I want to show my special thanks to one of my best friends, Tate, who accompanied me in the tough time of the pandemic period. I am also grateful to be a member of Oriel College, where I have participated in various activities and met new friends. The college provides great facilities and support to my DPhil study, and I really enjoy the time at the corner of the library with the soft evening light.

Finally, I would like to give my unique thanks to my parents and family who offers me the unconditional love and endless support to motivate me to keep exploring the wonderful world. Without them, I cannot accomplish this achievement!

Contents

Abstract i

Acknowledgements ii

Contents iii

Lists of Abbreviations vi

1. Introduction 1

1.1 Motivation 1
1.2 Introduction to ferroelectrics 6
1.2.1 History and typical applications of ferroelectrics 6
1.2.2 Essential concepts of ferroelectrics 8
1.3 Models of ferroelectrics 16
1.3.1 Micro-electromechanical models of ferroelectric switching 17
1.3.2 Phenomenological constitutive models of ferroelectrics 25
1.3.3 Other models for microstructures and nano-scale structures 29
1.3.4 Summary 34
1.4 Thesis structure 36

2. Literature review of energy harvesters 39

2.1 Piezoelectric energy harvesting 40
2.1.1 Improvements of structure design 43
2.1.2 Improvements of materials 49
2.2 Triboelectric energy harvesting 59
2.2.1 Four types of triboelectric nanogenerators 60
2.2.2 State-of-the-art designs of triboelectric generators 61
2.3 Ferroelectric energy harvesting 64
2.4 Summary 72

3. Methods 73

3.1 Model of the energy harvesting cycle 73
3.2 Experimental procedures 77
3.2.1 Specimen fabrication 77
3.2.2 Test arrangements 80

4. Prospects for energy harvesting using ferroelectric/ferroelastic switching 86

4.1 Introduction 87
4.2 Concept for a ferroelectric/ferroelastic energy harvester 89
4.3 Simulation of an energy harvesting cycle 94
4.4 Exploration of the energy harvesting cycle parameters 99
4.5 Summary 111

5. Energy harvesting based on compressive stress-induced ferroelectric/ferroelastic switching 112

5.1 Introduction 113
5.2 Working concept and design 115
5.3 Results and discussion 121
5.3.1 Quasi-static tests 121
5.3.2 Energy harvesting performance at low frequencies 126
5.4 Summary 134

6. Investigation of mechanical energy harvesting cycles using ferroelectric /ferroelastic switching 135

6.1 Introduction 136
6.2 Concept and design 138
6.3 Results and discussion 142
6.3.1 Preliminary tests at zero electrical load 142
6.3.2 Energy harvesting using tensile stress 147
6.3.3 Energy harvesting using compressive stress 152
6.4 Summary 158

7. Exploiting the method of energy harvesting using ferroelectric/ferroelastic switching at low frequency: resistive load optimization 159

7.1 Introduction 160
7.2 Design and test arrangement 162
7.3 Results and discussion 165
7.3.1 Quasi-static tests 165
7.3.2 Vibrational study 168

7.4 Summary 180

8. Conclusions and future work 182

8.1 Conclusions and discussion 183
8.2 Future work 188

Appendix 194

A.1 Energy harvesting cycles of 100% pre-poled 194
A.2 Energy harvesting cycles of 75% pre-poled 197
A.3 Energy harvesting cycles of 50% pre-poled 200
A.4 Energy harvesting cycles of 30% pre-poled 203

References 206

Lists of Abbreviations

AIN	Aluminium nitride
BCZT	$(Ba,Ca)(Zr,Ti)O_3$
BNNTs	Boron nitride nanotubes
BNT-BT	Sodium bismuth titanate-barium titanate
BZT-BCT	$(1-x)Ba(Zr_{0.2}Ti_{0.8})O_3–x(Ba_{0.7}Ca_{0.3})TiO_3$
CNFs	Cellulose nanofibril
FFET	Ferroelectric field effect transistor
IDEs	Interdigitated electrodes
IoTs	Internet of things
KNN	Sodium bismuth titanate
KNN–BNZ–AS–Fe	$0.91K_{0.48}Na_{0.52}NbO_3–0.04Bi_{0.5}Na_{0.5}ZrO_3$-$0.05AgSbO_3–0.2\%\ Fe_2O_3$
LVDT	Linear variable differential transformer
NKN	$(Na_{0.5},K_{0.5})NbO_3$
NKN-BNT	$(1-x)(Na_{0.5}K_{0.5})NbO_3–x(Bi_{0.5}Na_{0.5})TiO_3$
NWs	Nanowires
PDMS	Polydimethylsiloxane
PLZT	Lanthanum doped PZT
PMN- PT	$Pb(Mg_{1/3}Nb_{2/3})O_3–PbTiO_3$
PNN-PZT	Nickel-niobium-lead zirconate titanate

PPCB	Phononic piezoelectric cantilever beam
PVDF	Polyvinylidene fluoride
PVDF-TrFE	Polyvinylidenefluoride-co-trifluoroethylene
PZN-PT	$Pb(Zn_{1/3}Nb_{2/3})O_3–PbTiO_3$
PZT	Lead zirconate titanate
RVE	Representative volume element

Chapter 1

1. Introduction

1.1 Motivation

In last decades, electronics can be used in various aspects such as health monitoring, military engineering, agriculture, aerospace engineering[1-4]. Currently, there are four main trends in electronics' development, namely miniaturization, multi-functionality, portability and low power consumption[5, 6]. However, the limited lifetime, and energy density of batteries, limited energy storage capacity and the inflexibility of wired systems cannot satisfy all of the resulting power requirements such as compactness, long lifetime and flexibility[7-12]. For example, some implanted devices should not be replaced frequently[4, 13, 14]; some sensors are remotely located and must operate for long periods without servicing[8, 15-17]. Furthermore, batteries may have some other problems, which brought toxic waste that is difficult to process and are easily affected by temperature[18]. The energy cost through the use of electronics is significant, with demand of 1.269×10^{12} Watt-hours of energy per year in the US only, despite technological development that has promoted microwatt electronics[19, 20]. Therefore, energy harvesting technologies, converting ambient mechanical, solar, thermal, magnetic, optical and chemical energies into electrical energy, are attractive as one possible solution to provide sustainable power. Energy harvesting is potentially useful for wearable electronics, embedded microsystems,

wireless communication components, IoTs, intelligent devices, biomedical sensors and actuators[21-26]. This has the further advantage of providing renewable energy, thereby avoiding the ongoing cost of replacing batteries or installing wired systems[27-30]. However, it would not replace batteries as these applications would need a reliable energy source even when the ambient source was unavailable. Thus the energy harvester would typically work in conjunction with a battery powered system, providing a low level background top-up to the batteries.

There are various ways of energy harvesting based on different conversion mechanisms, serving as promising complementary systems to batteries. Electrical energy can be generated by photovoltaics, which are now well established[31-35]. Thermoelectric generators can use temperature gradients to generate electrical potential through the Seebeck effect[36-41]. Radio frequency energy can be harvested by using specific resonant circuits[42-44]. Triboelectric energy harvesters can convert mechanical energy into electrical energy, using the triboelectric effect to produce charge flows between two thin films in relative motion[45-49]. Temperature variation can be used to induce change of permanent dipole moment in pyroelectrics, and thereby generate a charge flow [50-53]. Similarly, piezoelectrics can convert kinetic energy into electrical current [54]. Related to piezoelectrics, and of most interest in the current project, ferroelastic switching, which is induced by external stress in ferroelectrics, can change the direction of spontaneous polarization, and thus cause a charge flow for energy harvesting.

1.1 Motivation

Among all the ambient power sources, mechanical/kinetic energy is widely distributed, having the advantages of cleanliness, stability, insensitivity to environment and allowing compact energy harvesters[55, 56]. Vibration, which can be created by machines, human motion and fluid flows is widely available in different environments[57, 58]. Generally, researchers have investigated three main mechanisms of mechanical-to-electrical conversion: piezoelectric[16, 59], electromagnetic[60] and electrostatic[61, 62]. These three main approaches of energy harvesting have their own advantages and disadvantages described in the literature. Piezoelectric energy harvesters are a simple type of solid state generator without complex geometry or moving components. They can provide high output voltages but typically with a low currents; this can reduce the loss of energy in the external circuit. Due to their high power density and high efficiency, energy harvesters using the piezoelectric effect have attracted great interest for extending battery life in portable electronics[29, 30]. Electromagnetic generators are more difficult to fabricate due to assembly and alignment problems. Their comparatively high output current with low output voltage can also cause some thermal losses. Electrostatic generators require an initial polarizing voltage to store charge on a capacitor. This type of energy harvester can provide a limited amount of current, which adds to the complexity of the design to get sufficient energy output.

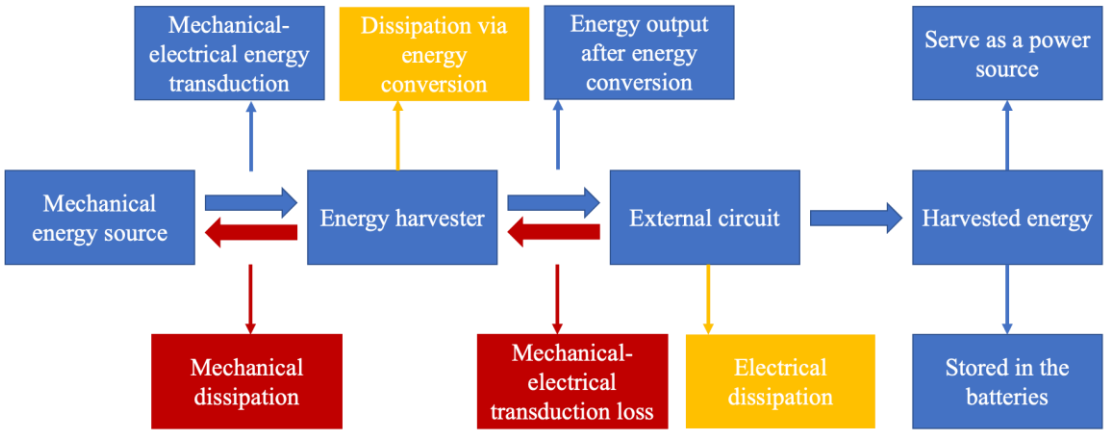


Figure 1.1 Energy flow of an energy harvester.[63]

The energy flow of a typical mechanical energy harvester is presented in figure 1.1[63], showing the energy dissipation and energy output during the energy harvesting process. Most vibrational energy harvesters are based on a simple configuration of a spring-mass-damping system, which reaches the peak energy output at a resonant frequency. By contrast, by also using off-resonance external force/excitations, the performance of energy harvesters can be optimized[64-69]. Specifically, they can be improved via mechanical modulations, such as excitation type conversion, frequency up-conversion and force/motion amplifications. The harvested energy can then be used as a direct energy source or be stored in batteries for subsequent use.

Given their simplicity and efficiency, piezoelectric materials have considerable potential for energy harvesting; various kinds of piezoelectric energy harvesters have been proposed and employed in last decade[70-72]. These systems, however, still suffer from relatively low energy density compared to the demands of typical portable electronics applications. Furthermore, they typically have very low power density at frequencies corresponding to common ambient vibrations (0-1kHz). Some attempts at

improving the performance of piezoelectric energy harvesters have been explored, by varying the materials and structures of the devices[73, 74]. Furthermore, an alternative approach, using the full ‘non-linear’ range of piezoelectric materials, such as ferroelectric/ferroelastic switching, can offer potentially much greater energy density, at the cost of loss of linearity. By contrast, there is a lack of work using this method to further develop piezoelectric energy harvester designs, and the theoretical models against experimentally observed results also need to be tested.

The objectives of my DPhil research are to design and model a stable and repeatable cycle of ferroelectric energy harvester and optimize the designs of energy harvesters by experimentation and modelling methods. The results of this work will contribute to the implementations and further research into ferroelectric transducers.

1.2 Introduction to ferroelectrics

1.2.1 History and typical applications of ferroelectrics

Ferroelectric materials are a subgroup of piezoelectrics and pyroelectrics, characterised by the presence of spontaneous polarization, which can be switched by external electric field[75-79]. They show a linear effect with small external loads, leading to piezoelectricity. Greater electrical or mechanical loads cause nonlinear coupling among electric field, electric displacement, stress and strain, which is characterized by the hysteresis loop of electric field versus electric displacement and hysteresis butterfly loop of electric field versus strain.

Valasek[80] was the first person to discover the ferroelectric properties of single crystal Rochelle salt in 1921. Later on, the perovskite oxide family of ferroelectrics with high dielectric constant, such as $BaTiO_3$, PZT, were found one after another[81, 82]. The widely used PZT's phase diagram displays a morphotropic boundary between tetragonal and rhombohedral phases[83]. Some compositions of PZT are also doped with niobium or iron to soften or harden the material, with the aim of increasing piezoelectric coefficients and dielectric permittivity by softening, or acquiring higher coercive fields and lower piezoelectric and dielectric parameters by hardening. PLZT is attractive due to its soft switching properties with low coercive field[84, 85]. Therefore, the non-linear behaviour of this material is easily accessed by applying stress or electric field, though the piezoelectric effect may be lost due to switching processes.

The discovery of relaxor based ferroelectric single crystals such as PZN-PT and PMN-PT by Shrout *et al*.[86] made a breakthrough by promoting the applications of single crystal ferroelectrics with high piezoelectric coefficients and ultrahigh strain induced by electric field. The advantages of the single crystal ferroelectrics include lower response time than ferroelectric ceramics, which increases the sensitivity of transducers.

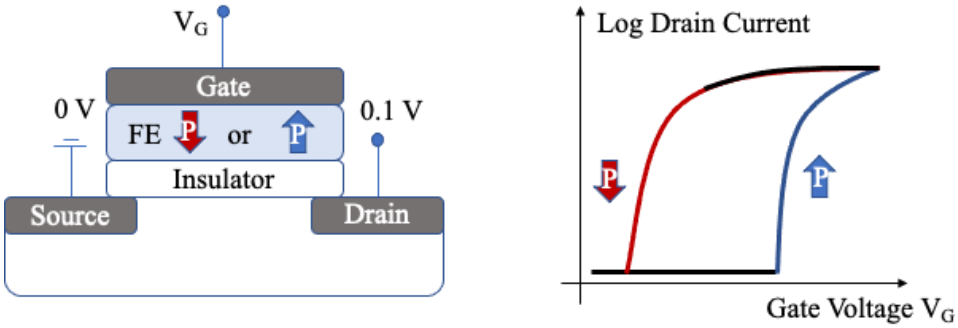


Figure 1.2 Illustration of ferroelectric field effect transistor functionality

Due to the coupling between various fields, ferroelectrics have given rise to a wide range of applications, including electric and optical devices, memory devices, diesel injection valves, ceramic capacitors, transducers, sensors, actuators, and energy harvesters[75, 76, 87-91]. For example, a successful commercialization of ferroelectrics is the FFET developed by Ferroelectric Memory Company[92], see figure 1.2. The main novelty of this memory device is to replace the dielectric layer of the gate by a ferroelectric Hafnium Oxide layer (blue part of figure 1.2), resulting in binary states with ‘on’ and ‘off’ control of the electron channel by controlling the threshold voltage of the transistor. Therefore, the transistor is non-volatile, and the design of the structure is also known as a ‘negative capacitor’.

1.2.2 Essential concepts of ferroelectrics

The spontaneous polarization induced by a non-centrosymmetric crystal structure is the key point to distinguish between ferroelectrics and ordinary dielectrics. Ferroelectrics have polarization without external electric field below a critical temperature, known as the Curie Temperature (T_c), while other dielectrics normally have polarization only with external electric field due to the dielectric effect. Spontaneous polarization (P_0) is a physical quantity that represents the net dipole moment per unit volume[93]. However, at temperatures above the Curie Temperature, a typical ferroelectric single crystal will show a paraelectric phase with a symmetric structure instead of a ferroelectric state (for example tetragonal, orthorhombic or rhombohedral)[75]. Given its simplicity, the tetragonal example of the perovskite family ABO_3 structure is regarded as a reference to understand the behaviour of ferroelectrics, see figure 1.3(a). Here, a lattice having Pb^{2+} or Ba^{2+} at the corners of the unit cell, combines with a Ti^{4+} ion occupying the central cation site and O^{2-} ions at the centre of every face of the cubic geometry[94-99]. When the single crystal structure cools below the Curie Temperature, the Ti^{4+} ion in the centre moves off centre and a tetragonal structure is formed, leading to a dipole moment of the unit cell. The Ti^{4+} ion can be moved along the direction parallel to the edges of the cubic geometry to six symmetrical positions, and this will form six spontaneous variants due to the different direction vectors. Additionally, as the tetragonal state is c in height and a in width and length from a uniform length a_0 after the cooling process, the movement of the

central ion gives rise to specific strain change of the lattice, which can be defined as spontaneous strain with a relationship of $e_0 = (c-a)/a_0$. Similarly, the orthorhombic and rhombohedral crystals have three equal axes with oblique angles and three unequal axes at right angles respectively[100-104].

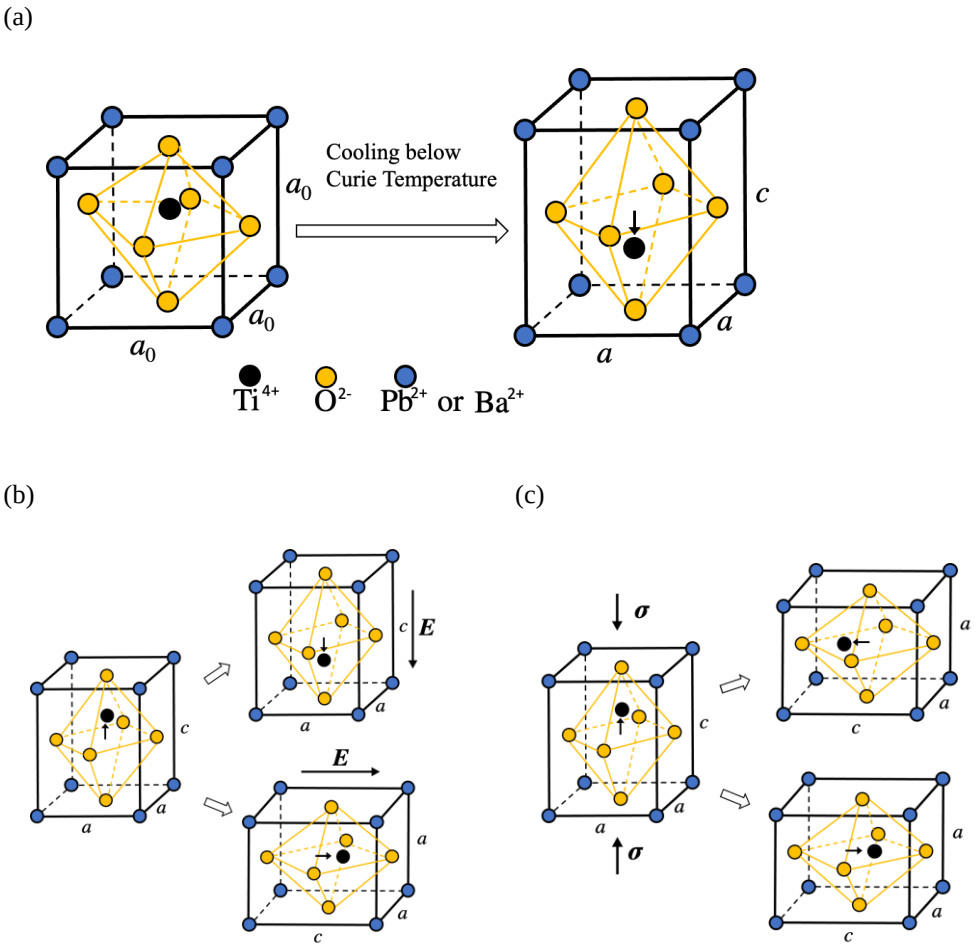


Figure 1.3 (a) The lattice structure of an ABO_3 perovskite type oxide with the phase change from paraelectric to ferroelectric state. (b) 180 degree and 90 degree ferroelectric switching induced by electric field. (c) 90 degree ferroelastic switching induced by stress.

Under small electric field or stress, the tetragonal unit cell would undergo small movement of the central positive or negative ion thereby making a thermodynamically reversible change of the polarization and strain, known as the piezoelectric effect and

converse piezoelectric effect [105-109]. This linear effect can be seen in many materials including inorganic crystals and the polymer PVDF where the polarization and strain changes would be proportional to the applied stress and electric field [110-112]. The constitutive equations of the linear elastic, dielectric and piezoelectric are described by[87, 88]

$$\begin{aligned} e_{ij} &= s_{ijkl}\sigma_{kl} + d_{kij}E_k \\ D_i &= d_{ikl}\sigma_{kl} + \kappa_{ik}E_k \end{aligned} \qquad (1.1)$$

where e_{ij} is strain, D_i is electric displacement, s_{ijkl} is the elastic compliance, d_{kij} is the third-ranked tensor piezoelectric coefficient, and κ_{ik} is the dielectric permittivity. And E_k and σ_{kl} is electric field and stress. Conversely, the E_k and σ_{kl} can also be obtained from D_i and σ_{kl}. These constitutive equations demonstrate the coupling between electrical and mechanical fields in piezoelectrics. This effect is used in energy harvesting devices, and detailed information can be found in Chapter 2.

In addition, the spontaneous polarization of ferroelectrics varies with temperature, which is defined as pyroelectricity[53, 113-119]. In PZT this is because the temperature changes the position of Ti^{4+} ion and induces a polarization change in the crystal. However, the polarization will no longer change if the temperature stays constant, which is different from thermoelectrics working by the Seebeck effect[120-124]. The pyroelectric effect is of great importance in ferroelectrics, which exhibit the combined effect of strain change due to the pyroelectric effect and the piezoelectric contribution. Pyroelectricity can be used in energy harvesters[52, 125], heat sensors[126, 127] and pyroelectric fusion[128].

Below the Curie Temperature, ferroelectric/ferroelastic switching occurs with strong electric field or stress, contributing to non-linearity of the material[85, 129]. This thermodynamically non-reversible switching process demonstrates a shape memory effect. As for ferroelectric switching, when an applied electric field exceeds the coercive field, it could induce the movement of the central ion and thereby align the direction of polarization towards that of the electric field. In figure 1.3(b), the examples of 180° and 90° switching caused by the electric field are presented. The 180° switching reverses the net polarization vector but has no effect on the strain, while 90° switching changes both the polarization and strain simultaneously. Stress aligned with the polarization vector can only induce the 90° ferroelastic switching, but the new direction of the polarization is uncertain due to the symmetry of the tetragonal cell. There are four possible new directions of the new polarization vector, and figure 1.3(c) gives two of them. The other two possible directions are perpendicular to the in-plane vectors. The result is that cycling stress does not give rise to a cyclic variation of polarization. However, combining stress with a small bias electric field in an energy harvesting cycle can direct the polarization to a specific new direction, which is discussed in detail in Chapter 4. This is the basis of an energy harvesting cycle developed in this thesis, using ferroelectric/ferroelastic switching. The introduction of a small bias electric field is used to guide the polarization direction, and thereby a working energy harvesting cycle could be established.

At the macroscopic scale (bulk ferroelectrics), ferroelectric single crystals have greater piezoelectric coefficient than ceramics, but their much greater cost compared to ferroelectric ceramics limits wide application. Therefore, the most commonly used ferroelectrics in applications are ferroelectric ceramics, fabricated through the sintering of an agglomerate of ferroelectric crystallites[85, 93]. After sintering, ferroelectric ceramics form a polycrystalline structure with randomly oriented grains. In this state the ceramics have no net polarization or piezoelectric effect, due to the zero-average over all grains, although each grain shows the single crystal's properties. In order to acquire a macroscopic non-zero polarization, the poling process is used: a strong electric field is provided to align the grains' polarizations. The ferroelectric ceramic then has similar macroscopic properties to single crystals, but with the complication of grain-grain interactions. Hence, the local polarizations are not perfectly aligned with the direction of electric field after poling process, as shown in figure 1.4.

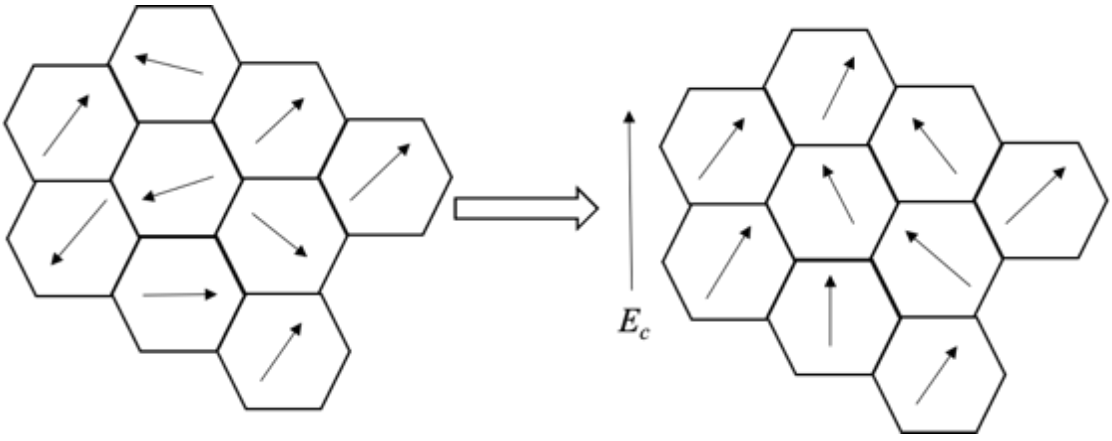


Figure 1.4 Schematic showing the behaviour of the ferroelectric ceramic grains in poling process.

The concept of ferroelectric switching can be used to explain the non-linear effects and hysteresis loop in figure 1.5 [88]. The surface charge of ferroelectrics can be

recorded to monitor the change of electric displacement, while a voltage applied to electrodes placed across the material sample defines the electric field. In figure 1.5, at the beginning, when applied electric field is much smaller than a critical value, the electric displacement change is small due to the linear dielectric effect. The coercive field is defined as the strength of the electric field at which the macroscopic polarization of the ferroelectrics undergoes large changes. The increase of electric field to the coercive value can give rise to the rotation of polarizations, which induces a rapid, non-linear rise of electric displacement and strain with a small change of electric field. When the electric field continues to rise, the switching process reaches a saturated state of polarizations; Removal of the electric field leaves a remanent state of polarization (P^r) and remanent strain (e^r).

A reversed electric field can reverse the polarizations, which means the guidance of electric field will lead ferroelectric polarizations to be switched to the directions aligned with the direction of reversed electric field. In the hysteresis loops, this is seen as a significant decrease from positive value to negative value of electric displacement, while the strain decreases to zero and then increases rapidly towards a saturated value. The absolute value of electric field, where the electric displacement becomes zero, defines the coercive field of the material. Afterwards, if the electric field returns to zero this will leave a negative remanent polarization state, but positive remanent strain. After that, if positive electric field is applied again, the polarized path is slightly different from the first half cycle due to that the state of the ferroelectric material having been

changed from the unpoled state. Then with the application of alternating electric field, a symmetric hysteresis loop can be formed, see figure 1.5.

Interestingly, the mechanical loads can impose an effect on the hysteresis loops, which has been studied by Lynch *et al.*[85]. A compressive stress aligned with the electric field induces out-of-plane switching, so that some of the grains do not switch their polarization to the direction aligned with the electric field, and thereby the remanent values of polarization and strain are reduced by compressive stress.

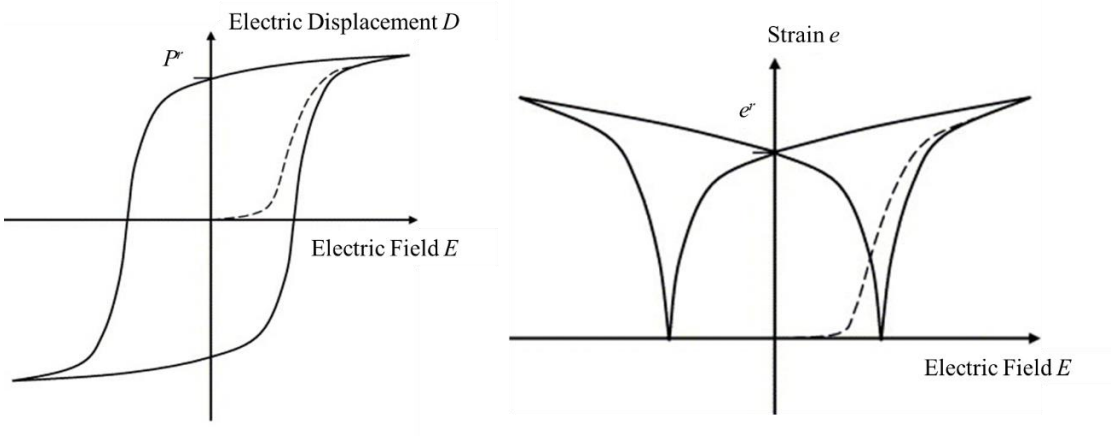


Figure 1.5 Schematic of the hysteresis loop and hysteresis butterfly loop. The stable non-linear response and the initial behaviour are shown in solid line and dashed line respectively.

To investigate ferroelectric devices, an understanding of the concept of ferroelectric domains is of great importance [130-132]. A ferroelectric domain is defined as a region with uniform spontaneous polarization; the boundary between two adjacent domains is a domain wall, see figure 1.6(a). ferroelectric switching can be seen as domain wall motion, with one domain growing and another shrinking in the transformation[133, 134]. The well-known 180° and 90° domain walls are observed in tetragonal ferroelectrics[78], see figure 1.6(b) and (c).

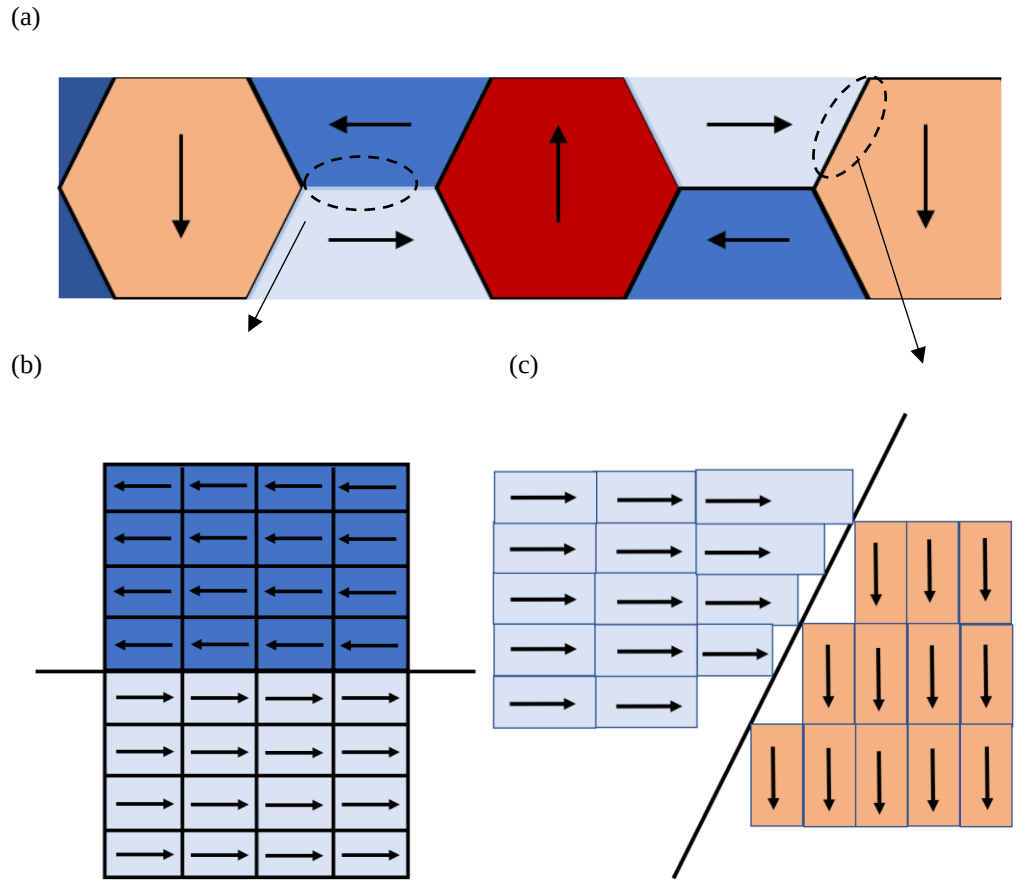


Figure 1.6. Schematic representation of ferroelectric domains. (a) a ferroelectric layer with domains. (b) 180° domain wall. (c) 90° domain wall

1.3 Models of ferroelectrics

For the design or optimization of ferroelectric devices, it is desirable to have modelling methods to predict the behaviour of ferroelectrics. So various ferroelectric models, such as first-principle models, micromechanical models, phenomenological models, phase field models and molecular dynamics models, have all been developed to investigate the ferroelectric switching in polycrystals and single crystals, covering a wide range of problems related to microstructure, domain patterns, grain-to-grain interaction and macroscopic behaviour [87, 88, 135]. Some models focus on the response in microstructure, while others regard the macroscopic behaviour of ferroelectric ceramic and single crystals as the main aspect of ferroelectric switching. The models are mainly based on fundamental physical laws including mechanical equilibrium, geometric compatibility, Gauss' law and Maxwell's law[87]. Internal variables are commonly used to track the material state after applying electric field and stress. The constitutive equation of ferroelectrics under quasi-static conditions can be written as[87, 88]

$$\begin{aligned} e_{ij} &= s_{ijkl}\sigma_{kl} + d_{kij}E_k + e_{ij}^r \\ D_i &= d_{ikl}\sigma_{kl} + \kappa_{ik}E_k + P_i^r \end{aligned} \qquad (1.2)$$

where e_{ij}^r and P_i^r are the remanent parts of strain and polarization respectively, and they play a role similar to that of the plastic strain in deformation theory.

This section mainly focuses on the micromechanical modelling of ferroelectric switching and macroscopic phenomenological models for ferroelectric energy

harvesting cycle analysis. Other models such as phase field and molecular dynamics are also briefly discussed below.

1.3.1 Micro-electromechanical models of ferroelectric switching

Micro-electromechanical models mainly focus on the ferroelectric switching criterion and change of remanent polarization and strain. Specifically, the domain configuration of ferroelectrics is considered by evaluating the change of remanent strain and polarization, which can be tracked using internal variables such as variants and volume fractions. Actually, the micro-electromechanical constitutive models are one kind of macroscopic phenomenological models because they are concerned with the macroscopic averaged behaviour of the ferroelectrics. By contrast, the bulk phenomenological models treat the material as a continuum and postulate polarization and strain fields using fewer internal variables, which do not specify a configuration of domains. Therefore, the micro-electromechanical models can be used to capture some of the behaviour of microstructure in ferroelectrics.

One of the methods to simulate the ferroelectric switching is averaging the remanent polarization and remanent strain over the individual grains. Hwang *et al.*[136] developed a simple ferroelectric/ferroelastic polarization switching model by using a Reuss approximation, assuming uniform stress and electric field inside the material. In the model of Hwang *et al.*, the ceramic is treated as a composite of independently acting grains, with random crystallographic orientations. For simplicity, each grain is regarded

as being in a tetragonal state and comprising a single polarized domain. The properties, including polarization and strain of the ceramic, are approximated by the average values over all the grains. Hwang's model does not account for the details of grain-grain interactions and variation of stress or electric field through the ceramic. In this respect it has been superseded by more sophisticated models of switching in ceramics[137]. However, the model has advantages in rapidity, simplicity and reliability.

With regard to the switching criterion, Hwang *et al.*[136] proposed critical values of both electric field and stress for switching, based on the work dissipated during the switching process, and applicable to both 90° switching and 180° switching. When the combined electrical and mechanical work for a possible switch exceed the critical value $2P^0E_0$ (where E_0 is equal to coercive electric field), switching occurs. The switching criterion can be expressed as

$$E_i\Delta P_i + \sigma_{jk}\Delta e_{jk} \geq 2P^0E_0 \tag{1.3}$$

where E_i and σ_{jk} are the components of the applied electric field and stress, and ΔP_i , Δe_{jk} are the changes in spontaneous polarization and strain respectively. There can be a possibility for multiple switches to be energetically equivalent, in which case the simulation would proceed by choosing randomly among the equivalent switching processes. By averaging over all the grains in the ceramic, the macroscopic changes in polarization and strain can be estimated.

Based on Hwang's model, a constrained domain-switching model for polycrystalline ferroelectric ceramics was proposed [138], considering the interaction

among the grains in the crystal. The switching criterion is also energy based on using equation (1.3), but the model introduced internal stress induced by domain switching, which is expressed by

$$\sigma_{ij}^{in} = -2\mu \frac{7-5\nu}{15(1-\nu)} e_{ij}^{r} \tag{1.4}$$

where σ_{ij}^{in}, μ and ν are the internal stress, the shear modulus of the ceramic and Poisson's ratio respectively. The model uses the idea of the Eshelby constraint tensor to account for elastic constraint of switching by surrounding grains. Then, the stress experienced by a grain is

$$\sigma_{ij} = \sigma_{ij}^{app} + \sigma_{ij}^{in} \tag{1.5}$$

where σ_{ij}^{app} is element of the external applied stress. This model has improved results based on using internal stress, and agrees better with experimental results.

Lynch *et al.*[137] improved Hwang's model by using interaction energy. The interaction energy can change due to the mismatch of electric displacement and mismatch of strain between the grain and the ceramic matrix. Hence the criterion of ferroelectric switching is defined as

$$E_i \Delta P_i + \sigma_{jk} \Delta e_{jk} - U_I \geq 2P^0 E_0 \tag{1.6}$$

where U_I is the change of interaction energy. The results show that when the ceramic is under mechanical loading, the change of interaction energy can significantly affect the ferroelectric switching.

The models mentioned above are mainly based on a modified switching criterion assuming a complete switch, and this assumption can also be seen in other works [139-

143]. However, sudden change of strain or polarization may give rise to very high interaction fields and lead to an instability in calculation. Therefore, more sophisticated methods, like incremental switching theories, were introduced [144-162]. This method can provide smoother and more accurate prediction of hysteresis results, avoiding the instability due to grain interaction. Besides, another advantage of this model is that it can increase the accuracy in representing gradual switching by domain wall motion. As an example of improved accuracy, the incremental switching model can produce 90° switching during the unloading part of the hysteresis loop; this phenomenon is also observed in experiments [163].

Several incremental switching models have been built, and the interaction of grains was treated using Kroner's method[147, 148], Mori-Tanaka method[146, 149-153] and Hill's method[154-156]. A good example of these models is the model proposed in 1998 by Huber *et al.*[144]. Huber *et al.* developed a constitutive model for ferroelectric switching by using elastic-plastic crystal plasticity theory. In this model, the ferroelectric switching is described by the motion of domain walls, which is regarded as dissipative and induced by reduction of free energy of the system in the ceramic as its thermodynamic driving force. To be more specific, the domain wall motion gives rise to the change of the proportions of distinct crystal variants in each grain, which can be seen in figure 1.7. In observed microstructure, multiple domains are found in one grain. Hence, the concept representing domains by the volume fractions (c_I , $I = 1, 2, ..., N$) of each variant are adopted in this model. Here, the volume

fraction has two constraints, $c_I \geq 0$ and $\sum c_I = 1$. For simplicity, figure 1.7 just shows two variants in the switching process. With increments of shear stress, the material response is initially elastic. Then the volume of variant 2 increases due to the domain wall motion when the shear stress reaches a critical value. This is followed by the 'lock-up' phenomenon precluding additional ferroelectric switching with zero volume fraction of variant 2.

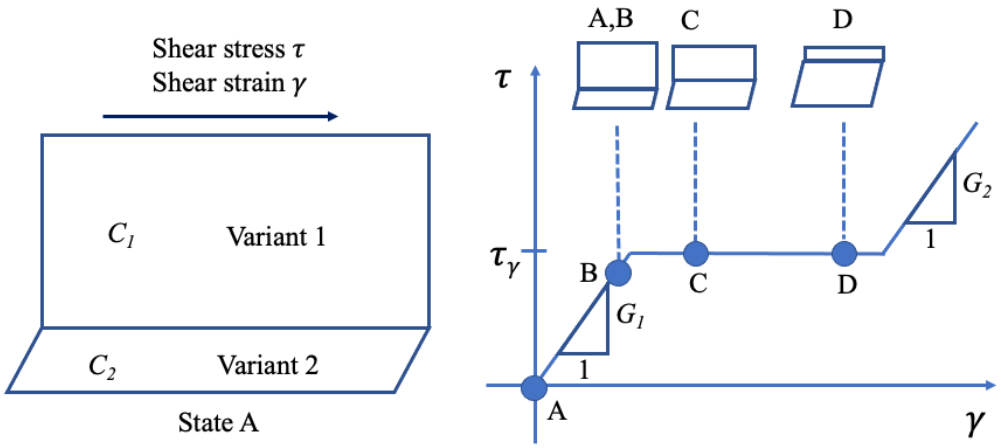


Figure 1.7 The progressive nature of ferroelectric transformation within a crystal due to domain wall motion.

In this incremental switching model, there is a set of M transformation systems α, which can be used to track the switching process from one variant state to another variant state. The number of transformation systems can be obtained by $M = N(N-1)$. The rate of switching $\dot{f}^{\alpha}$ is the incremental rate of change of volume fractions due to switching system α, and the rates of remanent strain and remanent polarization of a single crystal can be written as

$$\begin{aligned} \dot{e}_{ij}^{r} &= \sum_{\alpha=1}^{M} \dot{f}^{\alpha} \Delta e_{ij}^{r,\alpha} \\ \dot{P}_{i}^{r} &= \sum_{\alpha=1}^{M} \dot{f}^{\alpha} \Delta P_{i}^{r,\alpha} \end{aligned} \tag{1.7}$$

where $\Delta e_{ij}^{r,\alpha}$ and $\Delta P_{i}^{r,\alpha}$ are the changes of remanent strain and remanent polarization in each transformation system. In switching, the linear parameters in equation (1.2) can also change:

$$\begin{aligned} \dot{s}_{ijkl}^{E} &= \sum_{\alpha=1}^{M} \dot{f}^{\alpha} \Delta s_{ijkl}^{E,\alpha} \\ \dot{d}_{kij} &= \sum_{\alpha=1}^{M} \dot{f}^{\alpha} \Delta d_{kij}^{\alpha} \\ \kappa_{ik}^{\sigma} &= \sum_{\alpha=1}^{M} \dot{f}^{\alpha} \Delta \kappa_{ik}^{\sigma,\alpha} \end{aligned} \tag{1.8}$$

where $\Delta s_{ijkl}^{E,\alpha}$ is the elastic compliance change, Δd_{kij}^{α} is the piezoelectric coefficient change and $\Delta \kappa_{ik}^{\sigma,\alpha}$ is the dielectric permittivity change. Accordingly, $\dot{s}_{ijkl}^{E}$, $\dot{d}_{kij}$ and κ_{ik}^{σ} are the incremental rate of elastic compliance change, piezoelectric coefficient change and dielectric permittivity change respectively. So the switching criterion, which could determine the active transformation systems, can be written as

$$E_i \Delta P_i + \sigma_{ij} \Delta e_{ij} + \frac{1}{2} \sigma_{ij} \Delta s_{ijkl}^{E,\alpha} \sigma_{kl} + E_i \Delta d_{ikl}^{\alpha} \sigma_{kl} + \frac{1}{2} E_i \Delta \kappa_{ik}^{\sigma,\alpha} E_k \geq 2P^0 E_0 \tag{1.9}$$

The first two terms in equation (1.9) are the same as Hwang's model, but the extra three terms consider the internal energy change induced by the change of linear parameters. According to the second law of thermodynamics, the dissipation rate should always be positive during switching. The switching associated dissipation rate is $\dot{w} = G^{\alpha} \dot{f}^{\alpha}$, where $\dot{w}$ represents the dissipation rate and G^{α} is the driving force, so the $\dot{f}^{\alpha}$

should be positive to ensure the dissipation rate is above zero. One form of $\dot{f}^{\alpha}$ can be given by [161]

$$\dot{f}^{\alpha} = \dot{f}_0 \left| \frac{G^{\alpha}}{G_c^{\alpha}} \right|^m \left(\frac{c_I}{c_0} \right)^{1/k} \tag{1.10}$$

In the above, the $\dot{f}_0$ is a multiplier parameter, G_c^{α} is critical driving force and c_0 is an initial volume fraction. Then m and k are parameters determining the transformation rate and saturation sensitivity. Equation (1.10) is closely related to viscoplasticity in crystal plasticity models, wherein the shear rate on slip system is subjected to resolved shear stress at a slip resistance.

McMeeking *et al.* and Huber *et al.* [145, 162] produced finite element models based on incremental switching. These two dimensional and three dimensional finite element models were used to simulate a polycrystal. The finite element simulations generated effective results. Finite element models for the interactions of grains have been used by several authors in ferroelectrics modelling[161, 164-167]. Each domain, grain, or group of grains, is then represented by a specific element or group of elements with different remanent states, and the details of grain-grain interactions and non-uniform fields can be captured by using this method.

Ricoeur *et al.*[168-170] developed a condensed method based on thermodynamic framework and single-crystal constitutive relationships developed by Huber *et al.*[144] for polycrystalline ferroelectric materials, which is applicable to multiphase, multi grain and multiconstituent systems without being limited by specific material law. Additionally, this approach considers grain interaction, local residual stress and electric

displacement, which is associated with the local constraints by embedding single grains into an effective medium constituted by all the grains. Due to its wide applications, this method has been introduced to energy harvesting prediction using ferroelectric switching[171].

To avoid the discretization of finite element method, this method uses an averaging technique to calculate the remanent part of mechanical and electrical tensors for polycrystalline materials, showing smooth hysteresis loops of the bulk material under the external mechanical and electrical loading with the consideration of residual stress for each grain. A RVE with multiple grains with different material orientations are given in figure 1.8 for calculation, in which three exemplary grains with in-plane variants orientations α_i in tetragonal ferroeletrics are presented[170]. All the variants can be condensed to one material point, which can exhibit all possible variants in the grains, however, the switching can only occur in the six variants (four in-plane and two out-of-plane variants) of each grain.

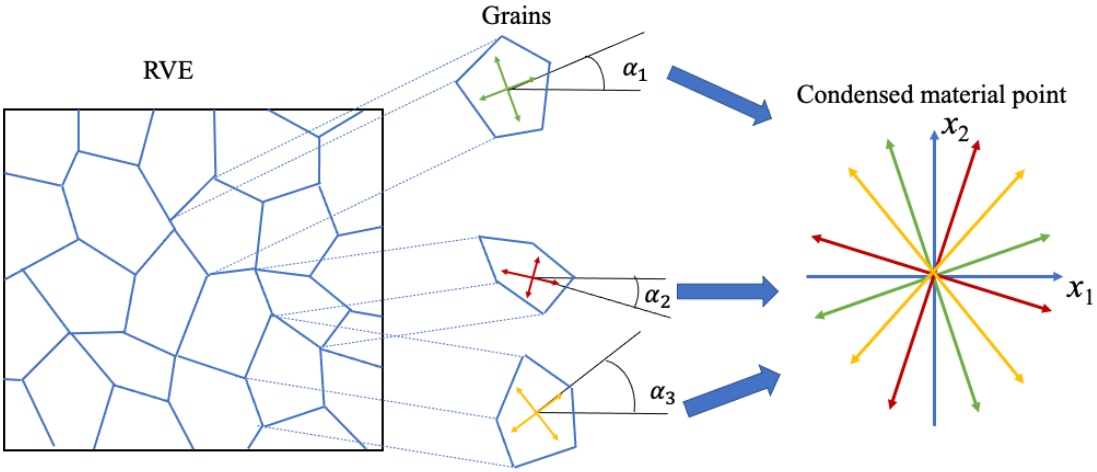


Figure 1.8 Representative volume element of a polycrystal and illustration of the condensed method.

An advantage of this methods is that it can be used to predict the material degradation of ferroelectrics wherein the residual stresses induce the growth of micro-cracks, with in-expensive calculation compared to the finite element method[172]. However, the condensed model also has some limitations, such as the difficulty in applying macroscopic field gradients and inaccuracy for problems where the domain's shape is significant.

1.3.2 Phenomenological constitutive models of ferroelectrics

The enormous number of internal variables of micro-electromechanical models may be a burden for calculation, and sometimes it is not necessary to acquire the states of each grain if only macroscopic properties are of interest[87]. Therefore, fewer internal variables are adopted in phenomenological models to simplify the calculation. These models construct constitutive relations between state variables in an empirical way, but maintaining consistency with the fundamentals of thermodynamics. The models have some similarity to the J_2 flow theory of plasticity, but they have been devised to predict the behaviour of ferroelectrics under arbitrary loading history.

In 1949, the earliest phenomenological model was proposed by Devonshire[173], with temperature-dependent remanent strain and dielectric parameters, considering a free energy function to describe the electrical non-linearity of ferroelectrics. Chen *et al.*[174, 175] developed models that can be used to explain the coupling between electric and mechanical properties. A one-dimensional model can be used to capture

the butterfly and dielectric hysteresis loop. A thermodynamically consistent model of ferroelectrics was presented by Bassiouny *et al.*[176-178], using a free energy function with temperature, polarization and strain as variables. This model introduces rate-dependent properties and the concept of electric hardening into the analysis.

Cocks *et al.*[179] developed a model based on two internal variables, remanent polarization and remanent strain to describe the thermodynamic state of ferroelectrics under isothermal condition. This model uses a convex yield surface, which is similar to metal plasticity theory. Within the convex yield surface, there is reversible change, meaning the linear response of the material. Increments of stress or electric field at the yield surface will cause irreversible changes. Considering Helmholtz free energy, the form of the free energy can be divided into two parts:

$$\Phi = \Phi^L(e_{ij}^L, D_i^L) + \Phi^r(e_{ij}^r, D_i^r) \tag{1.11}$$

where $\Phi^L(e^L, D^L)$ is the reversible part and $\Phi^r(e^r, D^r)$ is the irreversible part. The reversible part represents the energy stored due to elastic, piezoelectric and dielectric energy, while the irreversible part is the energy due to the ferroelectric switching arising from the internal fields. According to the second law of thermodynamics (Clausius-Duhem inequality), the rate of energy dissipation must not be negative:

$$\sigma_{ij}\dot{e}_{ij} + E_i\dot{D}_i - \dot{\Phi} \geq 0 \tag{1.12}$$

Then the convex yield surface can be assumed, of the form

$$\sqrt{\left(E - \frac{\partial \Phi^r}{\partial e^r}\right)^2 + \alpha\left(\sigma - \frac{\partial \Phi^r}{\partial D^r}\right)^2} - E_{con} = 0 \tag{1.13}$$

Here, the parameters α and E_{con} are material constants. The rates of remanent strain and polarization increase can be expressed as normals to the yield surface

$$\begin{aligned} \dot{e}^r &= \lambda \frac{\partial E_e}{\partial \sigma} \\ \dot{P}^r &= \lambda \frac{\partial E_e}{\partial E} \end{aligned} \tag{1.14}$$

where λ represents a multiplier, equivalent to the plastic multiplier in plasticity theory, and $E_e = \sqrt{\left(E - \frac{\partial \Phi^r}{\partial e^r} \right)^2 + \alpha \left(\sigma - \frac{\partial \Phi^r}{\partial D^r} \right)^2}$. Therefore, the remanent states can only be changed when the applied fields meet the yield criterion.

Landis [180] further developed a multi-axial generalization based on the uniaxial model of Cocks *et al.* [179] by using the remanent strain tensor and remanent polarization vector with a different free energy form. This model also accounts for the changes of elastic, dielectric and piezoelectric properties with switching. The resulting modified Clausius-Duhem inequality then gives

$$\begin{aligned} &\sigma_{ij}\dot{e}_{ij} + E_i \dot{D}_i - \dot{\Phi} \geq 0 \\ &\rightarrow \left(\sigma_{ij} - \frac{\partial \Phi^r}{\partial e_{ij}^r} + \frac{1}{2} \frac{\partial s_{pqrs}^E}{\partial e_{ij}^r} \sigma_{pq} \sigma_{rs} + \frac{\partial d_{rpq}}{\partial e_{ij}^r} E_r \sigma_{pq} + \frac{1}{2} \frac{\partial \kappa_{pq}^\sigma}{\partial e_{ij}^r} E_p E_q \right) \dot{e}_{ij}^r \\ &+ \left(E_i - \frac{\partial \Phi^r}{\partial P_i^r} + \frac{1}{2} \frac{\partial s_{pqrs}^E}{\partial P_i^r} \sigma_{pq} \sigma_{rs} + \frac{\partial d_{rpq}}{\partial P_i^r} E_r \sigma_{pq} + \frac{1}{2} \frac{\partial \kappa_{pq}^\sigma}{\partial P_i^r} E_p E_q \right) \dot{P}_i^r \geq 0 \end{aligned} \tag{1.15}$$

The methods discussed above are subject to the first law and second law of thermodynamics, and the assumption of maximum dissipation rate. But they are still built on an empirical basis to describe the response of ferroelectrics. It is necessary to define the linear parameters, such as piezoelectric coefficient, as a function of remanent strain and remanent polarization. In order to solve this problem, many researchers

simplify the models by assuming the piezoelectric tensor is linearly proportional to the remanent polarization[180, 181]. So a widely used form of yield surface is given by

$$\Phi = \frac{3\tilde{s}_{ij}\tilde{s}_{ij}}{2\sigma_0^2} + \frac{\tilde{E}_i\tilde{E}_i}{E_0^2} + \frac{\beta\tilde{s}_{ij}\tilde{E}_i P_j^r}{\sigma_0 E_0 P_0} - 1 \tag{1.16}$$

where σ_0 and E_0 are the coercive stress and coercive field, $\tilde{s}_{ij}$ is a deviatoric part of the first bracket in equation (1.15), and β is a constant. However, Shieh *et al.*[182] observed that the yield surface may have corners at loading points, which is an unexpected problem for the model discussed above. To track the corners, new internal variables would be needed.

It is also necessary, in the phenomenological models, to define the saturation of the switching process as observed in the experiment. This is done through a saturation surface, which can be defined as the boundary of states of remanent strain and polarization that can be attained. All states within the surface can occur, but states out of the surface cannot. In order to achieve this, the irreversible part of equation (1.11) would tend to infinity as the state reaches the saturation surface[180]. Experimental data is used to specify the surface.

Kamlah *et al.*[183] proposed a phenomenological constitutive model by using remanent strain and polarization as the internal variables, and extended it to three-dimensional problem analysis[184]. Later, Klinkel *et al.*[185] defined irreversible electric field as an internal variable instead of remanent polarization. Laxman *et al.*[186] developed a phenomenological model for nonlinear behaviour and creep response of ferroelectrics under the framework of irreversible thermodynamics. This

model used a non-iterative method to capture properties of ferroelectric materials such as electrical creep and mechanical creep. Kamlah *et al.*[187] also developed a model by using a number of unspecified internal variables. Using these unspecified internal variables, the remanent strain and polarization and even the linear elastic piezoelectric and dielectric properties can be described. This approach is somewhat similar to micro-electromechanical models, representing the domains' orientations by using a small number of internal variables, so that it can directly predict the saturation surface.

1.3.3 Other models for microstructures and nano-scale structures

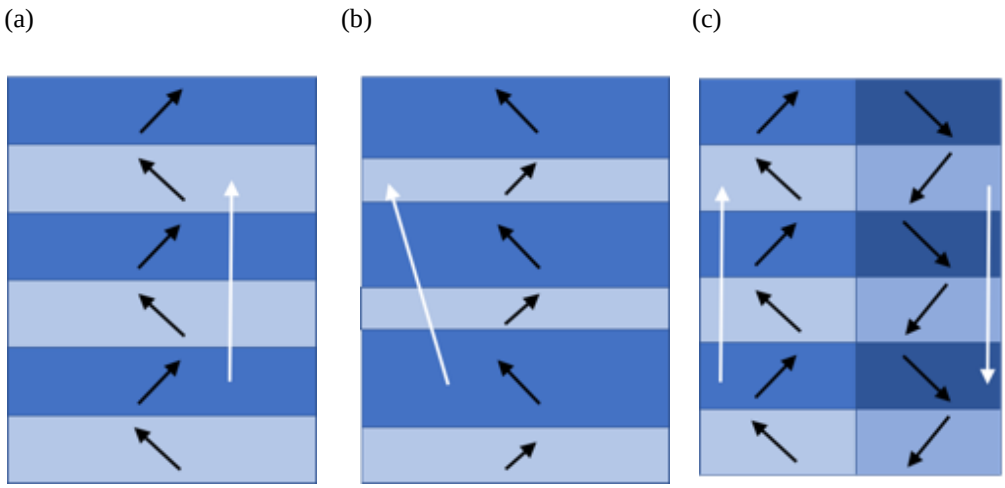


Figure 1.9. (a) Schematic illustration of laminar domain stack consisting of 90° domains. (b) Switching of polarization by the displacement of domain walls. (c) Switching of polarization by generating the new domain walls

Prior to a discussion of the models for microstructures and nano-scale structures, the range of the applications for micro-electromechanical and phenomenological simulation techniques should be discussed. Most of the phenomenological and micro-

electromechanical models do not consider the real shapes of grains, and the information about field variation within grains is lost. Although some researchers began to use finite element methods to represent the grains in ferroelectrics and so capture the detailed behavior within each grain, this approach needs extensive computation to produce meaningful results. Besides, phenomenological models designed to capture the response of bulk ferroelectric materials are poorly suited for use within the individual grains. However, advances in miniaturized ferroelectric devices require more accurate modelling techniques for microstructure and nano-scale structure of ferroelectrics to study such problems as fracture and fatigue of the materials caused by the intergranular stresses [188-193]. Therefore, theories such as the laminate theory of domains, phase-field methods, Monte Carlo simulation and atomic methods have been introduced to investigate the specific arrangement of microstructure or nano-scale structures.

The idea of lamellar domains arranged on the basis of energy minimization principles to reduce the internal electric charge and misfit strain at interfaces was proposed by Weng *et al.*[149-151] and Kreher *et al.*[147, 148] Figure 1.9 gives the details of a typical laminar domain with 90° domains. Models show that a minimum energy configuration could be established with an average randomly oriented remanent polarization or strain. Li *et al.*[194] followed the martensitic microstructure investigations of James *et al.*[195] to propose a theory of multi-rank laminates using the principles of domain wall compatibility. These models treat the microstructure as a

periodic, multi-rank laminate of ferroelectric domains, and low energy structure is given due to the compatibility at each level of lamination.

(a) (b) (c)

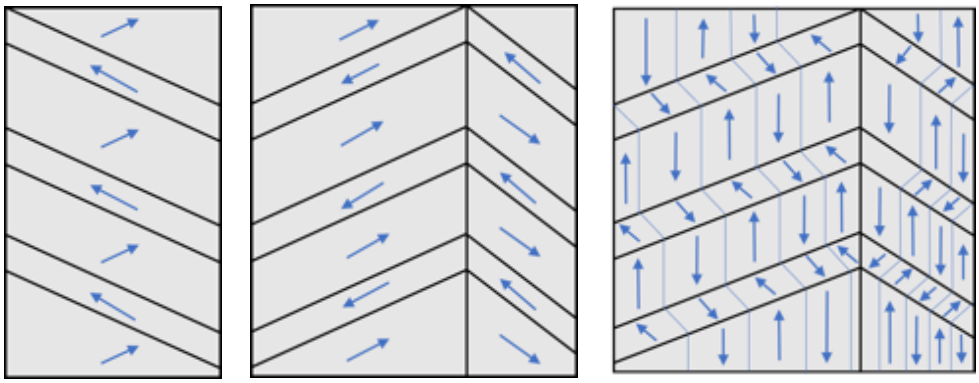
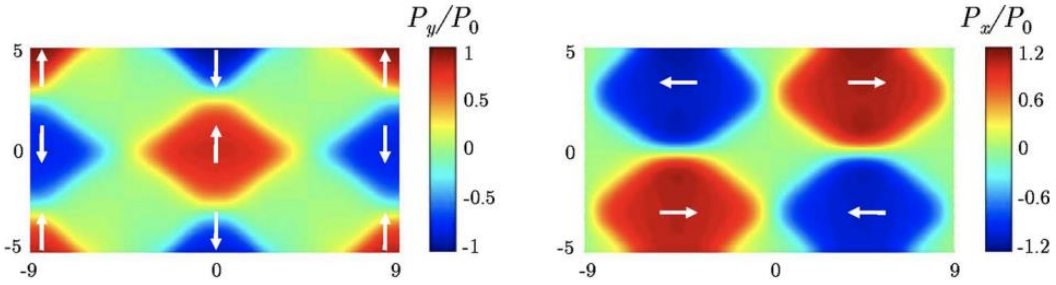


Figure 1.10 Schematic illustrations for periodic (a) rank-1, (b) rank-2, and (c) rank-3 laminate structures.

Figure 1.10 shows typical laminate domain structures. This also allows the linear parameters, such as piezoelectric and elastic coefficients, to be computed using exact expressions. By making use of the advantages of these models, large single crystals with organized domains and realistic microstructures can be studied to have a better understanding of ferroelectric microstructures.

The phase field model[196, 197] is developed to predict the behaviour of ferroelectric film and specific domain patterns, such as band-like and stripe-like patterns observed in experiments, and it is also a useful tool to investigate the energy harvesting devices with specific domain patterns. Specifically, the phase-field models focus on the modelling of motion of individual domain walls. This kind of model treats spontaneous polarization as a gradient order parameter, which can vary continuously through the domain walls [198-206], see figure 1.11.

(a)



(b)

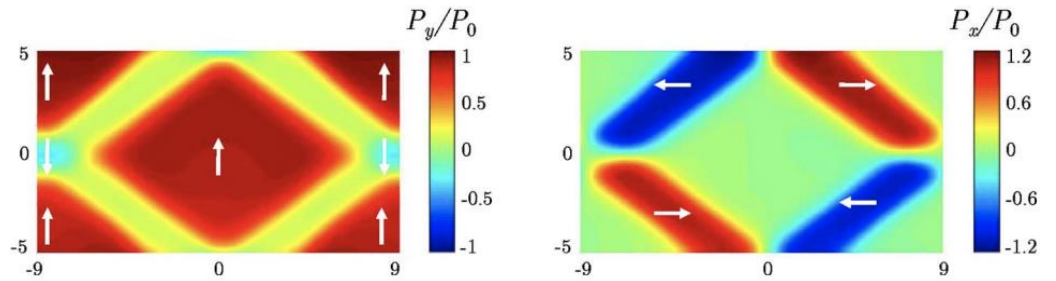


Figure 1.11 Equilibrium polarization distributions of x-y plane normalized by the spontaneous polarization. (a) Electric field E=0; (b) Electric field E=2.066E_0. Reprinted from Ref. [196], with permission from The American Society of Mechanical Engineers(ASME).

Among these models, the minimization of free energy such as the elastic energy and gradient energy, is used to infer the motion of domain wall. This can also be regarded as an equilibrium of energy between the work done by external loads and energy stored in domain walls. The resulting evolution law is the time-dependent Ginzburg-Landau equation given by

$$\frac{\partial \vec{P}(\vec{r},t)}{\partial t} = -L\frac{\partial F}{\partial \vec{P}(\vec{r},t)} \tag{1.17}$$

Here $\vec{P}$, t, $\vec{r}$, L and F are order parameter, time, position vector , kinetic coefficient of motion of domain walls and free energy respectively. Models of this kind

allow the formation and evolution of the domains without having to consider the response of specific domains or domain walls. They are particularly useful for solving some problems at the nano-scale, such as estimating the lattice mismatch or misfit stress, distortion due to electric field, surface effects, intergranular stresses, nucleation of domains and size-dependent effects, which play a great role in the design of nano-scale actuators and energy harvester. However, these models are computationally intensive and at present are typically limited to micrometer sized volumes because of the scale of computation required.

At atomistic level, there are two kinds of ferroelectric models used to interpret the crystal structure and atomic interactions, namely the first principles methods and molecular dynamics methods. These models do not need any macroscopic empirical data to assist the analysis, hence they are well placed to predict the behaviour of hypothetical material structures. First principles calculations[207, 208] use quantum-mechanical theories to simulate the interactive atomic forces, and typically study minimum energy states to find a stable structure. However, this method is normally only used at absolute zero temperature, and any application at other temperatures requires extrapolation that may not be completely reliable. Molecular dynamics methods[209-211] treat the interaction of atoms as non-linear springs, and the minimization of energy stored in these springs can also identify stable states. The methods used here are akin to the principles used in phase-field models, but these

models are computationally expensive, limiting their ability to simulate the behaviour of numerous unit cells.

1.3.4 Summary

In this thesis, an energy harvesting system using ferroelectric switching is to be developed, using a bulk polycrystalline ferroelectric layer with randomly oriented microstructures, with a substrate to apply stress to the ferroelectrics. To understand this macro-scale energy harvesting, it should be sufficient to consider macroscopic models where only the average change of polarization and strain over the grains is considered. It may not be necessary to consider the domains and domian walls in detail. Based on the discussion above, the micro-electromechanical and phenomenological models appear suitable for investigation of the energy harvesting cycles. The phenomenological models have the advantage of simplicity and reliability due to fewer internal variables. However, the empirical data should also be introduced to calibrate the constitutive relations and state variables, which requires corresponding experiments. The micro-electromechanical models can capture the behaviour of each grain, so the configuration change during energy harvesting cycles can be obtained. In terms of the design of energy harvesting, the model developed by Hwang *et al.*[66] is one of the best choices due to its simplicity and low computing cost. Thus it can be an efficient and effective way to explore new concepts for energy harvesters using ferroelectric switching. However, this model does not consider the interactions of

grains, which may influence the results of energy harvesting cycles. A finite element model[92] based on incremental switching could be used to improve the accuracy of Hwang's model for energy harvesting applications. Although the finite element model requires more intensive computing power, the details of grain-grain interactions and structural interactions with a substrate can then be captured providing an improved insight into the operation of energy harvesting cycles, and assisting optimization.

1.4 Thesis structure

Four chapters of original work are presented in this thesis, wherein each chapter details the results focused on a specific research topic. The research work firstly proposes the concept of using ferroelectric/ferroelastic switching in polycrystalline materials for energy harvesting. This is further verified through experiments. The chapters are arranged as follows: Chapter 1 provides the basic idea and motivations for the research, as well as the key concepts of ferroelectric materials and the material models.

Chapter 2: This chapter evaluates the relevant literature about vibrational energy harvesters, including piezoelectrics, triboelectrics and ferroelectrics. Some typical and high-performance piezoelectric, triboelectric and ferroelectric energy harvesters based on vibrations are described and the mechanisms, advantages and disadvantages and characteristics of each of them are discussed in detail. This chapter provides a critical review to identify the significance of the research and give the rationale for the approach taken in this work.

Chapter 3: This chapter gives detailed information about the methods used in both modelling and experiments. Firstly, a modelling method describing the micromechanical model - Hwang's model is presented for energy harvesting cycle calculation, which provides the fundamental analysis for Chapter 4. Additionally, the

fabrication of specimens in the experiments for Chapter 5-7 are given, and the test arrangements can also be found in this chapter.

Chapter 4: A prospective energy harvesting cycle based on ferroelectric/ferroelastic switching is developed. Hwang's switching model is then used to analyse the proposed cycle. The cycle uses depolarization by stress, followed by repolarization with combined electromechanical loading. This chapter provides a fundamental and theoretical analysis for energy harvesting and paves a pathway for the subsequent work of practical devices in Chapters 5-7.

Chapter 5: A novel, practical ferroelectric energy harvester for low-frequency applications is experimentally established by exploiting partial ferroelectric/ferroelastic switching. A partially poled PLZT ceramic layer and stiff steel substrate are bonded together. The poling process is then completed, resulting in a state of residual stress in the electroceramic. The internal residual electric fields, generated during a partial depoling of an electroceramic, provide "memory" of a preferred direction for repolarizing the energy harvester in each cycle of loading. The resulting energy harvesting cycles achieve much greater energy density than conventional piezoelectric devices, comparable with triboelectric generators. This cycle is explored through quasi-static tests and vibrational tests, which are detailed in Chapters 6 and 7.

Chapter 6: This chapter focuses on exploring the energy harvesting cycle based on partial ferroelectric/ferroelastic switching, in quasi-static experiments. Various

engineered states of the ferroelectric material element, which are associated with residual fields in the materials, are established and presented. The energy output is measured and the material state is varied in a parametric study. Here, four kinds of specimens with 100%, 75%, 50% and 30% pre-poled states are tested and analysed. Cycles using either tensile stress or compressive stress are discussed here, and the amplitudes of mechanical loads are also varied.

Chapter 7: This chapter explores the energy harvesting system in dynamic cyclic loading. The stability and robustness of the selected energy harvesting cycles are tested, along with the frequency dependence of the energy harvesting cycle. The performance of partially pre-poled specimens is explored at a range of operating frequency, and the effect of external resistive loads is studied. Furthermore, the results include fatigue data and an optimization of resistive loads at one specific frequency with up to 0.55 million cycles. This chapter is an extensive supplement to the discussion in Chapter 5.

Chapter 8: Conclusions are given, drawing together and discussing the most important arguments in each chapter of this thesis, and highlighting the advantages and disadvantages of the ferroelectric energy harvester compared to others. The final part of the thesis is a discussion of future work that could follow from this DPhil research project.

Chapter 2

2. Literature review of energy harvesters

This chapter reviews the literature to date relevant to the developments of transducers using piezoelectrics, triboelectrics and ferroelectrics. The review focuses on the introduction of the various energy harvesters, the importance and significance of them, the comparison of different kinds of energy harvesters and the working situations associated therewith. The review of vibrational mechanical energy harvesting covers several aspects such as improvements in piezoelectric energy harvester design, multi-direction energy harvesting and materials optimization. Some new energy harvesting methods using triboelectricity and ferroelectricity are also described in this chapter.

The layout of this chapter is organized as follows: section 2.1 introduces piezoelectric energy harvesting and then focuses on the improvement of piezoelectric energy harvesters by varying the materials and structures, some of which are controlling the resonant frequency and broadening the bandwidth. The selection of materials is also discussed. In section 2.2, four types of triboelectric energy harvesters are presented, and the applications of them are briefly shown. Section 2.3 mainly demonstrates the working principle of energy harvesters using ferroelectric/ferroelastic switching systematically. Finally, the conclusion and perspective for future development are given in section 2.4.

2.1 Piezoelectric energy harvesting

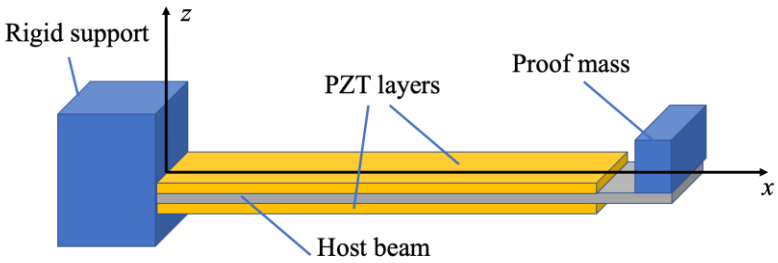


Figure 2.1 Basic prototype of the piezoelectric energy harvester.

The basic concept of piezoelectric energy harvester is a cantilever with an inertial mass at the end and piezoelectric layers, as proposed by Lu *et al.* in 2003[212], see figure 2.1. For this cantilever piezoelectric energy harvester, there are bimorph and unimorph modes consisting of two or one piezoelectric layers, respectively. Lu *et al.*[212] analyzed the characteristics of the basic prototype of the piezoelectric energy harvester. During the vibrational cycle, the piezoelectric layer can convert mechanical strain caused by the beam movement into charge [11, 213], through the piezoelectric effect. Then an appropriate external circuit can store the electrical energy or use the energy directly.

The piezoelectric tensor is a third-ranked tensor of piezoelectric coefficients, wherein the coefficient is measured in the direction of applied field the longitudinal coefficient (d_{33}), in the direction perpendicular to the field the transverse coefficient (d_{31}) and other piezoelectric coefficients are shear coefficients (d_{15}). Due to the symmetries of the strain and stress, the number of independent piezoelectric coefficients is thus reduced from 27 to 18, which can be further reduced by the

symmetry of the material. The matrix of piezoelectric coefficients usually has 6×3 dimensions with 5 non-zero elements [214].

There are two working modes of piezoelectric energy harvesters, which have continuous electrodes in d_{31} mode and interdigital electrodes in d_{33} mode[215, 216]. d_{31} mode uses the stress or strain perpendicular to the polarization to generate electrical potential, while the stress or strain along the polarization axis can produce electrical change in d_{33} mode. Generally, the value of d_{33} is about twice that for d_{31}, so using d_{33} mode can improve the energy output. By optimizing the IDEs design, the d_{33} mode can produce greater energy output and voltage than d_{31} mode [216, 217]. However, due to the high voltage, electrical breakdown in d_{33} mode should be considered when it is designed. Despite the higher piezoelectric constant in d_{33} mode, the results show that only when the parameters are appropriately designed, can the output power be higher than that of d_{31} mode energy harvester. Therefore, d_{31} is more widely used in practical applications because of the simple structure.

There has been great interest in optimization of piezoelectric transducers, including changing device configuration, optimizing material choice, and extending to multi-direction energy scavenging[218-225]. It is known that if the resonant frequency of the structure is close to the ambient vibration frequency, the amplitude of the resonant vibration can reach a maximum value, which would generate more energy because of the greater mechanical displacement[226, 227]. Based on this, the generator should be designed to absorb the ambient vibrational energy near its resonant

frequency. In Lu *et al.*'s work [212], the maximum output power was 0.64 mW at the frequency of 2939 Hz. However, the generator is not effective for harvesting low frequency vibration energy that is more commonly found in the environment. To improve the efficiency of piezoelectric energy harvesters, researchers have attempted optimizing their structures. Some researchers concentrated on reducing resonant frequency, or fitting the ambient vibration source's frequency[66], while others focused on broadening the vibration frequency range to enhance the adaptability[71, 228-231].

Furthermore, although the one-dimensional piezoelectric energy harvesters are widely investigated to optimize their operating frequency, the vibration sources with random directions raise a challenge for their practical implementation in ambient environment. The challenge is clear: the energy harvester can harvest energy in their designed direction but cannot work with other vibration directions. Thus vibrational energy harvesting for multiple directions was also developed in recent years to adapt to the random vibration sources[232-236].

Improvements in the materials used in energy harvesters are also highlighted as a good way to improve efficiency of the systems and broaden the applications [237-243]. In general, several piezoceramics, like $LiNbO_3$, $BaTiO_3$, $PbTiO_3$, $LiTaO_3$ and PZT are discussed for piezoelectric energy harvesting. Besides, PVDF, ZnO and single crystals including PZN-PT and PMN-PT have also been introduced in energy harvester designs and fabrications [4-6, 221]. PZT is the most popular piezoelectric material used in the past owing to its high piezoelectric coefficient, and the lanthanum doped PZT is used

in the current work due to its relatively lower coercive field than that of other PZT materials. This section mainly reviews the typical structures and materials selection in piezoelectric energy harvesters separately.

2.1.1 Improvements of structure design

In last decade, to reduce the resonant frequency, many configurations have been tried out, and some typical examples are discussed here.

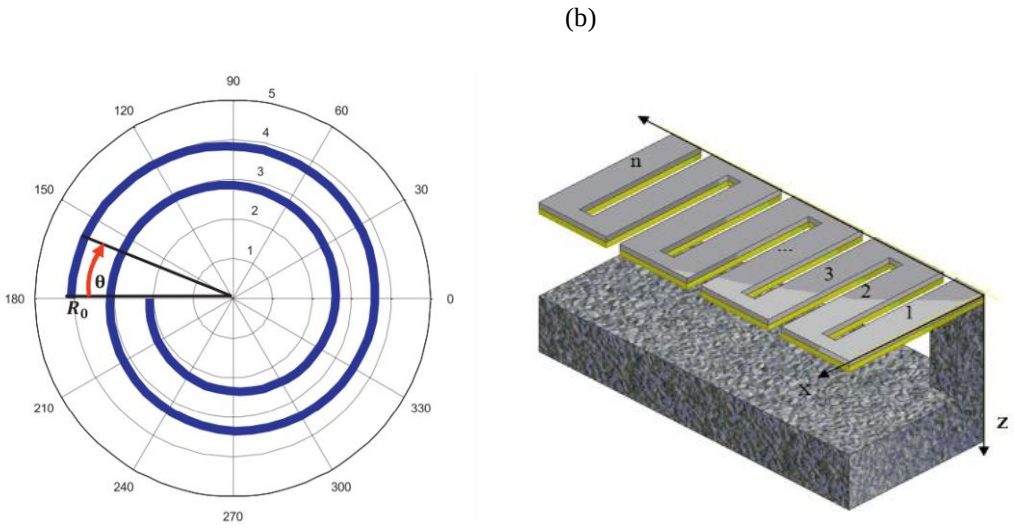


Figure 2.2 (a) Vertical view of spiral beam. Reprinted with the permission from [244]. Copy right 2010 Elsevier. (b) The zigzag energy harvesting structure. Reprinted with the permission from [245]. Copy right 2011 ASME Publishing.

One of the effective methods for decreasing the resonant frequency is to reduce the stiffness of the structure. Through changing the parameters of the cantilever, Fang *et al.*[246] developed a composite MEMS-based piezoelectric energy harvester, which decreased the resonant frequency and improved energy output. This energy harvester's ratio of length to thickness is above 100, reducing the resonant frequency to 608 Hz. In

2005, Leland *et al.*[226] proposed a structure with preload, which is different from other cantilever energy harvesters. It can be seen that the resonant frequency can be adjusted by the preload from 200 Hz to 250 Hz. This method provides an effective way of controlling energy harvesting using a varying vibration source. Although the resonant frequency can be reduced by adjusting the geometrical parameters of the cantilever, space limitation may affect the operation in some situations, especially when the frequency is below 100 Hz. Thus, a spiral beam was proposed by Karami *et al.*[244], see figure 2.2(a), wherein both bending and torsional vibration are considered. Although these two vibration modes can generate electric energy, it is noted that torsional vibration energy is very difficult to collect, demanding the addition of one more pairs of electrodes. This structure was further then developed by Zhao *et al.*[247], establishing a three dimensional energy harvester with triple working frequency. Karami *et al.*[245] presented a zigzag microstructure for energy harvesting, see figure 2.2(b). This structure increases the length of the beam, reducing resonant frequency. In addition, if the same load is applied at the end of a zigzag beam or a cantilever, the deflection of the zigzag beam is several times as much as that of the cantilever, indicating the potential for larger power output. Later, a two-dimensional zigzag-like energy harvester was proposed by Sharpes *et al.* [248], which utilized the concentrated stress to improve the energy output. By changing the two-dimensional shape of the beam, the torsional effect was eliminated, and the resonant frequency does not change much. A ring shaped cantilever was presented to harvest low frequency vibrational

energy[249]. It is like a curved long cantilever, which is similar to the zigzag shape beam, where the resonant frequency is low. Rezaeisaray *et al.*[250] designed, fabricated and tested a multi-degree of freedom micro-energy harvester with a proof mass supported by four piezoelectric elements. One of the advantages of this structure is that first three vibration modes (71.8, 84.5, and 188.4 Hz) were in the low frequency range, which are below 200 Hz. Additionally, due to the multi-degree of freedom design, the deflection is larger.

Table 2.1 Summary of attempts for reducing resonant frequency in piezoelectric energy harvesting (NG: Not Given)

Reference	Year	Active material	Shape/ strategy	Resonant frequency /Hz	Active material Volume/cm^3	Power output/mW	Cycle energy density / mJ cm^{-3}
Lu[212]	2003	PZT-PIC 255	Cantilever	2939	5×10^{-4}	0.64	0.435
Fang[246]	2006	PZT	Cantilever	608	1.97×10^{-6}	2.16×10^{-3}	1.81
Leland [226]	2006	PZT	Preload	200-250	77×10^{-3}	0.3-0.4	$20\text{-}21\times10^{-3}$
Karami [244]	2010	NG	Spiral	10^{-2}-10^{6}	NG	NG	NG
Karami [245]	2010	NG	Zigzag	8.18-142	1.55×10^{4}	NG	NG
Massaro [249]	2011	AIN	Ring	64	NG	NG	0.47
Sharpes [248]	2015	PZT	Zigzag	68.1	NG	81.3×10^{-3}	NG
Rezaeisaray [250]	2015	AIN	Multi DOF	97	NG	0.136×10^{-3}	NG
Zhao [247]	2016	PZT	Spiral	16	6.6	0.33	3.13×10^{-3}

A performance summary of these attempts for reducing resonant frequency in piezoelectric energy harvesting is listed in Table 2.1, wherein the cycle energy density is the amount of energy generated by the energy harvester per unit volume of active material in a working cycle. This table shows that the resonant frequency has been

gradually reduced by optimising the structural designs of piezoelectric transducers. By contrast, the energy density per cycle seems not to be remarkably increased, because the lower resonant frequency may require more tricky designs of structures.

In order to widen the applications of piezoelectric energy harvesters, another effective way is to broaden the bandwidth around the resonant frequency of the structures. Then, the piezoelectric transducers can be used in varying vibration environment. Song *et al.*[251] proposed a stopper model, see figure 2.3(a), decreasing the effective length of the vibration cantilever, leading to a higher resonant frequency of the structure. By modifying the distance between the stopper and cantilever, the resonant frequency can be changed with the increase of distance. To increase the vibration bandwidth of the structure, Erturk *et al.*[252] proposed an L-shaped piezoelectric energy harvester, as shown in figure 2.3(b). The structure consists of two basic vibration elements. The two beams and proof masses arrangement ensures a broad vibration band, as the two-degree-of-freedom system can make the first two resonant frequencies relatively close to each other, or further apart by changing the mass and beam parameters. Based on this structure, Li *et al.*[253] further studied the torsional effect during energy harvesting cycles. A novel energy harvester was proposed by Chen *et al.*[254], as shown in figure 2.3(c). This one-dimensional PPCB is separated into parts by adding mass at several positions. If the lengths of beams are different, there would be a band gap between different parts. Therefore, vibrational wave cannot be

conveyed through this direction, and different parts can absorb energy with different driving frequency, broadening the bandwidth of the energy harvester.

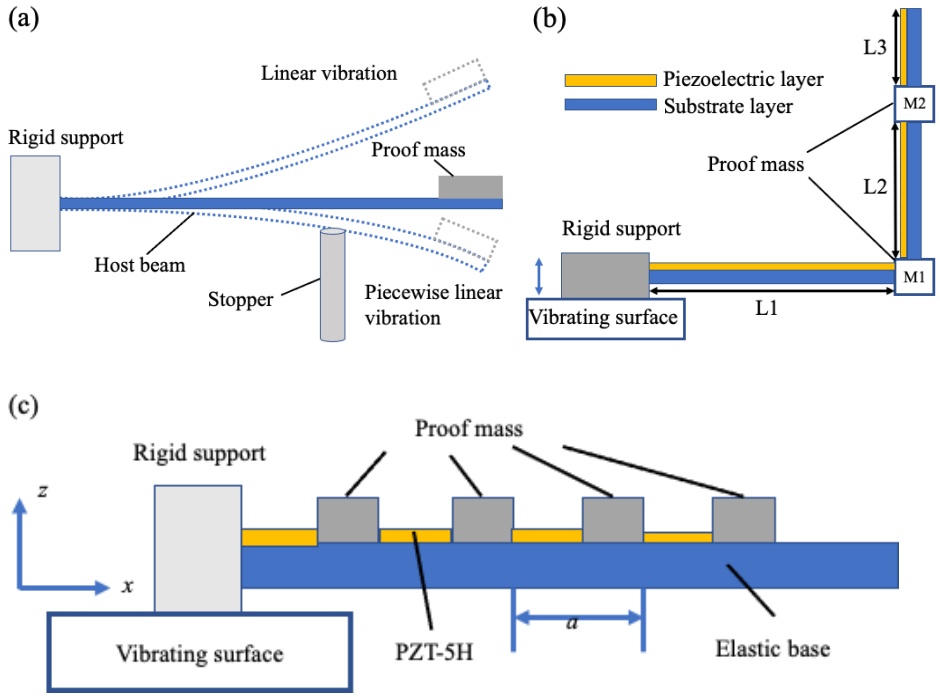


Figure 2.3 (a) Cantilever vibration with a stopper. (b) Schematic of the L-shaped piezoelectric energy harvester.(c)Diagram of a one-dimensional PPCB.

Regarding the bandwidth of energy harvesters, many researchers have investigated this area by using a cantilever array of the energy harvesters [227, 255-257]. This cannot only widen the bandwidth, but also increase the output power. Liu *et al.*[227] used three cantilevers to harvest ambient vibration energy, with resonant frequency 229 Hz, 234 Hz and 226 Hz, respectively. Under 0.5g vibration acceleration, output power density is 140 mW/cm^3. The total output power is not a simple sum of the individual cantilever powers due to the phase difference.

For higher output power and wider resonant frequency band, researchers investigated bistable energy harvester. Daqaq *et al.*[258] have summarized the

development of this area. By adding permanent magnets, a ferromagnetic cantilever can be under ferromagnetic force to generate non-linear effect. This will help to create larger displacement of the cantilever even when the driving frequency is not far from the resonant frequency. This approach can improve the energy output with the resonant frequency of the structure ranges from 4 to 22 Hz, or from 9.4 to 15.8 Hz by using attractive force or repulsive force. Other designs of this type can be seen in [54, 259-261].

Additionally, to enhance the power density of piezoelectric transducers, some improvements to structures have been made. A cymbal type energy harvester was proposed by Li *et al.*[262]. The cymbal elastic element can convert the vertical load into two parts: tensional stress perpendicular to the poling direction and compressive stress in the poling direction, improving the stability of the structure and increasing the power density. Other similar designs can be found in [263, 264], one of which can amplify the force 21 times, with an 18% energy conversion efficiency. A shell structure or ‘rainbow’ design can create larger strain than the conventional flat plate structure. Thus some shell type energy harvesters were presented in [265, 266]. A piezoelectric circular energy harvester has been proposed by Wang *et al.*[267], with a working principle like a beam with fixed ends and pre-loads. The array energy harvester can get higher output voltage and power density than single energy harvester. Other designs based on a circular membrane can be found in [268-271], with various loads patterns. As for a bending cantilever, there is a stress concentration at the fixed end of the

structure and no stress at the free end. Trapezoidal geometry of cantilever can make the strain distribution more even, which will result in greater energy density than the rectangle shape[272]. It is demonstrated that the trapezoidal geometry can provide more than twice the power density of a normal energy harvester. This method has been developed using both simulation and experimental work[273]. The piezoelectric coefficient d_{15} is greater than d_{33}, hence Ren *et al.*[274] designed a piezoelectric energy harvester based on d_{15} mode. By attaching the PMN-PT wafer to the base and beam, the shear force generated in the wafer can drive the energy harvesting cycle with an appropriate polarization direction. The output energy density per cycle was 0.88 mJ/cm^3 obtained at 60 Hz. Furthermore, it can use smaller volume of PMN-PT to achieve this high output voltage and power. By contrast, the problems are that the structure may be unstable due to the weak attachment between wafer and base and the manufacturing problems.

2.1.2 Improvements of materials

Various types of continuously developed piezoelectric materials, such as single crystals, ceramics, polymers and composites are used for energy harvesting to improve the performance of transducers. Piezoelectric ceramics have high piezoelectric coefficient and dielectric constant, but they cannot be subjected to large strain due to being brittle. Piezoelectric single crystals may have larger piezoelectric coefficient than ceramics, but have drawbacks of high cost, reduced toughness and high damping.

Piezoelectric polymers have more flexibility, but the piezoelectric coefficient is relatively low. Hence, by combining single crystals and polymers, polymeric piezoelectric composites can be used for flexible and high energy output energy harvesting. Furthermore, due to the toxicity of lead, new materials without lead have attracted attention. In this section, typical enhanced piezoelectric energy harvesters using single crystals, ceramics, polymers, NWs, porous piezoelectrics and composites are briefly discussed and reviewed.

The common materials used for energy harvesting are piezoelectric ceramics, such as PZT, with high piezoelectric coefficient and relatively low cost[275]. Due to its high electromechanical coupling, the electroceramic can be a good choice for energy harvesting using ferroelectric/ferroelastic switching. However, the performance of PZT can be improved upon. The piezoelectric coefficients d_{31} and d_{33}, which are generally around -50 pC/N and +100 pC/N respectively. Some researchers focused on improving the coupling coefficient of piezoelectric ceramics. For example, Gao *et al.*[276] fabricated a piezoelectric ceramic PNN-PZT, where the coupling coefficient reaches a similar level to that of high-performance piezoelectric single crystals. Another newly developed piezoelectric ceramic for energy harvesting is MnO_2 doped PZN-PZT by Yue *et al.*[277], whose d_{33} coefficient is 314 pC/N. Apart from the high coupling properties, researchers also focus on reducing the toxicity of the lead-based piezoelectric ceramics by developing lead-free piezoelectric materials. Lead-free piezoelectric materials are reviewed in [278, 279]. The improvements of piezoelectric

ceramics are summarized in Table 2.2, including both the electroceramics with high coupling coefficient and lead-free compositions. It can be seen that the piezoelectric coefficients of lead free electroceramics can be significantly improved for energy harvesting; however they are still less than that of the lead based ceramics.

Table 2.2 Summary of piezoelectric ceramics for energy harvesting (NG: Not Given)

Reference	Year	Active material	Shape/ strategy	d_{31}/pCN^{-1}	d_{33}/pCN^{-1}	Operation frequency/Hz	Active material Volume/cm^3	Power output/mW	Cycle energy density/ mJ cm^{-3}
Kim[280]	2015	NKN-BNT	Pressing	NG	204	1	0.0785	19.3×10^{-6}	0.246×10^{-6}
Kang [281]	2015	BNT-BT	Pressing	NG	164	NG	NG	18×10^{-6}	NG
Yang [215]	2016	PZT-5H	Cantilever	-275	NG	39.5	0.0288	0.11	0.0967
Yue[277]	2017	PZN-PZT+ MnO_2	Cantilever	NG	314	90	NG	0.098	0.324
Zheng [282]	2017	Mn-KNN	Cantilever	NG	122	90	0.5	0.016	0.0036
Gao[276]	2018	PNN-PZT	Cymbal	NG	1753	780	53.2×10^{-3}	14	0.34
Shin [283]	2018	BZT-BCT	Pressing	NG	464	NG	NG	NG	0.158
Yan[284]	2018	Mn BZT-BCT	Cantilever	-130	NG	92	5.51	0.068	0.013
Wu[285]	2018	KNN–BNZ–AS–Fe	Pressing	NG	500	2	NG	NG	NG

It is known that single crystals can have greater piezoelectric coefficients than general PZT ceramics. Therefore, some researchers use single crystals instead of PZT in energy harvesting devices. It is also promising to use single crystals in ferroelectric energy harvesting, but the fatigue performance and the costs should be taken into account carefully. Some typical uses of single crystals for energy harvesting are

summarised in Table 2.3, where most of the cycle energy densities of single crystals are greater than those of the electroceramics in Table 2.2.

Table 2.3 Summary of piezoelectric single crystals for energy harvesting (NG: Not Given)

Reference	Year	Active material	Shape/ strategy	d_{31}/pCN^{-1}	d_{33} /pCN^{-1}	Operation frequency/Hz	Active material Volume/cm^3	Power output/mW	Cycle energy density/ mJ cm^{-3}
Eturk [286]	2008	PMN-PZT	Cantilever	2252pm /V	NG	1744	0.106	1.41	7.6×10^{-3}
Mathers [287]	2009	PMN-PT	Cantilever	NG	400	1300	1.63×10^{-3}	0.3	0.14
Moon [288]	2009	PMN-PZT	Cantilever	NG	NG	630	0.0313	0.28	0.5×10^{-3}
Xu[289]	2012	PMN-PT	Cantilever	-650	NG	102	0.125	3.7	0.3
Yang [215]	2016	PZN-PT	Cantilever	NG	NG	37.5	0.0288	0.43	0.398
Yang [215]	2016	PMN-PT	Cantilever	-920	NG	38	0.0288	0.257	0.235

Among all the energy harvesters using single crystals, Xu *et al.*[289] used a low-frequency and high-performance cantilever piezoelectric energy harvester using single crystal material $0.71Pb(Mg_{1/3}Nb_{2/3})O_3$-$0.29PbTiO_3$. Other typical energy harvesters using piezoelectric single crystalline PMN-PT and PMN-PZT are given in [286-288], with great improvements of the power output. Yang *et al.*[215] analysed technical characteristics of cantilever energy harvesters using PZT, PZN-PT and PMN-PT, which can illustrate the difference between ceramics and single crystals. The results show that the output power density, output voltage of PZN-PT energy harvester and PMN-PT are higher than those of PZT(See Table 2.2 and 2.3). Shahab *et al.*[290] compared the performances of several piezoelectric ceramics and single crystals in the bimorph cantilever energy harvester, in which soft ceramics, hard ceramics, soft single crystals

and hard single crystals are investigated. The results suggest that PMN-PT is the best choice for band-limited off-resonance vibration, while hard piezoelectric ceramics outperform other materials under wideband random excitation.

The piezoelectric polymer PVDF, has widespread use due to its light weight, low cost and flexibility, despite its piezoelectric coefficient being quite low at less than one tenth that of PZT. Besides, due to its high coercive field, this kind of material is not suitable for energy harvesting using ferroelectric/ferroelastic switching. However, by increasing the percentage of β phase, the piezoelectric coefficient of PVDF can be improved: this can be used for flexible and wearable electronics. Several research groups concentrated efforts on increasing the proportion of β phase to 62%~88.5%, by a variety of methods. The results showed increased piezoelectric coefficients, by a factor of maximum 4.26 and improved efficiency. Cycle energy densities of 0.7~3.1 mJ/cm^3 were achieved[291-298].

Piezoelectric composites combine the advantages of both crystals and polymers, which have high piezoelectric coefficient and high flexibility and robustness. There is great research interest in implementing composites into energy harvesting to improve the performance. Some typical piezoelectric composites for energy harvesting are summarised in Table 2.4, wherein the cycle energy densities are generally greater than the values listed in Table 2.2 and 2.3. Besides, by embedding nanoparticles or nanowires, the material properties have been significantly improved relative to

conventional polymer ferroelectrics, exhibiting greater performance of piezoelectric coefficients, transparency, light weight, sensitivity and flexible configurations.

Table 2.4 Summary of piezoelectric composites for energy harvesting (NG: Not Given)

Reference	Year	Active material	Shape/ strategy	d_{31}/ pCN^{-1}	d_{33}/ pCN^{-1}	Operation frequency/Hz	Active material Volume/cm^3	Power output/mW	Cycle energy density/ mJ cm^{-3}
Jung[299]	2011	$NaNbO_3$ NWs/PDMS	Bending	NG	NG	0.33	NG	NG	2
Park[300]	2012	$BaTiO_3$-Carbon/PDMS	Bending	NG	NG	2.5	0.3	NG	NG
Yu[301]	2013	PVDF/MWCNTs	Bending	NG	NG	0.8	NG	81.8×10^{-6}	NG
Xu[302]	2013	PZT NWs/PVDF	Pressing	NG	371 pmV^{-1}	NG	0.0158	NG	NG
Siddiqui [303]	2015	BaTiO3/PVDF-TrFE	Bending	NG	960	2.7	3×10^{-3}	NG	1.67
Siddiqui [304]	2016	$BaTiO_3$/PVDF-TrFE	Bending	NG	NG	0.6	9×10^{-3}	NG	0.253
Liu[305]	2016	PVDF/Graphene	Bending	NG	-63.25pmV^{-1}	4	NG	NG	NG
Fu[306]	2018	BaTi2O5/PVDF	Pressing	NG	NG	13	NG	4×10^{-3}	2.11×10^{-3}
Zhang [307]	2018	BCZT/PDMS	Pressing	164	54	4	NG	NG	6.5×10^{-3}
Singh [308]	2018	MgO/P(VDF-TrFE)	Bending	NG	-65 pmV^{-1}	1	9.8×10^{-4}	NG	NG
Dutta [309]	2018	NiO@SiO2/PVDF	Pressing	NG	NG	4	0.08	NG	0.685
Thakur [310]	2018	ZnO/PVDF	Pressing	NG	50	5	NG	NG	6.5
Ye[311]	2019	P(VDF-TrFE)/BNNTs	Pressing	NG	14	2	0.012	NG	0.94
Guan [312]	2020	Pdop-BaTiO3@P(VDF-TrFE)	Bending	NG	NG	3	NG	NG	1.46
Yang [313]	2020	Piezoelectric polyimids	Pressing	NG	420	3.5	0.225	1.17	1.49

Piezoelectric composites are manifold with a large amount of methods to increase the energy output of the energy harvesters. For example, some high-performance

composited based piezoelectric energy harvesters can be found in [301, 305, 314], wherein the graphene, carbon nanotube and graphene oxide are utilized. Fu *et al.*[306] established a highly durable piezoelectric energy harvester by using oriented $BaTi_2O_5$ nanorods and PVDF matrix, requiring hot pressing to align the directions of nanorods. Similar composite structures with NWs can be seen in [299, 302, 315]. Besides, some metal oxide based composites[308-310, 316, 317], including MgO, ZnO, NiO and TiO_2, are also developed to enhance the power output of the energy harvesters.

A new strategy to improve the performance of piezoelectric energy harvester is to use vertically aligned ZnO NWs, which is firstly proposed by Wang *et al.* [318], regardless of loading frequency and excitation patterns. Each NW is a single crystal and has uniform shape, and the NWs were deflected by atomic force microscopy to test piezoelectricity. This kind of material may not yet be suitable for ferroelectric energy harvesters, due to the requirement for complex designs without engineering its structure to a specific domain pattern. However, due to its great potential for energy harvesting, this field was further developed by researchers with various designs and optimisations, which are summarised in Table 2.5.

Table 2.5 Summary of piezoelectric NWs for energy harvesting (NG: Not Given)

Reference	Year	Active material	Shape/ strategy	Length of NWs/μm	Operation frequency/ Hz	Active material Volume/cm^3	Power output/mW	Cycle energy density/ mJ cm^{-3}
Wang [319]	2008	ZnO NWs	Brushing	3.5	1	NG	NG	2.9-11.4(Estimated)
Yang [320]	2009	ZnO NW	Stretching	200-300	0.067	3.5×10^{-6}	2.51×10^{-9}	11×10^{-3}
Sodano [321]	2009	PZT NWs	NG	7-8	NG	NG	NG	NG

Xu[322]	2010	ZnO NWs	Bending	5	2	NG	NG	1.35
Xu[323]	2010	PZT NWs	Pressing	5	50×10^{-3}	3×10^{-5}	NG	56×10^{-6}
Briscoe [324]	2012	ZnO NWs	Bending	1.3	175	2.6×10^{-3}	NG	2.2×10^{-3}
Sohn[325]	2013	ZnO NWs	Sound drvien	2.5	100	NG	NG	0.9×10^{-3}
Shin[326]	2014	Li/ZnO NWs	Bending	NG	0.5	1.7	90	5.29
Moorthy [327]	2017	PMN-PT NW	Bending	10	0.25	NG	NG	0.701×10^{6}
Sodano [328]	2013	$BaTiO_3$ NWs	Vibration driven	1	190	NG	NG	33×10^{-6}
Sodano [329]	2014	$BaTiO_3$ NWs	Vibration driven	40	155	4×10^{-3}	0.123×10^{-6}	0.2×10^{-3}
Zhou [330]	2014	PZT NWs	Cantilever	NG	43	NG	NG	55.8×10^{-3}
Whiter [331]	2014	P(VDF-TrFE) NWs	Pressing	NG	5	2×10^{-3}	16.5×10^{-6}	8.25×10^{-3}
Sodano [332]	2016	BZT-BCT NWs	Cantilever	NG	37	NG	NG	60.8×10^{-3}
Seo[333]	2017	$BaTiO_3$ NWs	Bending	450	2.5	0.135	3×10^{-3}	8.8×10^{-3}
Chen [334]	2017	PMN-PT nanobelts	Pressing	100	50	NG	0.6	NG
Nafari [335]	2017	PZT NWs	Cantilever	45	187	NG	0.67×10^{-3}	2.65×10^{-3}
Gu[336]	2018	PZT NWs	Pressing	6	10	NG	$0.79/1.48\times10^{-3}$	3.95/7.4

It can be seen in Table 2.5 that ZnO NWs are well developed to improve the performance of energy harvesters, while PZT, $BaTiO_3$, PMN-PT, P(VDF-TrFE) and BZT-BCT NWs for energy harvesting made rapid progress in recent years, which generally increased the energy output of NWs based energy harvesters.

Although this strategy can generate greater cycle energy density than either using electroceramics or the single crystals in Table 2.2 and Table 2.3, it did not show any

significant increase in energy harvesting relative to piezoelectric composites. By contrast, this kind of energy harvester is still promising for energy harvesting practical applications; this can be used for the small-scale devices and wearable textiles and electronics. Additionally, another advantage of NW energy harvesters is that they may adapt to the extreme ambient environments. With the development of technologies, the ultra-long lead titanate NWs nanogenerators with high Curie temperature were proposed by Nafari *et al.*[335, 337], which can be used in an extremely high-temperature environment such as beyond 300 °C. And they further developed these NWs to be ultra-long, so they are more sensitive to mechanical loads and have low resonant frequency[329, 338].

With the reduction of thickness, the thin-film electroceramics have increased flexibility, which can be used in highly integrated devices, such as flexible, wearable and even implantable electronics[339]. Due to its large strain and dynamic sensitivity, this is a good choice for the fabrication of self-powered electronics using thin film piezoelectric energy harvesters, and a review can be found in [340]. Several research groups have investigated this field by using $BaTiO_3$[341], PZT[342], PVDF-TrFE[343], PMN-PT[344] and $BaTiO_3$ nanoparticle composite[345] thin films for energy harvesting, indicating a high robustness and an improved cycle energy density 23.3 mJ/cm^3[341].

Porous piezoelectrics have been developed for energy harvesting due to their reduced dielectric constant and increased effective coupling coefficient. The pores in

the material essentially have a decoupling effect of the transverse piezoelectric coefficient from the d_{31} components, and this further contributes to an increase in the overall hydrostatic component. Thus porous piezoelectrics can be applied to improve the performance of nanogenerators. Asadi *et al.*[346] introduced 45% porosity to PVDF-TrFE, which increased the piezopolymer's electromechanical coupling coefficient. The output power is about 500 times greater than that of pristine PVDF-TrFE. Roscow *et al.*[347] fabricated a porous barium titanate structure, in which d_{33} is comparable to that of dense material. Zheng *et al.*[348] reported an excellent piezoelectric energy harvester using porous CNFs/PDMS aerogel film, with a cycle energy density of 0.63 mJ/cm^3. This energy harvester used biomaterial CNFs, which shows great compatibility and has no environmental harms.

2.2 Triboelectric energy harvesting

Another effective and efficient transduction mechanism for scavenging surrounding mechanical energy, triboelectric energy harvesting, has becomes a hot topic since the first triboelectric nanogenerator was proposed by Wang *et al.*[349] in 2012. This novel kind of energy harvesting method stands out as a promising substitute of piezoelectrics, with merits of a higher power density, simple and diverse architectures, significantly flexibility, and cost effectiveness [350-357]. The working principle combines contact electrification (triboelectrification) and electrostatic induction, by using two different material plates with different triboelectric polarity. A periodic contact-separation process can generate stable and sustainable energy output to an external circuit [353, 358-360]. Due to excellent performance in power density, triboelectric generators are not only used in energy harvesting technologies harvesting energies by human motions, air flow, waves, and sound, but also are implemented in self-powered devices, including sensing systems, actuations, and multi-functional electronics and devices [361-366]. With the development of technology, triboelectric nanogenerators have been improved from various aspects, such as structures, materials and working modes[367]. This part mainly reviews a small number of state-of-the-art structures and materials improvement for triboelectric energy harvesting, and the working modes are also briefly introduced.

2.2.1 Four types of triboelectric nanogenerators

There are four kinds of working modes of triboelectric nanogenerators, namely vertical contact-separation, in-plane sliding, single-electrode and free-standing triboelectric mode [47, 368]. The first prototype of triboelectric nanogenerator was based on the contact-separation working mode using Kapton and polyester as triboelectric layers. This working mode uses two kinds of materials with different electron affinity. When the two plates contact each other, the electrons accumulate on the interface because of triboelectricity. Two more working modes were investigated using in-plane sliding[369-372] and electrode sliding modes[373-375], whose designs are more versatile and convenient. The in-plane sliding mode of triboelectric nanogenerator, uses similar charge build-up to the vertical contact-separation mode with an improvement that one layer slides over the other. Furthermore, to reduce the fabrication complexity and cost, single electrode is introduced, which can be used in both vertical contact-separation and in-plane sliding. This working cycle uses the potential difference between the dielectric material and ground, simplifying the structure and making it more versatile. The fourth type of triboelectric nanogenerator uses a free layer to conduct the charges onto and off the different electrodes [376-380], further improving the versatility of the structure. The working principle is that the dielectric layer can induce triboelectricity on both electrodes, which can generate a potential difference between them, and thereby generate current from external load with a periodic movement.

2.2.2 State-of-the-art designs of triboelectric generators

Due to the flexibility and universality, the structures of triboelectric generators are manifold, which can be used to harvest blue energy (water wave energy), vibrational energy and biokinetic energy. In this section, only a small number of significant prototypes are presented.

Wang *et al.*[381] designed a three-dimensional triboelectric nanogenerator, where out-of-plane contact-separation mode and in-plane sliding mode are both used to broaden the potential applications. Three springs and an inertial mass are used, where the triboelectric layer is attached to the mass. In this case, the triboelectric nanogenerator can capture multi-direction vibration energy to induce in-plane or out-of-plane energy harvesting working cycles.

A non-contact mode of triboelectric nanogenerator was reported by Wang *et al.*[382] in 2020, in which the centrifugal force induced by rotation can trigger an automatic transition between contact mode and non-contact mode. The built-in traction rope structure is the key segment to stabilize the positions of triboelectric masses. This working mode can significantly reduce the abrasion of triboelectric layer, increasing the lifetime. Another non-contact structure is realized in [383], wherein a grating-structured freestanding triboelectric layer is connected with four springs.

Piezoelectric materials are introduced to increase the power output of triboelectric nanogenerators by utilizing both piezoelectric and triboelectric effects [384, 385]. Guo *et al.*[386] reported a hybrid energy harvesting method using both triboelectrics and

piezoelectrics, wherein a piezoelectric layer PVDF provides contact electrification effect and piezoelectric effect. The structure does not change much but uses piezoelectric layer to replace one of the contact materials. In figure 2.4, the working mechanism is shown. This energy harvester has a cycle energy density of 0.155 mJ/cm^2, with the benefits of flexible appearance and good air permeability.

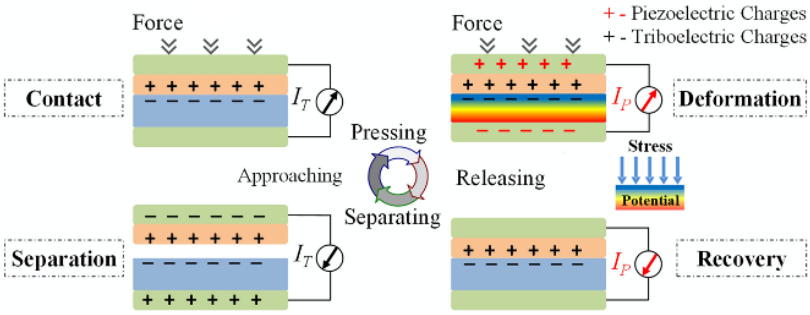


Figure 2.4 Schematic view of the operating principle of the hybrid nanogenerator. Reprinted with the permission from[386]. Copyright 2018 Elsevier.

Furthermore, many researchers try to expand the range of applicable conditions to harvest energy created by raindrop [387], water waves [388, 389] and tires [390], where liquid-solid contact working principle and rolling contact devices are implemented. A metal-grating structure was presented in [391], and the energy conversion efficiency can reach 50% with a 3.3 mJ/cm^3 energy density. Besides, Wang *et al.*[392] proposed a disk-structured triboelectric nanogenerator with a narrow grating by using mature printed circuit board technology, and the cycle energy density is about 0.089 mJ/cm^2. A jellyfish inspired bionic triboelectric nanogenerator is proposed by Wang *et al.*[393], wherein the liquid pressure-induced contact-separation working mode can generate an elastic resilience of this structure. This can also be used to monitor the wave surface

due to its high sensitivity. In 2018, wireless transmission and storage structures are designed for triboelectric nanogenerator, which can be used for the wireless nodes in IoTs[394, 395].

2.3 Ferroelectric energy harvesting

Based on to the non-linear effect and dielectric hysteresis, ferroelectric/ferroelastic switching can induce a sudden increase or decrease in polarization. Consequently, ferroelectric/ferroelastic switching can induce greater charge flows than piezoelectrics: this has attracted attention in energy harvesting. The non-linear properties of the materials have the potential of improving the performance relative to traditional piezoelectric transducers, which suffer from low power density. Ferroelectric energy harvesting can adopt the simple configurations of piezoelectric transducers, and need not require complex systems. By contrast, the challenges of nonlinearity, fatigue degradation induced by stress and the difficulty of driving an electrical cycle by stress have limited ferroelectrics' use in energy harvesting applications. Furthermore, the ferroelectric/ferroelastic switching requires more mechanical work input than piezoelectrics, though this can be optimized by proper design. Thus ferroelectric energy harvesting systems are rarely reported in previous works. Building on the previous studies, some theoretical designs of energy harvesters using ferroelectric/ferroelastic switching were proposed in last decade.

In 2011, Muench *et al.*[396] proposed two kinds of energy generator with an engineered and epitaxially sputtered nanodot ferroelectric thin film on a substrate, and this concept was explored by using phase field model to simulate the ferroelectric switching of the film. A partial top electrode on a rectangular shaped nanodot was

proposed to direct the poling of the nano layer in an initial step, and then the removal of electric field can lead to a stable domain topology. The working cycle can be driven by tensile strain in the plane of the substrate. This design topology stabilizes the cycles. An improved L-shape design was presented with a similar effect if the loading pattern is the same as the first method, which is stabilized by surface flux closure effects. A compressive strain was introduced to improve the performance. Subsequently, a new ferroelectric energy harvester concept was developed based on the previous one by Muench *et al.*[397] with a continuous film and an interdigitated electrode; this kind of nanogenerator is coupled to a rectifier to realize power generation.

Vaish *et al.*[398] proposed an energy harvesting method using bulk ferroelectric materials, see figure 2.5. This energy harvester should be assisted with a Sawyer-Tower circuit to provide the necessary electric field. The working cycle begins with a small electric field E_L at point 1, and then a large electric field E is applied to fully polarize the material. Afterwards, the compressive stress is applied aligned with the polarization direction to depolarize it, with the holding of electric field E_s to produce energy output. Finally, the electric field reduces to E_L before the stress unloads. The results show that the output energy densities per cycle are hundreds of times higher than those of piezoelectric energy harvesters. This energy harvester does not require a complex structure, but it relies on complicated external circuits. Additionally, this method is still based on a material aspect, and the challenge for fabricating an energy harvesting

device using this method remains unsolved and requires appropriate designs. Similar works can be found in [399, 400].

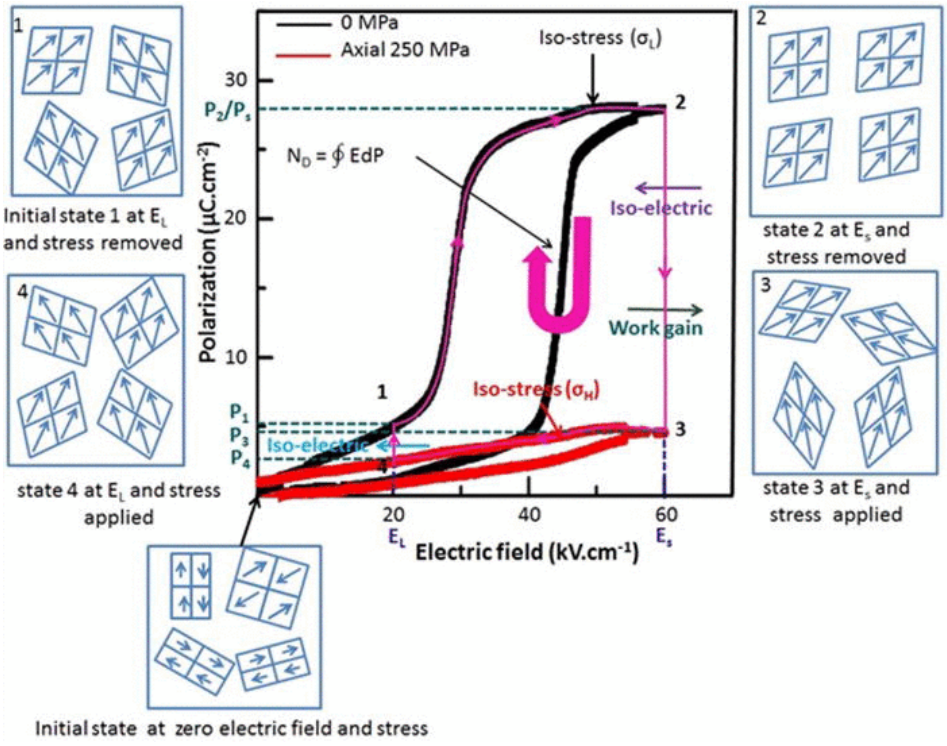


Figure 2.5 Proposed processes for giant mechanical energy conversion using ferroelectric switching. Reprinted with the permission from [398]. Copyright 2014 American Institute of Physics.

Lynch *et al.*[401-403] proposed a new energy harvesting method based on phase transformation from rhombohedral to orthorhombic in ferroelectric single crystals, which is driven by a combination of stress and electric field. This strategy can induce giant polarization change during the phase transformation, increasing the power density by order of 10^2- 10^3 relative to piezoelectrics. A working cycle was established between a high and a low compressive uniaxial stress on the ferroelectric materials, which are both beyond the coercive stresses required for the forward and reverse phase transformation. Specifically, the energy harvesting cycle starts from the low

compressive stress, changing to the high value under open-circuit conditions, generating an opposing electric field to stablise the rhombohedral phase. Then the circuit is closed while the stress holds constant and the built up electric field was decreased, with a charge flow across a resistor. After that, the stress reduces to the low initial value under open-circuit conditions again to build an opposing electric field for stability of orthorhombic phase. And finally the closed circuit can make sure the orthorhombic phase returns to rhomboheral phase. The results show that the cycle can be operated at 100 Hz, and the peak efficiency can reach 36% by optimizing the mechanical loads. Although this kind of energy harvester has great potential for practical applications, it has not been widely used due to its complex external circuit. Furthermore, this concept was only tested in a material perspective, without a practical attempt for energy harvesting by fabricating a prototype device, which may require further complicated designs.

Designing patterned domains may solve the problem of unstable working cycles of ferroelectric energy harvesters: Balakrishna *et al.*[404] presented a thin-film ferroelectric energy harvester concept with a continuous film and continuous electrode, see figure 2.6. By exploring various domain patterns of ferroelectrics at the nano scale, the specific pattern in figure 2.6(a) suggested stability and robustness. From figure 2.6(b), when a tetragonal ferroelectric material experiences uniaxial tensile stress, the spontaneous polarization vectors can align with the axis of stress due to ferroelastic switching. With appropriately placed electrodes, the process can drive a flow of charge,

and the active interface against the charge flow can generate energy output. By contrast, compressive stress can make the spontaneous polarization vectors switch back, reversing the charge flow. The resulting output power density is greater than typical piezoelectric energy harvesters. However, the design proposed by Balakrishna *et al.* relies on a specific domain pattern that is difficult to fabricate and may be susceptible to mechanical shock.

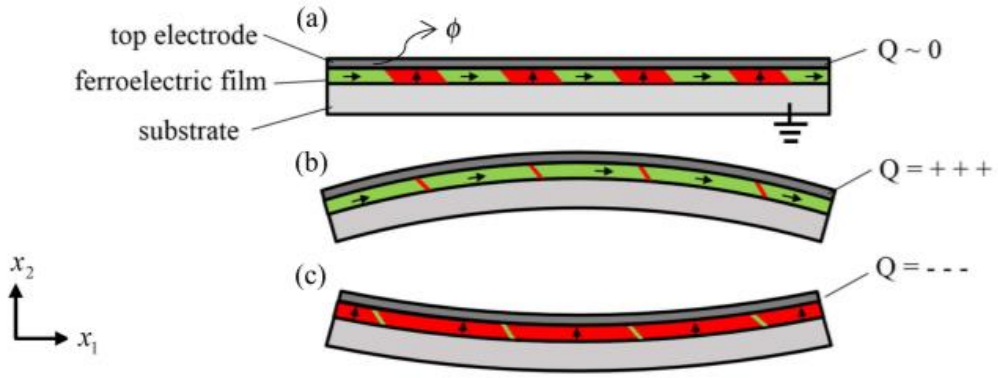


Figure 2.6 (a)–(c): Schematic illustration of the working concept of the energy harvester. Reprinted with the permission from reference[404]. Copyright 2016 IOP Publishing.

Instead of using domain patterns to enable a work cycle in a ferroelectric energy harvester, Wang *et al.* [19, 63] proposed an improved design, using a bias field to stabilize the energy harvester. The prototypes are similar to existing cantilever-type piezoelectric energy harvesters, with the advantage of simplicity of manufacture. There are two kinds of electrodes placed on the energy harvester, with the electrodes matching the d_{31} and d_{33} modes of piezoelectric energy harvesters. In the first method, a continuous electrode was adopted. The key problem is that the vertical spontaneous polarization vectors cannot switch towards a preferred direction without bias voltage. Thus a bias electric field was proposed to assist the switching back. A second prototype

uses a different working principle with the interdigitated electrodes. A compressive uniaxial stress depolarizes the material and bias electric field restores the polarization. This has better performance than the first model, but it increases the complexity of the device. The materials' influence was also studied in the literature [63].

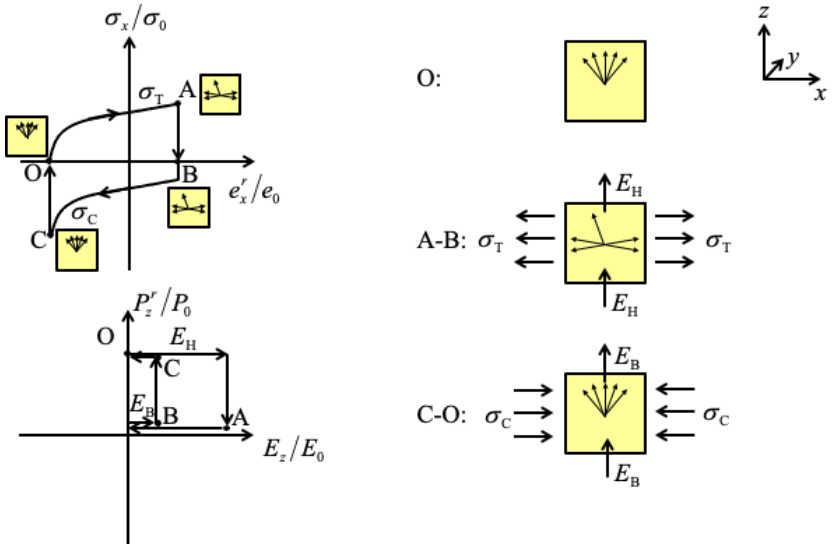


Figure 2.7 Working cycle of energy harvesting concept using ferroelectric/ferroelastic switching in polycrystalline materials

A key problem with ferroelectric/ferroelastic energy harvesting is that a depolarized material cannot easily be repolarized with stress alone. Therefore, a bias electric field is sometimes applied. Considering the complexity and difficulty of establishing the energy harvesters by using above methods, Kang *et al.*[405] provided a more general way to use ferroelectric switching in ceramics with random grains, which is presented in Chapter 4. No engineered domains or structures are required, which simplifies fabrication. The working cycle is shown in figure 2.7. This energy harvester starts with a strong electric field used to fully polarize the ferroelectric

ceramic, and then a tensile stress in the direction perpendicular to the polarization direction is applied to depolarize the ferroelectric while a harvesting electric field is applied against the charge flow to produce positive energy output. Finally, compressive stress is applied and a small bias electric field is introduced to assist repolarization of the electroceramic. Model results suggest that the energy conversion can reach about 20% with optimization, and the potential energy density is much greater than that of piezoelectrics.

The modelling work of Kang *et al.*[405] did not consider the grain-to-grain interactions of the materials; hence a more precise model can be used to predict the behavior of materials to further understand the working principle. Based on the idea proposed by Kang *et al.*, Behlen *et al.*[171] further analysed the working cycle using ferroelectric switching by adopting a more sophisticated condensed model and suggested a modified six parameter process, finding the best parameters for optimum performance.

A novel and practical energy harvesting method using ferroelectric/ferroelastic switching has been developed and studied by Kang *et al.*[406, 407], which is the main subject of this thesis and is discussed in Chapters 5-7. By engineering the poling degree of the polycrystalline ferroelectrics, an internal residual electric fields can provide “memory” of a preferred direction for repolarizing it. The device was prepared by partially polarizing a ferroelectric layer, followed by bonding with a stiff substrate and

then completing the poling. Afterwards, a tensile stress is required to depolarise it, before the periodic compressive stress can drive working cycles. The resulting energy harvesting cycles achieve much greater energy density than conventional piezoelectric devices, comparable with triboelectric generators. Besides, the cycles yield promising mechanical attributes, where the device remained robust up to order of 10^6 cycles. Furthermore, another working mode by using tensile stress to drive the cycles shows even greater energy output: however but the fatigue performance is relatively poor.

2.4 Summary

Mechanical energy harvesting has been widely used and developed. In this review, an in-depth survey of design and configuration has been presented.

The development of energy harvesting is still at a research stage, and is mainly not ready for commercialization. The low energy output, unstable output and high fabrication costs limit applications. There are several aspects that can be improved: (1) advances in materials and structures to promote the improved energy conversion, (2) new fabrication techniques of materials to realize cost-effective assembly line production, (3) new energy conversion methods and hybrid energy harvesting, which can combine working mechanism for optimum performance.

Energy harvesting using ferroelectric/ferroelastic switching may become a promising method to convert mechanical energy into electrical energy. It potentially offers high energy density and low cost, but requires further research to enable stable working cycles without material degradation and solve the challenges associated with nonlinearity. Another key problem of ferroelectric energy harvesting is that a depolarised electroceramic cannot be repolarised by stress only. This has required specific microstructures or an external bias fields in previous designs to assist the repolarization. To solve this problem, the investigation of ferroelectric /ferroelastic energy harvesting cycles is the topic for the remaining chapters of this thesis.

Chapter 3

3. Methods

This chapter gives detailed information about the methods for both modelling and experiments used in chapters 4-7. First of all, this portion provides a thorough description of Hwang's model, wherein the relationship between the local coordinate system of each grain and the global coordinate system, the mechanical work input, net electric work output and the conversion efficiency ignoring the reversible linear piezoelectric, dielectric and elastic effects are presented. The modelling method provides the fundamental mathematical and physical description for Chapter 4. In addition, the experimental procedures, including material selection, specimen fabrication and test arrangements for both quasi-static and vibrational experiments in chapters 5-7, are shown in this chapter. Specifically, the material selection, the dimensions of the specimens and the preparation of conductive adhesive are given in this section. Besides, the circuits, equipment and test fixture are also presented in this chapter, providing the basic sketch of the experiments in chapters 5-7.

3.1 Model of the energy harvesting cycle

The proposed working cycle in Chapter 4 for energy harvesting is studied by simulating a notional material point, which is a small region of polycrystal consisting of 10000 randomly oriented grains. The model was implemented in software

MATLAB. Hwang *et al.* [408] developed a simple ferroelectric/ferroelastic polarization switching model, in order to predict the polarization switching in ferroelectric materials, which has been widely used [87, 137, 409]. In the model of Hwang *et al.* [408], the ceramic is treated as a composite of independently acting grains, with random crystallographic orientations. For simplicity, each grain is regarded as being in a tetragonal state and comprising a single polarized domain. The properties, including polarization and strain of the ceramic, are approximated by the average values over all the grains. Hwang's model does not account for the details of grain-grain interactions and variation of stress or electric field through the ceramic. In this respect it has been superseded by more sophisticated models of switching in ceramics [38]. However, the model has advantages in rapidity, simplicity and reliability. The rapidity of the calculations is particularly advantageous for assessing a range of harvesting cycles in order to find and optimize a viable cycle. Hwang's model is also rate independent, and so does not account for the effect of varying cyclic frequency. However, it is known that several material parameters, such as dielectric and piezoelectric properties are frequency dependent [410-412]. Of particular significance, the coercive field and coercive stress can be expected to increase with frequency [413]. Nevertheless, there is evidence that the coercive field is reasonably stable over the likely range of operating frequencies of the energy harvester(1 Hz -1 kHz)[85]. Mechanical resonance would also be a significant issue in the design of a particular realization of the harvesting cycle.

3.1 Model of the energy harvesting cycle

The strain or remanent polarization in a local coordinate system of each grain can be transformed to a global coordinate system by:

$$\overline{P}_j = a_{kj} P_k \tag{3.1}$$

$$\overline{e_{ij}} = a_{ki} a_{lj} e_{kl} \tag{3.2}$$

where $\overline{P}_j$ and P_k are the components of the polarization of each grain in the global and local coordinate systems respectively, and the a_{kj} are the direction cosines of each grain's local coordinate system. $\overline{e_{ij}}$ and e_{kl} are the components of the spontaneous strain in the global and local coordinate systems respectively. In the local coordinates, the polarization is aligned to one of the three orthogonal co-ordinate axes and has magnitude P^0. Similarly, the spontaneous strain components in each grain are $(c-a_0)/a_0 = 2/3 e_0$ parallel to the polarization direction and $(a-a_0)/a_0 = -1/3 e_0$ perpendicular to the direction of polarization, where $e_0 = (c-a)/a_0$ is the axial strain change caused by 90° switching, while c, a and a_0 are the edge lengths of the tetragonal unit cell and a reference cubic unit cell respectively. Equal stress and electric field are applied to each grain in the global coordinate system. Each grain is then checked for switching and if a switching criterion is satisfied, its polarization and strain are switched accordingly. Simulation proceeds stepwise applying successive changes in loading and tracking the state of each grain as it switches.

With regard to the switching criterion, the details can be found in Chapter 1. By averaging over all the grains in the ceramic, the macroscopic changes in polarization and strain can be estimated. Hence the model provides a very simple way to evaluate

the working cycle of an energy harvester concept: externally imposed stresses and electric fields drive the material between states, and the resulting energy flows may be assessed to find whether a net electrical energy output has been achieved. The working mechanism of the energy harvester is ferroelectric/ferroelastic switching but the material need not be fully depolarized or repolarized during the working cycle.

To assess the energy flows in the harvesting cycle, ignoring the reversible linear piezoelectric, dielectric and elastic effects, the net electrical work input over the cycle can be expressed as

$$W_{\mathrm{e}} = \oint E_i dP_i \tag{3.3}$$

Similarly, the mechanical work input is

$$W_{\mathrm{m}} = \oint \sigma_{ij} de_{ij} \tag{3.4}$$

The net electrical energy output $-W_e$ can be decomposed into an input part, in which increments $E_i dP_i$ are positive and an output part, where the work increments are negative, giving

$$-W_{\mathrm{e}} = W_{\mathrm{e\text{-}out}} - W_{\mathrm{e\text{-}in}} \tag{3.5}$$

A similar decomposition for mechanical work allows the various energy flows into and out of the material to be assessed. Whilst several ways of assessing efficiency are possible, in the present work we adopt a simple definition given by

$$\eta = \frac{-W_{\mathrm{e}}}{W_{\mathrm{m}}} \tag{3.6}$$

This measure indicates the conversion efficiency of net mechanical work input into net electrical work output. The related results can be found in Chapter 4.

3.2 Experimental procedures

3.2.1 Specimen fabrication

Relaxor ferroelectric materials, with nano-length scale domains, have higher dielectric constants than conventional ferroelectric materials with micro-length scale. They take less energy to align the polarizations [414]. 8/65/35 PLZT is a relaxor ferroelectric that, in the unpoled state, displays nano-polar regions. During poling, these regions grow to form domains and the poled or partially poled material exhibits ferroelectric behaviour, similar to a rhombohedral ferroelectric. The material response to stress displays ferroelastic switching due to reorientation of domains[85]. In the present work of chapters 5-7, the energy harvesting device exploits both ferroelastic and ferroelectric switching.

In chapters 5-7, A ferroelectric energy harvester was implemented using 8/65/35 PLZT as the working material. The design is generic and any ferroelectric material that also exhibits ferroelastic switching could be used. By contrast, the design of the ferroelectric energy harvester, including the choice of active material, substrate, residual fields, and mechanical load amplitude should be adjusted accordingly depending on the coercive field of the active material, and thereby the energy output will be enhanced through the optimization. This design exploration has been planned for future work. In this work, the selected PLZT material, with 8% lanthanum substitution into a 65% lead zirconate and 35% lead titanate solid solution, has the

advantages of low coercive field (0.36 MV m^{-1}) and a soft composition allowing ferroelastic switching at stresses of a few MPa [85, 136]. The material has a rhombohedral-tetragonal morphotropic structure, and fine grain size (~ 1 μm), which is advantageous in enhancing fracture toughness. The Curie temperature is 110°C [85, 136] and the maximum polarization at room temperature is 0.25 C m^{-2}. The PLZT wafers used in the experiments were all taken from the same bulk sample of commercial 8/65/35 PLZT material. The sample response varied systematically and repeatably as the design parameters were varied, giving confidence that the observed performance is not due to material variability. The energy harvester was built on a tool-steel substrate of thickness 1mm onto which a PLZT wafer of thickness 0.33 mm was adhered with conductive adhesive, see figure 3.1. A top electrode was formed using a thin coating of conductive paint. Connections were made to the substrate and top electrode using conductive epoxy (RS PRO Liquid Adhesive), which is a 2-part thermosetting material that contains silver flakes in a epoxy resin adhesive base. By mixing the hardener and resin at a ratio 1:1, the conductive epoxy can be cured at room temperature after 36 hours. In current work, the conductive epoxy was cured with pressure to ensure a bonding without pores between the substrate and the PLZT layer. Note that shear sliding may occur if the conductive epoxy is subjected to a bending moment. The substrate dimensions were 68 x 4 x 1 mm with the active layer covering a central portion of length 38 mm. It also shows an edge view identifying the steel substrate, adhesive and PLZT layers. The conductive paint layer is flexible and much thinner than the

PLZT and cannot be seen in this view; it is expected to have negligible effect on the mechanical loading.

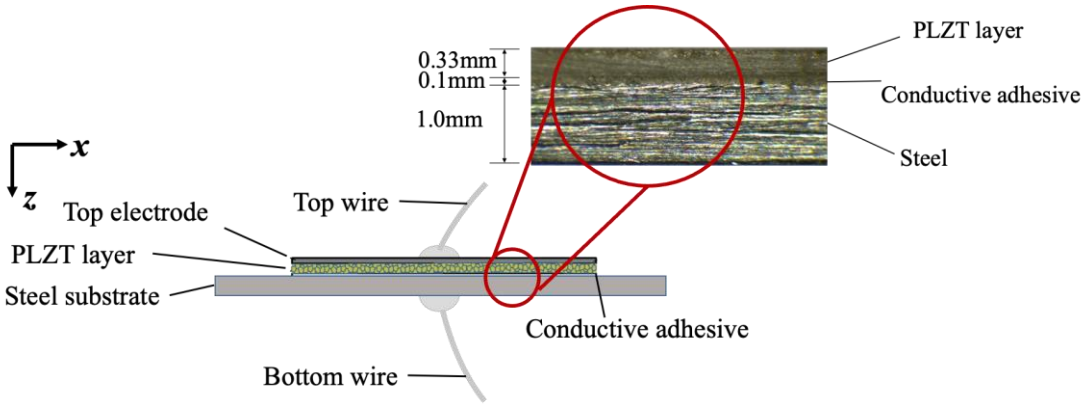


Figure 3.1 Arrangement of the energy harvester and optical micrograph of the layered structure.

A key feature of the device design is the poling process. The ceramic layer was partially poled, by controlling electric displacement, before being adhered to the substrate. The purpose of this partial poling process in a mechanically unconstrained state was to limit the development of in-plane tensile stresses that were shown in preliminary tests to promote degradation by cracking. The degree of partial pre-poling, from 0% up to 100% (relative to the full polarization of 0.25 C m^{-2}) was varied to find optimum operating conditions. Initial tests were carried out with 100%, 75%, 50% and 30% pre-poled samples. Once adhered to the steel substrate, the poling process was then completed such that the ceramic layer was fully poled to near 0.25 C m^{-2}. The results of initial tests show that an increase of pre-poling level can result in a decrease of energy output per cycle, and a 30% pre-poled sample can achieve a good balance between energy output and material degradation in the further poling process.

Specimens fabricated with less than 30% pre-poling commonly cracked during subsequent on-substrate poling. The residual stress occurring in the poling process can be estimated based on the degree of the partially pre-poled state, but in the present work it has not been measured. Based on the estimation, an increase of pre-poling level can reduce the residual stress in the specimens. The measurement problem is challenging due to the varying material state and domain structure. Ferroelectric switching and residual strain can be identified using X-ray diffraction[415], which is planned for future work.

3.2.2 Test arrangements

The test arrangements for the tests in chapters 5-7 are shown in figure 3.2(a)-(e). For quasi-static testing of the energy harvesting cycle in Chpater 5, an open-circuit arrangement was used and mechanical loading was carried out using a Deben microtest system (Figure 3.2(a),(d)). The steel substrate was connected to ground through a capacitive electrometer. The capacitive electrometer is to record charge flows in the circuit, and the electric displacement change can be calculated by $D = C*V / A$, where C, V and A are capacitance of the electrometer, measured voltage on the electrometer and the area of the top electrode. At the top electrode, voltage was controlled using Labview software and a high voltage amplifier (Trek, model 20/20C). A steady voltage opposing the charge flow during the energy harvesting cycle was used to simulate electrical load. This voltage was removed during the mechanical unloading

part of the cycle. In figure 3.2(d), the signs of force and electric field are both negative, where the electric field direction is upward and $F<0$ indicates the cases to produce in-plane compressive stresses in active layer. In Chpater 6, we use the convention that $F > 0$ results in tensile loading of the PLZT layer, while $F < 0$ results in compression. Variation of the total force amplitude, F, was explored during testing as this could change the energy harvesting performance.

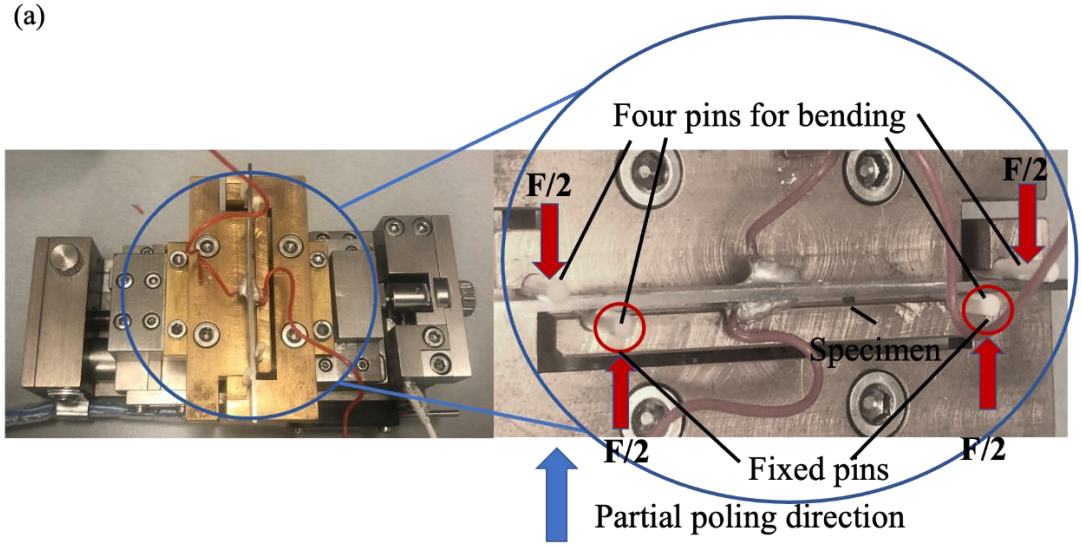
Mechanical loading was applied by four-point bending using four alumina pins in two pairs. Each pair of pins was spaced 5 mm apart with a central span of 38.5 mm experiencing uniform bending moment. Note that the pin loads were applied directly to the substrate, in end sections beyond the region where the active material was adhered. The pin positions were monitored continually using digital image correlation. To test various force amplitudes, a triangular waveform of mechanical loading was applied as shown in figure 3.2(b), while other loading patterns are more difficult to be implemented on Deben microtester.

In the quasi-static tests, the applied electric field can be written as λE_0, where E_0 is the coercive field and λ is a factor to represent various electrical loads. For both energy harvesting methods, the energy harvesting cycle was tested by applying the following pattern of loading: i) Apply voltage to the upper electrode with the lower electrode grounded to produce electric field λE_0, switching the cycle ‘on’. This electric field provides the load against which the energy harvester works, referred to here as the “harvesting electric field”. ii) With the harvesting electric field held constant, apply a

mechanical loading force increasing to $F/2$ at each pin. This force drives in-plane tension or compression of the ferroelectric wafer. iii) With the loading pins held fixed (i.e. at approximately constant loading), reduce the applied electric field to zero. This switches the energy harvesting part of the cycle 'off'. iv) Reduce the mechanical load to zero.

In addition, Figure 3.2(e) shows the external circuits for quasi-static tests with the variation of resistive loads in Chapter 7, and a capacitive electrometer is adopted to record the charge flow. The bottom substrate electrode is connected to the ground, while the top electrode is connected through a load resistor. Voltage measurements across this resistor indicate charge flow from the upper electrode. For quasi-static tests, the experiment was conducted at a frequency of 0.0167 Hz, with the load resistors varied between 0.1 MΩ to 12 MΩ.

(a)



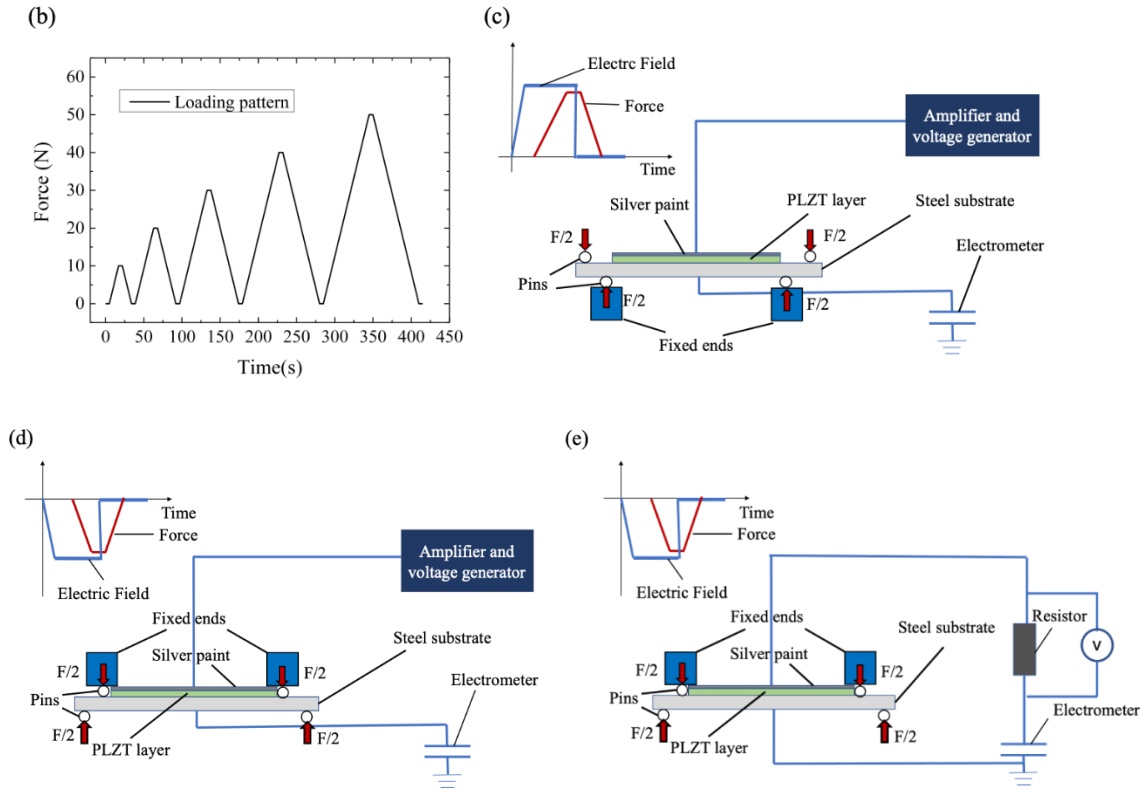


Figure 3.2 Schematics of quasi-static test arrangements. (a) The four-point bending test using the Deben microtest loading stage. (b) The loading path for tension and compression tests. (c) Open circuit arrangement used for quasi-static energy harvesting tests using cyclic tensile loading. (d) Open circuit arrangement used for quasi-static energy harvesting tests using cyclic compressive loading. (e) Closed circuit for testing at a range of frequencies and electrical loads.

Once a quasi-static working cycle was established, the effect of loading at a range of frequencies and with a range of passive resistive loads was studied. Cyclic mechanical loading was applied using an in-house hydraulic test machine with a four-point bend loading fixture, as shown in Figure 3.3(a). Displacement control was achieved via feedback from a LVDT in the experiments of Chapter 5 and 7. The signs of displacement for vibrational tests is negative, where the signs indicate that the cross-

head movement measured by the LVDT results in in-plane compressive stresses in the ferroelectric layer. The four-point bend fixture was made from tool steel, with alumina pins, spaced as in the quasi-static experiments. The electrical circuit included a load resistor (labelled Resistor 2 in Figure 3.3(b), a potential divider (Resistor 1) used to infer voltage at the electrode, and a capacitive electrometer to measure charge flow. Voltages at the electrometer were kept at the mV level to avoid offsetting of the sample electrode voltage, which was typically 1-50 V. In Chapter 5, Resistor 2 was varied in the range 3 kΩ-15 MΩ, and the operating frequency varied from 0.5 Hz-20 Hz. Runs of 0.5×10^6 cycles were used to test for stability and fatigue with all data logged using LabView software.

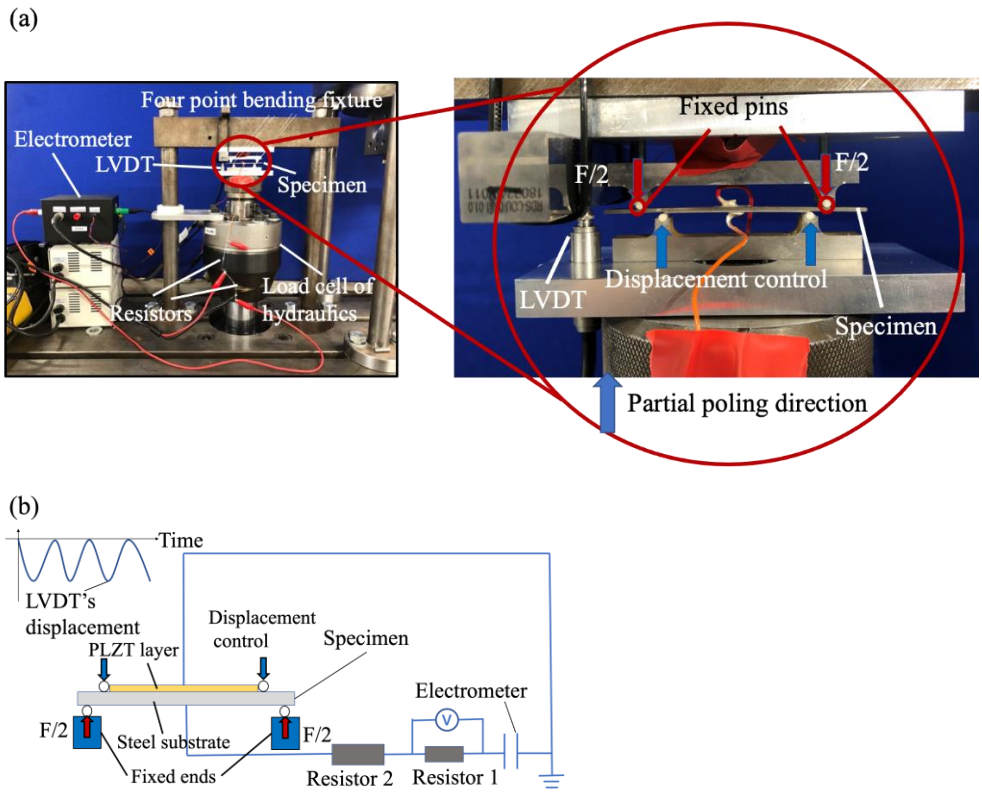


Figure 3.3 Schematics of vibrational test arrangements. (a) The four-point bending test design using hydraulic test machine. (b) Closed circuit for testing at a range of frequencies and electrical loads.

3.2 Experimental procedures

For vibrational tests in Chapter 7, a verification study of non-linearity of between load amplitude and voltage in the energy harvesting cycles were firstly conducted at 15 Hz and 20 Hz. Then the vibrational tests were carried out at 10Hz, with a range of resistive loads from 3 kΩ-15 MΩ. A long series of 5.5×10^5 cycles of maximum power density at 10 Hz with 1.1 MΩ are run to test its stability and robustness.

Chapter 4

4. Prospects for energy harvesting using ferroelectric/ferroelastic switching

This chapter aims to establish a stable and robust cycle of energy harvesting based on ferroelectric switching by using a micromechanical model, providing the basic analysis and insights for future experiments.

Piezoelectric transducers have been widely employed for energy harvesting from vibration or kinetic energy sources. These systems, however, suffer from low energy density and consequently low power density at frequencies corresponding to common ambient vibrations. An alternative approach, using ferroelectric and ferroelastic switching offers potentially much greater energy density, at the cost of loss of linearity. Using a simple model, Hwang's model of switching[136], a working cycle that could generate electrical energy from a harmonically varying source of stress is explored in this chapter. The cycle uses depolarization by stress, followed by repolarization with combined electromechanical loading. A harvesting electric field and bias electric field are imposed to ensure a stable repeatable working cycle during the depolarization process and repolarization process, respectively. The bias electric field affects ferroelectric/ferroelastic switching, leading to a preferred direction of repolarization. By contrast, without bias electric field, stress alone would not trigger repolarization because of mechanically equivalent states with opposite polarization. The results

illustrate that the bias electric field can be much lower than the harvesting electric field, requiring only a small electrical energy input during the cycle. Finally, the conversion efficiency of this cycle is estimated and improvements to the cycle are explored by adjusting the electrical and mechanical field amplitudes.

The cycle has the advantage of exploiting large changes in electrical polarization during switching to provide a greater energy density than that usually achieved in piezoelectric energy harvesters. A further advantage is that the cycle could potentially be realized in a simple device such as a thin layer of ferroelectric material on a bending beam substrate: the complex switching cycle is achieved by external electrical control. The results indicate that the energy harvesting cycle could generate energy output and conversion efficiency that are competitive with, or improve upon, existing piezoelectric energy harvesters. But the model does not consider the ceramic grains' interactions, which needs to be developed in experiments and more sophisticated models. The contents of this chapter were published by Kang and Huber in 2019[405].

4.1 Introduction

Existing research has shown that piezoelectric energy harvesters perform most effectively and efficiently near resonance [226, 227, 416]. Ferroelectric materials offer the potential for increased power density, relative to piezoelectrics, by exploiting ferroelectric switching, which is a non-linear phenomenon resulting from the presence of multiple symmetry variants below the Curie temperature [85].

4.1 Introduction

Building on previous work, a novel energy harvesting method depending on ferroelectric switching is discussed in this chapter. The system works by partially depolarizing a polycrystalline ferroelectric material with stress, and then repolarizing the material with combined electromechanical loading. The working cycle does not require any specific microstructure or domain patterning, so it could be used with ordinary bulk ferroelectrics. A possible realization would generate the stresses needed in the ferroelectric component by attaching it to a substrate whose curvature is varied during the harvesting cycle. Thus cantilever devices, similar to existing piezoelectric energy harvesters, could be used. The only added complexity is provided by external control of voltages, so the device would require a more complex external energy harvesting circuit than that needed for a piezoelectric energy harvester. For an initial study, we use Hwang's model of switching [408] to explore potential working cycles. This model has the advantage of simplicity and speed, though more sophisticated models, backed by experimental measurements, would be required for a fuller analysis. From the preliminary results, it is found that a working cycle with positive net energy output can be achieved. Additionally, the conversion efficiency of the cycle is estimated and improved by adjusting the electrical and mechanical field amplitudes.

4.2 Concept for a ferroelectric/ferroelastic energy harvester

Ferroelectric ceramic materials are produced by sintering powders, and when cooled to below the Curie temperature, they adopt a ferroelectric state such as a polar tetragonal, orthorhombic or rhombohedral crystal structure. For simplicity, we consider a tetragonal ferroelectric capable of 90° and 180° switching, as investigated by Lynch and Hwang *et al.* [85, 408] among others. Consider a unit cell of one crystal polarized parallel to the *z*-axis, as shown in figure 4.1(a). We restrict attention to the case where the unit cell has axes *c* and *a*, with $c > a$. The 180° switching process can be induced by electric fields in the -*z* direction that exceed the coercive electric field E_c and reverse the polarization direction. In addition to this, uniaxial tensile stress along the *x*-axis can cause 90° switching, but the new direction of polarization is uncertain due to symmetry of the tetragonal unit cell, as shown in figure 4.1(b). Similarly, in figure 4.1(c), the uniaxial compressive stress can give rise to 90° switching with an equal probability of four polarization directions. However, when a bias electric field, E_B, is applied in the +*z* direction at the same time as the uniaxial compressive stress, then the 90° switching has a preferred direction, as shown in figure 4.1(d). The bias field E_B can be much less than E_c. A cycle of switching can be made to drive charge onto and off surface electrodes, thereby providing an energy harvesting process in which mechanical energy is converted to electrical energy.

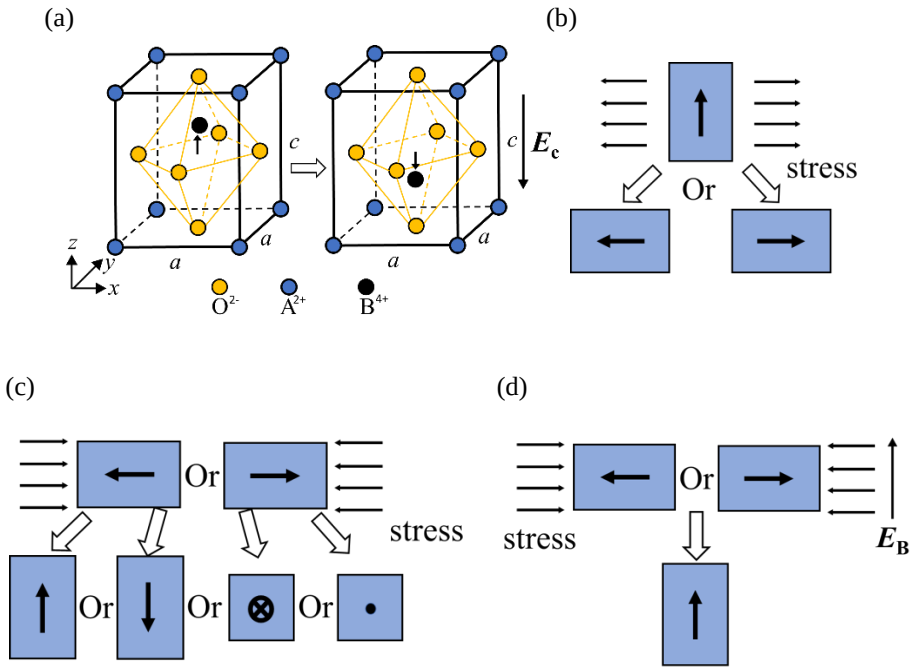


Figure 4.1 90° and 180° ferroelectric/ferroelastic switching processes (a) A tetragonal unit cell with $c > a$. 180° switching is induced by an electric field (b) Uniaxial tensile stress causes 90° switching, aligning polarization vectors with an axis. (c) Uniaxial compressive stress causes 90° switching, aligning polarization vectors with a plane. (d) 90° switching induced by compressive stress and bias electric field together aligns polarization vectors with a preferred direction.

One way of realizing such a process is illustrated in figure 4.2. A thin ferroelectric layer is bonded to a conductive substrate whose curvature then imposes strain on the ferroelectric material. The device is provided with an upper electrode, connected to an external circuit and the substrate is held at zero voltage. In the initial state (figure 4.2(a)), the ferroelectric layer is polarized in the downward direction with positive charges on the top electrode. When a tensile stress is applied to the ferroelectric film (figure 4.2(b)) charge flows from the top electrode to the external circuit. A harvesting

voltage can be applied, against which the device does work. The harvesting voltage is an external electrical load against the charge flow in the energy harvesting cycle to do work. The electromechanical repolarization process is as follows: The ferroelectric layer is first relaxed (figure 4.2(c)). Then, compressive stress and a small bias electric field are applied, figure 4.2(d); this repolarizes the device, allowing it to return to the state in figure 4.2(a).

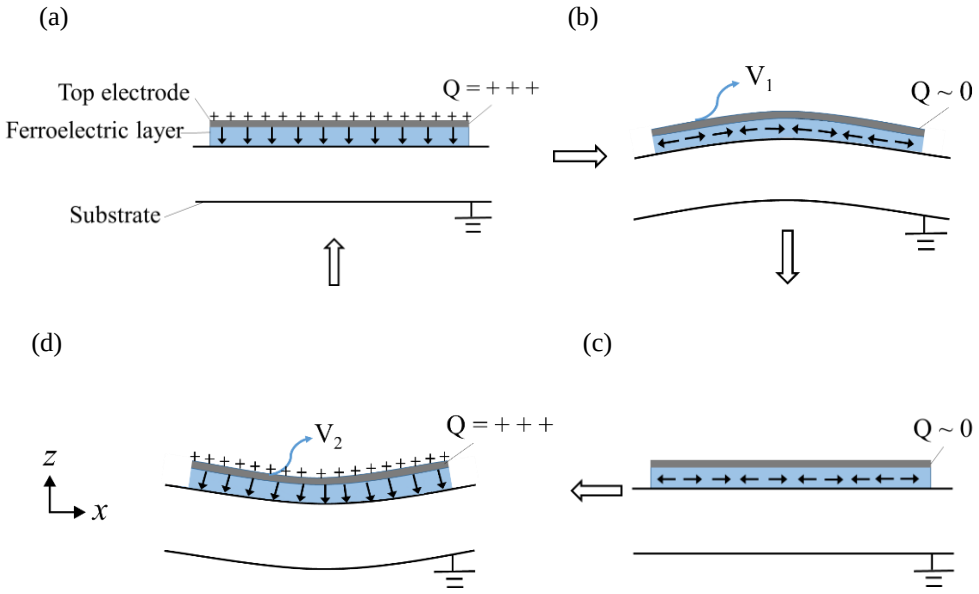


Figure 4.2 (a)-(d) Schematic illustration of one realization of an energy harvester concept. (a) The ferroelectric layer is polarized in the downward direction with positive charges on the top electrode. (b) A tensile stress is applied to the ferroelectric film charge flows from the top electrode to the external circuit. A harvesting voltage can be applied, against which the device does work. (c) Then the ferroelectric layer is relaxed. (d) A compressive stress and a small bias electric field are applied to repolarize the device.

While figure 4.2 illustrates a particular realization of an energy harvesting device, in the present work we explore only the working cycle at a notional material point,

making almost no assumptions about the material arrangement, mechanical loading, or external electrical circuit. The only assumptions external to the material model itself are the availability of a harmonically varying, uniaxial stress, aligned with the *x*-axis, and the ability to control electric fields aligned with the *z*-axis. An energy harvesting cycle is then modelled and explored.

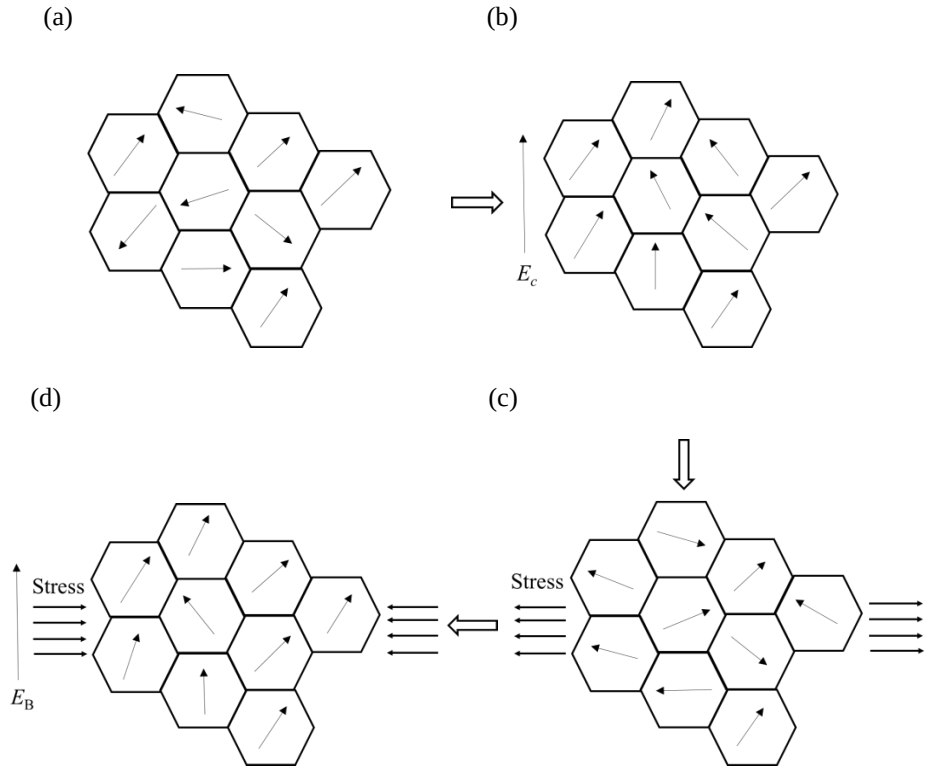


Figure 4.3 Ferroelectric switching in a ceramic at microscopic level (a) The unpoled state of a ferroelectric ceramic. (b) Switching induced by an electric field above the coercive field. (c) Switching induced by tensile stress above the coercive stress. (d) Switching induced by compressive stress and bias electric field. Hexagonal regions illustrate grains, with average polarization shown by arrows.

The energy harvesting cycle could work with either a single crystal or a polycrystalline ceramic ferroelectric. The macroscopic properties of the ceramic, especially the remanent polarization, arise from a combination of all the individual

grains. At the microscopic level, the polarization varies from grain to grain, see figure 4.3, and so individual grains will switch to differing degrees. However, the cycle will still work for a macroscopic aggregate of such grains, even though some individual grains may not contribute. The material point modelled here is assumed to consist of a sufficient number of grains such that the behavior of the individual grains is smeared out by the homogenizing effect of the polycrystal.

4.3 Simulation of an energy harvesting cycle

The simulation is initiated with a random distribution of polarization directions in the grains. The cycle then consists of uniaxial stress applied along the *x*-axis, varying between a maximum tensile stress σ_T and a maximum compressive stress σ_C. At the same time, an electric field is applied parallel to the *z*-axis, with a steady value E_H applied while the stress is tensile and increasing in magnitude, followed by zero electric field while the stress is tensile and decreasing. The applied field E_H resists the flow of charge during the depolarizing process; hence the material does external electrical work. During the repolarization process, when the stress is compressive and increasing in magnitude to σ_C a steady bias electric field E_B is applied along the *z*-axis, assisting repolarization. The electric field is then reset to zero when the stress is compressive and reducing – see figure 4.4.

The cycle is initiated with one of two pre-processes: the first half cycle is either the depolarization process, with tensile stress applied, or the repolarization process, with compressive stress. The first of these cases is shown in figures 4.4 and 4.5; here the cycle is initiated by the strong electric field applied concurrently with the tensile stress, and can be thought of as “electric field triggered”. The other case, where the repolarization process comes first, is shown in figures 4.6 and 4.7. This case can be thought of as “stress triggered”. In either case, the cycle eventually stabilizes, though it may take more than one full cycle to do so.

In figure 4.4(a), the changes of electric field and remanent polarization with time are shown for the electric field triggered process. The results are normalized by the parameters E_0, P^0, e_0 and σ_0, where the coercive stress $\sigma_0 = 2P^0E_0 / e_0$. The corresponding changes of stress and remanent strain are shown in figure 4.4(b), where $\bar{E}_z$ and $\bar{P}_z^r$ are the macroscopic electric field and remanent polarization respectively. $\bar{\sigma}$ and $\bar{e}_x^r$ are the applied stress and remanent strain in the *x*-axis respectively, and t/t_0 is the normalized time in the process. Since the model is rate independent, the time scale is arbitrary. The ceramic is initially unpoled with zero remanent polarization. When electric field is applied along the *z*-axis, the ferroelectric material becomes polarized, resulting in a significant increase of the remanent polarization $\bar{P}_z^r$ and a decrease of the remanent strain $\bar{e}_x^r$. The electric field is held constant during the energy harvesting stage ($0 < t < t_0$) while tensile stress is applied. During this process, the ceramic only partially depolarizes, because the harvesting electric field prevents the stress driven switching in some grains. Next, the harvesting electric field drops to zero while the stress is unloaded, $t_0 < t < 2t_0$. Following this, the compressive stress and bias electric field are applied in order to repolarize the ceramic. The simulation illustrates that remanent polarization $\bar{P}_z^r$ increases and remanent strain $\bar{e}_x^r$ decreases during this stage ($2t_0 < t < 3t_0$). Finally, from $3t_0$ to $4t_0$, the bias electric field returns to zero while the compressive stress is released. The loading cycle is repeated and the material response stabilizes during the second cycle. In the example shown in figures 4.4 and 4.5, the harvesting electric field $E_{\mathrm{H}} = 4E_0$ and the bias electric

field is $E_B = 0.2E_0$. The maximum compressive stress was $\sigma_C = 6\sigma_0$ and the maximum tensile stress was $\sigma_T = 4\sigma_0$. This tensile stress value should be kept low enough to avoid fracture in the ceramic.

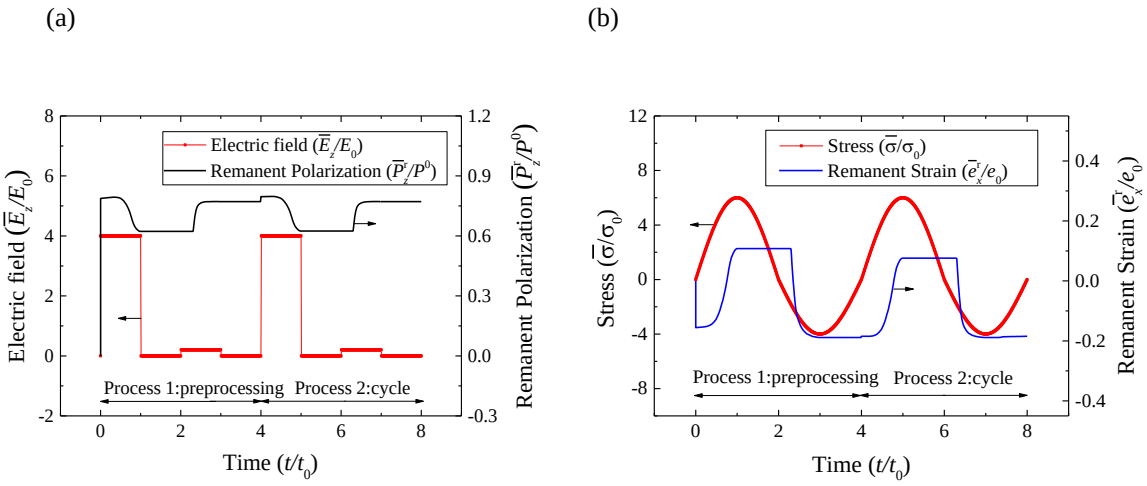


Figure 4.4 Simulation of the electric field triggered working cycle: (a) electric field and remanent polarization in preprocessing and stable cycle vs time. (b) stress and remanent strain in versus time.

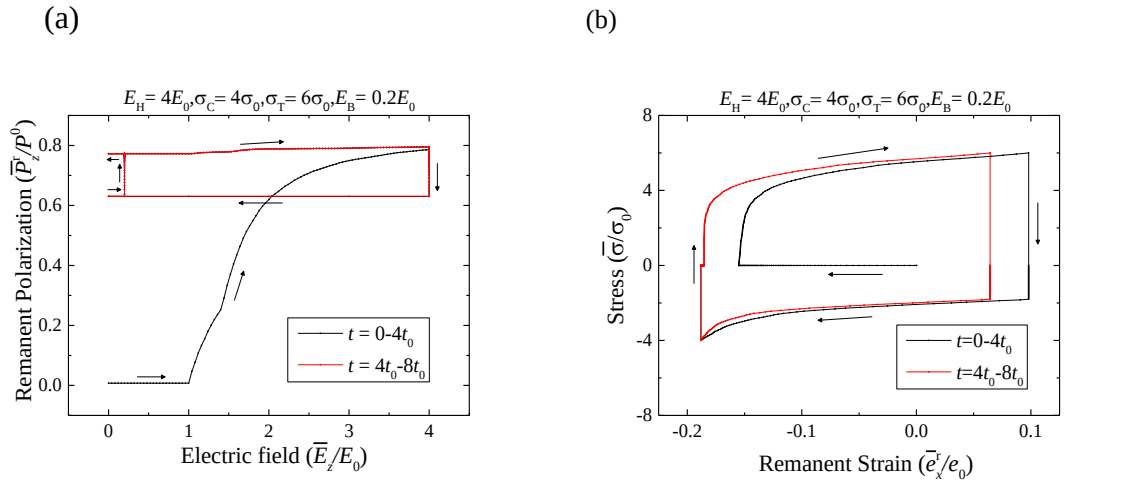


Figure 4.5 Simulation of the electric field triggered working cycle: (a) remanent polarization versus electric field. (b) stress versus remanent strain.

In figure 4.5(a), the pre-process and stable cycle is shown in electric field remanent polarization space. Figure 4.5(b) shows the corresponding change of remanent strain

with applied stress in the first two cycles. Initially, the strong electric field causes a rapid polarization process, which produces a negative strain along the *x*-axis. By time $t = t_0$, a tensile stress has been applied simultaneously with the high electric field, and the remanent strain has increased non-linearly while a partial depolarization occurred. The tensile stress peaks at approximately $6\sigma_0$ and reduces to zero, after which compressive stress is applied with bias field, causing repolarization. The hysteresis loop closes during the second cycle.

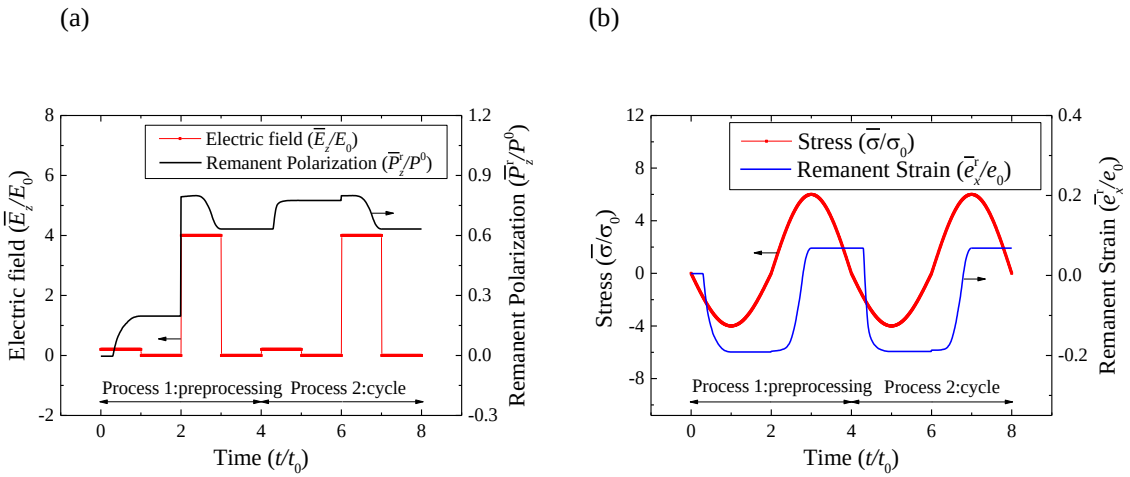


Figure 4.6 Simulation of bias electric field and compressive stress triggered working cycle: (a) electric field and remanent polarization in preprocessing and stable cycle versus time. (b) stress and remanent strain versus time.

A second way of initiating the stable harvesting cycle is shown in figure 4.6. The parameters used in this case are the same as for the first method, but the cycle starts with compressive stress. During the first stage, $0 < t < t_0$, although there is a bias electric field inducing polarization, the remanent polarization of the ceramic does not reach the

fully polarized state. From $2t_0$ to $3t_0$, the harvesting electric field is applied, which polarizes the ceramic and this initiates the stable energy harvesting cycle.

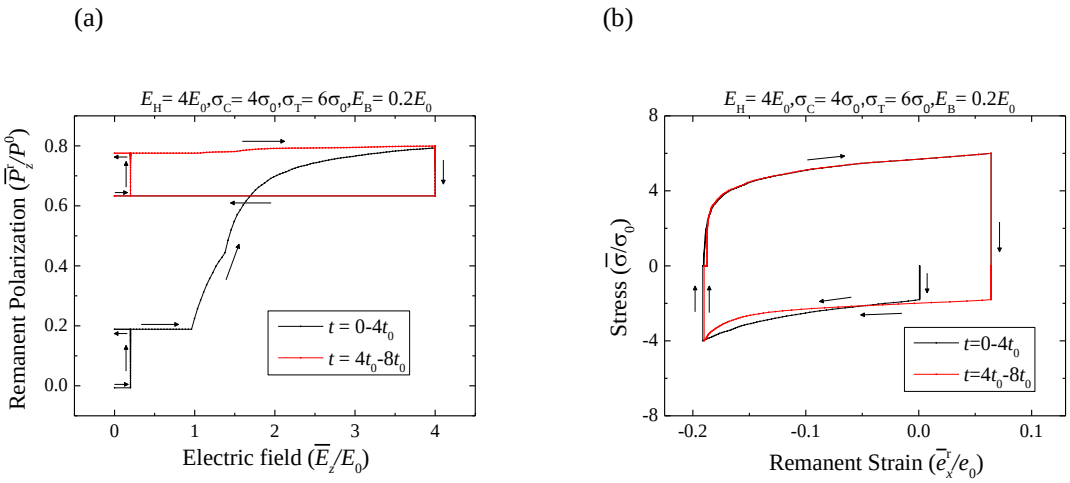


Figure 4.7 Simulation of working preprocessing of the compressive stress triggered cycle. (a) remanent polarization versus electric field. (b) stress versus remanent strain

Figure 4.7, shows the stress-triggered preprocess and the stable energy harvesting cycle. This indicates that, in order to polarize the ceramic, a strong electric field E_z is needed for both trigger methods. However the cycle is robust in the sense that if the ferroelectric material becomes fully depolarized at any point, the application of electric field $E_z = E_H$ will repolarize the ceramic and restart the energy harvesting cycle. This robustness relies on the harvesting field E_H being greater than the coercive field of the material.

4.4 Exploration of the energy harvesting cycle parameters

Based on simulations, the conversion efficiency of this energy harvesting cycle can be estimated and the cycle optimized. By varying the values of harvesting electric field E_{H}, bias electric field E_{B}, maximum tensile stress σ_{T}, and maximum compressive stress σ_{C}, a parametric search for an improved working cycle is made.

First consider the effect of varying the harvesting electric field E_{H}, while keeping $\sigma_{\mathrm{C}} = 4\sigma_0$, $\sigma_{\mathrm{T}} = 6\sigma_0$, and $E_{\mathrm{B}} = 0.2E_0$. Figure 4.8 shows a selection of stable remanent polarization-electric field hysteresis loops and the corresponding stress-remanent strain hysteresis. The harvesting field is varied in the range $1-10E_0$. The magnitude of the harvesting electric field should be neither too great, nor too small. If it is too small, there is little electrical work done against the field during the energy harvesting stage, but if it is too great, it will hold the polarization aligned with the *z*-axis, and prevent switching.

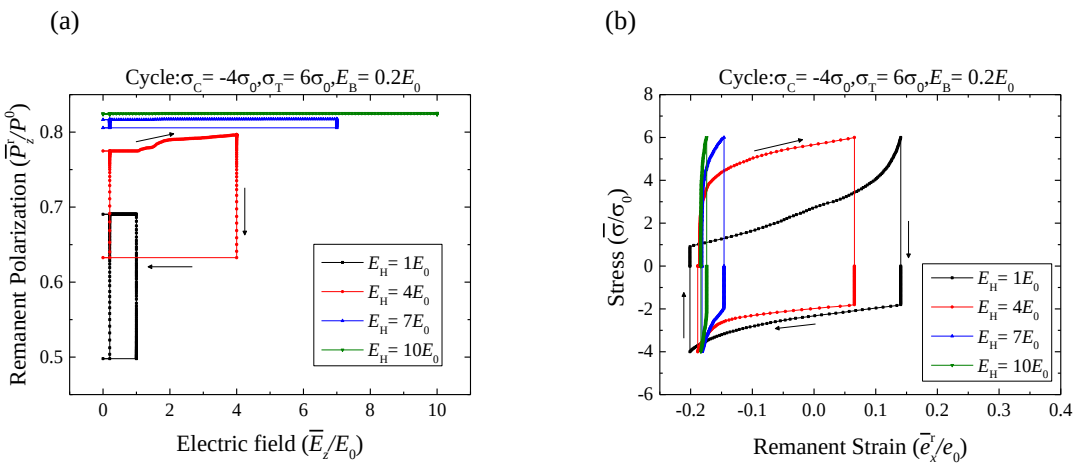


Figure 4.8 The effect of harvesting electric field E_{H} on the energy harvesting cycle: (a) Remanent polarization versus electric field. (b) Stress versus remanent strain.

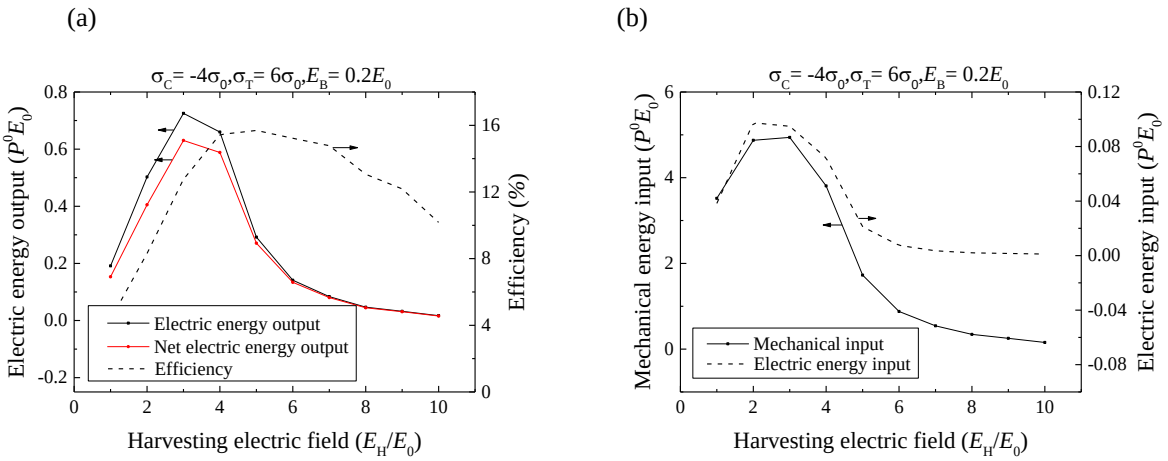


Figure 4.9 The effect of harvesting electric field E_{H} on energy flows (a) The electric energy output and conversion efficiency. (b) Energy inputs.

Figure 4.9(a) shows the electrical energy output and energy conversion efficiency at various values of harvesting electric field E_{H}. With the increase of harvesting electric field, the electrical energy output and net electrical energy output first rise to their peaks at about $0.75\,P^0E_0$ and $0.65\,P^0E_0$ respectively, and then reduce as E_{H} is increased beyond $3E_0$. A good choice for E_{H} appears to be about $3-4E_0$ in order to maximize energy output. Furthermore, the choice of E_{H} strongly affects the conversion efficiency, which reaches a maximum of around 16%, when $E_{\mathrm{H}}=4E_0$.

Figure 4.9(b) shows how the electrical energy input and mechanical energy input vary with E_{H}. The mechanical energy input peaks at about $5\,P^0E_0$ when $E_{\mathrm{H}}=4E_0$ is applied, while approximately $0.1\,P^0E_0$ of electrical energy is put into the cycle. Thus, the mechanical energy is the main energy source; only a small amount of electrical energy input is required.

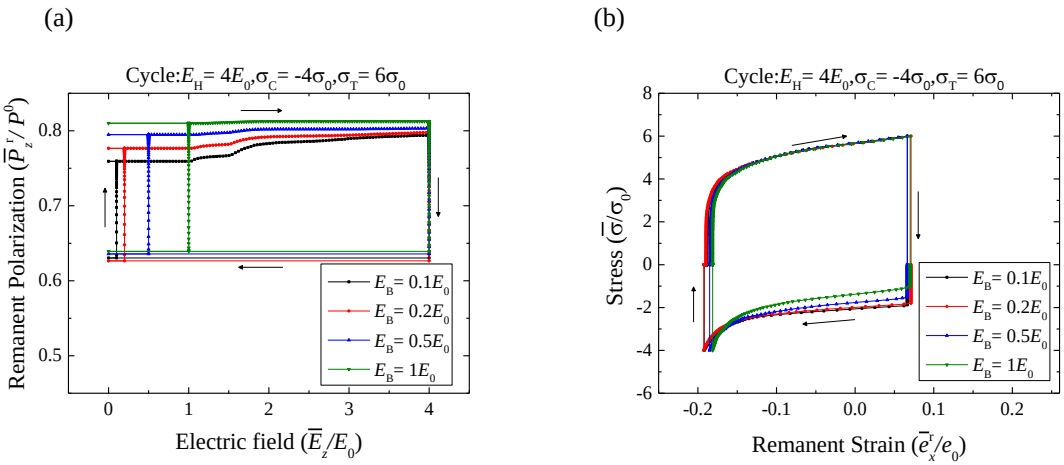


Figure 4.10 The effect of varying the bias electric field: (a) Remanent polarization versus electric field. (b) Stress versus remanent strain.

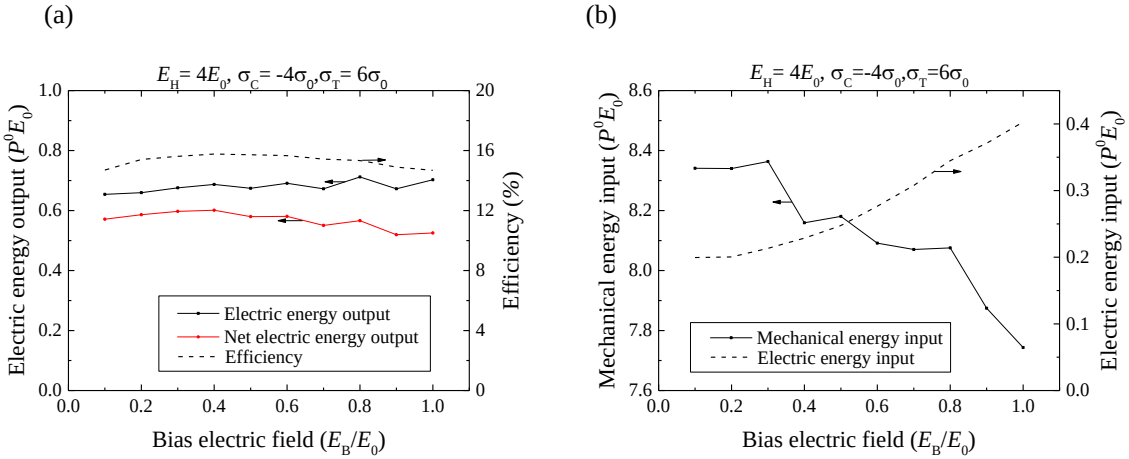


Figure 4.11 The effect of varying the bias electric field: (a) Electrical energy output and conversion efficiency (b) Energy inputs.

Next consider the repolarization process, and variation of the bias electric field E_{B}. Figure 4.10 shows the electrical and mechanical hysteresis loops for E_{B} values in the range $0.1-1E_0$. The other parameters are held at $\sigma_{\mathrm{C}}=4\sigma_0$, $\sigma_{\mathrm{T}}=6\sigma_0$, and $E_{\mathrm{H}}=4E_0$. The results show that varying the bias electric field does not greatly affect the process. A small magnitude of E_{B} has the effect that some of the repolarization is

driven by the harvesting field E_H instead of the intended stress-driven repolarization process. Thus as E_B is reduced, the cycle efficiency reduces, see Figure 4.11.

The maximum compressive stress, σ_C, can also affect the repolarization process. Figure 4.12(a) shows the effect of varying σ_C in the range $3-6\sigma_0$, keeping $E_B = 0.2E_0$, $\sigma_T = 6\sigma_0$ and $E_H = 4E_0$. Counterintuitively, increasing the maximum compressive stress does not necessarily enhance the repolarization process. Note that uniaxial compression along the *x*-axis tends to align the polarization vectors with the *y*-*z* plane. Thus, for high values of σ_C, some grains with polarization direction close to the *z*-axis can undergo ferroelastic switching to states that force the polarization away from the *z*-axis. The result is a reduction in polarization. The *z*-axis polarization, $\overline{P}_z^r$, as a function of *x*-axis uniaxial compressive stress σ is shown in figure 4.12(b), with various values of bias field E_B. The reduction in $\overline{P}_z^r$ at high values of *x*-axis compressive stress can be seen. Notice also that, when $E_B = 0$, the compressive stress tends to depolarize the ceramic. A small magnitude of bias field, $E_B = 0.2E_0$ is sufficient to allow repolarization by compressive stress, and stronger bias field generally enhances the repolarization process. The reduction in efficiency with increasing magnitude of compressive stress can be understood with reference to figure 4.13(b). Increasing the compressive stress magnitude also increases the mechanical work input. However, as can be seen from figure 4.12(a), the electrical work output does not change much. Hence the efficiency falls off with increasing magnitude of σ_C

. Figure 4.12(c) shows the remanent strain versus stress hysteresis loops, corresponding to the cases shown in figure 4.12(a).

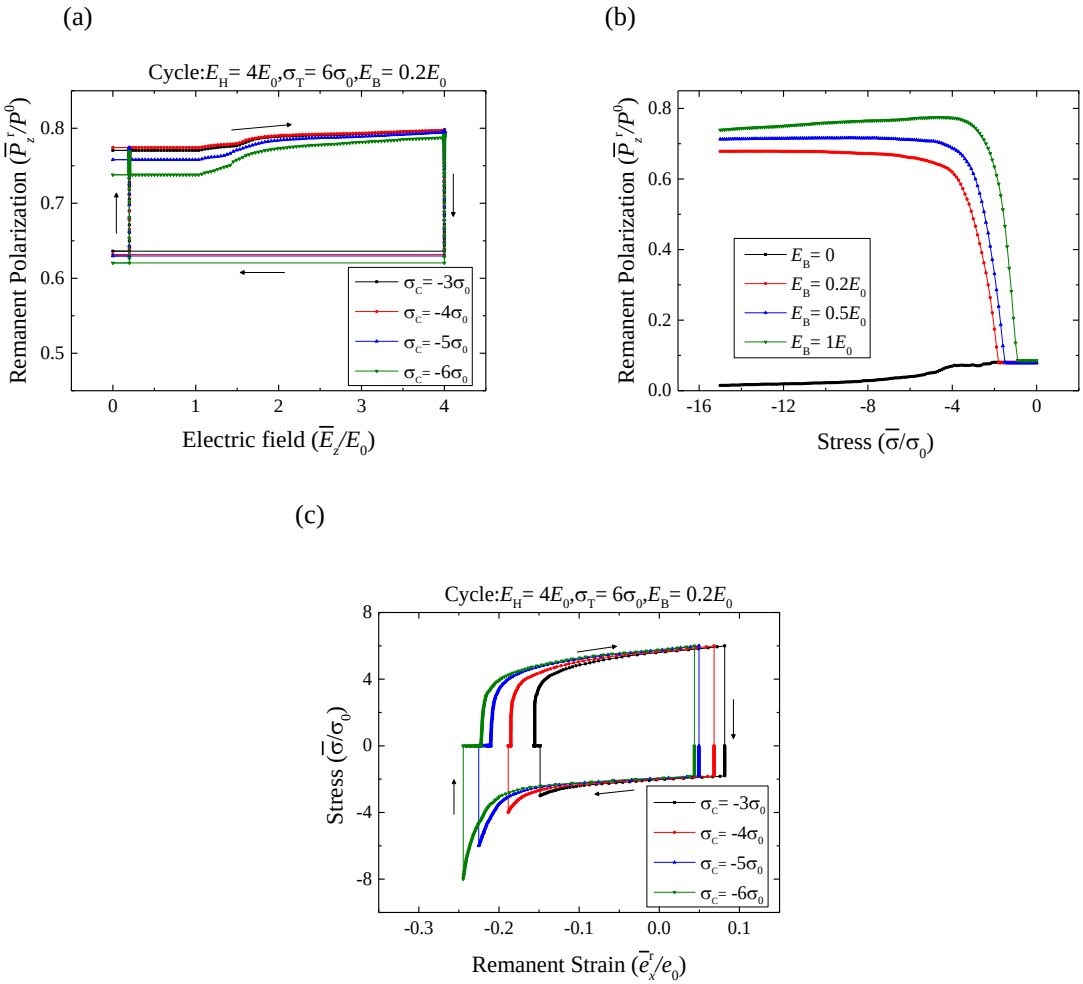


Figure 4.12 The effect of maximum compressive stress on the energy harvesting cycle (a) Remanent polarization versus electric field. (b) The repolarization process at various values of bias field (c) Stress versus remanent strain.

The efficiency and energy flows corresponding to figure 4.12 are shown in figure 4.13. Evidently, although varying σ_C has some effect on the mechanical and electrical energy inputs, it does not greatly affect the outputs or overall efficiency. The choice of σ_C can then be largely based on providing the minimum compression sufficient to

substantially repolarize the ceramic; $\sigma_C = 4\sigma_0$ appears sufficient. The importance of the bias electric field E_B is most clearly seen in figure 4.12(b). If E_B is too small, the repolarization process does not happen and the cycle breaks down. However, provided E_B is great enough to enable the cycle, it has relatively little effect on energy output or efficiency-see figure 4.11(a).

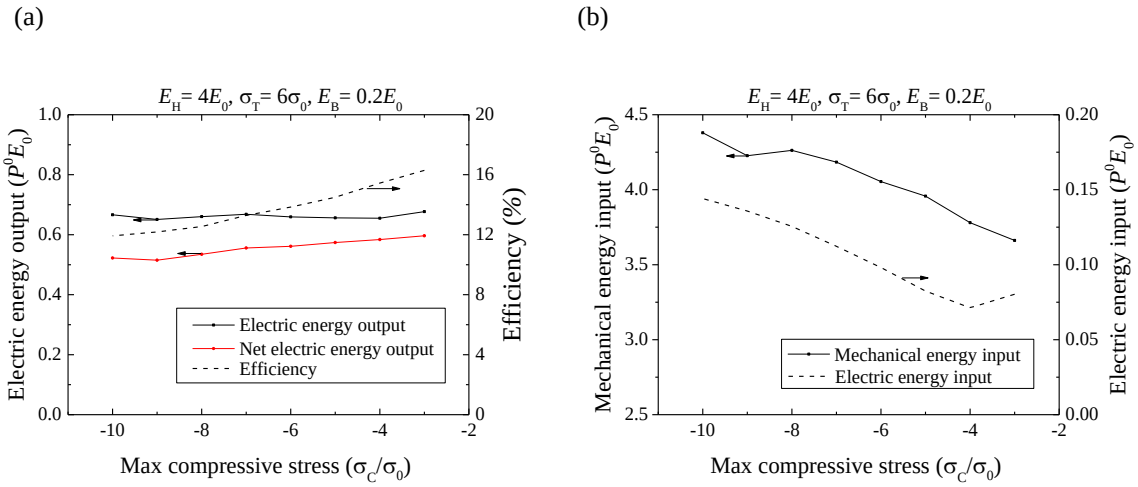


Figure 4.13 The effect of maximum compressive stress on the energy harvesting cycle (a) Electrical energy output and conversion efficiency (b) Energy inputs.

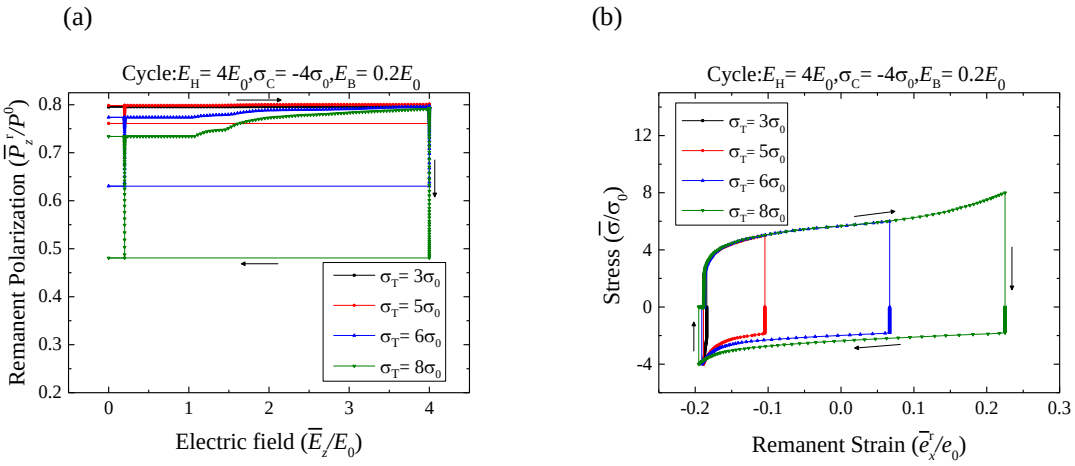


Figure 4.14 The effect of varying the maximum tensile stress: (a) Remanent polarization versus electric field. (b) stress versus remanent strain.

4.4 Exploration of the energy harvesting cycle parameters

Finally, the influence of the maximum tensile stress along the *x*-axis, σ_T, is explored. Due to the risk of fracture, the maximum tensile stress magnitude should generally be kept small. Initial estimates based on data for PLZT [417], wherein the strength is 67.3 MPa, suggesting that $\sigma_T < 10\sigma_0$ may be acceptable with a $\sigma_0 = 7$ MPa. However, specific tests in the device geometry would be needed to confirm safe tensile loading limits. Figure 4.14 shows the effect of varying σ_T on the harvesting cycle, keeping other parameters constant as before. This shows the importance of the tensile stress for depolarizing the ceramic: with $\sigma_T \leq 3\sigma_0$ almost no depolarization is seen. Increasing σ_T causes more grains to switch into polarization directions aligned to the $\pm x$ axis, and so decreases the remanent polarization $\bar{P}_z^r$ of the ceramic. Thus, greater tensile stress is desirable to improve the working cycle of the energy harvester. When $\sigma_T \geq 6\sigma_0$, the enlarged stress-remanent strain loop shows an effective working cycle.

(a) (b)

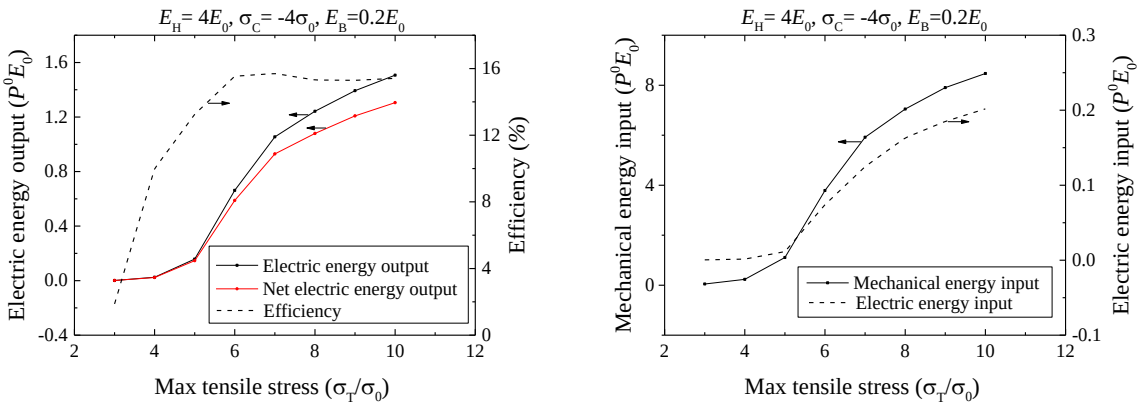
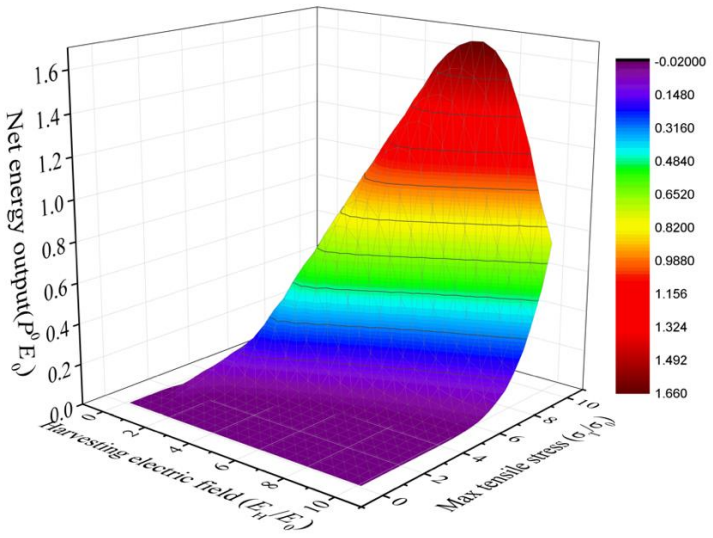


Figure 4.15 The effect of varying the maximum tensile stress on the energy harvesting cycle: (a) Electrical energy output and conversion efficiency (b) Energy inputs.

(a)



(b)

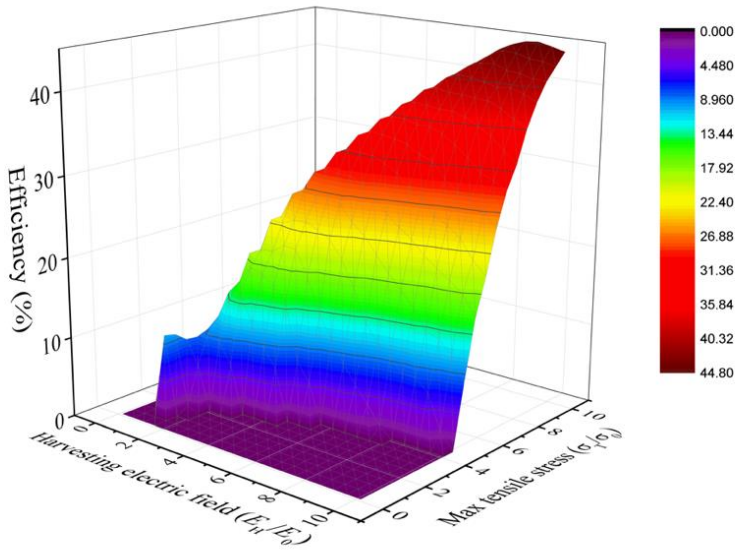


Figure 4.16 The effect of varying the maximum tensile stress and harvesting electric field on the energy harvesting cycle: (a) Electrical energy output and (b) conversion efficiency.

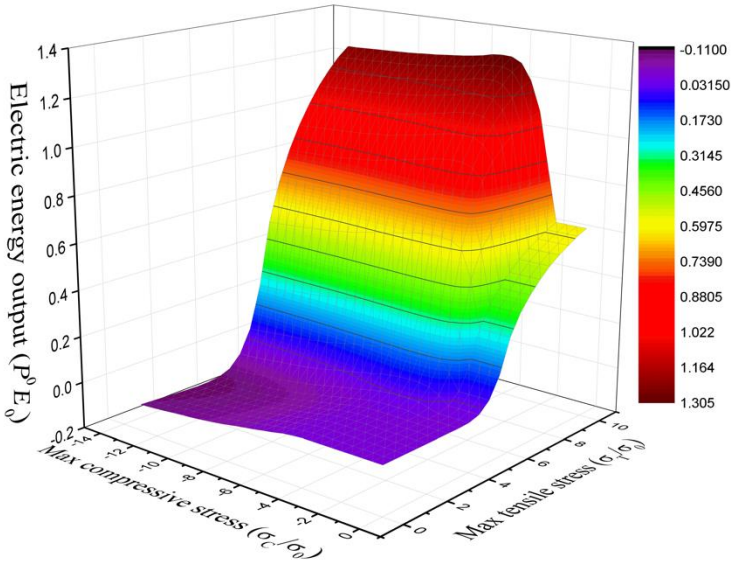
Figure 4.15 shows that efficiency and electrical work output increase with σ_T, but the efficiency does not increase much beyond $\sigma_T = 6\sigma_0$ due to the gradual exhaustion of switching systems in the depolarization process. The analysis suggests

that σ_T should be at least $6\sigma_0$ and as great as possible whilst avoiding mechanical failure.

A further space parametric exploration for energy harvesting optimization is shown in figure 4.16 and figure 4.17. In figure 4.16(a), the net energy output and efficiency of the energy harvesting cycles are presented by varying σ_T and E_H, keeping $\sigma_C = 4\sigma_0$ and $E_B = 0.2E_0$. The results indicate that the rise of σ_T can increase the energy output, but the high harvesting electric field inhibits the switching in the most of the grains. Thus the maximum net energy output reaches a peak at $E_H = 6E_0$ and $\sigma_T = 10\sigma_0$. Figure 4.16(b) shows the corresponding energy conversion efficiency for energy harvesting, wherein the increases of σ_T and E_H increase the efficiency when $\sigma_T > 4\sigma_0$.

In figure 4.17, keeping $E_B = 0.2E_0$ and $E_H = 4E_0$, the effects of varying maximum tensile stress and maximum compressive stress on the net energy output and conversion efficiency are shown. From the figure, although the decrease of maximum compressive stress can make a climb in energy conversion efficiency, the energy output drops significantly. Besides, the maximum tensile stress plays a more important role in the energy harvesting, while maximum compressive stress has a limited effect on energy harvesting cycles.

(a)



(b)

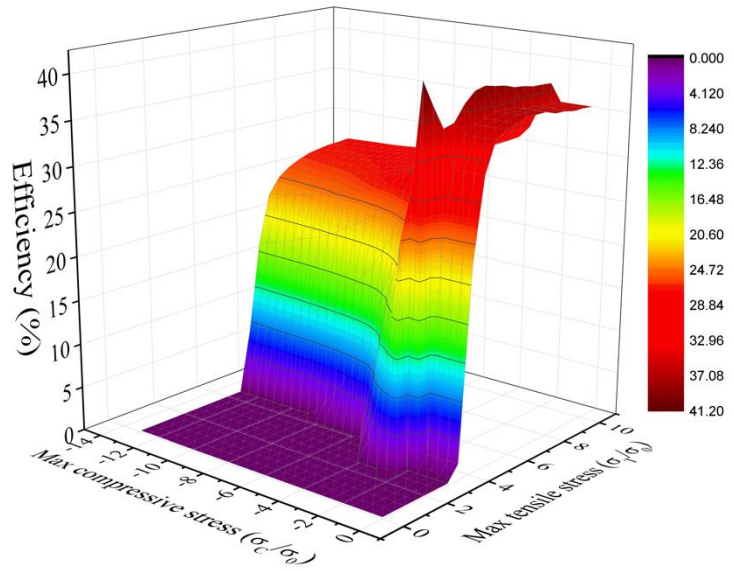


Figure 4.17 The effect of varying the maximum tensile stress and maximum compressive stress on the energy harvesting cycle: (a) Electrical energy output and (b) conversion efficiency.

The performance of the proposed energy harvesting cycle can be assessed in comparison to other proposed or real devices. For instance, based on the above analysis,

an 8/65/35 PLZT layer with $P^0 = 0.3$ Cm^{-2} and $E_0 = 0.36$ MVm^{-1} would generate about 0.16 Jm^{-2} per micrometre of thickness on each cycle and offer area power density of 160 Wm^{-2} per micrometre of thickness at 1 kHz under ideal conditions (neglecting losses in the external circuit). This power density is much greater than that of existing piezoelectric energy harvesters, and several times greater that of the proposed ferroelectric energy harvester concept in reference [79] operating at the same frequency. The conversion efficiency can reach about 16% ~20%, which is comparable to that of commercial photovoltaics [31-33]. The reported range of efficiencies for linear piezoelectric energy harvesters is wide, but values in the region of 10-20% appear typical[418], suggesting that the proposed cycle may be competitive, in energetic terms, if it can be realized in practice. However, it should be noted that the model used was simplistic, neglecting grain-grain interactions, rate effects, thermal effects and cyclic fatigue in the ceramic, as well as assuming uniformity of stress and strain, that would not be accurate in cantilever-type devices. The theoretical development also neglects several practical difficulties that would need to be considered in developing a working device: fracture and/or mechanical fatigue will limit the acceptable levels of tensile stress, while the electric fields required in some ceramics could exceed the breakdown strength of air, requiring additional insulating layers that may influence mechanical performance. Here, the electric breakdown strength of air is a critical value of electric field that can induce a process, in which an electrical insulating material suddenly becomes an electrical conductor and electric current flows through it. This can be

avoided by carefully fabricating the electrodes in the experiments shown in the following chapters. In this model, edge and end effects have been ignored. Similarly, clamping of the ceramic by electrode layers or substrates has been ignored. In particular, clamping of the *y*-axis strain by a substrate could be significant if the widely-used cantilever configuration is employed. The development of an external circuit to control the harvester is also a significant consideration, since an active circuit is required to provide the bias field at the appropriate point in the cycle. Thus further development and experimental confirmation would be needed to be confident of the system's practical value. In this sense, the results reported here represent only an initial assessment of a concept, intended to demonstrate its potential.

4.5 Summary

In conclusion, a novel energy harvesting cycle based on ferroelectric switching has been proposed and investigated using Hwang's model of ferroelectric switching in this chapter. The cycle has the advantage of exploiting large changes in electrical polarization during switching to provide a greater energy density than that usually achieved in piezoelectric energy harvesters. A further advantage is that the cycle could potentially be realized in a simple device such as a thin layer of ferroelectric material on a bending beam substrate: the complex switching cycle is achieved by external electrical control. The energy harvesting cycle was explored by adjusting the electromechanical parameters, and the energy output and conversion efficiency were estimated. The results indicate that the energy harvesting cycle could generate power density and conversion efficiency that are competitive with, or improve upon, existing piezoelectric energy harvesters. This makes the proposed ferroelectric/ferroelastic energy harvesting cycle a promising candidate for further development.

Chapter 5

5. Energy harvesting based on compressive stress-induced ferroelectric/ferroelastic switching

Ferroelectric/ferroelastic switching is attractive because of the greater energies and charge flows involved. However, the associated non-linearities and the difficulty of establishing a stable working cycle have prevented significant progress. Some theoretical works are cited that attempt to solve this problem, but no significant work was reported for the practical applications. In the work of Chapter 4, the energy harvesting working cycles are theoretically predicted, but that concept was not practical for application due to the requirements of a synchronized external bias electric field, which would greatly complicate the design of devices. In this chapter, a novel and robust ferroelectric energy harvester based on partial ferroelectric switching is explored. The device is of simple construction and achieves a per-cycle energy density of about 1 mJ cm^{-3}, orders of magnitude greater than that of typical piezoelectrics. It is shown that only periodic compressive stress is needed to induce the energy harvesting cycles, yielding unique and promising mechanical attributes that limit fatigue or fracture during cyclic loading. The results show this prototype device operating stably over 0.5×10^{6} cycles at 20 Hz frequency, demonstrating promise for practical applications. The main novelty is to define the ferroelectric material's state using a

partial pre-poling process and to use the internal ‘residual fields’ to direct to polarization switching induced by stress only. This is newly developed: no partially polarized ferroelectric energy harvesting devices were reported in previous research to date. This is a lead chapter for the experimental works: initial quasi-static tests were carried out with 100%, 75%, 50% and 30% pre-poled samples, and only the 100% and 30% pre-poled sampels are compared in this chapter. The detailed results for the energy harvesting cycles explored can be found in Chapter 6. The investigation of load resistor selection investigation for a 30% pre-poled sample with the same experimental set-up is given in Chapter 7. The work in this chapter has been published as [406].

5.1 Introduction

While several of the energy harvesters that have been developed make use of ferroelectric materials, none make direct use of ferroelectric or ferroelastic switching as a transduction mechanism. Ferroelectrics exhibit non-linear hysteresis relating electric field, stress, strain and electric displacement.[75, 419, 420] The non-linearity is intrinsically related to ferroelectric/ferroelastic switching, and the hysteresis arises due to switching of domains, a process that can cause much greater charge flows than those found in piezoelectric transduction. Despite the potential of ferroelectrics for mechanical energy harvesting with high energy density, the challenges of non-linearity, fatigue degradation and the difficulty of driving an electrical cycle by stress have limited their use in energy harvesting applications. Vaish *et al.*[399, 400] proposed an

energy harvesting method at material level based on modified Olsen cycle by ferroelectric switching induced by mechanical stress, showing prospective of energy conversion and storage. A few theoretical designs of ferroelectric energy harvester devices have been proposed[19, 63, 171, 396, 397, 404, 405], but successful implementation was not reported.

In this chapter, a novel, practical ferroelectric energy harvester for low-frequency applications is established by exploiting partial ferroelectric/ferroelastic switching. Although the present work does not adopt new materials and structures, the main novelty is to engineer the material state of electroceramics in such a way as to make a stable ferroelectric/ferroelastic energy harvesting cycle possible using cyclic compression alone. Specifically, a partially poled electroceramic layer and stiff substrate are bonded together. The poling process is then completed, resulting in a state of residual stress in the electroceramic. A residual stress state is then induced using bending loads to manipulate the electroceramic into a partially depolarized state in which the polarization is easily modified by stress. Subsequently, bending loads are used to induce cyclic compressive stress driven by the substrate's curvature. This results in a stable cycle of polarization changes driven by mechanical load, used to form an energy harvesting cycle. Both open-circuit and resistive load tests are explored, showing output energy density much greater than that of traditional piezoelectric energy harvesters. Fatigue tests demonstrate that the system is stable and robust.

5.2 Working concept and design

As the use of ferroelectric or ferroelastic switching for energy harvesting is relatively novel, it is instructive to set out the reasons for this approach and the challenges to be overcome. Typical piezoelectrics operate in a linear regime with electric fields up to about 10^5 V m^{-1} and electric displacement changes of order 10^{-3} - 10^{-2} C m^{-2}. Hence, the electrical energy harvested per cycle is much less than 1 mJ cm^{-3}; values of 10^{-2} - 10^{-1} mJ cm^{-3} are common in high-performance piezoelectric devices. By contrast, the full cycle of ferroelectric hysteresis commonly involves field amplitudes of order10^6 V m^{-1} and electric displacement amplitude of 0.1 – 0.6 C m^{-2}; thus the electrical energy density is orders of magnitude greater than that of a piezoelectric cycle. If even a fraction of this energy could be extracted for useful electrical work, then a significant improvement in energy density could be achieved relative to piezoelectrics. The opportunity is clear, but the obstacles are significant: applying mechanical loading to a poled ferroelectric can depolarize it, but will not normally re-polarize it. Existing designs of ferroelectric transducer are single shot devices designed to deliver a substantial pulse of electrical energy, but with no way of delivering continuous power. Thus, the main difficulty of energy harvesting using ferroelectric/ferroelastic switching is to establish a closed and robust working cycles by using stress only without external assistance. Meanwhile, the ferroelectric hysteresis

entails switching of domains, a lossy process that can lead to rapid material degradation if operated cyclically.

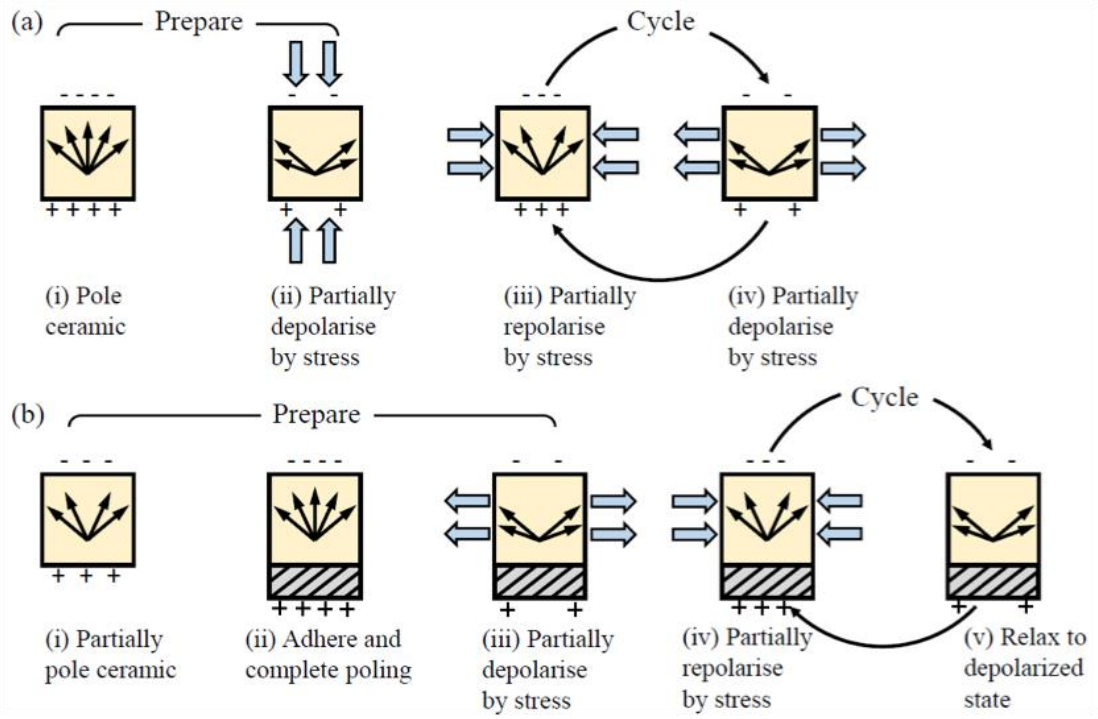


Figure 5.1 Preparation and working cycles for ferroelectric energy harvesting at material level (a) using cyclic compressive and tensile loading. (b) using a substrate and cyclic compressive loading. Black arrows indicate the polarization distribution. Hollow blue arrows indicate mechanical loading.

The problem of producing a stable cycle in which polarization changes are driven by mechanical stresses is fundamental: as a second order tensor, an applied stress does not define a vector direction, and so cannot produce polarization change unless there is some vector-type state variable to define a direction. For example, an unpoled electroceramic cannot be poled by uniform stress alone. The idea of using a small value of applied electric field to bias the polarization in a preferred direction has been discussed in Chapter 4. However, this concept still leaves considerable challenges, caused by inaccuracies in the prediction of working cycles and the high tensile stresses

required for switching. It is also challenging because of the requirements of a synchronized external bias electric field, which would complicate device design. Another possibility is to use a stress gradient or strain gradient to define a preferred direction, especially in thin-film devices. This relates to the flexoelectric effect, wherein the mechanical gradient field could influence the spontaneous polarization in a way analogous to electric field in ferroelectrics[421, 422]. Alternatively, residual electric fields could provide the necessary 'memory' of a preferred direction. This last approach is taken here. Thus, an objective of the present work is to identify a material state for a ferroelectric ceramic such that cyclic loading with stress produces a cyclic change in polarization. There are two methods demonstrating the potential mechanisms that can be used for energy harvesting based on this concept shown in figure 5.1. In the concept shown in figure 5.1(a), a ceramic is first poled, then partially depolarized using stress; finally, the stress is cycled to effect a cycle of electric displacement. A disadvantage of this cycle is that tensile loading is required; in preliminary experiments this was found to promote cracking of the ceramic, transverse to the tensile axis. An alternative using an elastic substrate, figure 5.1(b), uses only compressive loads during cycling. A residual state of tension is expected to develop in the ceramic during the cycle, but the substrate limits cracking by controlling displacement and strain in the ceramic layer. Figure 5.1 describes the cycle for an element of ceramic material consisting of many domains but subjected to a uniform state of loading. Electrical energy is obtained by the movement of charges to and from the surface of the ceramic, against a voltage. The

working concept of the energy harvester can be described as ferroelectric/ferroelastic switching because the polarization changes are driven by a combination of electric field and stress.

For practical application it is necessary to devise a means to convey mechanical loads into a bulk of ceramic material and to connect electrodes for extracting electrical work. The displaced charge is proportional to surface electrode area and thus a large surface area of electrodes is desirable. However, to keep the circuit voltages at a convenient low level (<50V), low thickness is also advantageous. Hence in this work the bulk ceramic is arranged as a thin wafer adhered to a stiff substrate producing a flexible beam structure. This arrangement also has the advantage that it is similar to the commonly used form of piezoelectric energy harvester in which a thin cantilever beam is subjected to inertial loading. However, the inertially loaded cantilever has the disadvantage that the curvature varies along its length, subjecting each element of the energy harvester to different loading conditions. In a linear material, this continuous variation of loading is tolerable, but in the ferroelectric device greater control of the loading cycle is needed and it is thus advantageous for each element of material to experience the same loading cycle. For this reason, a four-point bending arrangement has been adopted here, producing uniform bending moment and hence no variation along the beam. The finite thickness of the wafer can induce a stress distribution along the *z*-axis so that there is a through-thickness variation. The detailed information about specimen fabrication and test arrangements can be found in Chapter 3.

The material preparation and energy harvesting cycle in device perspective are illustrated in figure 5.2, and it mainly shows the device preparation and operation with a four-point bending arrangement, as well as the changes of electric displacemnt and strain of electroceramic induced by electric field and mechanical loads. Initial pre-poling OAB in figure 5.2(a) and (b) generates both through thickness electric displacement D_z and negative in-plane strain e_x, while the ceramic remains unstressed macroscopically ($\sigma_x = 0$). In this partially poled state the ferroelectric layer is adhered to a substrate, see figure 5.2(c). Then further poling (BCD) is applied to produce a fully polarized state with moderate in-plane tensile stress. Finally, bending load is applied to produce a controlled tension and partially depolarize the ceramic (DE). After the preparation, the energy harvesting cycle EFGH can be applied. In figure 5.2(a)and (b) the cycle shown is the quasi-static cycle with controlled voltage applied to the top electrode. This produces step changes in electric field E_z during stages EF, where the field is switched “on” and GH, were the field is switched “off”. While the field is “on”, mechanical loading produces compressive stress σ_z in the ceramic layer, causing it to repolarize in stage FG. This produces electrical work output against the applied electric field. Finally, in stage HE the mechanical loading is removed at zero electric field, allowing ferroelastic switching to return the cycle to its initial state. The area of quadrilateral EFGH in figure 5.2(a) represents the output electrical work per unit volume of active material in a single cycle, while the corresponding area in figure 5.2(b) is an input mechanical work per unit volume. In tests at frequency, the controlled

electric field was replaced by a passive load resistor which changes the detail of the cycle but keeps the essential features the same.

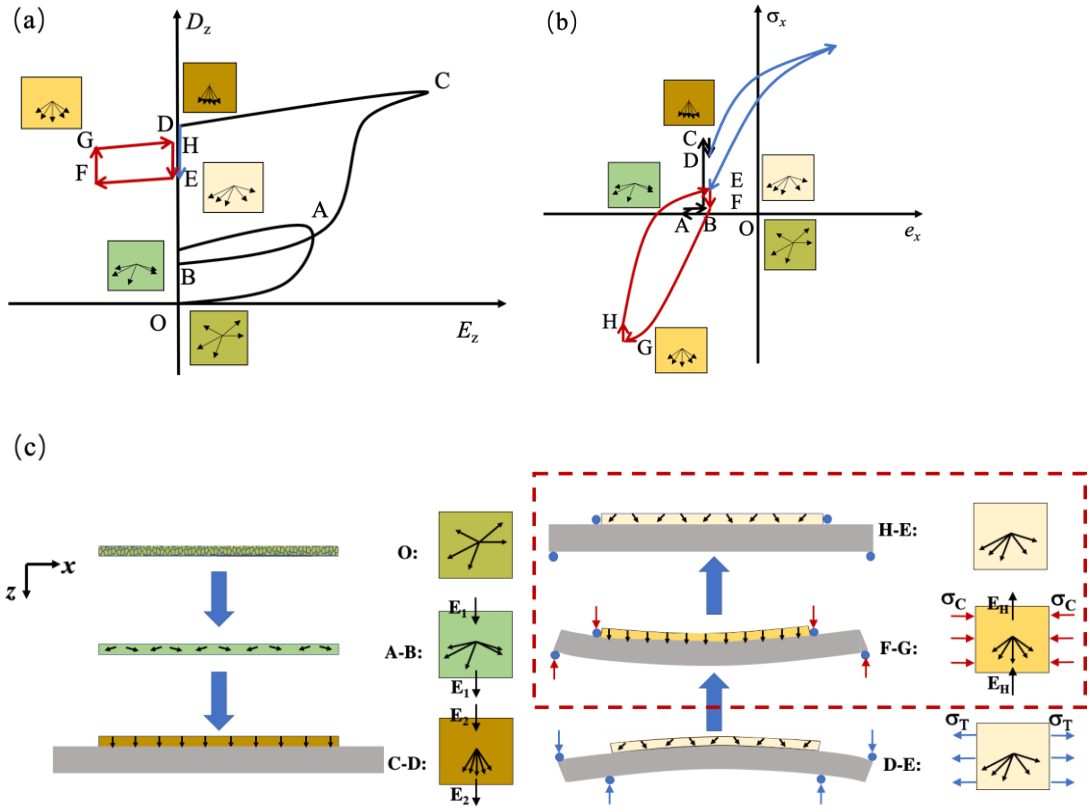


Figure 5.2 The preparation and operation of ferroelectric energy harvesting device and correponding changes in electroceramic. (a)Electric displacement versus electric field in the preparation and energy harvesting cycle (schematic). (b) The corresponding stress versus strain in the x-axis direction. (c) The preparation stages and energy harvesting cycle using four-point bend loading.

5.3 Results and discussion

A range of experimental conditions were considered in the tests. For example, 30%-100% pre-poled specimens were prepared for energy harvesting investigation. Besides, the influences of varying mechanical load, electrical load and frequency on energy harvesting were also studied. Here, a limited set of results is reported in order to convey the main findings.

5.3.1 Quasi-static tests

Quasi-static loading tests were carried out by taking the energy harvester through the following cycle: A voltage V_{app} was first applied to the device to produce an electric field αE_0 where $E_0 = 0.36$ MV m^{-1} is the coercive field and α is a factor that could be varied to represent different electrical loads. With this electric field held constant, mechanical loading force $F/2$ was applied at each pin; total force magnitude F could also be varied to modify the cycle. The force was applied in such a way as to cause in-plane compression in the active layer, and thus drive an increase in net polarization, against the applied electric field. Next, with the loading pins held fixed, the applied voltage was reduced to zero. Finally, the mechanical load was reduced to zero. The quasi-static cycle was traversed at a frequency of 10^{-2} Hz.

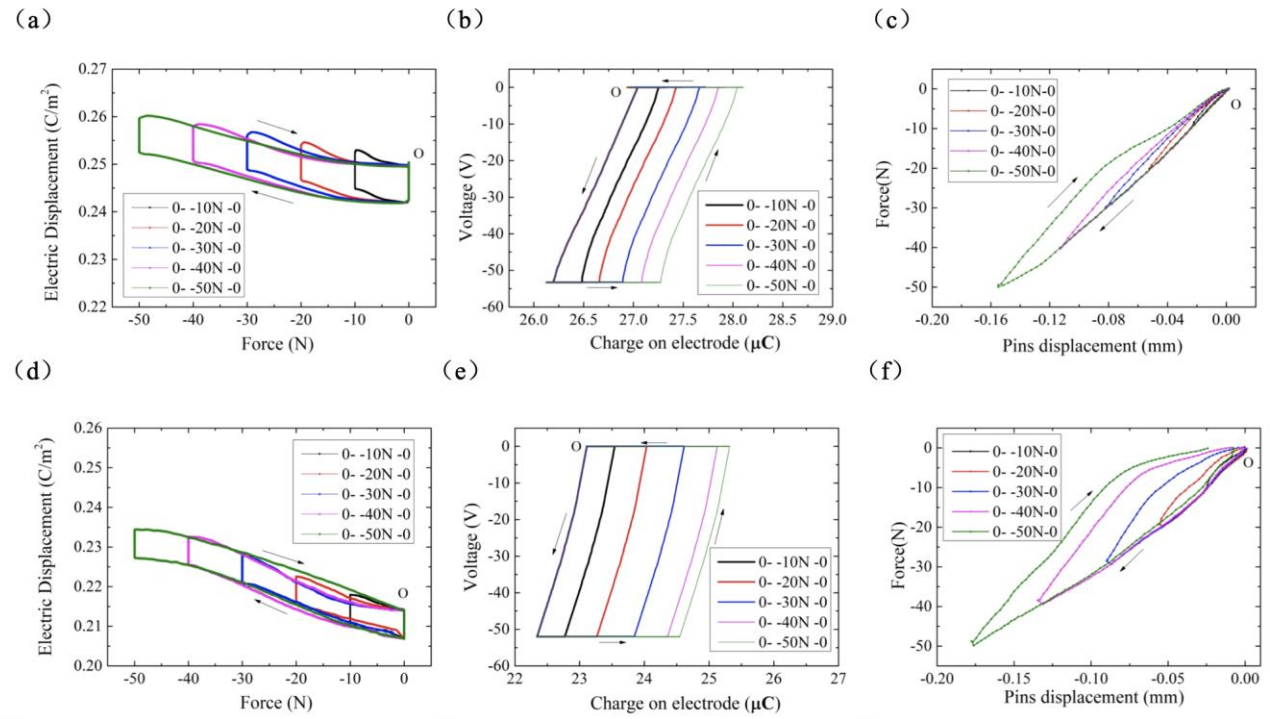


Figure 5.3 Comparison of the 100% pre-poled and 30% pre-poled energy harvesting cycles. (a-c) for 100% pre-poled specimen and (d-f) for 30% pre-poled specimen. (a,d). Electric Displacement versus applied bending force with electric field $0.4E_0$ applied during the energy harvesting cycle. (b,e) Corresponding voltage versus charge cycle. (c,f) Corresponding force versus loading pin displacement.

For brevity, only the results for α = -0.4 (V_{app} = -50 V), with the 100% pre-poled and 30% pre-poled samples are included here, see figure 5.3. The start of the cycle is marked 'O' in figure 5.3(a)-(f). The peak force value F was varied in the range from -10 N to -50 N. In figure 5.3(a) vertical straight segments in each cycle correspond to the changes in electric displacement at constant force, due to switching the electric field "on" or "off"; curved segments correspond to the application or removal of mechanical loading. The cycle is traversed in a clockwise direction. Conversely, in figure 5.3(b) horizontal straight segments are seen, due to the application or removal of mechanical load at constant voltage;

curved segments show the variation of surface charge as the electric field is switched. Here the cycle is traversed in an anti-clockwise direction. In the 100% pre-poled sample, very little ferroelastic switching is expected when the mechanical load is applied because the starting state is close to a saturated, fully polarized state. The magnitude of the electric displacement changes during mechanical loading is less than 10^{-2} C m^{-2}, comparable with what is typically achieved in piezoelectric energy harvesting. By comparison, the cycles shown in figure 5.3(d)-(f) for the 30% pre-poled sample are similar in character, but with much greater changes in electric displacement when mechanical loading is applied. This is consistent with ferroelastic switching caused by the mechanical loading; the cycle starts with a polarization of about 0.21 C m^{-2}, so there is freedom for the polarization to increase under mechanical loading. The enclosed area in the voltage-charge loops indicates the electrical energy output per cycle of loading. This is more than twice as great in the 30% pre-poled case than in the 100% pre-poled case, indicating the importance of the partial poling process. The input mechanical energy can be ascertained from the enclosed area in the force- displacement curves of figure 5.3(c),(f) ; this grows with applied load amplitude and is much greater in the 30% pre-poled case.

Figure 5.3 clearly demonstrates a working cycle for the ferroelectric/ferroelastic energy harvester, but leaves open the question of how to optimize performance. There are several compromises to consider: increasing the electric field by controlling α enhances the energy output per cycle, but if the field strength becomes too high it may cause ferroelectric switching and destroy the engineered state of the energy harvester. For this reason,

experimentation was constrained to $\alpha > -0.4$. Similarly, increasing the total applied force F increases the energy per cycle, but again high values may disturb the material state by permanent ferroelastic switching, or may promote fatigue. Figure 5.4 summarizes results for the energy output per cycle from a set of tests in which α and F were varied in both the 100% and 30% pre-poled samples.

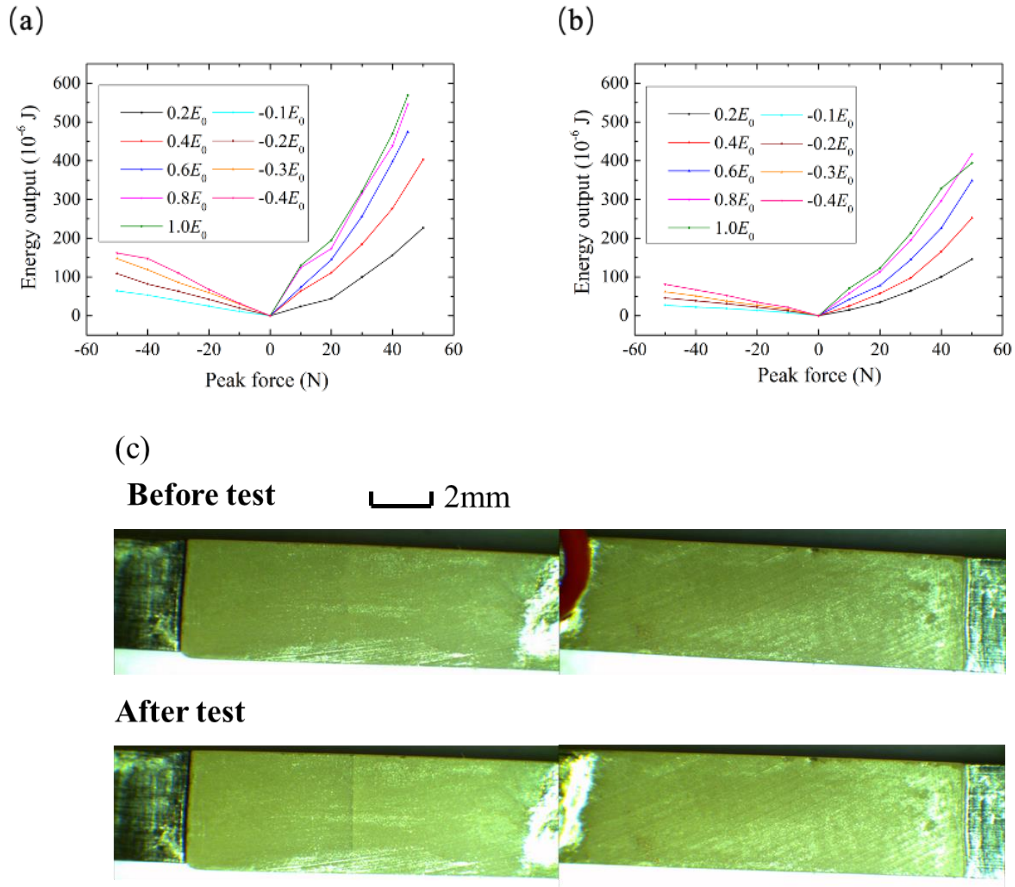


Figure 5.4 Energy output per cycle in quasi static tests with tensile and compressive loading. (a) 100% pre-poled samples (b) 30% pre-poled samples. (c) An example of cracks on the specimens.

The tests with $F > 0$ indicate cases where the sample was inverted in the loading fixture in order to produce in-plane tensile stresses in the active layer. It is found that the 30% pre-poled sample consistently produces greater energy output than that with 100% pre-poling. The 30% pre-poled sample generated about 120 μJ per cycle with F

= -50N and α = -0.4, which is much greater than that of typical piezoelectric energy harvesters. Even greater energy yields were achieved in tests with in-plane tension, but this mode of operation was observed to cause cracking in some cases, specifically, for α > 0.8 and *F* = 50 N. Because the PLZT layer was translucent, the formation of cracks could be observed as lines of dark contrast when the sample was back-lit. An example of a microscopic graph for cracks on the specimens can be seen in figure 5.4(c).

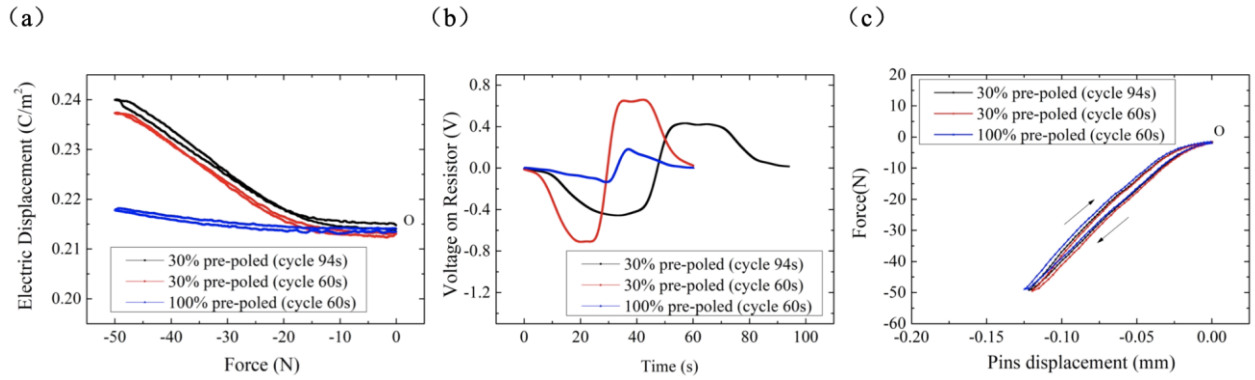


Figure 5.5 Quasi-static cycles with 4.62MΩ resisitve load. (a) Electric displacement versus force (b) Voltage versus time (c) Force versus displacement of loading pins.

In practical applications, it is typically the case that the voltages on an energy harvester are not controlled directly, but rather arise due to the impedance of an external circuit. To simulate this working condition, quasi-static tests were carried out for the case *F* = -50 N with a 4.62 MΩ external load resistor, see figure 5.5. Once again, the 100% and 30% pre-poled cases are compared. The 30% pre-poled sample was also tested using two different cycle times (94 s and 60 s). The force – electric displacement cycles in figure 5.5(a) show that the 30% pre-poled sample produces much greater, non-linear changes in electric displacement compared to the 100% pre-poled case. This further confirms that ferroelectric/ferroelastic switching is occurring in the device.

The cycle period has limited effect on the electric displacement changes but does affect the voltage across the device and hence the current flow, see figure 5.5(b). This could result in complex interactions between the device and the external circuit if the electric field in the device approaches the coercive field. Hence control of the external electrical load and both the cyclic frequency and amplitude of mechanical loading are critical for establishing a stable energy harvesting cycle. Even in figure 5.5, where the mechanical loading waveform is triangular and the voltages remain well below coercive levels, it is evident that the waveform of the generated voltage is not triangular, and is dependent on frequency.

5.3.2 Energy harvesting performance at low frequencies

Generally, human motion can generate vibrations in a frequency range 0.5 Hz – 15 Hz, while 15 Hz – 50 Hz vibrations are common in vehicles.[23] To test the response of the energy harvester at these frequencies, an in-house hydraulic test rig was used, and variation of pre-poling states, load resistor and frequency were explored. The mechanical displacement waveform was sinusoidal in these tests. The results presented here are a small selection intended to convey the main findings.

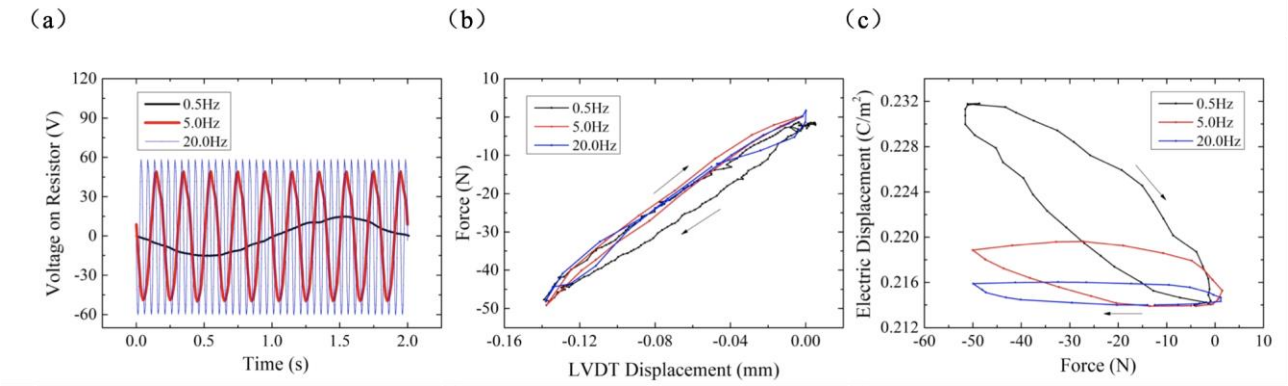


Figure 5.6 The 30% pre-poled energy harvester tested at various frequencies. (a) Voltage across the energy harvester versus time, (b) Force versus LVDT displacement, (c) Electric displacement versus force.

Figure 5.6 presents the effect of frequency on the 30% pre-poled energy harvester, driven with 50 N force amplitude in compression, and working against a 4.67 MΩ electrical load. Figure 5.6(a), shows that the generated voltage amplitude increases with frequency, though the increase from 5 Hz to 20 Hz is only a few per-cent and further tests indicate that the generated voltage amplitude stabilizes as frequency increases. The generated voltage waveform is not sinusoidal, indicating non-linearity. The electric displacement changes during each cycle at 0.5 Hz are slightly less in magnitude than the corresponding values in the quasi-static tests; the electric displacement amplitude reduces with increasing frequency. This is expected because high rates of electric displacement require high currents and hence high voltages, which in turn resist ferroelectric/ferroelastic switching. Thus, the electrical load tends to stabilize the voltage amplitude and limit switching at higher frequencies.

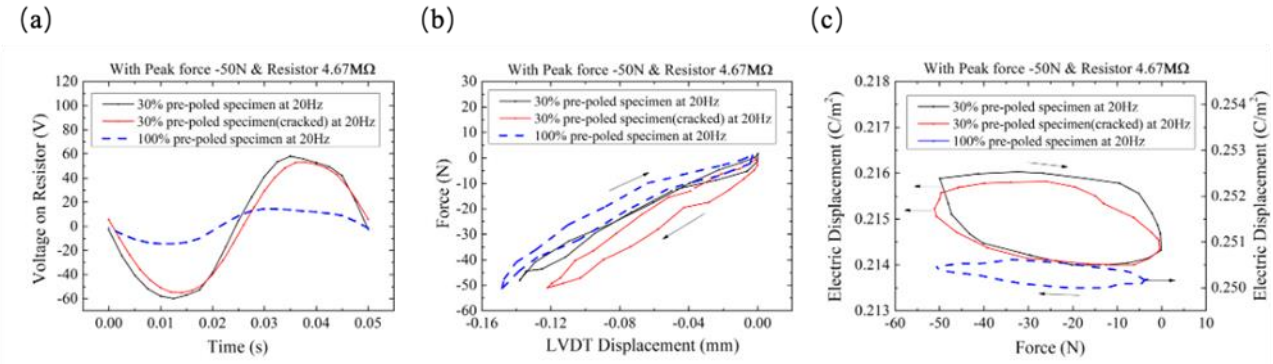


Figure 5.7 A comparison of the 30% pre-poled energy harvester and the 100% pre-poled specimen operating at 20Hz with external resistor 4.67MΩ. Also shown are results from a 30% pre-poled device with cracked active material. (a) Voltage waveform, (b) applied total force versus displacement, (c) electric displacement versus applied force.

Figure 5.7 provides a performance comparison between the 30% pre-poled and 100% pre-poled energy harvesters operating at 20 Hz. As with the quasi-static tests, the 30% pre-poled specimen demonstrates greater voltage and electric displacement amplitude – hence greater power output. As remarked earlier, some operating conditions caused the formation of cracks in the active layer, running perpendicular to the *x*-axis direction. However, these cracks did not greatly affect energy harvesting performance, as seen in figure 5.7, where results for both an uncracked and a cracked sample are shown. Tests were also carried out to establish whether the performance was sensitive to the sample preparation process. It was found that the results were repeatable across different samples, to within a few percent. Note that the force measurements in Figure 5.7(b) show a lack of smoothness; this appears to be an artefact of the load cell accuracy when operating at 20 Hz frequency, which was approximately +/- 3N.

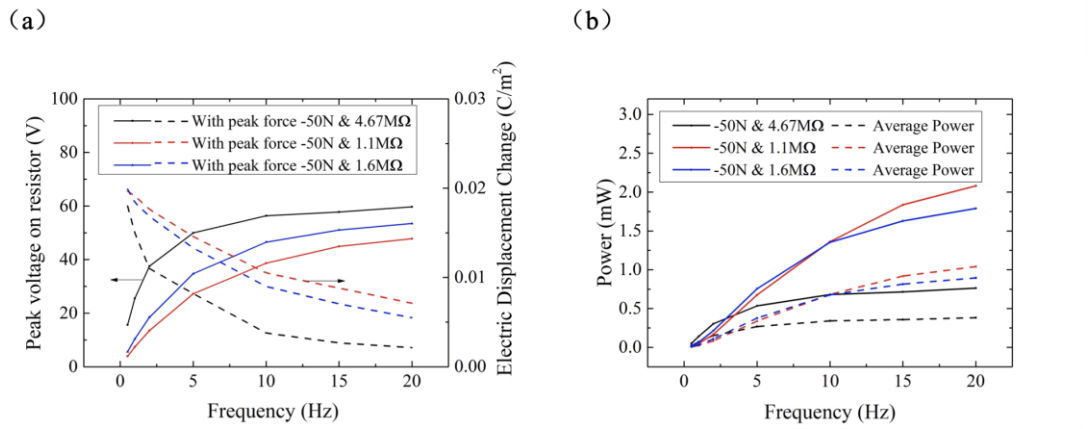


Figure 5.8 The effect of frequency on peak voltage, electric displacement change and power output. (a) The effect of frequency on peak voltage and electric displacement change of 30% pre-poled specimen with 1.1, 1.6, 4.67 MΩ. (b) The effect of frequency on power output and average power output of 30% pre-poled specimen with 1.1, 1.6, 4.67 MΩ.

It is of interest to optimize the electrical load for maximum power output. Figure 5.8 shows the peak voltage, electric displacement change, peak power output and average power output of energy harvesters using 1.1, 1.6 and 4.67 MΩ load resistors at a range of frequencies. The peak voltages increase monotonically with frequency, whereas the electric displacement amplitude decreases monotonically. Variation of the load resistor changes the *RC* time constant and hence affects power matching. This is seen in figure 5.8(b) where the 4.67 MΩ resistor achieves greatest power for frequencies less than 3 Hz, the 1.6 MΩ from 3-10 Hz, and then the 1.1 MΩ resistor becomes preferable for frequencies greater than 10 Hz. Because the voltage waveform varies, the average power is not directly given, as for piezoelectric harvesters, by $V^2/2R$[423]. Instead, the average power values in figure 5.8(b) were computed by

integration of the instantaneous power over the cycle. The average power shows a similar trend to the peak power data.

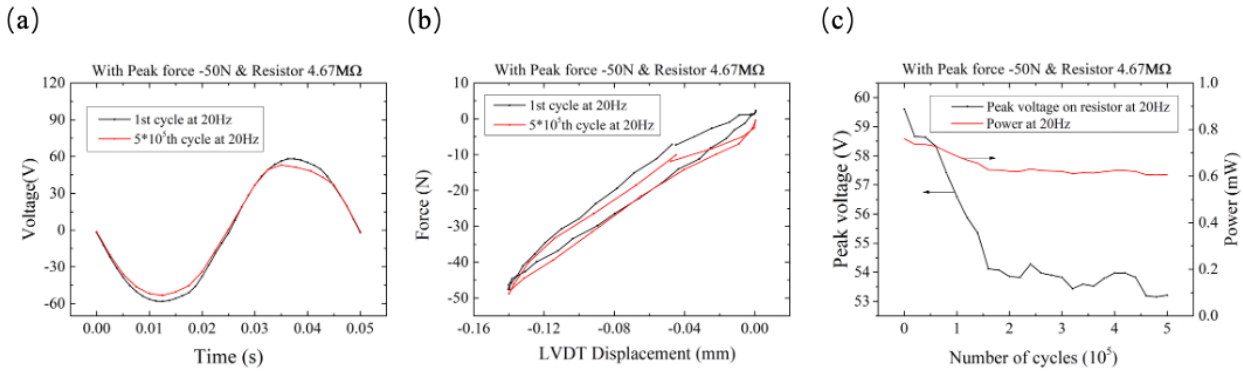


Figure 5.9 Fatigue testing of the 30% pre-poled energy harvester at 20Hz with a 4.67 MΩ load resistor.(a) Comparison of voltage for 1st and 5×10^5 th cycle (b) Corresponding comparison of the mechanical load cycles. (c) The degradation of peak voltage and power output with cycle number.

For practical applications the energy harvester should be able to operate cyclically without degradation. Fatigue tests were run in various operating conditions, up to 0.5×10^6 cycles; results for a 30% pre-poled sample loaded to 50 N at 20 Hz are shown in figure 5.9. Following a bedding-in period, the output voltage and force-displacement cycle remained reasonably stable over the course of these tests, as seen in figure 5.9(a),(b). The output voltage amplitude was found to drop by approximately 10% in the first 10^5 cycles, with a corresponding 20% drop in peak power, see figure 5.9(c). Beyond 2×10^5 cycles the power output appears stable. No cracks were observed in the active layer, demonstrating the stability and robustness of this ferroelectric energy harvester. The fatigue test indicates that the mechanical loads do not induce material degradation. Another important factor is the stability of the partially poled state. It is well-known that the poled state of electroceramic may decay over long time periods,

for example 10-15 years. But there is currently little evidence to show the stability of polarization in partially poled electroceramics. This may affect the energy output of the energy harvester over time and is a subject of future investigation. Additionally, the quality of bond between the substrate and active material, which induces the residual stress in the poling process, should be considered. The stressed state may relax over time or after a larger number of loading cycles. In the present work we have observed only a small changes in performance with cycling, but further work is needed to confirm the stability of the substrate-ferroelectric bond.

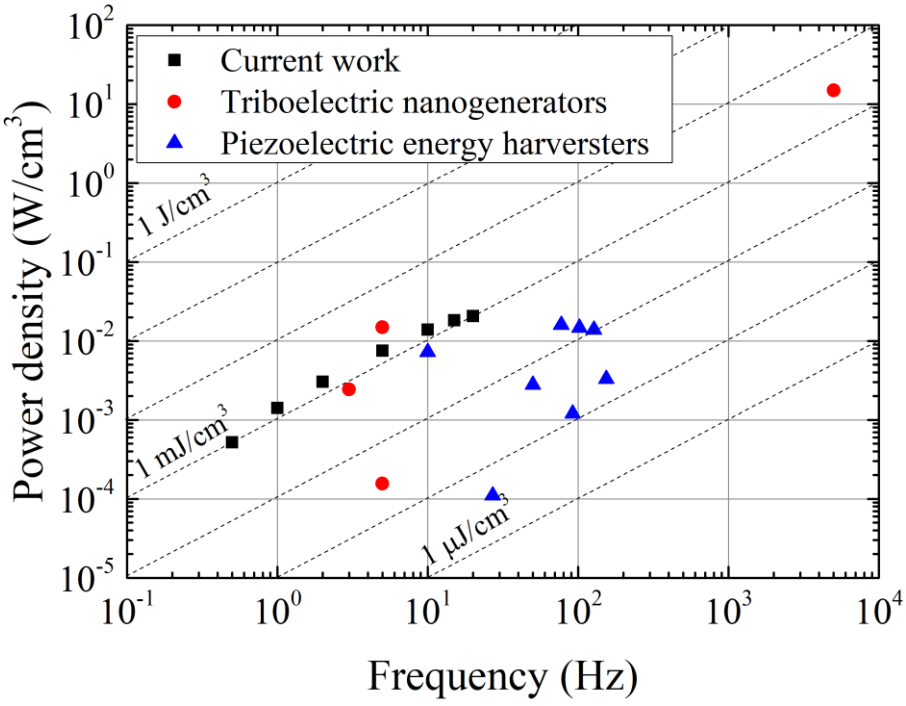


Figure 5.10 Frequency-power characteristic for various energy harvesters.[65-76] Lines of constant cycle work density are shown.

The frequency – power performances of various high-power vibration energy harvesters are shown in figure 5.10. The ultimate objective of the present work is to

improve upon the energy and power density of existing piezoelectric energy harvesting technologies. Figure 5.10 indicates that the ferroelectric/ferroelastic energy harvester in the present work compares favourably with a range of piezoelectric devices,[273, 284, 289, 323, 336, 424-426] offering greater cycle energy density and greater power. The power densities are presented with various mechanical amplitudes and frequencies, but they are all constants for each system. No random vibrational conditions are compared. The device remains effective at low frequencies, typical of structural and mechanical vibrations, as well as human motion. The device has comparable cycle energy density to triboelectric energy harvesters.[46, 390, 391, 427] Here it should be noted that some triboelectric devices are characterised by sliding velocity rather than operating frequency and the comparison with oscillating devices has been made by assuming an amplitude and calculating the frequency that provides the required peak velocity at that amplitude. The amplitude used for comparison purposes was the amplitude of displacement applied to the loading pins in our experiment. Although the force/pressure is also of great importance for energy harvesting, the differences of loading and operation systems of all types of energy harvesters inhibit a comparison of energy output per unit force. By contrast, the peak loads used in present work are constant. As for triboelectric energy harvesters, the cycle energy densities vary widely and can exceed that offered by the ferroelectric energy harvester in its current implementation. Specifically, the ferroelectric energy harvester presented here achieved a maximum cycle energy density in the region of 2 mJ cm^{-3}. Power output

varies with frequency and was about 20 mW cm^{-3} at 20 Hz, the maximum frequency tested here.

In this chapter, the ferroelectric energy harvester has not been optimized for a particular application so that the strategy can be universally applied to a range of energy harvesting applications, such as wireless sensors, medical devices and mobile electronics through specific designs. Energy output could potentially be enhanced by tailoring such designs to the requirements of the application. . For future studies, there are various options for improving performance, including choice of material and geometry for the active element and substrate, control of the pre-poling procedure that initializes the energy harvester, and choice of external mechanical or electrical loads. In practical vibrational applications, the selection of a suitable inertial mass, and limitation of the duty cycle to prevent overload will be critical. The nature of the energy harvesting cycle is also such that a stable amplitude of mechanical loading is advantageous, which may be a limiting factor in applications with variable or unpredictable vibrations. The focus of the present chapter was instead the demonstration of a working ferroelectric energy harvesting cycle with high energy density and robustness against cyclic fatigue.

5.4 Summary

A novel energy harvesting method using ferroelectric/ferroelastic switching has been proposed and tested. The method works by partially depolarizing a poled ferroelectric using a single application of tensile stress, and then using cycles of compression to vary the polarization state. A crucial feature is the control of residual stress by poling the active material in stages, first in a mechanically unconstrained state, then adhering it to a substrate before completing the poling process. The resulting energy harvesting cycles were shown to achieve much greater energy density than typical piezoelectric devices, and comparable performance with some triboelectric generators. Even greater energy density was achieved by using tensile stress states: although this mode of loading compromised robustness, it may still be useful for applications with low cycle numbers. In compression, the cycles were shown to be reasonably stable and the device remained robust up to 0.5×10^6 cycles. Further robustness verification should be tested with greater cycle numbers in the future. Given the simplicity and ease of construction of the proposed device it is likely to be suitable for a range of applications. It is likely that significant further improvements could be made through a more extensive design study. The investigations in this chapter provide a preliminary demonstration of the working principle for an energy harvester using ferroelectric/ferroelastic switching and show the concept is promising for high power and high energy density vibrational energy harvesting at low frequencies.

Chapter 6

6. Investigation of mechanical energy harvesting cycles using ferroelectric /ferroelastic switching

In this work, novel, practical and stable energy harvesting cycles using ferroelectric/ferroelastic switching are established, and explored under quasi-static experimental conditions. A prototype device with a simple 'sandwich' configuration is tested. This chapter will focus on the cycle exploration of energy harvesting by using partial ferroelectric/ferroelastic switching. A quasi-static experiment using a Deben loading stage is adopted to test the performance of energy harvesting cycles with the variation of pre-poled states for PLZT ceramic, which is bonded onto a steel substrate. Here, four kinds of specimens with 100%, 75%, 50% and 30% pre-poled are tested, showing that lower values of polarization in the pre-poled state generate higher residual fields, and this effectively increases the polarization change induced by ferroelectric/ferroelastic switching. Cycles using either tensile stress or compressive stress are discussed here, and the amplitudes of mechanical loads are also varied. The results show that the cycle energy density can reach 11 mJ/cm^3 under tensile loading and 3.2 mJ/cm^3 under compression, demonstrating potential for practical applications. Although the tensile stress can promote the degradation of the ferroelectric material, it

can also generate more energy output, which can be used for some applications with limited numbers of cycles. The work in this chapter has been published in [407].

6.1 Introduction

The chapter focuses on establishing and optimising a quasi-static ferroelectric/ferroelastic cycle that converts mechanical to electrical energy. The state of the ferroelectric is prepared by an initial step of partial poling to produce a pre-poled condition. States with 30% - 100% of the full remanent polarization are produced in a soft, PLZT wafer. The pre-poled wafer is then adhered to a substrate before completing the poling process; this produces a state of residual stress that enhances ferroelastic switching at low levels of externally applied stress. Electromechanical energy harvesting cycles driven by stress are then presented. Two distinct kinds of energy harvesting cycles are identified. In the first, bending of the substrate is used to induce tension in the ferroelectric wafer, causing partial depolarization; relaxation of the mechanical load enables switching back to a near fully polarized state. In the second type of cycle, which has been briefly studied in Chapter 5, bending loads are used to produce compression in the wafer, increasing the polarization from a partially polarized starting state. Then, upon relaxing the mechanical loads, the wafer returns to the partially polarized state. An opposing electric field is used during energy harvesting to simulate an electrical load, and the effect of this on device performance is explored.

6.1 Introduction

The quasi-static tests reveal a functioning energy harvesting cycle with great potential for the development of high energy density devices.

6.2 Concept and design

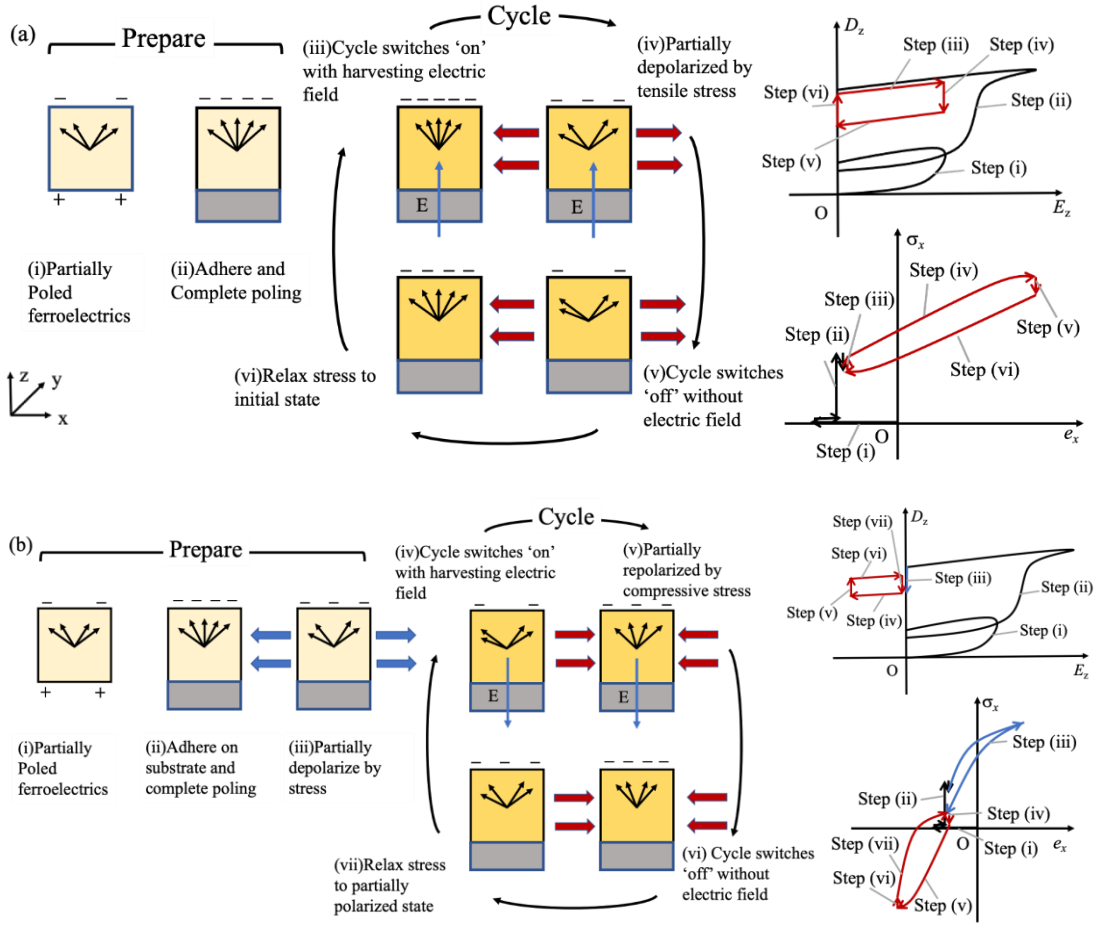


Figure 6.1 Preparation and ferroelectric energy harvesting cycles (a) Using cyclic tensile loading with a substrate (b) Using cyclic compressive loading with a substrate. Black arrows indicate the polarization distribution. Red arrows indicate mechanical loading.

Two kinds of ferroelectric energy harvesting cycles based on the concept of internal bias fields are presented in figure 6.1. These use cyclic uniform tensile or compressive loads applied along the *x*-axis to control the *z*-axis polarization. The cycle shown in figure 6.1(a) uses tensile stress. The ferroelectric element is first partially poled along *z*-axis, then adhered to a stiff substrate before the poling is completed.

When a cyclic tensile load is applied along the *x*-axis, there is a resulting cyclic polarization change along the *z*-axis. Since the ferroelectric element is mechanically coupled to the substrate, strain along the *x*-axis induced by increasing polarization is resisted by the substrate, resulting in tensile residual stress in the ferroelectric. Cracking of the ferroelectric element can be avoided by controlling the degree of partial poling at step (i). An alternative way to exploit internal fields can be seen in figure 6.1(b), which uses a compressive load cycle. This is the method used in Chapter 5. In the preparation stage, the ferroelectric ceramic is first partially poled before it is bonded on the substrate, it is then fully polarized, which produces a state of tensile residual stress along the *x*-axis. In a final preparation step, a single tensile loading cycle is used to partially depolarize the ceramic. This depolarization reduces the residual tensile stress. Afterwards, a compressive cyclic load can be applied to the ferroelectric ceramic layer to drive the cyclic change in polarization. The compressive external load has the effect of reducing the residual tensile stress in the ferroelectric element and putting the material into compression along the *x*-axis, which will result in an increase in polarization. Relaxing the compressive stress in the ferroelectric element restores the partially depolarized state. Displacement of charge is associated with the change in polarization, providing the ability to do work against an electrical load (e.g. providing power to a load, such as charging a battery). The corresponding change of electric displacement versus electric field, and stress versus strain are sketched in figure 6.1, where red arrows indicate the cyclic hysteresis loop with positive mechanical work

input and electrical work output. The method of figure 6.1(b), using compressive stress, may be preferable in reducing fatigue damage to the ferroelectric element.

In this work, a wafer (~ 300 μm thick) of bulk ferroelectric ceramic is used, with a 1mm thick substrate. Uniformity of the load conditions along the *x*-axis is achieved by applying four-point bending on the substrate, producing uniform bending moment. A variation of stress distribution along the thickness is induced by the finite thickness of active materials.

Leakage current tests were carried out to check for leakage across the ferroelectric element. Leakage was found to increase with the electric field, and was dependent on the quality of the applied electrodes; the leakage values were small enough to have negligible effect on the measurement of electric displacement changes.

The leakage current of each of 100%, 75%, 50% and 30% pre-poled specimens were tested before the working cycle verifications, see figure 6.2. It is observed that the leakage current increases with the increase of electric field for all the specimens. This is due to an unintentional electrical connection that occurs between the ground and voltage generated by amplifier. An effective way to reduce the leakage current is to improve the quality of the thin silver top electrode in the experiments, but it is difficult to eliminate the effect of the leakage currents altogether. In the tests of this chapter, all the energy harvesting results with harvesting voltage, reported in section 5.4, have been corrected for leakage by adjusting the measured changes in electric displacement according to the leakage rate and time spent at each voltage.

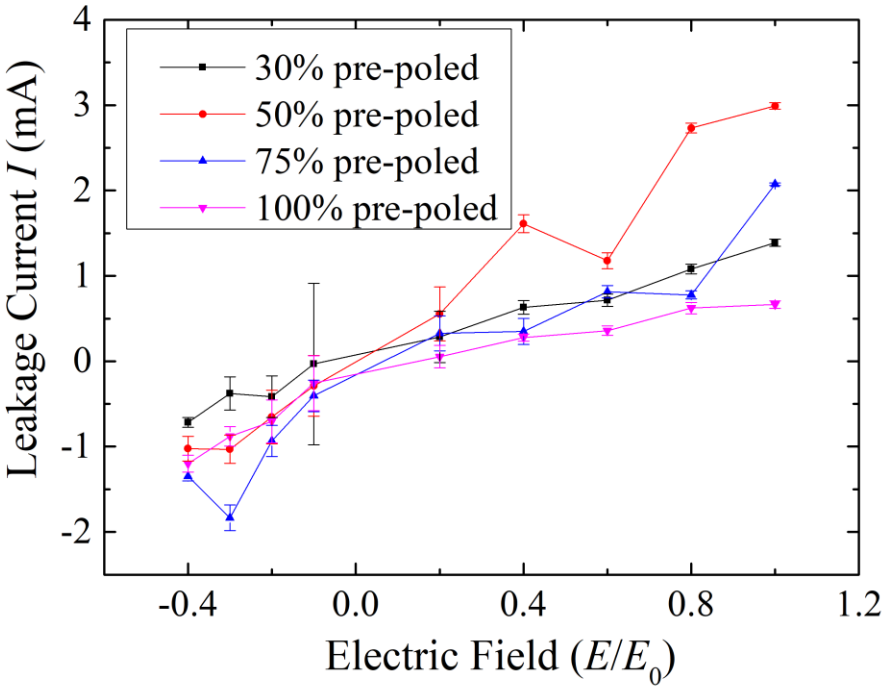


Figure 6.2 Leakage current for four kinds of pre-poled specimens.

6.3 Results and discussion

6.3.1 Preliminary tests at zero electrical load

Initial tests were conducted without electrical load ($\lambda = 0$) to investigate the behavior of fully or partially pre-poled specimens under quasi-static mechanical loading. The electric displacement versus mechanical load curves are shown in figure 6.3 (tension) and figure 6.4 (compression). The corresponding mechanical force versus loading pin displacement is also presented. Note that the 100% pre-poled specimens do not have residual tensile stress, having been fully poled off the substrate, while the 75%, 50% and 30% pre-poled specimens are expected to have increasing values of residual tensile stress, as poling was completed on the substrate in these cases. The peak absolute value F was varied in the range from 10 N to 50 N. From figure 6.3 and figure 6.4, it can be seen that greater electric displacement changes occur in the samples with less pre-poling.

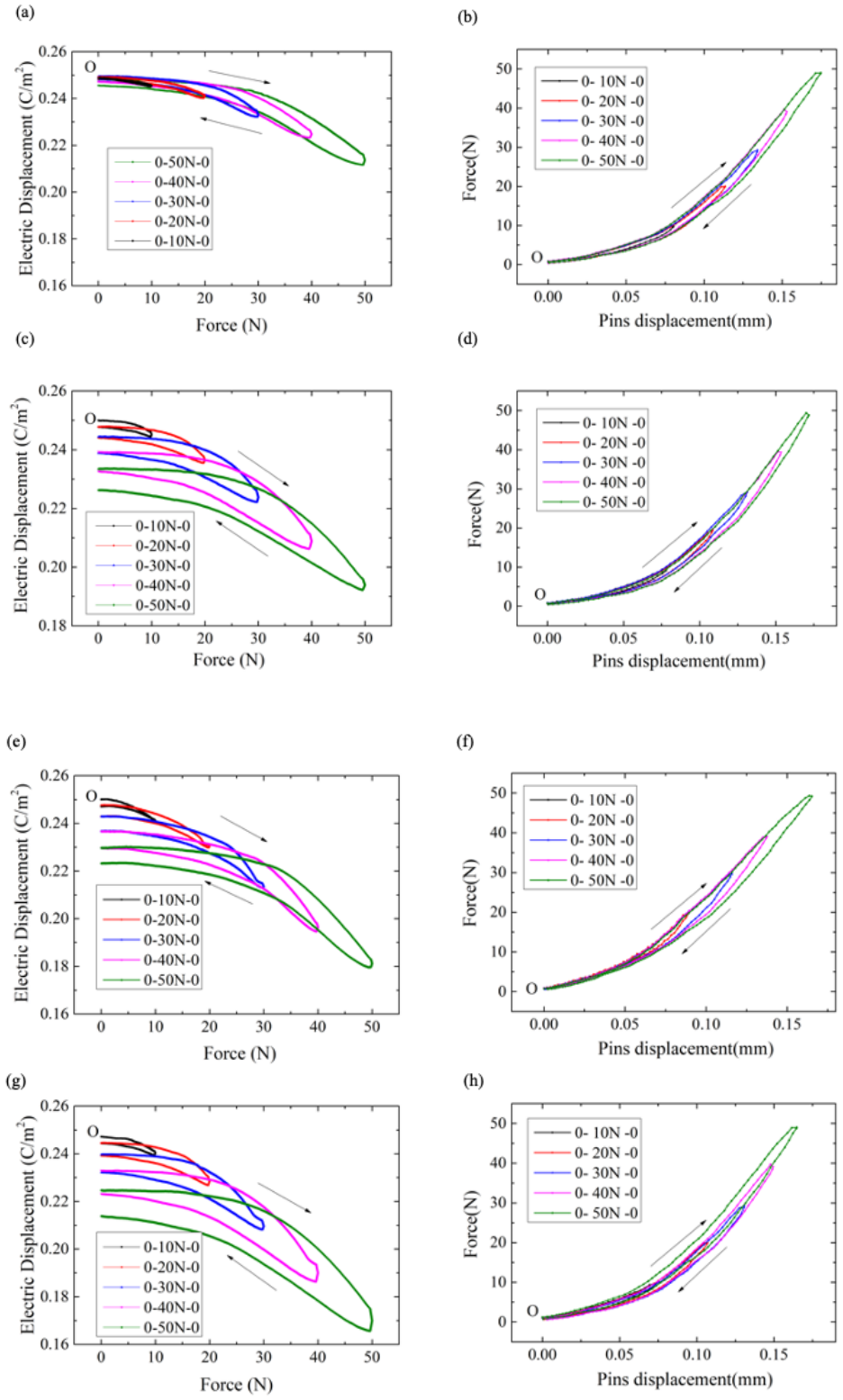


Figure 6.3 The behavior of specimens under tensile stress. (a,c,e,g) Electric displacement versus force on pins; (b,d,f,h) Force versus pin displacement. Pre-poling states as follows: (a,b) 100%, (c,d) 75% (e,f) 50% (g,h) 30%.

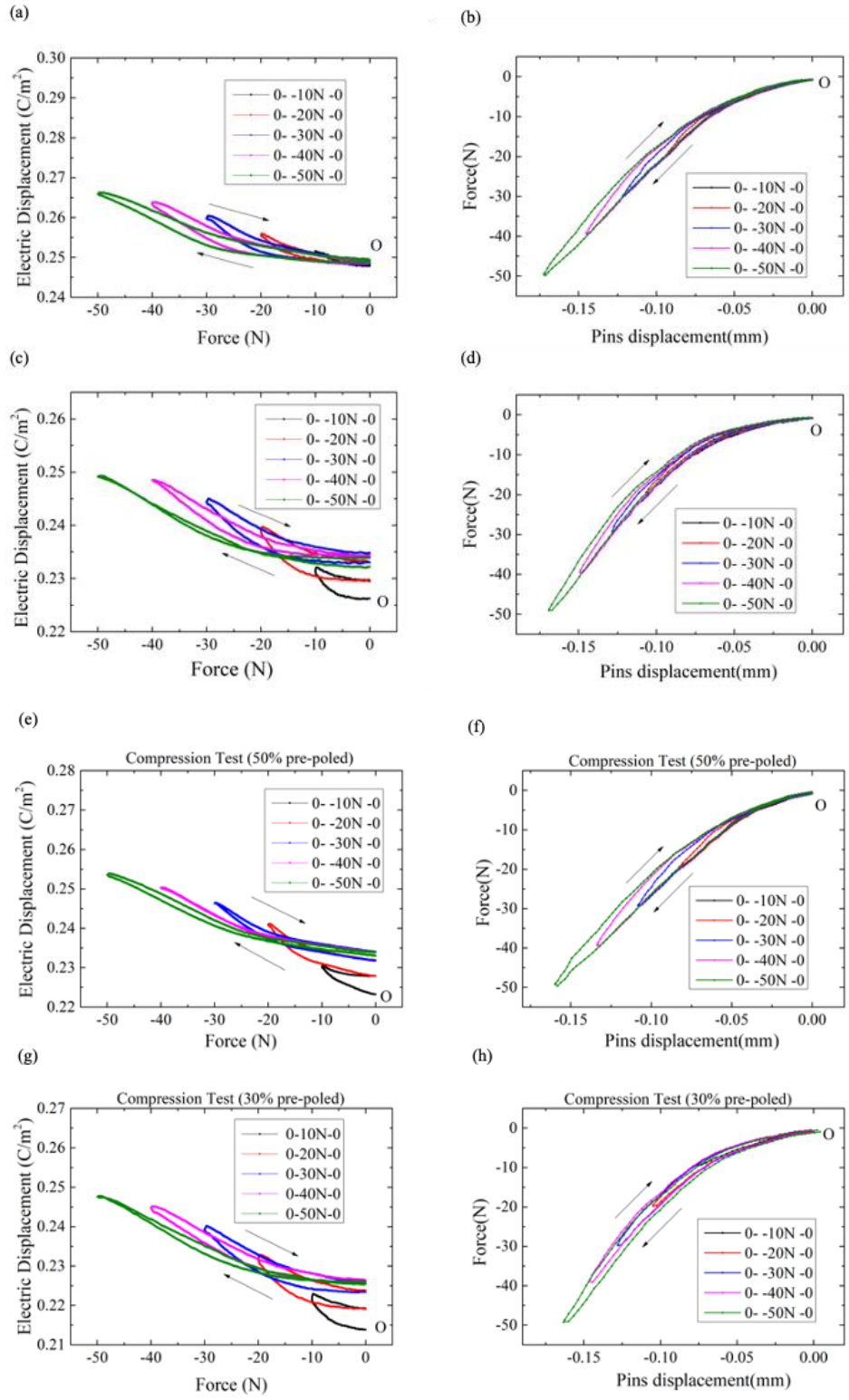


Figure 6.4 The behavior of specimens under compressive stress. (a,c,e,g) Electric displacement versus force on pins; (b,d,f,h) Force versus pin displacement. Pre-poling states as follows: (a,b) 100%, (c,d) 75% (e,f) 50% (g,h) 30%.

6.3 Results and discussion

Figure 6.3(a,b) show the behavior of 100% pre-poled specimens under tensile stress at zero electrical load. Mechanical loading partially depolarizes the PLZT layer while unloading allows the polarization to switch back, as seen in figure 6.3(a). Non-linearity of the response becomes pronounced once the force magnitude reaches 30N, suggesting the stretching of PLZT layer triggers ferroelastic switching. Upon unloading, the partially depolarized wafer is compressed by interaction with the substrate causing the polarization to switch back towards the initial state. Some electric displacement change due to the piezoelectric effect is also observed but there is additional ferroelastic/ferroelectric switching due to the applied stress.

In the 30%-75% partially pre-poled specimens, residual tensile stress can assist switching and hence enhance polarization changes in the PLZT wafer. When the 75% pre-poled samples were tested in tension, this resulted in increased changes in electric displacement, see figure 6.3(c). However, upon unloading the force, the fully polarized material state is not restored: some of the material has not switched back. A bias electric field would be needed to restore the initial polarization value. In figure 6.3(c), pin loads as low as 10 N induce non-linearity and switching, due to the assistance of residual tensile stress. The results for 50% pre-poled and 30% pre-poled wafers are given in figure 6.3 (e-h). These show similar features to the results for the 75% pre-poled sample, with the residual tensile stress assisting depolarization. There are visible jumps in displacement and electric displacement at peak force in figure 6.3, especially at high load amplitudes; this can be attributed to the effect of friction between the ceramic

loading pins and the steel substrate causing hysteresis where the direction of motion reverses. From all the results in figure 6.3 it is evident that working cycles with cyclic mechanical load producing non-linear changes in electric displacement can be achieved using tensile stress.

Next, compare the results of figure 6.3 with similar tests in which the loading of the PLZT is compressive, presented in figure 6.4. By contrast with the tensile loading results, the compression tests of figure 6.4(a) have relatively small polarization changes; this may be expected because the material is already in a near saturated state of polarization and transverse compression cannot drive the polarization much further. However, in the 75%-30% pre-poled states, figure 6.4(c-h), significant polarization changes are seen, and closed cycles of force versus electric displacement can be achieved in some cases. Initial loading at small amplitudes (10-20 N) ratchets up the electric displacement a little, but subsequent loading to 30-50 N produces closed cycles. The results assist the selection of a working cycle to optimize the closed-circuit electric displacement change, enabling a compromise to be struck between stability or closure of the cycle and the magnitude of the polarization change achieved in each cycle. Good cycle stability with significant polarization switching can be achieved in the case of 30% pre-poling with 50 N cyclic load.

6.3.2 Energy harvesting using tensile stress

We now consider cyclic tensile loading of the energy harvester, while imposing an electric field that simulates an external electrical load. For brevity, results for a 30% pre-poled sample are shown in this chapter, and the detailed information can be found in Appendix. The electrical load is switched 'on' during the energy harvesting part of the cycle and then switched 'off' while the mechanical load is relaxed to restore the initial state. Measurement of the working cycles was carried out for tensile loading cases with a harvesting electric field λE_0, where E_0 is the coercive field of PLZT. An example of an energy harvesting cycle is shown in figure 6.5, in which the electrical loading was set to $\lambda = 1.0$ and the amplitude of the applied force was varied in the range 10 N to 50 N.

Each cycle starts at the point marked 'O'. The relationship between electric displacement and the force applied on pins is shown for the tensile loading case in figure 6.5(a). The cycle proceeds clockwise from point 'O'; vertical segments of the force-electric displacement response indicate rapid changes of electric displacement due to switching the electric field 'on' or 'off'. The curved segments correspond to the application or removal of the mechanical loading. The same cycles are plotted as voltage versus charge on the electrode in figure 6.5(b); here straight horizontal segments indicate mechanical loading or unloading at constant voltage, while the

curved portions of the cycle show change in electric displacement induced by switching the electric field ‘on’ or ‘off’.

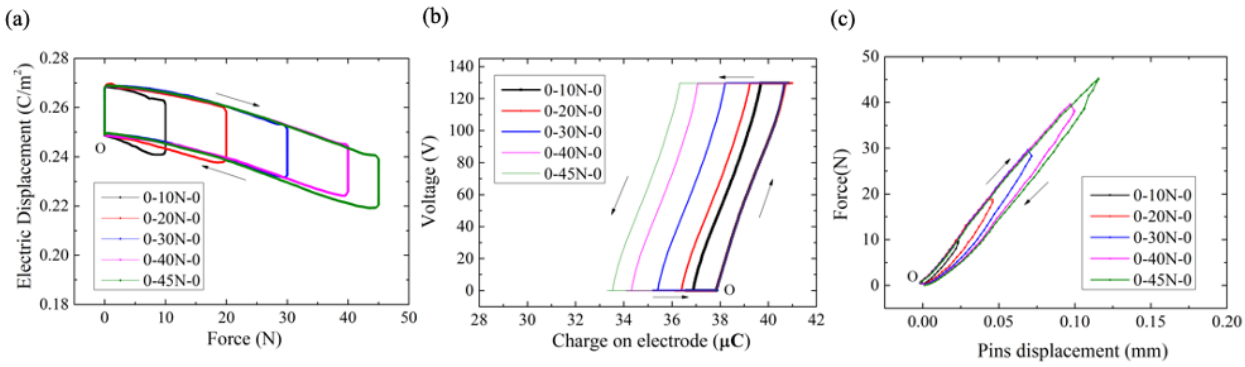


Figure 6.5 An example of energy harvesting cycle using tensile stress with harvesting electric field of magnitude $1.0E_0$ for 30% pre-poled material. (a) Electric displacement versus force. (b) Voltage versus charge on electrode. (c) Force versus pins displacement.

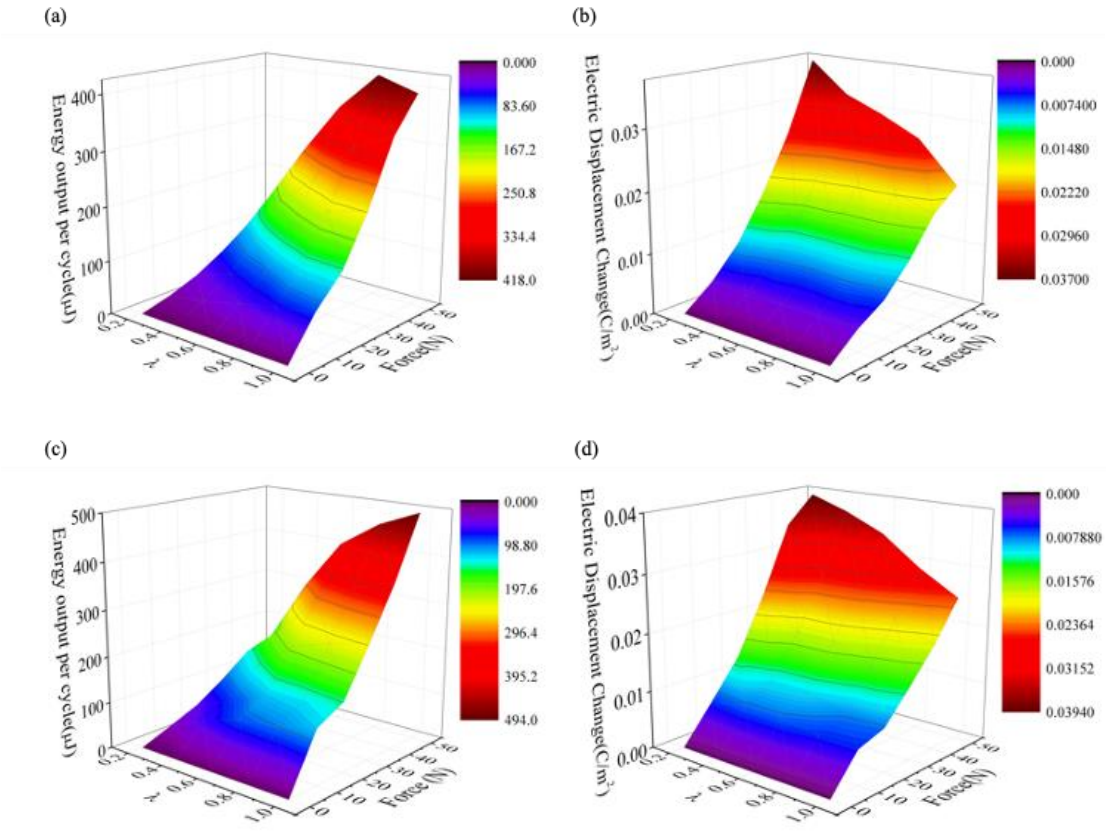
In figure 6.5(a), the magnitude of the electric displacement change is greater than 0.03 C/m^2. This magnitude is significantly less than that in the closed-circuit case at zero electrical load of figure 6.3: the electrical load resists ferroelectric/ferroelastic switching somewhat. However, the electric displacement changes are still much greater than those typically achieved in piezoelectric energy harvesters. The enclosed area in each loop of figure 6.5(b) represents the electrical energy output per cycle. The corresponding mechanical energy input can be estimated using the enclosed area of the force versus displacement curves in figure 6.5(c).

The key parameters controlling the energy output of the cycle are the force amplitude and the electrical load. Several factors affect the choice of these parameters. Increasing the force amplitude drives increased switching to produce more energy

output. However, high force may damage the ferroelectric wafer, especially in the tensile mode of operation. During operation, cracks were observed to form in the ferroelectric wafer in the 30% and 50% pre-poled specimens when $F > 40$ N and $\lambda > 0.8$ in some cases. Lines of dark contrast were seen through the back-lit translucent material when cracks formed. Furthermore, setting the force amplitude too high can result in an unstable cycle that rapidly degrades, reducing the energy output. Another key parameter is the harvesting electric field, simulating an electrical load. In practical applications the field amplitude will be determined by the nature of the external circuit; this can be controlled to a degree by choosing the load components that condition the electrical output of the harvester for downstream use. Increasing λ can result in increased electric work, but can also reduce the extent of mechanically induced switching: an optimum should be found if work output is to be maximized. Additionally, when λ exceeds unity, the field strength becomes great enough to cause extensive ferroelectric switching that can overwrite the engineered material state of the energy harvester.

To investigate further, the energy output per cycle, and electric displacement change under tensile stress, are shown versus the mechanical loading F and electrical load factor λ in figure 6.6. These results are for 30%-100% pre-poled specimens and summarize a series of tests in which λ and F were varied in the ranges $0.2 \leq \lambda \leq 1$ and $10 \leq F \leq 50$ N. The energy output typically increases with force amplitude and the applied field strength, as may be expected, but there are some exceptions where

increasing the field strength too far blocks switching and results in reduced energy output. The energy output per cycle reaches a maximum of 295 μJ for the 100% pre-poled specimen with $\lambda = 1.0$ and F = 50 N. Comparing this with the 30% pre-poled specimen in figure 6.6(g) indicates that the energy output can increase to over 405 μJ by exploiting the partially poled state. Although increasing the harvesting electric field generally increases energy output, figure 6.6(b) shows that it can reduce the electric displacement change.



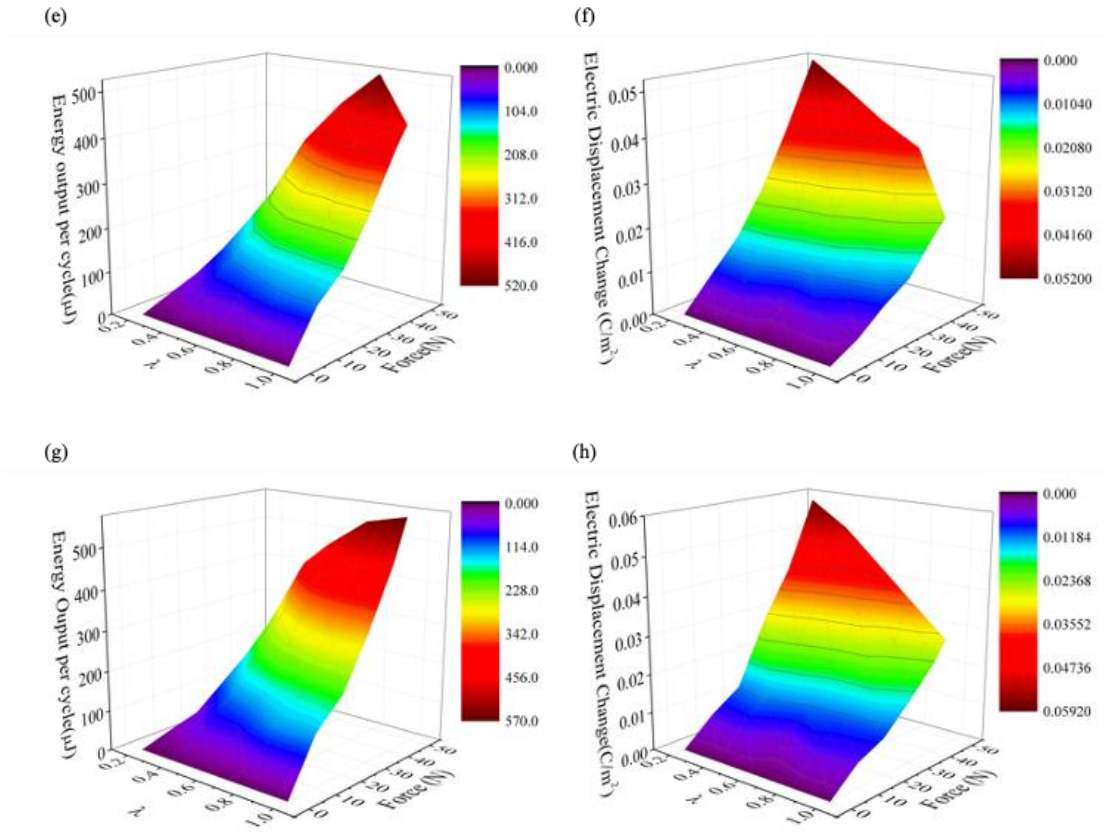


Figure 6.6 Energy output and electric displacement performance of the energy harvesters in tensile loading with various operating conditions: (a,c,e,g) Energy output per cycle versus peak force and harvesting electric field magnitude, (b,d,f,h) Corresponding magnitude of electric displacement change in each cycle. Pre-poling states as follows: (a,b) 100%, (c,d) 75% (e,f) 50% (g,h) 30%.

The peak electric displacement change reduces from 0.037 C/m^2 with $\lambda = 0.2$ to 0.019 C/m^2 when $\lambda = 1.0$. Steady increases in the maximum energy output per cycle and electric displacement change at the peak mechanical force are seen as the degree of pre-poling is reduced. However, to avoid cracking, the peak mechanical load was reduced to 45 N when $\lambda > 0.6$ for 50% pre-poled specimen and when $\lambda > 0.4$ for 30% pre-poled specimen. Based on this investigation the 30% pre-poled samples gave the greatest energy output per cycle, at 405 μJ and avoided cracking of the ferroelectric

element during the final poling process. Samples pre-poled by less than 30% of the full remanent polarization typically cracked when fully poled on the substrate, indicating that in these cases the residual stresses developed in the final poling process could exceed the tensile strength of the ceramic.

6.3.3 Energy harvesting using compressive stress

The energy harvesting performance under cyclic mechanical compressive loading, with the applied electric field reversed ($\lambda < 0$), is studied in this section. The working cycle is similar to the cycles under tensile stress: the electric field is switched 'on' during the energy harvesting part and switched 'off' when the force is relaxed to restore the initial material state. The peak applied force was varied in the range -10 N to -50 N.

Figure 6.7(a-c) shows typical working cycles, these being obtained using compressive loading with λ = -0.3 for the 30% pre-poled specimen. Starting at the point marked 'O' the cycle proceeds clockwise in figure 6.7(a). The magnitude of the electric displacement change in this working mode with a peak force of -50 N is about 0.025 C/m^2. This is less than that of the tensile cycle, but still a significant improvement relative to typical piezoelectric energy harvesters. Comparing with the cases at zero electric load in figure 6.4, the resistance to switching caused by the electrical load is evident. An open shape of hysteresis curve in figure 6.7(c) indicates a greater

mechanical energy input in this case, and the enclosed area of charge versus voltage in figure 6.7(b) representing electrical energy output per cycle, increases accordingly.

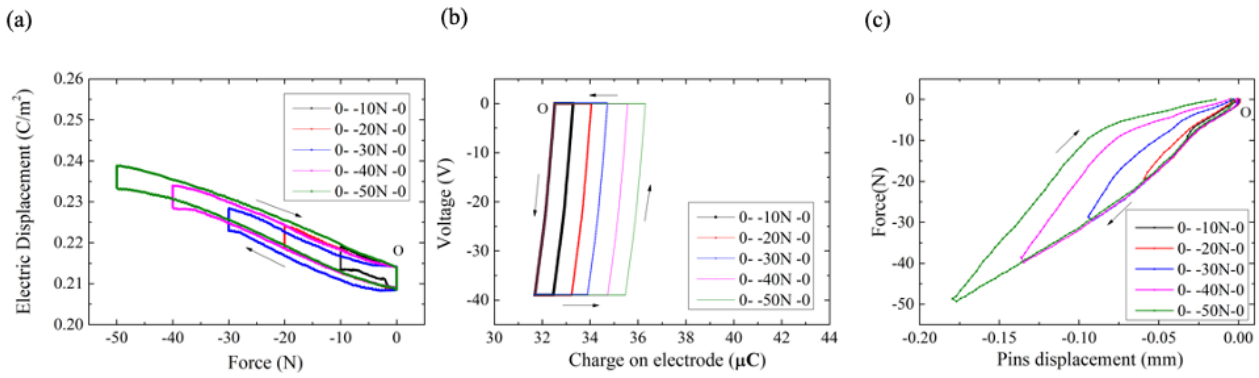
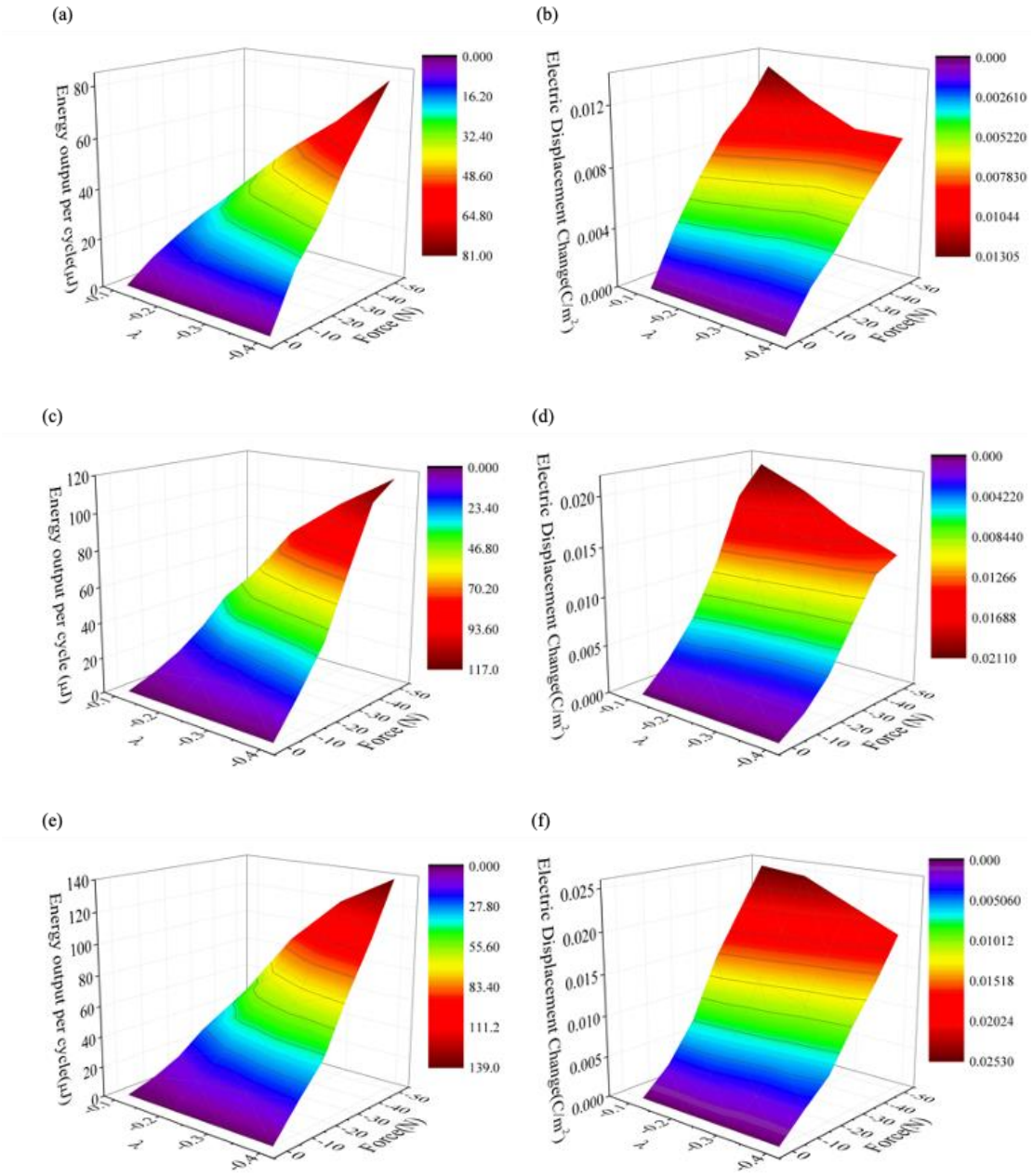


Figure 6.7 An example of energy harvesting cycle using compressive load stress with harvesting field -0.3E_0 for 30% pre-poled samples. (a) Electric displacement versus force. (b) Voltage versus charge on the electrode. (c) Force versus pins displacement.

The selection of force and electric field amplitude for maximum energy output in compression is next considered. The energy output per cycle and corresponding electric displacement change are shown versus force and electric field amplitude in figure 6.8. In figure 6.8(a), it is found that the energy output for the 100% pre-poled specimen increases monotonically with the rise of applied field strength, and the energy output per cycle reaches a maximum of 57 μJ in the range tested. As expected, high values of the harvesting electric field reduce the electric displacement change, see figure 6.8(b), despite the energy output continuing to increase with electric field. In the fully polarized state very limited switching is possible; the observed electric displacement changes combine polarization switching and the piezoelectric effect. Greater electric displacement change and energy output can be observed in figure 6.8(c-h) with a

maximum energy output per cycle of 115 μJ in the 30% pre-poled samples. As the degree of pre-poling is reduced, the maximum energy output per cycle rises due to the increased freedom for polarization switching. A significant advantage of the compressive working mode is that the risk of cracking in the electroceramic during the energy harvesting cycle is greatly reduced: no cracking was observed in the range of parameters tested.



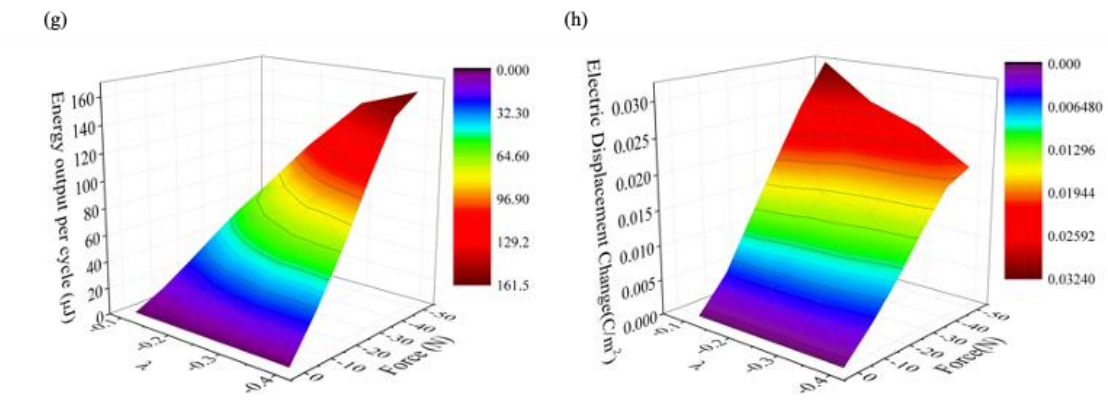


Figure 6.8 Energy output and electric displacement performance of the energy harvesters in compressive loading with various operating conditions: (a,c,e,g) Energy output per cycle versus peak force and harvesting electric field magnitude, (b,d,f,h) Corresponding magnitude of electric displacement change in each cycle. Pre-poling states as follows: (a,b) 100%, (c,d) 75% (e,f) 50% (g,h) 30%.

The energy output per cycle is an important performance metric for energy harvesting. However, when comparing different systems, volume scaling should be factored in. The ferroelectric/ferroelastic energy harvesters presented here achieved energy densities of 11 mJ/cm^3 and 3.2 mJ/cm^3 in tension and compression respectively. The system was operated in quasi-static conditions (<0.02 Hz); however, stable operation at frequencies up to 20 Hz has been tested and appears viable. Other high-power piezoelectric [276, 277, 289, 291, 303, 312, 348, 428] and triboelectric [429-438] energy harvesters exhibit a wide range of cycle energy densities, from 0.005 mJ/cm^3 up to about 10 mJ/cm^3. Thus the proposed system operates towards the top end of this range.

Table 6.1 Approximate efficiency of energy harvesting cycles at various amplitudes of mechanical and electrical loading.

Loading type	Load amplitude	Electric field amplitude / E_0	Measured efficiency
Tensile	10N	0.2	18-52%
Tensile	50N	0.2	10-25%
Tensile	10N	0.8	70-98%
Tensile	50N	0.8	30-67%
Compressive	10N	0.1	5-10%
Compressive	50N	0.1	2-3%
Compressive	10N	0.4	21-37%
Compressive	50N	0.4	4-6%

Another key factor for evaluating the working cycles is the energy conversion efficiency, which may vary from a few percent to more than 90%. To estimate the overall conversion efficiency, the input mechanical energy was computed from the enclosed area of the force versus loading pin displacement loops. Since the input energy calculated in this way includes frictional losses at the loading pins, as well as material and electrical losses in the energy harvester itself, the estimate gives an approximate measure, but can illustrate the typical efficiencies achieved. The resulting efficiencies are given for a range of operating parameters in Table 6.1. Since the same operating parameters were used with several different states of pre-poling, the table shows the range of efficiencies achieved in each operating state. In general it can be seen that an increase of amplitude of mechanical loading results in increased ferroelectric/ferroelastic switching, and thereby induces a drop in efficiency. In the few cases with 90% or more efficiency, the piezoelectric effect is dominant; these correspond to cases wherein the small amplitude of mechanical loading does not depolarise the electroceramic, when inhibited by the applied electric field.

Furthermore, the mechanical work input needed for the compression mode is greater than that for the tension mode. Thus the efficiencies acquired in the compression working mode are typically lower than those of the tension mode. Further investigation of the conversion efficiency is a topic for future research.

6.4 Summary

In the chapter, the behaviour of ferroelectric wafers in partially poled states with residual stress was tested with a view to developing ferroelectric/ferroelastic energy harvesting cycles. The testing was quasi-static, and electric field was applied to simulate the impedance provided by an external electrical load. The experiments verify that the biased states of residual stress produced by the partial pre-poling process enable ferroelectric/ferroelastic switching to occur during the working cycle, and can guide the repolarization process under mechanical loading without the use of an external bias electric field to complete the energy harvesting cycle. The resulting devices have a simple structure and show much greater energy output per unit volume of active material than typical piezoelectrics. By varying the polarization state of the ferroelectric wafer, and the electrical and mechanical load amplitudes, a range of behaviour was explored. In general, reducing the extent of off-substrate pre-poling increased the energy output. However, this is also expected to increase the residual stresses and led to cracking in some cases. A 30% pre-poled sample gave a good balance of high energy output whilst avoiding degradation by cracking. While tensile loading gave the greatest energy output per cycle, compressive load cycles also yielded high energy density, with the advantage of greater robustness. The results demonstrate the basic working principle of a novel and practical ferroelectric/ferroelastic working cycle for mechanical to electrical energy conversion.

Chapter 7

7. Exploiting the method of energy harvesting using ferroelectric/ferroelastic switching at low frequency: resistive load optimization

In this chapter, a novel and robust stress-driven energy harvester using internal fields, which is designed for low-frequency applications, is tested and optimized, with the exploration of load impedance and fatigue degradation. This chapter is an extended investigation of the vibrational study in Chapter 5. The device has simple configuration and could achieve energy density performance up to 1.4 mJ/cm^3 at low frequency, which is a significant advance over piezoelectric transducers. Additionally, the results show that an appropriate choice of load impedance can optimize the energy output at a specific frequency, and the optimal working cycle can be stable after 0.55×10^6 cycles at 10 Hz. This provides a new perspective for energy harvesting based on ferroelectric/ferroelastic switching to maximize the energy conversion based on ferroelectric/ferroelastic switching and control performance. Finally, a quantitative estimation of errors in the experiments presented in Chapter 5, 6, 7 are shown and discussed.

Although Chapter 5 gives the power output of the energy harvester by varying the frequency and external load resistors, as well as the fatigue performance with 4.67 MΩ

at 20Hz, it did not optimize the energy output at a specific frequency with a constant mechanical load amplitude and test the robustness of the optimal energy harvesting cycle. The resistor value was selected based on the best performance of the 30% pre-poled specimen in the quasi-static tests, which was calculated by $R = V/(\Delta Q/\Delta t)$, where V, ΔQ and Δt are the harvesting voltage, charge change during mechanical loading and time for mechanical loading respectively. Without changing the size of the device, this chapter hence presents some new aspects of the device: (1) the energy output could reach an optimal value at a specific frequency, for example 10 Hz, with the same mechanical load amplitude; (2) the fatigue test showed stable and robust performance using the optimal energy harvesting cycle at 10Hz; (3) the non-linear phenomenon was further verified by changing the mechanical load amplitude at the specific frequencies at 15 Hz and 20 Hz instead of comparing the results of 30% pre-poled and 100% pre-poled samples; (4) the quasi-static tests were found to be more sensitive to the choice of load resistors.

7.1 Introduction

Building on the work in Chapter 5, a novel prototype device is proposed using internal fields instead of external bias field to direct the ferroelectric/ferroelastic switching, demonstrating high values of energy output and advantageous properties of avoiding fracture and fatigue degradation. By controlling the polarization state and intrinsic residual tensile stress, only cyclic compressive stress was needed to drive the

cycles, while partial ferroelectric/ferroelastic switching occurs during the cycles. The fabrication process requires partial prepoling of electroceramic before it is bonded with a stiff substrate. Afterwards, strong electric field is applied to further complete the poling, and then a tensile stress is introduced to partially depolarize the electroceramic. Based on the prototype device in Chapter 5, this chapter focuses on the cycle optimization and load impedance selection at a specific low frequency; the variation of frequency and the optimization of material states are not discussed. Both the quasi-static and vibrational tests for a 30% pre-poled specimen are explored, and the selection of resistive load is found to be of great importance to maximize the energy output. Subsequently, fatigue tests show that the cycle of maximum energy output can be stable and robust at specific low frequency. In the end, the estimation of errors show that the vibrational tests have smaller errors in electrical energy output and mechanical energy input than those in quasi-static tests, and further improvements could be done to reduce the measurement errors that occurred in the experiments.

7.2 Design and test arrangement

The working cycle is presented in Figure 7.1. In the beginning, the electroceramic is partially polarized from an unpoled state with random dipole moments at A, wherein the material is not constrained by external loads. Then the partially pre-poled electroceramic is bonded with a stiff substrate, and the poling is completed by using a strong electric field. At C, residual tensile stress occurs due to the polarization changes in poling process, but the cracking caused by intrinsic stress can be avoided by controlling the prepoling from A to B. Afterwards, tensile stress is applied at D to partially depolarize the electroceramic, resulting in a decrease of residual tensile stress after the relaxation. Then, at E the state is ready for energy harvesting cycles, wherein the internal fields can provide a preferred direction for repolarization. The cycle starts with the application of compressive load stress to repolarize the electroceramic to F, and then the relaxation of compressive load enables material to return to the partially depolarized state. The working cycle is accompanied with electrical load due to an external impedance. Cycles with a combination of mechanical and electrical loadings have demonstrated stability and robustness.

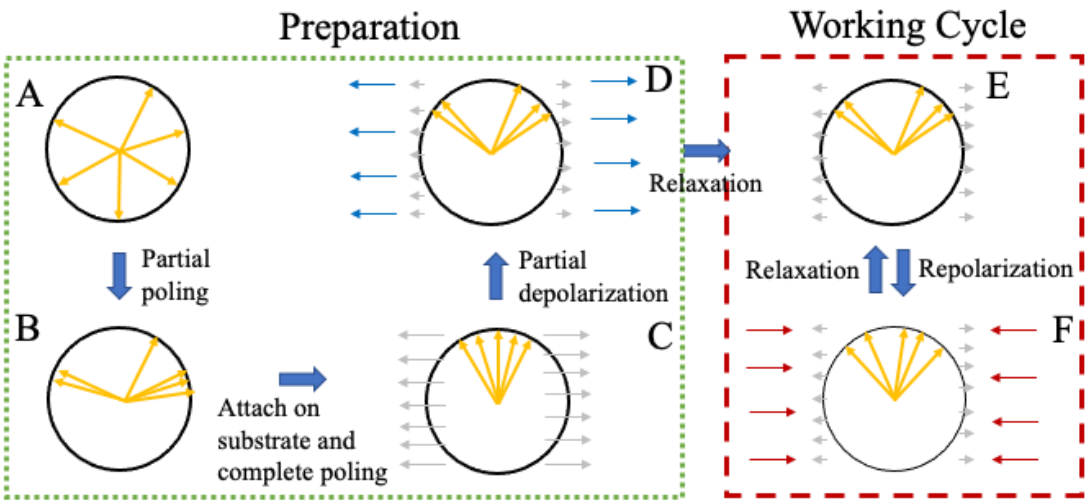


Figure 7.1 Schematic of cycle and preparation for energy harvesting using ferroelectric/ferroelastic switching. The yellow arrows inside the circles are spontaneous polarizations in the active layer, and the arrays of arrows represent stress. The grey arrow array illustrates residual stress of the active materials, and the blue and red arrows represent tensile loading stress and compressive loading stress respectively. The process from state A to F demonstrates the energy harvesting cycles and preparation. A-B: the active materials are partially polarized; B-C: attach the active materials onto a substrate and complete poling; C-D: partially depolarize the materials by using tensile loading stress; D-E: relax the active layer from the last step; E-F: cyclic compressive loading stress is applied to repolarize the materials and return to the partially depolarized state.

In this chapter, 30% pre-poled specimens were implemented in the experiments, and the preparation and test arrangements are detailed in Chapter 3. For quasi-static tests, the experiment was conducted at a frequency of 0.0167 Hz, with the load resistors varied between 0.1 MΩ to 12 MΩ. For vibrational tests, a verification study of non-linearity of between load amplitude and voltage in the energy harvesting cycles were firstly conducted at 15 Hz and 20 Hz. Then the vibrational tests were carried out at

10Hz, with a range of resistive loads from 3 kΩ-15 MΩ. A long series of 5.5×10^5 cycles of maximum power density at 10 Hz with 1.1 MΩ are run to test its stability and robustness.

7.3 Results and discussion

In practical applications, the impedance of the external circuit will result in an external voltage on the ferroelectric layer during energy harvesting. Therefore, it is worth investigating the effect of energy harvesting cycles using various resistors to optimize the performance of the 30% pre-poled device. The quasi-static loading condition and the condition at a specific frequency 10 Hz are chosen as examples for discussion. And the non-linearity between load amplitude and voltage is also explored at 15 Hz and 20 Hz.

7.3.1 Quasi-static tests

The stable energy harvesting cycle can be affected by many factors, such as amplitude of mechanical loading, frequency and external electrical load. The discussion below demonstrates the importance of the external electrical load, which can have complicated interactions with the device.

The quasi-static tests are carried out by applying a peak force F=-50 N with a range of resistor's value 0.1 MΩ -12.10 MΩ on 30% pre-poled specimens, as shown in figure 7.2. In figure 7.2(a), the electric displacement versus applied peak force curves of various resistors are compared, demonstrating non-linear behavior during energy harvesting. When the force F increases from 0 to 20 N, the applied force is proportional to the electric displacement change, which can be regarded as the linear effect. By

contrast, the applied force can induce non-linear change of polarization when $F > -20$ N. Then the relaxation of F can induce a depolarization of the material, which would switch back to the start point to form a closed cycle. The electric displacement changes are approximately the same with various resistors, however, in the case with 0.1 MΩ the cycle is not closed, despite the electric displacement change being greater. This shows that small resistive loads can impose a limited effect on ferroelectric/ferroelstic switching, and the applied force can repolarise the ferroelectric layer a little bit. Here, the electric displacement versus force curve with 0.1 MΩ resistor is similar to that with only mechanical loads in Chapter 6 and no electrical load, indicating the distinctive role of electrical load to form a closed cycle. Hence, although the resistive loads have limited effect on electric displacement change, it is critical to acquire a closed cycle by controlling the value of the impedance.

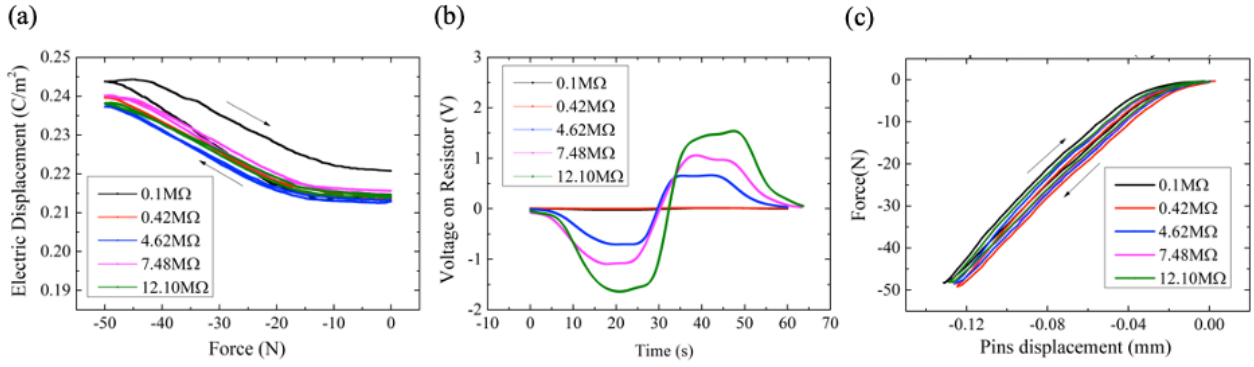


Figure 7.2 Quasi-static cycles with various resistive loads for 30% pre-poled specimen at 0.0167Hz. (a) Electric displacement versus force. (b) Voltage versus time. (c) Force versus pins displacement.

Figure 7.2(b) shows the corresponding voltage across the device during the cycles, with an increase of voltage, as expected, when the resistor value becomes larger. The

charge flow of the energy harvesting cycle with various resistors in the quasi-static tests remains constant, which means the currents driven by mechanical loading do not change, and thereby the voltage has nearly a linear relationship with resistive load. From figure 7.2(b), the voltage of the case with 0.1 MΩ is much smaller than those of the cases with larger resistors, and the small voltage with 0.1 MΩ resistor did not help form a closed cycle. It is of great interest that the shape of voltage versus time curves shown in figure 7.2(b) are not triangular, although the mechanical loading has a triangular waveform, indicating the non-linearity between the mechanical loading and electrical response. The corresponding relationship of force and pins displacement is given in figure 7.2(c), wherein the mechanical load amplitude remains constant and mechanical input can also be ascertained from the enclosed force versus pins displacement curves.

The energy output per cycle is shown as a function of resistive loads in figure 7.3, and the change of electric displacement with variation of resistors is also presented. It is observed that the energy output would be larger with an increase of resistor value from 0.1 MΩ to 12.10 MΩ, and the energy output reaches maximum to about 18×10^{-6} J with 12.10 MΩ at 0.0167 Hz per cycle. By contrast, this does not mean the greater voltage will result in higher energy output, because the greater resistor may inhibit the ferroelectric switching and smaller voltage on the resistor may be required. But if the resistance is too small, the cycle cannot be stable. The corresponding electric displacement change shows that the ferroelectric/ferroelastic switching induces a

change of at least 0.025 C/m^2, indicating significant non-linear change: compare piezoelectrics, whose electric displacement change is typically between 0 and 0.01 C/m^2. The variation of resistive loads does not remarkably affect the polarization switching induced by mechanical loading, except in the case with 0.1 MΩ. However, although it shows that ferroelectric/ferroelastic switching occurs during the cycles, the time for each cycle was about 1 minute and thus the power output of the system is low. Hence it is desirable to investigate the resistor's effect on the performance at a higher frequency.

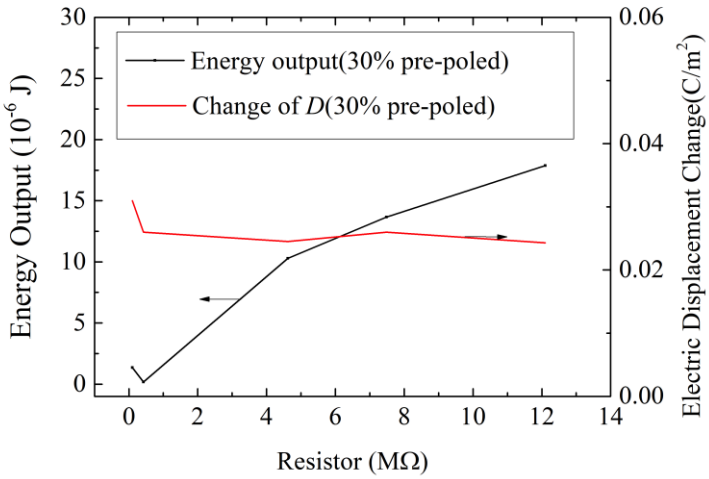


Figure 7.3 The energy output per cycle with various resistors

7.3.2 Vibrational study

Noting that the vibrations created by human motion or vehicle motion are commonly in the range 0.5 – 50 Hz, a test was conducted at 10 Hz to explore the load resistor's effect on the energy harvesting cycle. Besides, a verification test for non-linearity was conducted at 15 Hz and 20 Hz to further demonstrate the

ferroelectric/ferroelastic during the energy harvesting cycles. The vibrational tests are driven by a sinusoidal wave of displacement controlled by LVDT, and a verification test of ferroelectric/ferroelastic switching by varying the amplitude of displacement (applied force) was done.

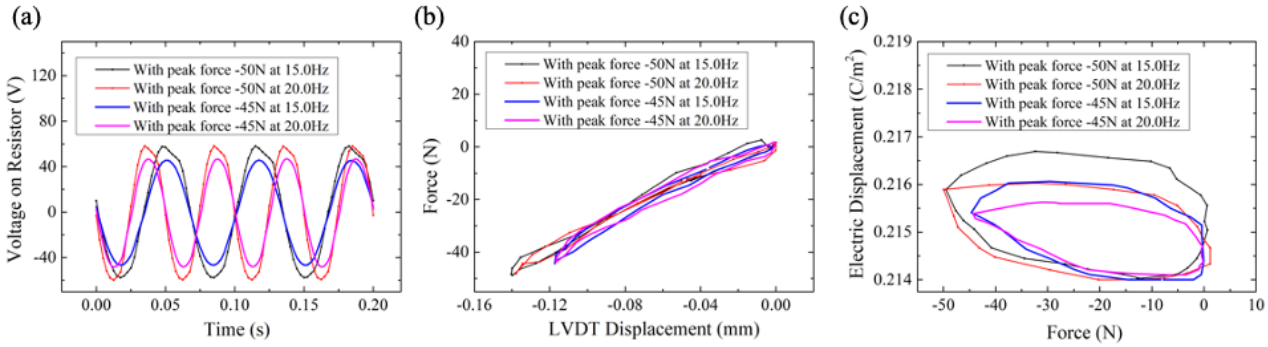


Figure 7.4 The 30% pre-poled energy harvester tested with 4.67 MΩ and -50 N and -45 N amplitude of force at 15 Hz and 20 Hz respectively (a) Voltage across the energy harvester versus time. (b) Force versus LVDT displacement. (c) Electric displacement versus force.

The verification test is implemented by -50 N and -45 N force amplitude, which can be adjusted by LVDT displacement, at various frequencies with a resistor load 4.67 MΩ, and some of the results can be seen in figure 7.4. The voltage amplitude generated in Figure 7.4(a) shows the comparison of generated voltage with force amplitude -50 N and -45 N at 15 Hz and 20 Hz, and it is observed that the 10% change of mechanical loading can induce a more than 20% change of electrical voltage. This demonstrates the non-linearity between load amplitude and voltage during operation. Also, the shape of voltage versus time curves in figure 7.4(a) is not sinusoidal, indicating a non-linear correspondence to the mechanical loading. The amplitude of voltage at 15 Hz is similar to that at 20 Hz, while the corresponding electric displacement amplitude reduces with

the rise of frequency, see figure 7.4(c). Additionally, the values of electric displacement change are slightly smaller than those obtained that with quasi-static working cycles. There are two main findings. Firstly, it is expected that increasing the frequency can generate higher voltage, but the generated high voltage will inhibit ferroelectric/ferroelastic switching induced by stress so that the voltage stabilizes with the increase of frequency from 15 Hz to 20 Hz. Furthermore, the higher frequency can induce greater total charge flow, but the current appears to be limited. High rate of charge flows require high currents and associated high voltage, which will resist ferroelectric/ferroelastic switching to in turn limit the rate of charge flows.

Figure 7.4(b) shows the corresponding mechanical loading path for the operation, the curves are consistent with the results under quasi-static condition. The curves in figure 7.4(b) are not perfectly smooth, resulting from the load cell accuracy of +/-3 N.

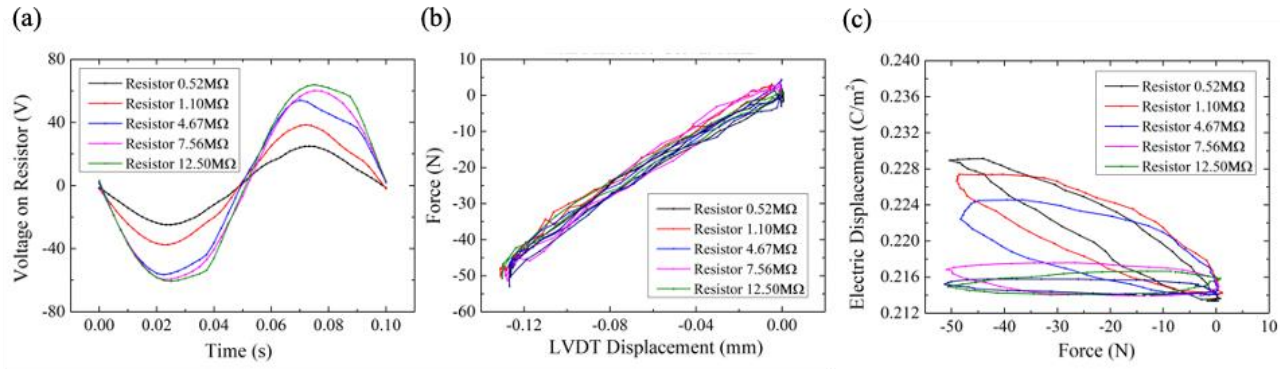


Figure 7.5 The 30% pre-poled energy harvester tested with various resistive loads with 4.67MΩ (a) Voltage across the energy harvester versus time. (b) Force versus LVDT displacement. (c) Electric displacement versus force.

Figure 7.5 shows the working cycles with various resistive loads at 10 Hz, driven by a compression force amplitude F=-50 N. From Figure 7.5(a), the voltage amplitude increases with the rise of resistor's value, but it increases just a few percent once the resistance is greater than 4.67 MΩ. This indicates that the voltage amplitude tends to stabilize as the resistor becomes large. Specifically, this phenomenon further demonstrates that the higher voltage can inhibit the ferroelectric switching, and thereby resist the larger charge flow and affect the voltage across the load impedance. In figure 7.5(c), the corresponding electric displacement is presented, showing that the higher impedance has a smaller change of electric displacement during cycles. This means the charge flow is also smaller with high impedance, and hence the voltage tends to be stable with the increase of resistive loads. The force versus LVDT displacement figure is shown in Figure 7.5(b), wherein the mechanical loading path remains approximately the same during the tests.

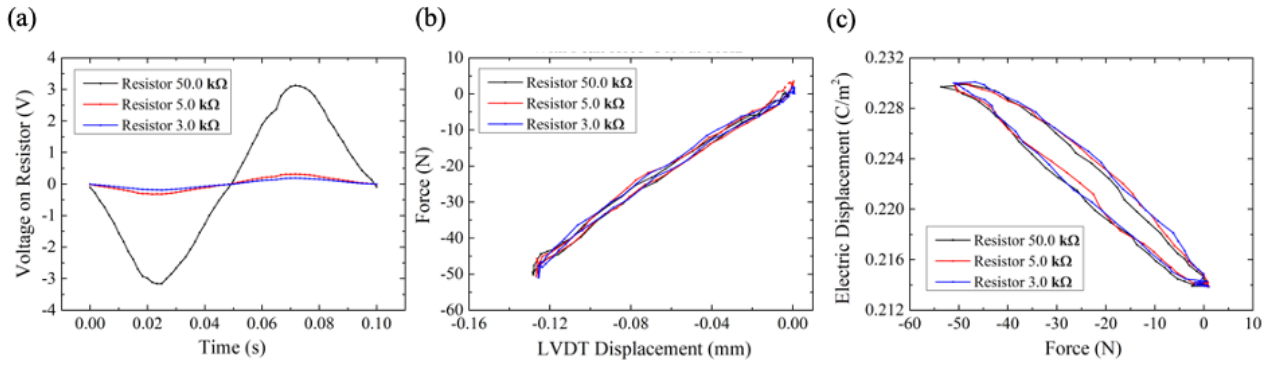


Figure 7.6 The 30% pre-poled energy harvester tested with various small resistive loads with 4.67 MΩ at 10 Hz (a) Voltage across the energy harvester versus time. (b) Force versus LVDT displacement. (c) Electric displacement versus force.

It is of interest to explore the effect of small resistive loads, as shown in Figure 7.6. The tests are operated with 50 kΩ, 5 kΩ and 3 kΩ at 10 Hz, driven by the force amplitude of -50 N. It is shown that the voltage amplitudes on the resistive loads are lower than 0.3 V, similar to the values found in quasi-static tests, especially when the resistor's value is below 10 kΩ. By contrast, the small resistive load at 10 Hz can also form a closed cycle, see figure 7.6(c). The electric displacement change is stable, and slightly smaller than the corresponding data from quasi-static tests. Therefore, the challenge of establishing a stable cycle requires critical choice of frequency, amplitude of mechanical load and electrical loads, and the key factors may vary at different specific frequency, as the results of quasi-static and vibrational tests here shown here.

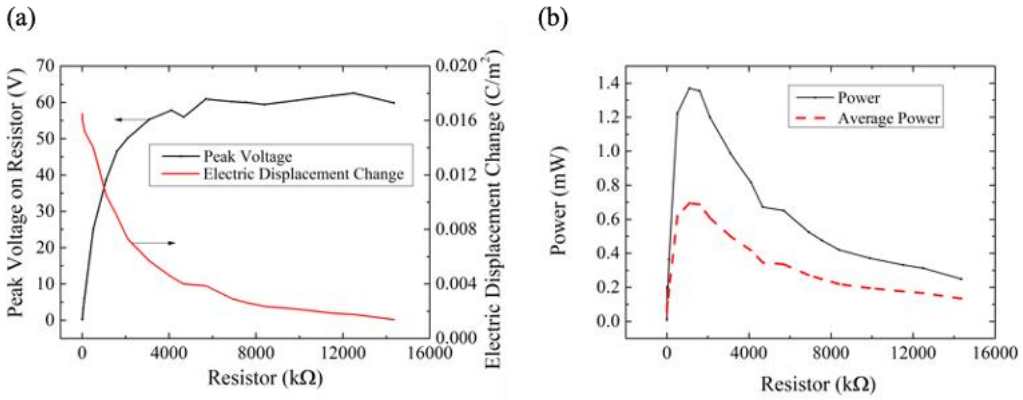


Figure 7.7 The effect of resistive loads of 30% pre-poled specimen at 10Hz (a) Peak voltage and electric displacement. (b) Power output.

Figure 7.7 summarizes results of voltage on the load impedance, electric displacement changes and power output with the variation of load resistors, measured at 10 Hz. This shows that increase of the resistor's value makes the peak voltage increase sharply in the beginning, followed by a slow rise after it reaches around 1

MΩ. By contrast, the electric displacement change has an opposite trend, showing that larger resistors can inhibit the charge flow from working cycles and further limit the voltage amplitude. The amplitude of voltage stabilizes at about 60 V when the resistor reaches 5 MΩ in figure 7.7(a). In figure 7.7(b), the peak power and average power, obtained by integrating the instantaneous power over the cycle, are shown. This indicates that the 1.1 MΩ is the best choice for working cycles to maximise the power output with the specific mechanical load amplitude at 10 Hz. However, the optimal load resistor for energy harvesting cycles may vary due to the changes of mechanical load amplitude, device size and operating frequency, which requires further exploration systematically. The average power output in this work is approximately 0.7 mW, and the corresponding average cycle energy density is about 1.4 mJ/cm^3 at 10 Hz. This provides an excellent opportunity to substitute traditional piezoelectric transducers.

Unlike the energy output in quasi-static tests, the increase of load resistance cannot indefinitely enlarge the power output, and there is an optimum point reached by appropriately selecting the resistor's value. Similarly, it is expected that the optimum resistor would depend on frequency based on the comparison of quasi-static and vibrational studies in this work. This would need further development for specific practical applications.

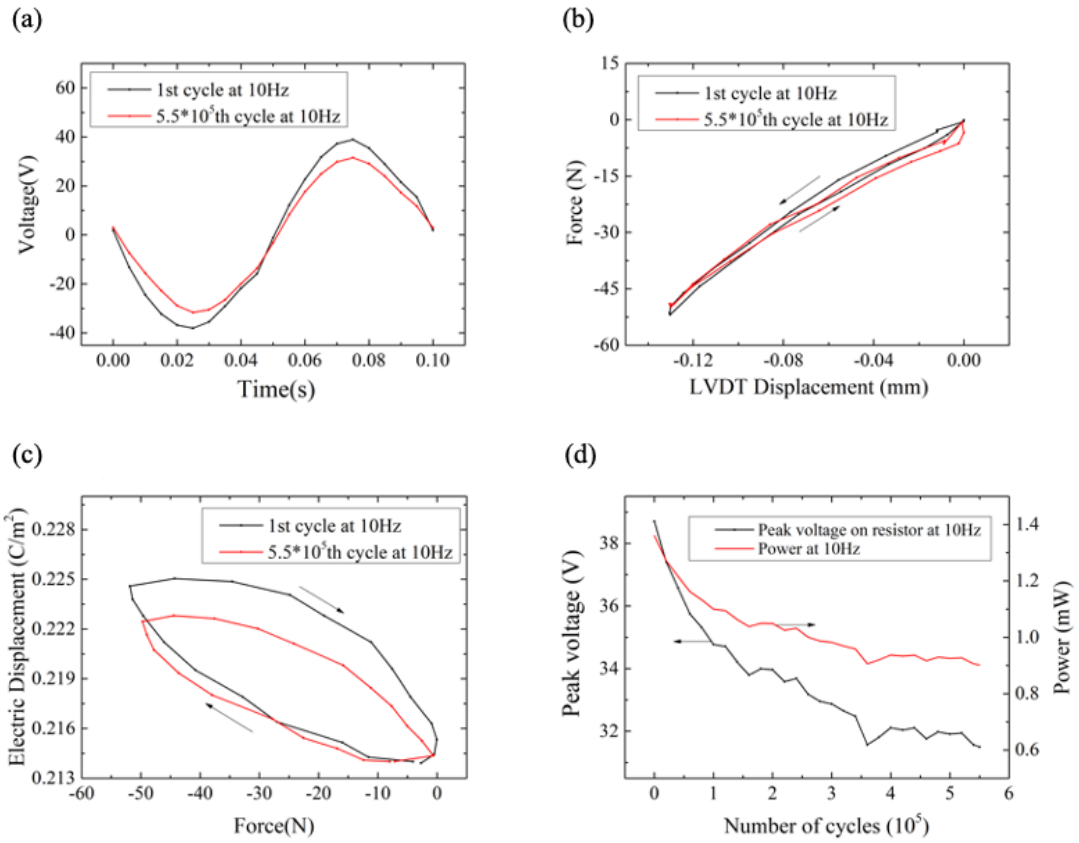


Figure 7.8 Fatigue testing of the 30% pre-poled energy harvester at 10Hz with a 1.1MΩ load resistor. (a) Comparison of voltage for 1st and 5.5×10^5 th cycle (b) Corresponding comparison of the mechanical load cycles. (c) Corresponding comparison of the electric displacement chagne. (d) The degradation of peak voltage and power output with cycle number.

To test the fatigue performance of the optimal energy harvesting cycle loaded -50 N at 10 Hz, 0.55×10^6 cycles were run with a 1.1 MΩ load resistor. The number of cycles in this test was set to 0.55 million, which is to the same as previous fatigue test in Chapter 5. This allows us to test whether the optimized cycle in Chapter 7 can remain stable and robust after many cycles of loading, giving a direct comparison with results in Chapter 5. Figure 7.8 reports the results of the fatigue test, showing slight degradation in performance. With the increasing number of cyclic electromechanical

loading, less polarizations may switch to a repolarized state in micro scale, resulting in the degradation in performance. With the same operating condition as shown in figure 7.8(b), the voltage and electric displacement remain almost constant during cycling, see figure 7.8(a) and (c). The amplitude of voltage on the resistor and power output can be seen in figure 7.8(d). It is observed that the first 10^5 cycles induce a drop by 10% in the peak voltage, resulting in a corresponding 21% change in power output. From 10^5 cycles to 5.5×10^5 cycles, the power output and voltage amplitude decrease slowly and tend to be stable. During the tests, the energy harvester did not appear to undergo mechanical degradation (no cracks were observed), and the energy harvesting cycle displays stability during the operation.

Finally, it is also of importance to give a summary of the quantitative estimations of experimental errors in Chapter 5, 6 and 7 and their effects on measurements of energy output. The detailed information about quasi-static tests and vibrational tests can be seen in Table 7.1 and 7.2 respectively. For both the quasi-static tests and vibrational study, the relative errors of both energy harvesting cycles with external voltage and load resistors are listed, and the maximum propagating errors of electric displacement, energy output per cycle, mechanical input per cycle and cycle energy density are given based on the relative propagating error calculations. Here, the maximum propagating errors were calculated by the equation of a product function: $\frac{\sigma_f}{f}=\sqrt{(\frac{\sigma_x}{x})^2+(\frac{\sigma_y}{y})^2+(\frac{\sigma_z}{z})^2}$, where the $\sigma_f,\sigma_x,\sigma_y,\sigma_z$ are the propagating error and

relative errors of variables, and f, x, y, z indicate the function and the variables. It is a root of the sum of the squares of relative error for each variable. For example, to calculate the electric displacement's relative error, which is based on the voltage measured on electrometer divided by the area of the electrode, and thereby the relative error of the electric displacement can be obtained by the root value of the sum of squares leakage current and area of electrode.

Regarding the detailed errors in both tests, the values were roughly determined based on the accuracies of the equipment for measurement, compliance of the test fixture and difference in specimen fabrication. For example, although the electric displacement change has reduced the effect of the leakage current, the fluctuation of the leakage current can also impose an effect on the electric displacement, which causes an error of 5%-10%. The area of the top electrode has errors, which depend on the quality of the silver paint. Additionally, electrometer measurement, resistor value, force on the pins measured using Deben microtester, load cell of hydraulics, amplifier generation accuracy and LVDT accuracies have errors due to limited accuracies of the measurement equipment. Some of them are derived from the practical measurements, and the others are based on the handbooks of the equipment for measurements.

For the tests with external voltage in Table 7.1, it can be seen that the relative errors of electric displacement induced by leakage current and area of electrode play key roles for percentage errors of electric displacement and cycle energy density, while the relative errors of force on the pins and pins displacement are the key factors to

determine the mechanical input energy. The energy output relative error was decided by the electrometer measurement. With the external voltage, the edges of the PLZT was kept clean instead of being silver painted in order to avoid high leakage currents, and thereby to further reduce the relative errors measured related to them, especially when the tests used $1.0E_0$ as a harvesting electric field in Chapter 6. Additionally, it indicates that the relative errors of mechanical input energy are sensitive to the amplitude of mechanical loads. For the cycles with small mechanical load amplitude, the relative error can become close to 100%, which was due to the compliance property of test rig. By contrast, with the increase of mechanical load amplitude, the relative error of mechanical input energy significantly reduced to 8.32%.

In terms of the quasi-static tests with external load resistor, the relative errors are smaller than those with external voltage in Table 7.1. This is because relatively small voltages were measured in the tests, wherein the relative errors of area of top electrode and leakage current can be neglected. However, it should be noted that the percentage error of energy output per cycle has increased.

Table 7.1 The estimated errors in quasi-static tests

Factors considered for error analysis/Quasi-static tests	Error estimations/with harvesting voltages	Error estimations/ with load resistors
Electric displacement induced by leakage current	+/- 5% ~ 10%	None
Area of top electrode	+/- 3.6% ~ 6.5%	+/- 0.28%
Thickness of PLZT layer	+/- 3.3%	+/- 3.3%
Electrometer measurement	+/- 0.5% ~ 1%	+/- 0.05% ~ 5%

Amplifier for voltage generation	+/- 5%	None
Pins displacement	8.3% ~ 100%	+ 8.3% ~ 100%
Force on the pins	-0.6%~ -2%	-0.6% ~ -2%
Resistor value	None	+/- 0.2%-0.5%
Percentage error of electric displacement	11.92%	5%
Percentage error of energy output per cycle	5.1%	7.09%
Percentage error of mechanical input per cycle	100%	None
Percentage error of cycle energy density	8.897%	7.83%

Table 7.2 The estimated errors in vibrational tests

Factors considered for error analysis/Vibrational tests	Error estimations/ with load resistors
Area of top electrode	+/- 0.28%
Thickness of PLZT layer	+/- 3.3%
Voltage collected by Labview	+/- 1.8%
Electrometer measurement	+/- 0.05% ~ 5%
LVDT	+/- 0.5%
Resistor value	+/- 0.2%~0.5%
Load cell	+/- 6%~ 10%
Percentage error of electric displacement	5%
Percentage error of energy output per cycle	2.59%
Percentage error of mechanical input per cycle	10.01%
Percentage error of cycle energy density	4.2%

The relative errors in the vibrational study are given in Table 7.2, where a typical relative error of LVDT was adopted in the analysis[439]. All the propagating errors presented in Table 7.2 are smaller than those discussed in Table 7.1 due to the smaller

relative errors of variables compared with Table 7.1. There are some main findings. First of all, the main contribution of the propagating errors was induced by the inaccuracy of load cell in Table 7.1, in which the percentage error of mechanical input energy was significantly affected. By contrast, the high quality LVDT can precisely control the displacement of pins, compensating some of the errors induced by load cell. Besides, due to the greater voltage measured than that measured in the quasi-static tests with external load resistors, which is about tens of volts, the relative error of electrometer measurement is reduced to about +/- 1%. However, the inaccuracy of load cell increased the overall value to 5%. This is reflected in the curves of force amplitude versus LVDT displacement and force versus electric displacement presented in Chapter 5 and 7. In this work we have only estimated the errors in the experiments, but further systematic work should be done to calculate the mean value and standard deviation by repeating the experiments, which will guide further experimental designs and avoid systematic errors induced by the limited accuracies of the equipment for measurement.

7.4 Summary

This chapter reported the effect of resistive loads on compressive stress-induced energy harvesting cycles using ferroelectric/ferroelastic switching. Results were reported for both quasi-static and low-frequency vibrational conditions. The prototype device was fabricated using a 30% prepoling process for the ferroelectric active layer, and then complete poling after it is attached on a substrate. Afterwards, uniaxial tensile stress was applied to partially depolarize the ferroelectrics, allowing some control of the state of polarization and residual tensile stress. The working cycle is driven by cyclic compressive stress, in which case the polarization change gives rise to charge flow against an electrical load to generate energy output. The tests in this work demonstrate the non-linear switching effect in the cycles, and provide some understanding of the external circuit's influence on ferroelectric/ferroelastic switching. By changing the mechanical load amplitude at 15Hz and 20Hz, the non-linear relationship between the force amplitude and generated voltage was presented, which further demonstrates the ferroelectric/ferroelastic switching occurred during the energy harvesting cycles. Additionally, the results show that the resistive loads can play a role to establish a closed working cycle at specific frequency. Quasi-static tests (0.0167 Hz) were more sensitive to the choice of resistor. An optimized energy output could be identified, with superior performance compared with typical piezoelectric transducers both for quasi-static and vibrational tests. The energy output could be improved by

increasing load resistance from 0.1 MΩ to 12.10 MΩ with quasi-static condition, while the power output was optimized by choosing an appropriate value of load resistor. In these tests the 1.1 MΩ resistor gave the greatest power output in the range of 3kΩ - 15 MΩ at 10 Hz. The optimized average cycle energy density reached 1.4 mJ/cm^3 at 10Hz, which is orders of magnitude greater than typical piezoelecric energy harvesters. The simple structure and high energy output indicates promise for further optimization and improvement with the potential to replace the current piezoelectric transducer devices. Finally, the error estimations for the experiments conducted in Chapter 5, 6, and 7 were presented and discussed, providing a useful guidance for design optimization and error reduction in future tests.

Chapter 8

8. Conclusions and future work

Compared with the piezoelectric effect, which is known as a thermodynamically reversible change, ferroelectric/ferroelastic switching can generate larger charge flows and have greater electrical output potential, but it is very difficult to guide the polarization to switch back by stress only. Thus many ferroelectric generators are single-shot applications, and they cannot be used continuously. The difficulty of establishing a closed cycle by mechanical loads only has prevented application up to now. In this thesis, the method of energy harvesting using ferroelectric/ferroelastic switching was explored numerically and experimentally, and a novel and stable energy harvester prototype device by using partially ferroelectric/ferroelastic switching was established. Initially, the modelling work was used as a design tool to develop the energy harvesting working cycles, giving understanding about polarization switching in polycrystalline materials. Then a practical energy harvester prototype device using partially ferroelectric/ferroelastic switching was fabricated, and the effects of engineered states of ferroelectrics, amplitude of force, external resistive impedance and varying frequency on energy harvesting performance were also investigated. In this chapter, the key results of current work and potential further work are discussed.

8.1 Conclusions and discussion

Hwang's model provided the prospect for energy harvesting by using ferroelectric/ferroelastic switching in Chapter 4, wherein an enclosed and stable energy harvesting cycle was established with the assistance of a bias electrical field. Based on the model, a ferroelectric energy harvester with random microstructures of polycrystalline ferroelectrics was investigated, and the simple application configuration was also given: a thin layer of ferroelectric bonded onto a beam substrate. Electromechanical loading was introduced to drive the cycles, in which a harvesting electric field and a small bias field generate energy output and guide the repolarization respectively. Without the bias field, the electrical polarization cannot switch back with stress only, and then the working cycles cannot be closed. The results show that greater energy density can be realized through the strategy than piezoelectric transducers, and the energy conversion efficiency can reach 20% by optimizing the electromechanical parameters. Therefore, there is potential to replace or improve the existing piezoelectric energy harvesters by using the energy harvesting cycle in Chapter 4. However, the model does not consider the grains' interactions, which needs to be developed in experiments and more sophisticated models.

Chapter 5 mainly introduced the key concept and performance of practical energy harvesting cycles using ferroelectric/ferroelastic switching. By engineering the material state of the ferroelectric, a residual stress, which can be varied by pre-poling levels, is generated between a ferroelectric layer and a substrate to achieve more effective

ferroelectric/ferroelastic switching. The strategy works by pre-poling the ferroelectric in an unconstrained state, and then complete poling after bonding with a substrate. After the application of tensile stress to partially depolarize it, a stable working cycle can be achieved by using cyclic compression only. The experiments demonstrate that the working cycles can be stable without using external bias field. Instead, internal residual electric fields, generated during a partial depoling of an electroceramic, can provide "memory" of a preferred direction for repolarizing it. The 30% and 100% pre-poled specimens are compared in this chapter, and the non-linearity of 30% pre-poled sample can be observed through the results. Furthermore, the vibrational study indicated that the energy harvesting cycles can achieve much greater energy density than typical piezoelectric devices, and comparable performance with some triboelectric nanogenerators. Afterwards, a fatigue test was implemented to verify the robustness of the energy harvesting cycles, showing that the working cycle can stay stable up to 0.5 million cycles. The advantages of this prototype device are clear: the simple configuration provides more possibilities for a wide range of applications, and the working principle can also be utilized further to optimize the performance by a deeper design study.

In Chapter 6, four kinds of specimens with various material state, from 30% to 100% pre-poled levels, are explored and optimized through a quasi-static test on Deben stage. By varying the states of pre-poling using different electric field levels, it was possible to produce a state of residual stress in the ferroelectric, which can enhances

the ferroelastic switching with a low amplitude of mechanical loads. The experiments show that the resulting biased states can also guide the repolarization when the mechanical loads are relaxed, without the need for external electrical assistance. There are two working methods by which the energy harvesting cycles can be achieved using electromechanical loads. The first approach uses tensile stress to drive the polarization switching, and internal bias fields can guide the polarizations to switch back. The second method was studied in Chapter 5. Although the first approach using tensile stress can generate greater energy output per cycle, the advantages of robustness for the second method using compression make it as a promising candidate for practical use. Additionally, it is of importance to find the balance between pre-poling level and energy output. On the one hand, the decrease of pre-poling level can lead to greater energy output. On the other hand, the reduced pre-poled state can increase the residual stress and cause cracking. The results show that 30% pre-poled samples could be a good choice to provide high energy output whilst avoiding the fracture in the PLZT ferroelectric tested.

Finally, an optimization study of resistive impedance selection was presented in Chapter 7, wherein a 30% pre-poled specimen was selected to optimize the working performance based on the working cycles proposed in Chapter 5. The results show that the resistive loads can affect the establishment of closed working cycles. Resistor with a small value of 0.1 MΩ results in insufficient electric field in the ferroelectric to guide the polarization to switch back in quasi-static conditions. By contrast, this problem was

not found in low-frequency vibrational tests. In these cases, there are sufficient electric fields to guide the polarizations to switch back by using the resistors smaller than 0.1MΩ, resulting from the higher currents, which are associated with charge flows driven by the increase of frequency, than that in the quasi-static tests. The energy output for quasi-static tests increases monotonically with the increase of resistive value, while the power output can be optimized by using an appropriate value, which was in the range of 3 kΩ - 15 MΩ at 10 Hz for the system tested. The optimized cycle energy density can reached 1.4 mJ/cm^3 at 10Hz, and the optimized working cycle was reasonably robust during the fatigue test up to 0.55 million cycles.

In conclusion, the main contributions of the work presented in this thesis are as follows: (1) A novel and stable energy harvesting cycle with a bias field was theoretically proposed based on Hwang's model, with an estimate of energy output and conversion efficiency. (2) A novel, robust and stable ferroelectric energy harvester device with simple configuration was practically established, which can improve the performance of piezoelectric transducers and compete with triboelectric nanogenerators. (3) An engineered state of ferroelectric material , associated with residual stress and electric field was proposed for energy harvesting, providing insights into the effect of microstructure and grain-to-grain interaction.(4) The behaviour of ferroelectric layers on a substrate was studied experimentally. The findings in these aspects will promote the energy harvesting method using ferroelectric/ferroelastic switching, and they will also provide a basis for future work. Besides, the concept of

an engineered state in polycrystalline ferroelectrics may facilitate the development of ferroelectric devices, such as actuators and sensors. The investigations of this thesis will thus provide insights for scientists and engineers.

8.2 Future work

Although the performance of the ferroelectric energy harvester in current work exceeds the performance of prior technology, it is necessary to improve the energy output and adaptability in the ambient environment to harvest mechanical energy from human motion, vehicle vibration or excitations induced by fluids. There are five key factors: material selection, structure optimization, frequency adaptability, fatigue properties and working ability under extreme conditions. These should be included in the future exploration, which may be focussed towards specific practical applications, such as flexible electronics and implantable devices. Therefore, there will be a large space for further development. For example, it may be possible to select ferroelectric single crystals or ceramic materials that increase the energy output; then the selections of substrate and adhesive materials for device preparation will also be important. Additionally, the fatigue properties and extreme environment working ability are both highly related to the material selection.

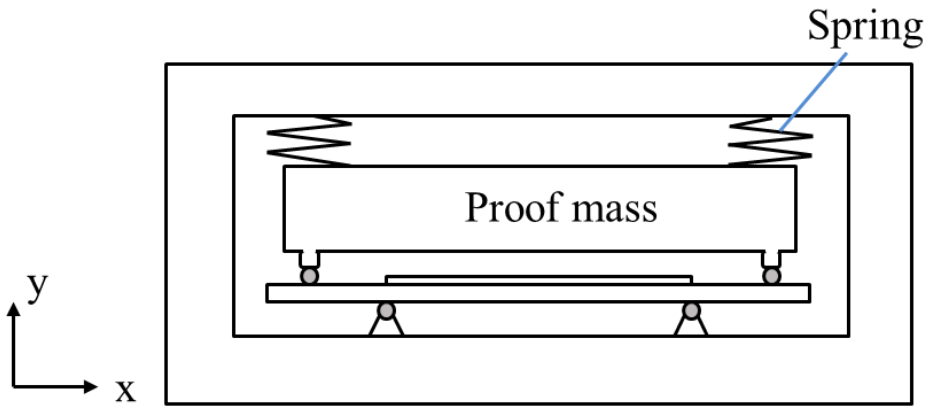


Figure 8.1 A vibrational four-point bending design

8.2 Future work

Instead of the four-point bending design under direct mechanical loading, a vibrational four-point bending structure is designed, see figure 8.1, which can be adapted to the varying ambient vibration environment. This is highly linked with the frequency adaptability study, wherein the proof mass and shape of structure should be designed for a specific frequency or a range of defined bandwidth. There are some interesting questions towards frequency adaptability. What would happen if random frequency and random mechanical load amplitude are applied during energy harvesting? What is the damping property of the energy harvester? What is the resonant frequency of the structure? These are all should be addressed in future study.

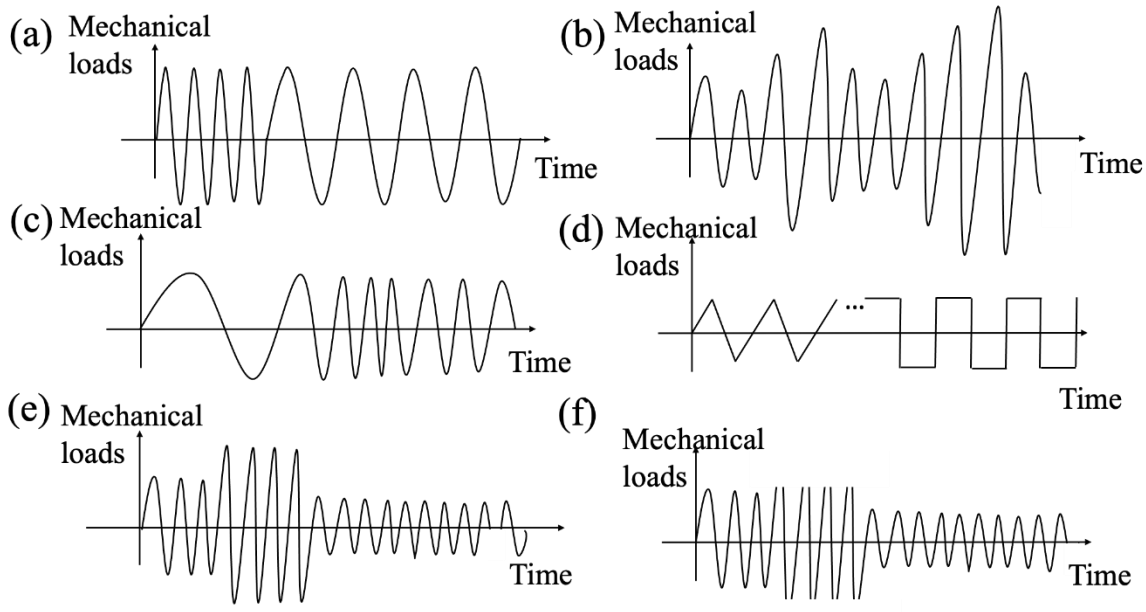


Figure 8.2 (a) Mechanical loads with steady harmonic waves and the same amplitude at various frequencies in current work. (b) Mechanical loads with random amplitude at fixed frequency. (c) Mechanical loads with fixed amplitude at varying frequency. (d) Mechanical loads with different waveforms. (e) Random signal of mechanical loads. (f) Random signal of mechanical loads, which is truncated at a specific level.

It is very interesting to further consider the effects of more realistic mechanical inputs, which are determined by the real vibration, on energy harvesting performance. In figure 8.2, there are several possible signal types with different amplitudes of mechanical loads and frequencies, which can be found in the general practical applications. Figure 8.2(a) shows the steady harmonic waves of mechanical loads at various frequencies, similar to what was used in the current work, while figure 8.2(b)-(f) give the various other possibilities: (b) random amplitude at fixed frequency; (c) fixed amplitude at varying frequency; (d) different waveforms such as square, triangle, which can be generated by digital control or simulated by a complex combination of infinite harmonic waves; (e) random signal of mechanical loads; (f) random signal of mechanical loads, which is truncated at a specific level. Under these unexplored loading conditions, it is challenging to ensure a continuous power output from the ferroelectric energy harvester. Two possible reasons may be dominant. First of all, the varying amplitude may significantly affect the power output of the energy harvester compared with the current work with appropriate mechanical load amplitude. If the mechanical loads are smaller than the value required to trigger ferroelectric/ferroelastic switching, only the linear effect of the ferroelectric can be used for energy harvesting at a loss of extra energy obtained due to the non-linear effect. Besides, as mentioned in Chapter 5, if the mechanical loads are too large, that may damage the engineered state of the ferroelectric, and also affect the performance of the energy harvester. For this reason it may be desirable to truncate the loading (for example with mechanical limiters) as

illustrated in figure 8.2(f). Another factor is that the varying frequency may also affect the power output. Based on the results in Chapter 5 the increase of frequency may monotonically increase the power output. Furthermore, as shown in Chapter 5 and 7, the optimal choice of resistive impedance may change with the variation of frequencies. Hence, the varying frequency may increase the difficulty in choosing the resistive impedances, which may complicate the external circuits to adapt to a range of frequencies. Therefore, based on the discussions above, the practical designs should consider the ranges of working frequency and mechanical load amplitude carefully to ensure a steady and continuous power output of the ferroelectric energy harvesters.

By further exploring the dynamic properties of the energy harvester, a robust and practical product that can adapt to varied ambient environment could be built and developed, in which the high-performance energy output is kept. The research requires novel design of device and practical implementation towards the five key factors mentioned above, hence it should be investigated by both experimentation and modelling methods to optimize the design and ‘proof-of-principle’ device.

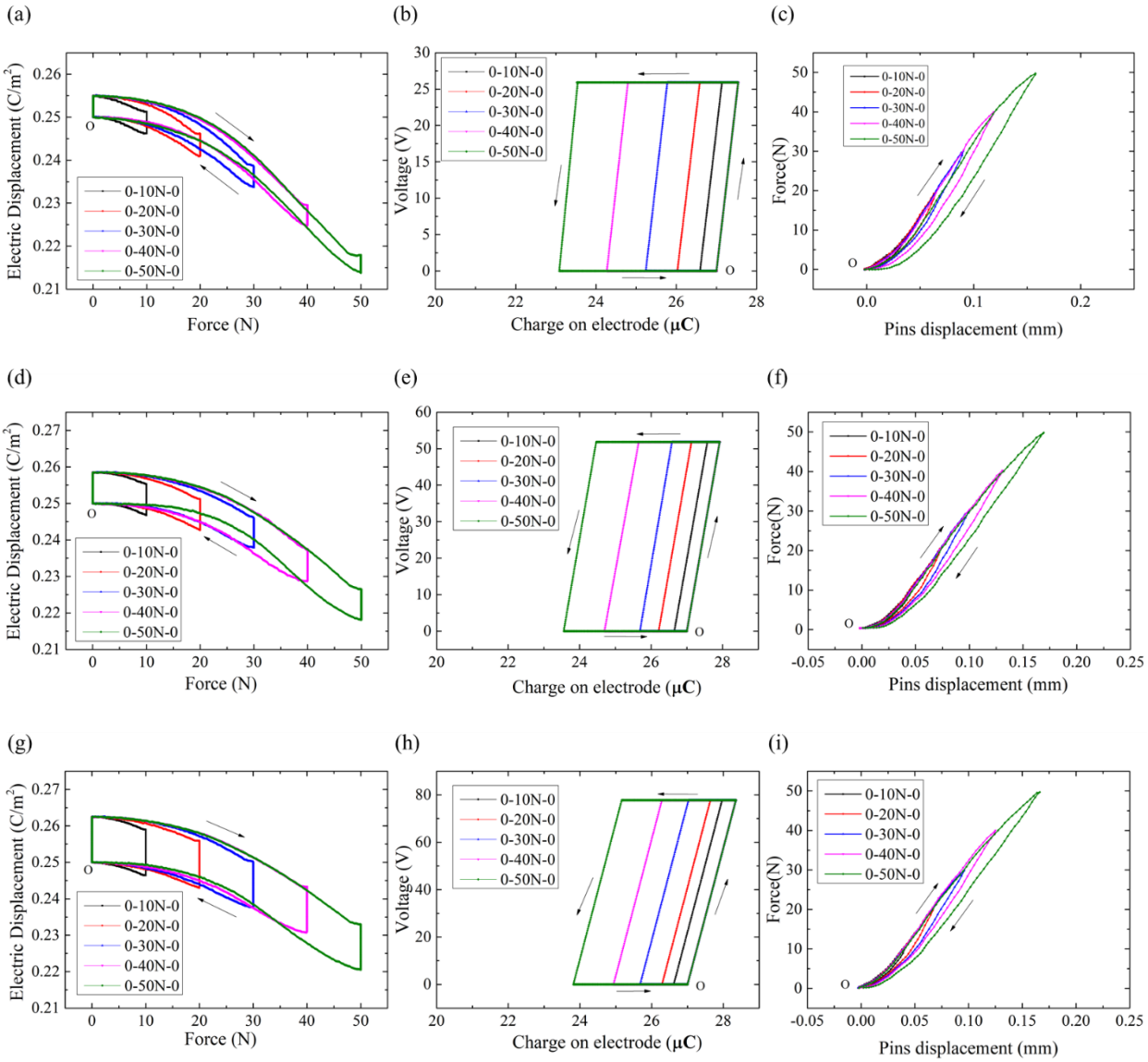
One approach is to design a more effective energy harvesting device by using modelling methods, which can be used to simulate the behaviour of the ferroelectric element with varying material, structure, mechanical and electrical loading amplitude and frequency. This requires reliable models of ferroelectric switching, including partial switching and “minor loops”. Ideally, modelling tools would also enable the assessment of damage, and thus enable a configuration with high energy output and

avoid material degradation. Ferroelectric switching models, such as micromechanical models and phenomenological models, can be used to do the exploration by considering grain-to-grain interactions and rate dependent properties. Note that the micromechanical models may require intensive calculation due to the large number of internal variables, hence the phenomenological models with relatively few internal variables may be the best choice. It is also desirable to build and test a 'proof-of-principle' device for practical applications. By considering the practical vibrational applications, the prototype of the ferroelectric energy harvester can be developed into many different structural designs. For example, like the piezoelectric energy harvester, the ferroelectric energy harvester can be shaped to a cantilever with a proof mass. By accurately designing the acceleration and the proof mass, the appropriate stress can be applied on the ferroelectric layer to induce the energy harvesting cycle. But this will affect the power output due to the variation of strain along the cantilever. A four-point bending vibrational structure with a proof mass is also a prospective to be further developed. This also needs careful selection of the proof mass, loading frequency and electrical impedance to enhance the power output. By testing the device on a shaker, the dynamic properties of the structure could be studied, which can provide further insight for device design. The energy harvesting device can be optimized step by step, until it can reach the practical requirements. Finally, after these lab tests, a prototype product will be established with external circuit and storage for practical tests on a

vehicle to test its practical performance under random ambient environment. This final step will pave the road for commercialization of the ferroelectric energy harvester.

Appendix

A.1 Energy harvesting cycles of 100% pre-poled



A.1 Energy harvesting cycles of 100% pre-poled

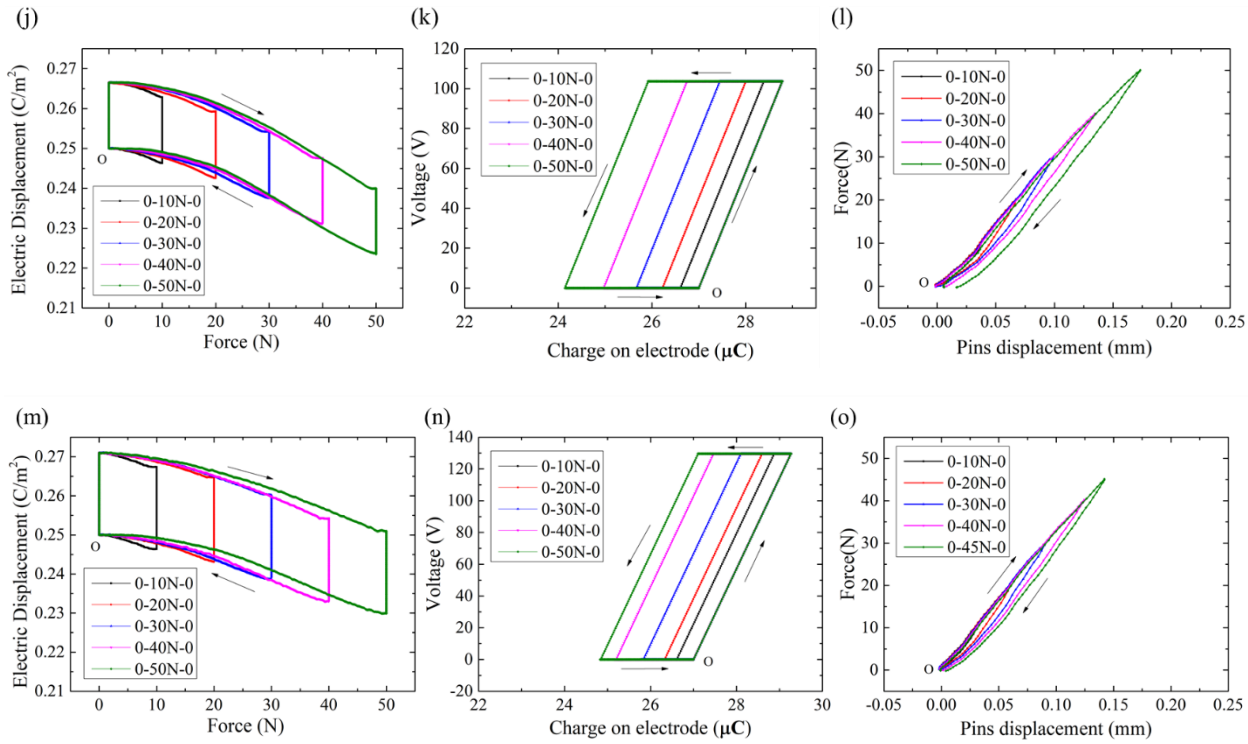


Figure A1. Energy harvesting cycles of the 100% pre-poled using tensile stress with harvesting electric field (a-c) $0.2E_0$, (d-f) $0.4E_0$, (g-i) $0.6E_0$, (j-l) $0.8E_0$, (m-o) $1.0E_0$. (a,d,g,j,m). Electric Displacement versus applied bending force (b,e,h,k,n) Corresponding voltage versus charge cycle. (c,f,I,l,o) Corresponding force versus loading pin displacement.

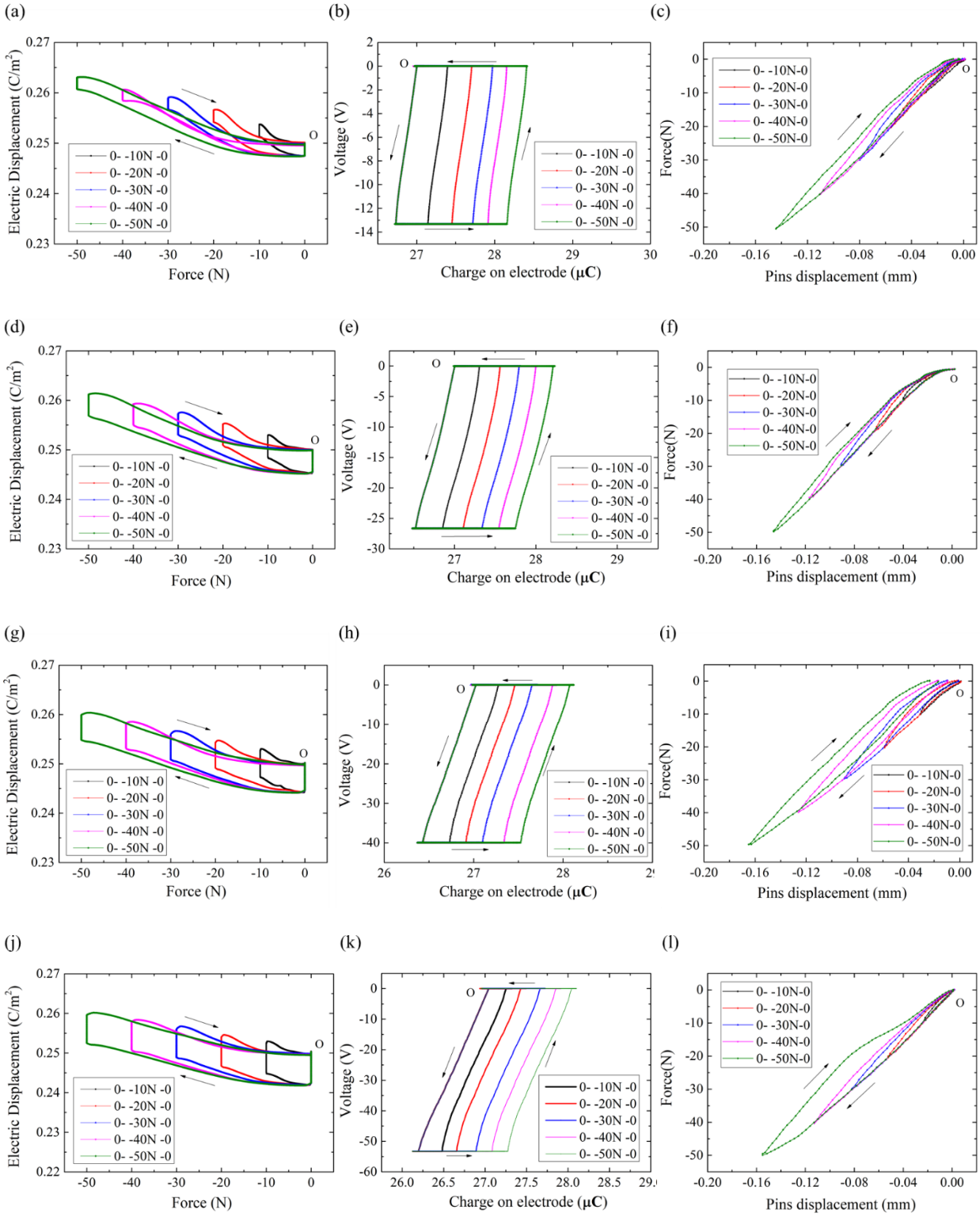
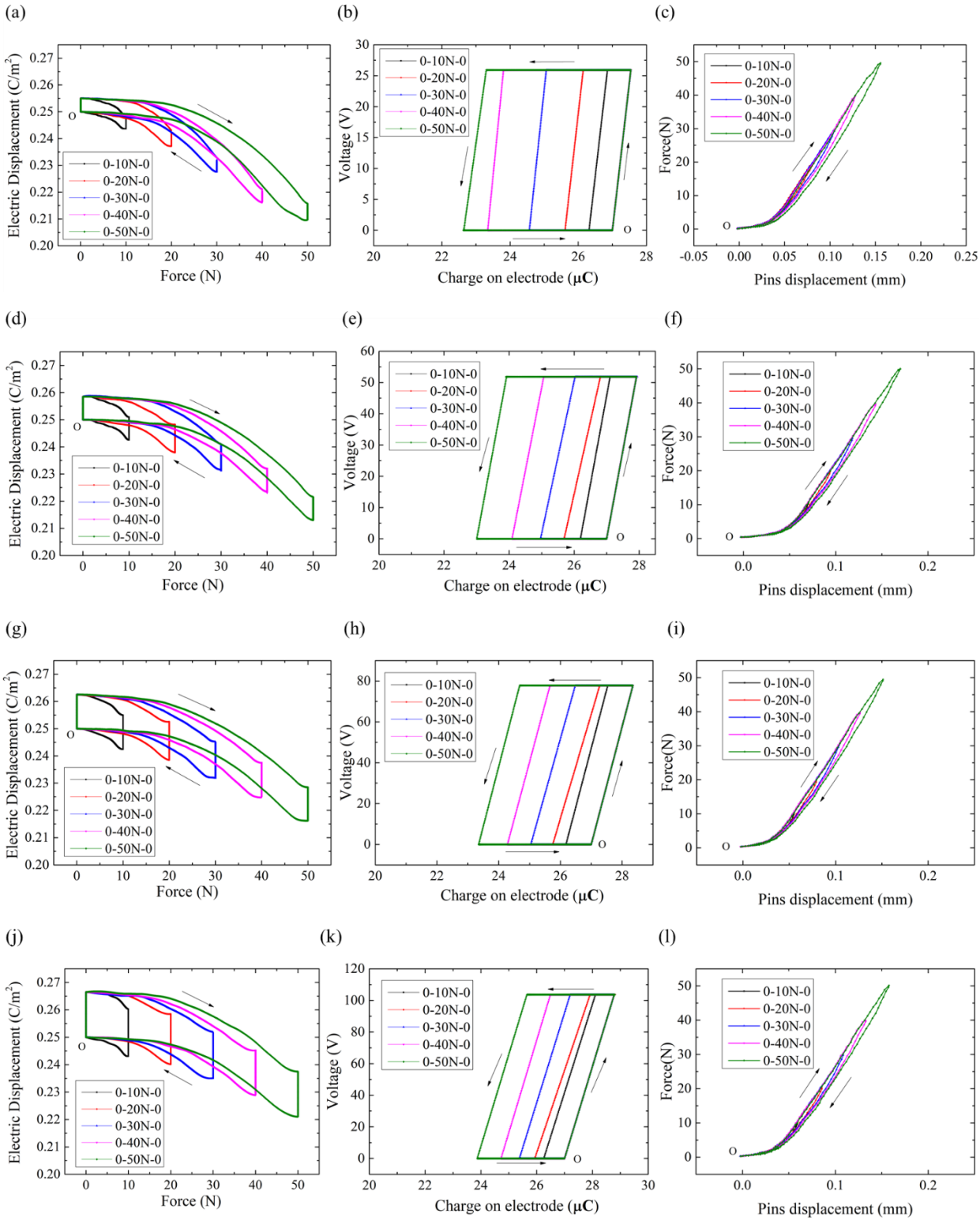


Figure A2. Energy harvesting cycles of the 100% pre-poled using compressive stress with harvesting electric field.(a-c)-0.1E_0, (d-f) -0.2E_0, (g-i) -0.3E_0, (j-l) -0.4E_0. (a,d,g,j). Electric Displacement versus applied bending force. (b,e,h,k) Corresponding voltage versus charge cycle. (c,f,I,l) Corresponding force versus loading pin displacement.

A.2 Energy harvesting cycles of 75% pre-poled



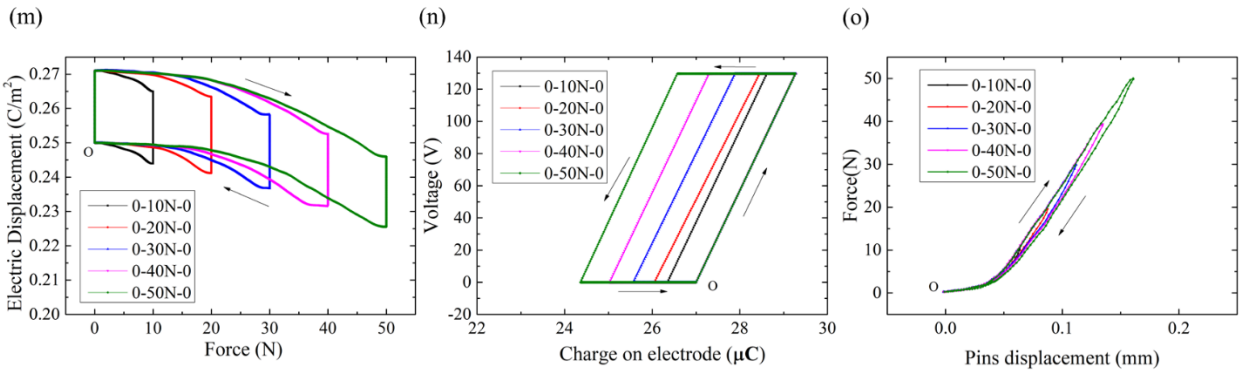


Figure A3. Energy harvesting cycles of the 75% pre-poled using tensile stress with harvesting electric field (a-c) 0.2E_0, (d-f) 0.4E_0, (g-i) 0.6E_0, (j-l) 0.8E_0, (m-o) 1.0E_0. (a,d,g,j,m). Electric Displacement versus applied bending force (b,e,h,k,n) Corresponding voltage versus charge cycle. (c,f,I,l,o) Corresponding force versus loading pin displacement.

A.2 Energy harvesting cycles of 75% pre-poled

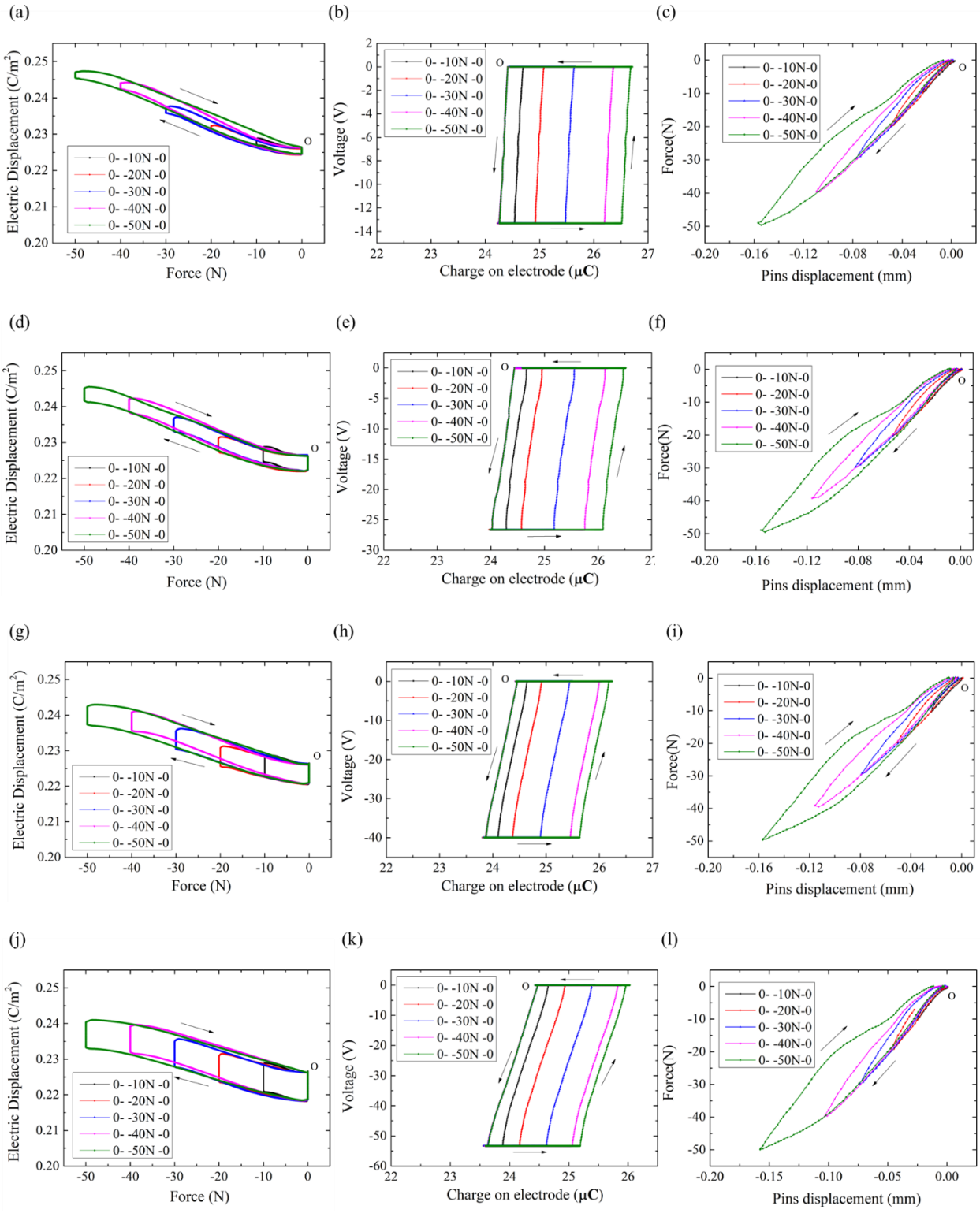
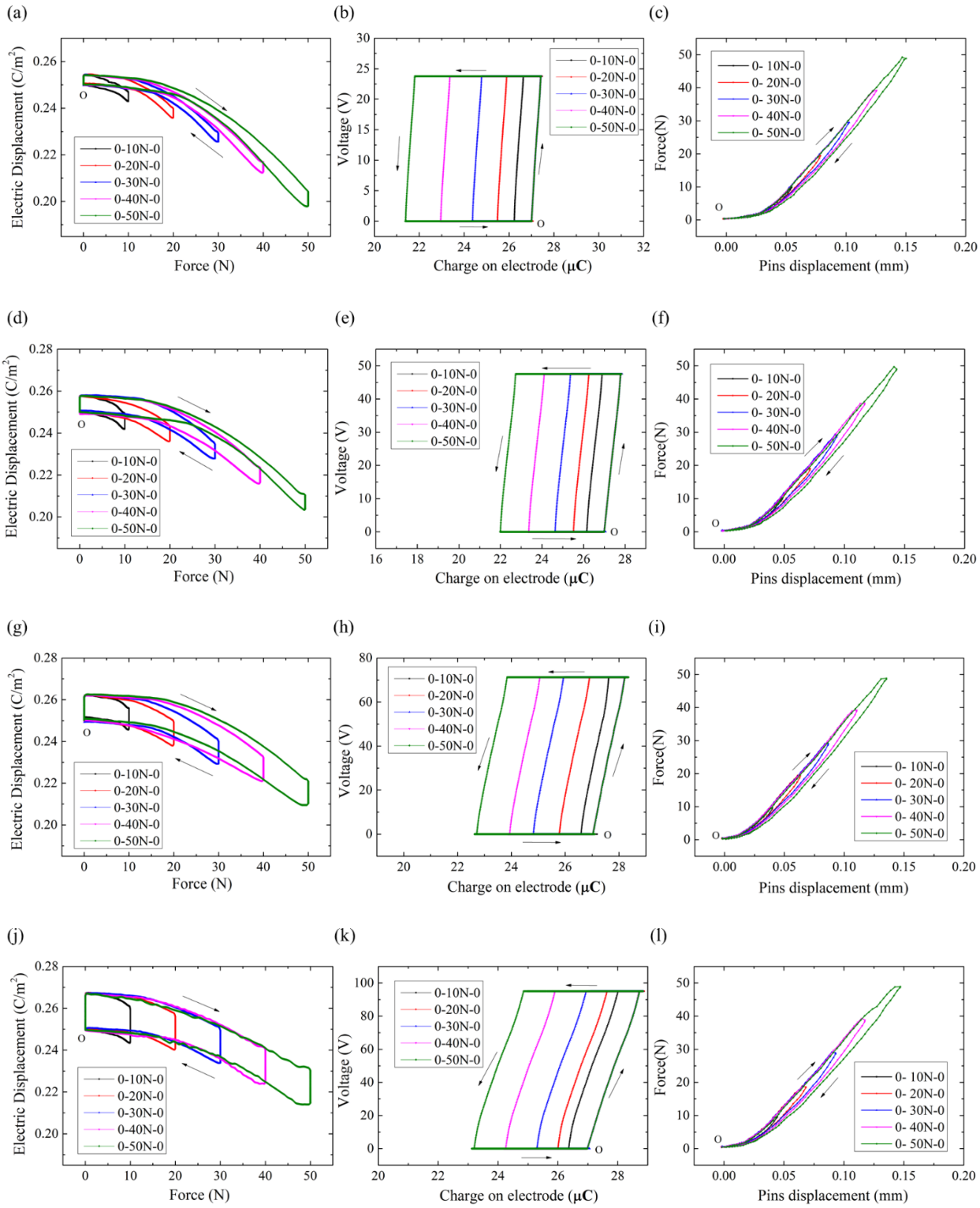


Figure A4. Energy harvesting cycles of the 75% pre-poled using compressive stress with harvesting electric field.(a-c)-0.1E_0, (d-f) -0.2E_0, (g-i) -0.3E_0, (j-l) -0.4E_0. (a,d,g,j). Electric Displacement versus applied bending force. (b,e,h,k) Corresponding voltage versus charge cycle. (c,f,I,l) Corresponding force versus loading pin displacement.

A.3 Energy harvesting cycles of 50% pre-poled



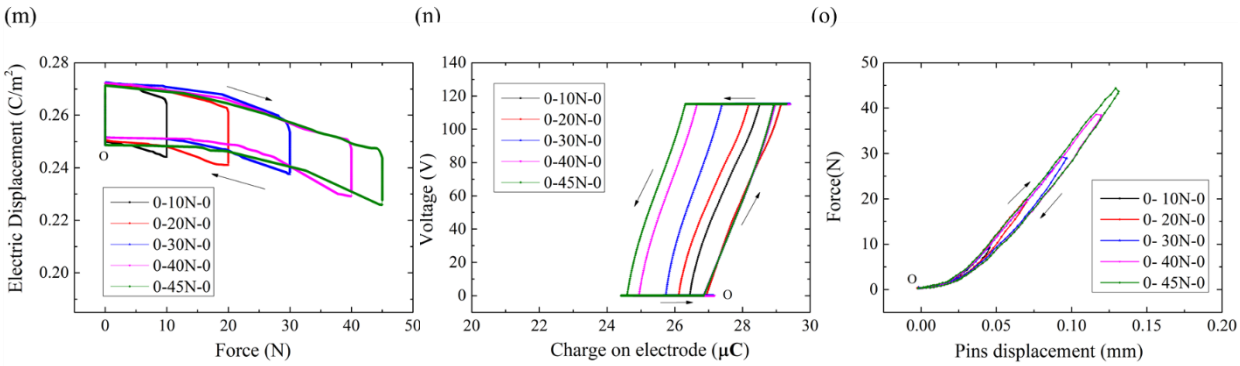


Figure A5. Energy harvesting cycles of the 50% pre-poled using tensile stress with harvesting electric field (a-c) 0.2E_0, (d-f) 0.4E_0, (g-i) 0.6E_0, (j-l) 0.8E_0, (m-o) 1.0E_0. (a,d,g,j,m). Electric Displacement versus applied bending force (b,e,h,k,n) Corresponding voltage versus charge cycle. (c,f,I,l,o) Corresponding force versus loading pin displacement.

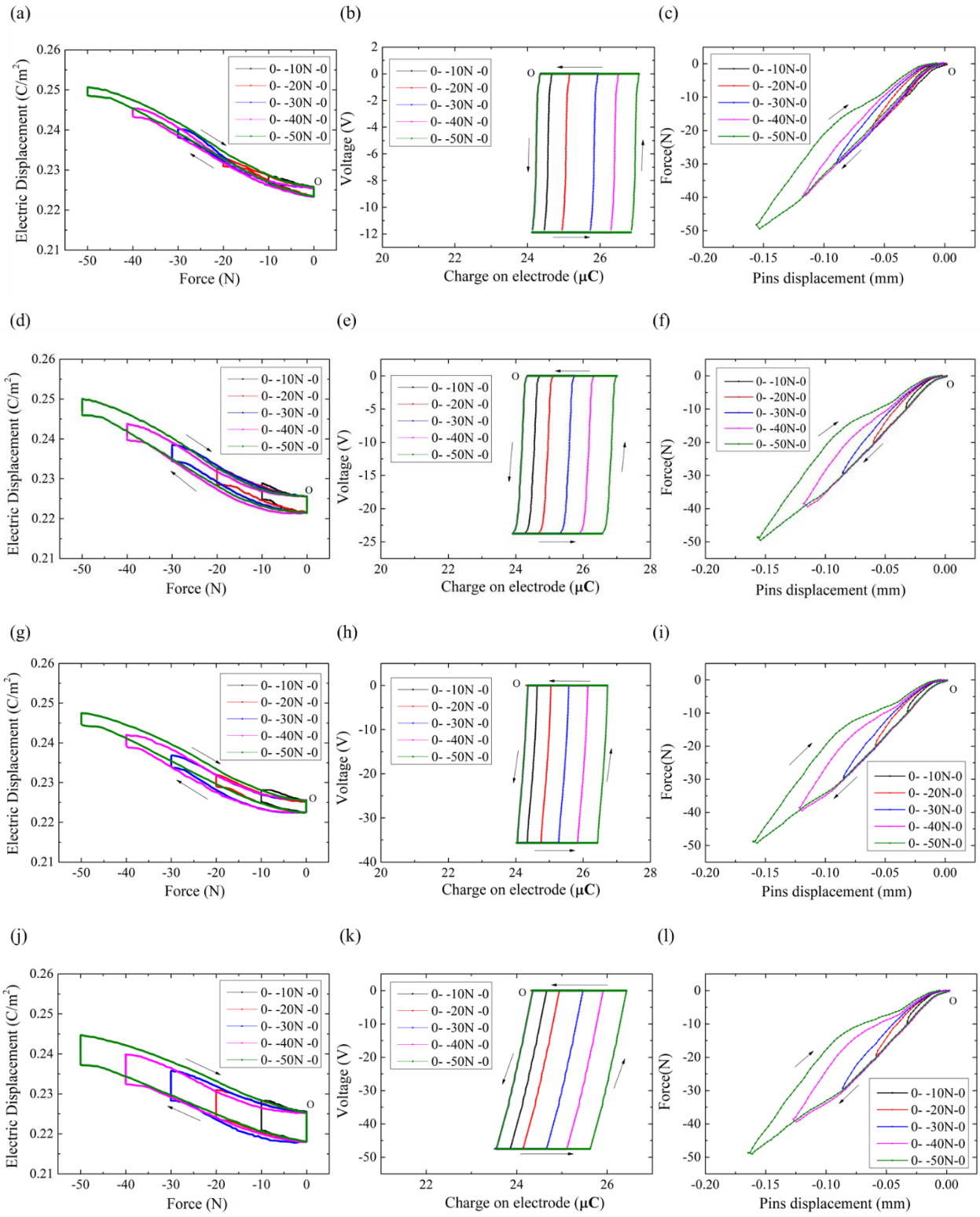
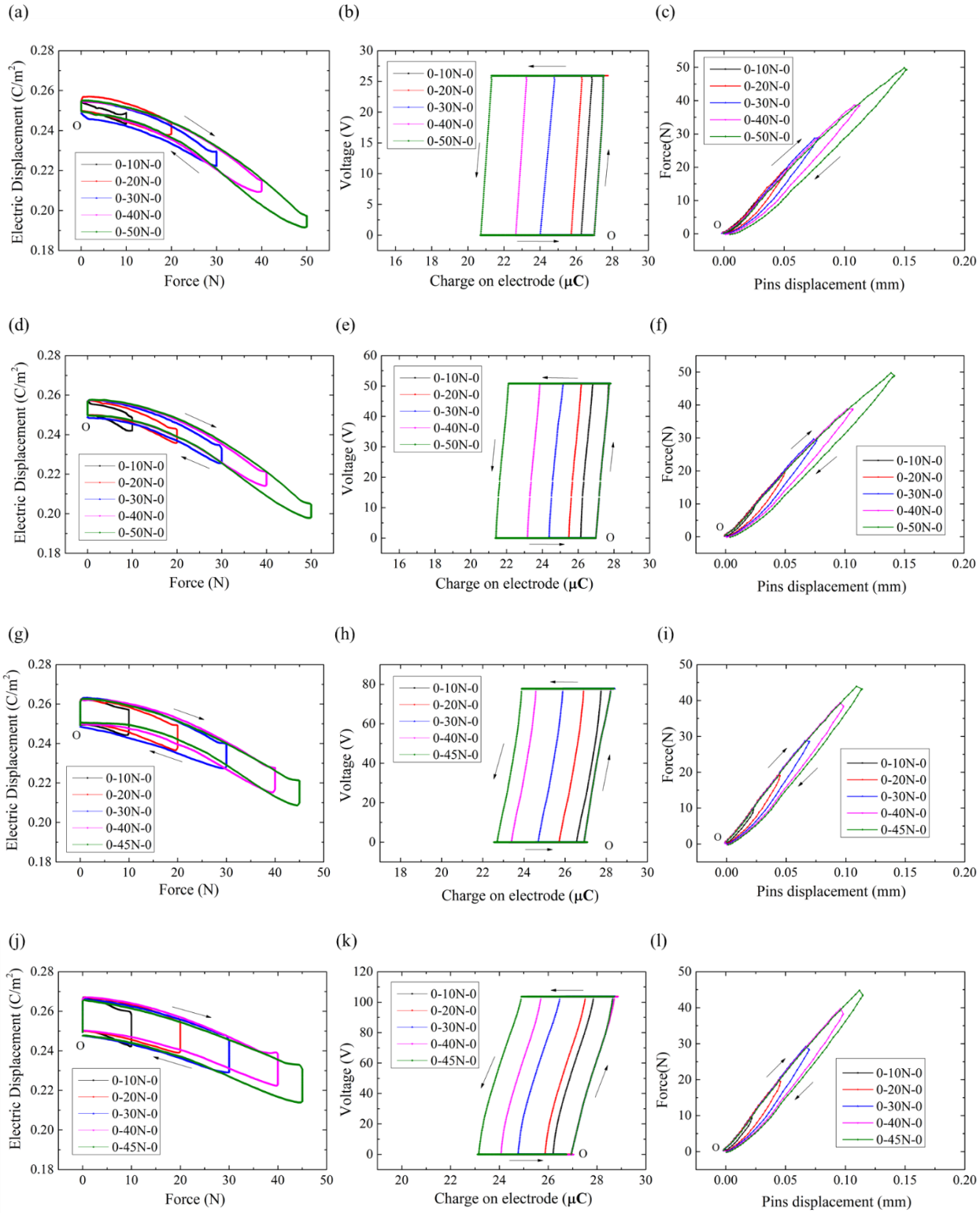


Figure A6. Energy harvesting cycles of the 50% pre-poled using compressive stress with harvesting electric field.(a-c)-0.1E_0, (d-f) -0.2E_0, (g-i) -0.3E_0, (j-l) -0.4E_0. (a,d,g,j). Electric Displacement versus applied bending force. (b,e,h,k) Corresponding voltage versus charge cycle. (c,f,I,l) Corresponding force versus loading pin displacement.

A.4 Energy harvesting cycles of 30% pre-poled



A.4 Energy harvesting cycles of 30% pre-poled

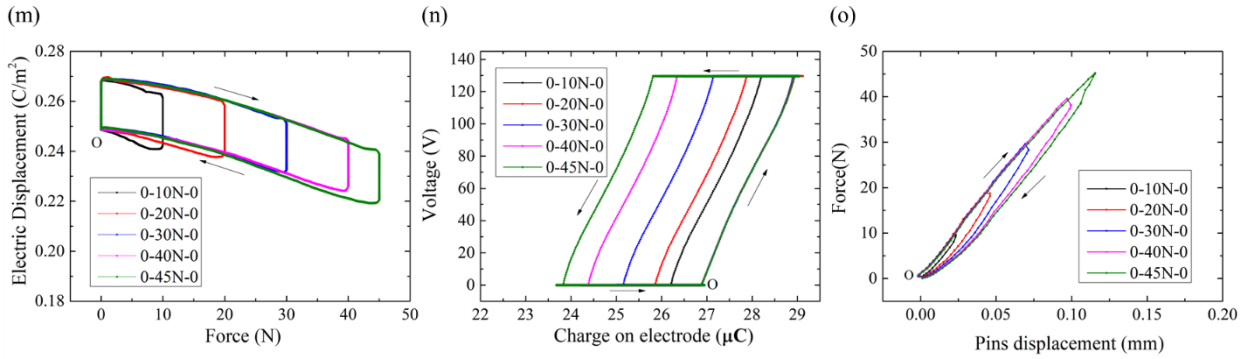


Figure A7. Energy harvesting cycles of the 30% pre-poled using tensile stress with harvesting electric field (a-c) 0.2E_0, (d-f) 0.4E_0, (g-i) 0.6E_0, (j-l) 0.8E_0, (m-o) 1.0E_0. (a,d,g,j,m). Electric Displacement versus applied bending force (b,e,h,k,n) Corresponding voltage versus charge cycle. (c,f,I,l,o) Corresponding force versus loading pin displacement.

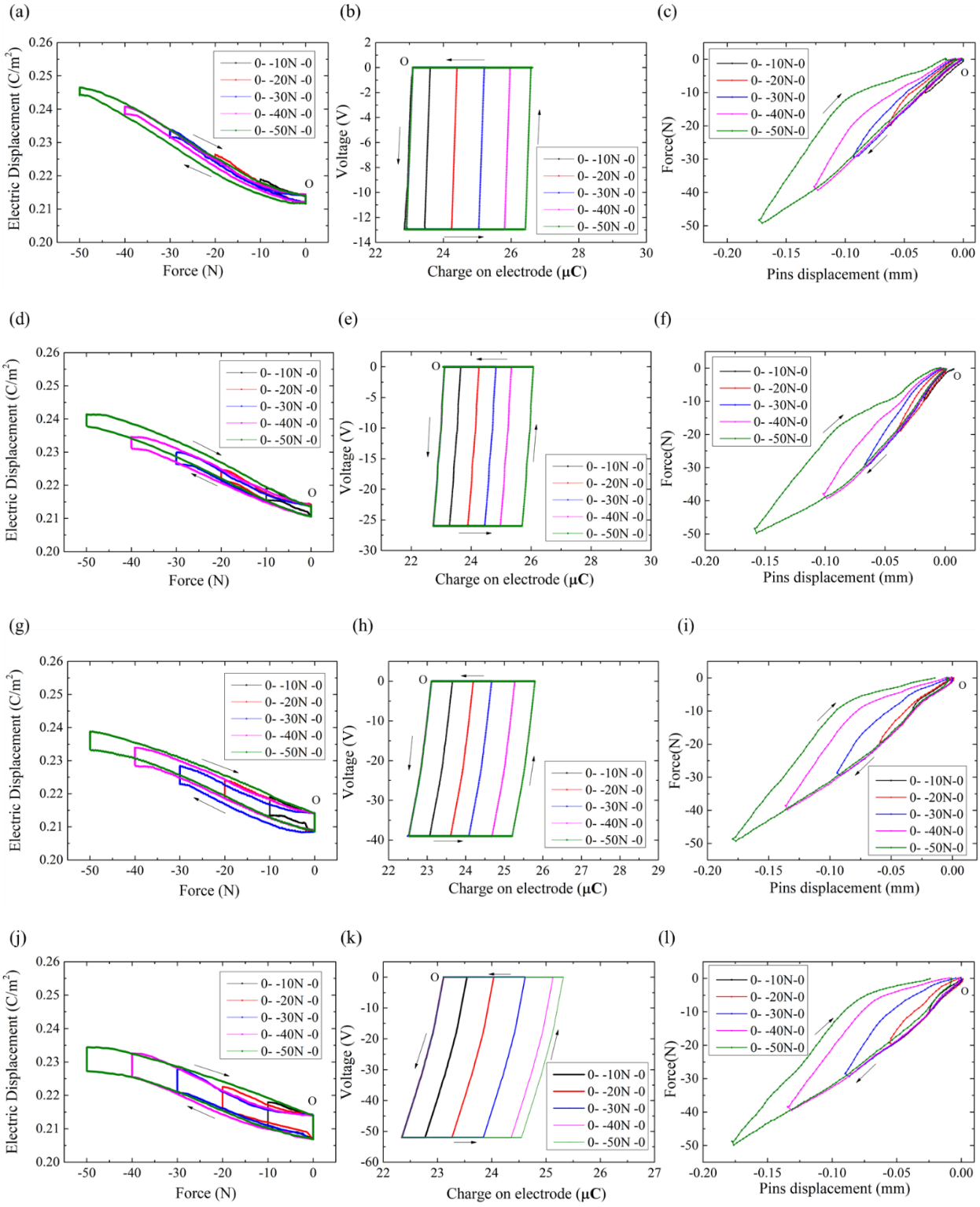


Figure A8. Energy harvesting cycles of the 30% pre-poled using compressive stress with harvesting electric field.(a-c)-0.1E_0, (d-f) -0.2E_0, (g-i) -0.3E_0, (j-l) -0.4E_0. (a,d,g,j). Electric Displacement versus applied bending force. (b,e,h,k) Corresponding voltage versus charge cycle. (c,f,I,l) Corresponding force versus loading pin displacement

References

[1] C. Xu, Y. Song, M. Han, H. Zhang, Portable and wearable self-powered systems based on emerging energy harvesting technology, Microsystems & Nanoengineering 7(1) (2021) 1-14.

[2] Y. Zou, V. Raveendran, J. Chen, Wearable triboelectric nanogenerators for biomechanical energy harvesting, Nano Energy 77 (2020) 105303.

[3] S. Khalid, I. Raouf, A. Khan, N. Kim, H.S. Kim, A review of human-powered energy harvesting for smart electronics: recent progress and challenges, International Journal of Precision Engineering and Manufacturing-Green Technology (2019) 1-31.

[4] G. Zhang, M. Li, H. Li, Q. Wang, S. Jiang, Harvesting energy from human activity: ferroelectric energy harvesters for portable, implantable, and biomedical electronics, Energy Technology 6(5) (2018) 791-812.

[5] N. Sezer, M. Koç, A Comprehensive Review on the State-of-the-Art of Piezoelectric Energy Harvesting, Nano Energy (2020) 105567.

[6] T.Y. Kim, S.K. Kim, S.W. Kim, Application of ferroelectric materials for improving output power of energy harvesters, Nano convergence 5(1) (2018) 30.

[7] L. Yang, D.K. Nandakumar, L. Miao, L. Suresh, D. Zhang, T. Xiong, J.V. Vaghasiya, K.C. Kwon, S.C. Tan, Energy harvesting from atmospheric humidity by a hydrogel-integrated ferroelectric-semiconductor system, Joule 4(1) (2020) 176-188.

[8] J. Wang, L. Geng, L. Ding, H. Zhu, D. Yurchenko, The state-of-the-art review on energy harvesting from flow-induced vibrations, Applied Energy 267 (2020) 114902.

[9] H. Wang, A. Jasim, X. Chen, Energy harvesting technologies in roadway and bridge for different applications–A comprehensive review, Applied Energy 212 (2018) 1083-1094.

[10] Y. Qiu, H. Zhang, L. Hu, D. Yang, L. Wang, B. Wang, J. Ji, G. Liu, X. Liu, J. Lin, Flexible piezoelectric nanogenerators based on ZnO nanorods grown on common paper substrates, Nanoscale 4(20) (2012) 6568-6573.

[11] F. Cottone, L. Gammaitoni, H. Vocca, M. Ferrari, V. Ferrari, Piezoelectric buckled beams for random vibration energy harvesting, Smart Materials and Structures 21(3) (2012) 035021.

[12] K.A. Cook-Chennault, N. Thambi, A.M. Sastry, Powering MEMS portable devices—a review of non-regenerative and regenerative power supply systems with special emphasis on piezoelectric energy harvesting systems, Smart Materials and Structures 17(4) (2008) 043001.

[13] B. Shi, Z. Li, Y. Fan, Implantable energy‐harvesting devices, Advanced Materials 30(44) (2018) 1801511.

[14] M.A. Hannan, S. Mutashar, S.A. Samad, A. Hussain, Energy harvesting for the implantable biomedical devices: issues and challenges, Biomedical Engineering Online 13(1) (2014) 1-23.

[15] H. Pan, L. Qi, Z. Zhang, J. Yan, Kinetic energy harvesting technologies for applications in land transportation: A comprehensive review, Applied Energy 286 (2021) 116518.
[16] C. Chen, A. Sharafi, J.Q. Sun, A high density piezoelectric energy harvesting device from highway traffic–Design analysis and laboratory validation, Applied Energy 269 (2020) 115073.
[17] F.K. Shaikh, S. Zeadally, Energy harvesting in wireless sensor networks: A comprehensive review, Renewable and Sustainable Energy Reviews 55 (2016) 1041-1054.
[18] H. Liu, J. Zhong, C. Lee, S.-W. Lee, L. Lin, A comprehensive review on piezoelectric energy harvesting technology: Materials, mechanisms, and applications, Applied Physics Reviews 5(4) (2018) 041306.
[19] D. Wang, L. Wang, R. Melnik, Vibration energy harvesting based on stress-induced polarization switching: a phase field approach, Smart Materials and Structures 26(6) (2017) 065022.
[20] R. Ahmed, F. Mir, S. Banerjee, A review on energy harvesting approaches for renewable energies from ambient vibrations and acoustic waves using piezoelectricity, Smart Materials and Structures 26(8) (2017) 085031.
[21] H. Röhm, T. Leonhard, A.D. Schulz, S. Wagner, M.J. Hoffmann, A. Colsmann, Ferroelectric properties of perovskite thin films and their implications for solar energy conversion, Advanced Materials 31(26) (2019) 1806661.
[22] Y. Bai, H. Jantunen, J. Juuti, Ferroelectric Oxides for Solar Energy Conversion, Multi‐Source Energy Harvesting/Sensing, and Opto‐Ferroelectric Applications, ChemSusChem 12(12) (2019) 2540.
[23] B. Maamer, A. Boughamoura, A.M.F. El Bab, L.A. Francis, F. Tounsi, A review on design improvements and techniques for mechanical energy harvesting using piezoelectric and electromagnetic schemes, Energy Conversion and Management 199 (2019) 111973.
[24] J.M. Donelan, Q. Li, V. Naing, J.A. Hoffer, D. Weber, A.D. Kuo, Biomechanical energy harvesting: generating electricity during walking with minimal user effort, Science 319(5864) (2008) 807-810.
[25] H. Ryu, S.W. Kim, Emerging pyroelectric nanogenerators to convert thermal energy into electrical energy, Small 17(9) (2021) 1903469.
[26] A. Nozariasbmarz, R.A. Kishore, B. Poudel, U. Saparamadu, W. Li, R. Cruz, S. Priya, High Power Density Body Heat Energy Harvesting, ACS Applied Materials & Interfaces 11(43) (2019) 40107-40113.
[27] H.S. Kim, J.H. Kim, J. Kim, A review of piezoelectric energy harvesting based on vibration, International journal of precision engineering and manufacturing 12(6) (2011) 1129-1141.
[28] F. Balestra, Beyond-CMOS Nanodevices 1, (2014).

[29] C. Wei, X. Jing, A comprehensive review on vibration energy harvesting: Modelling and realization, Renewable and Sustainable Energy Reviews 74 (2017) 1-18.
[30] T. Yildirim, M.H. Ghayesh, W. Li, G. Alici, A review on performance enhancement techniques for ambient vibration energy harvesters, Renewable and Sustainable Energy Reviews 71 (2017) 435-449.
[31] W. Wang, M.T. Winkler, O. Gunawan, T. Gokmen, T.K. Todorov, Y. Zhu, D.B. Mitzi, Device characteristics of CZTSSe thin‐film solar cells with 12.6% efficiency, Advanced Energy Materials 4(7) (2014) 1301465.
[32] J. You, L. Dou, K. Yoshimura, T. Kato, K. Ohya, T. Moriarty, K. Emery, C.-C. Chen, J. Gao, G. Li, A polymer tandem solar cell with 10.6% power conversion efficiency, Nature Communications 4(1) (2013) 1-10.
[33] B. O'regan, M. Grätzel, A low-cost, high-efficiency solar cell based on dye-sensitized colloidal TiO_2 films, Nature 353(6346) (1991) 737-740.
[34] P.D. Frischmann, K. Mahata, F. Würthner, Powering the future of molecular artificial photosynthesis with light-harvesting metallosupramolecular dye assemblies, Chemical Society Reviews 42(4) (2013) 1847-1870.
[35] X. Yan, X. Cui, B. Li, L. Li, Large, solution-processable graphene quantum dots as light absorbers for photovoltaics, Nano Letters 10(5) (2010) 1869-1873.
[36] X. Liao, Y. Liu, J. Ren, L. Guan, X. Sang, B. Wang, H. Zhang, Q. Wang, T. Ma, Investigation of a double-PCM-based thermoelectric energy-harvesting device using temperature fluctuations in an ambient environment, Energy 202 (2020) 117724.
[37] D. Charris, D. Gomez, A.R. Ortega, M. Carmona, M. Pardo, A thermoelectric energy harvesting scheme with passive cooling for outdoor IoT sensors, Energies 13(11) (2020) 2782.
[38] J. Liu, Y. Jia, Q. Jiang, F. Jiang, C. Li, X. Wang, P. Liu, P. Liu, F. Hu, Y. Du, Highly conductive hydrogel polymer fibers toward promising wearable thermoelectric energy harvesting, ACS Applied Materials & Interfaces 10(50) (2018) 44033-44040.
[39] D. Enescu, Thermoelectric energy harvesting: basic principles and applications, Green energy advances (2019) 1.
[40] Y. Wu, H. Zhang, L. Zuo, Thermoelectric energy harvesting for the gas turbine sensing and monitoring system, Energy Conversion and Management 157 (2018) 215-223.
[41] A. Nozariasbmarz, H. Collins, K. Dsouza, M.H. Polash, M. Hosseini, M. Hyland, J. Liu, A. Malhotra, F.M. Ortiz, F. Mohaddes, Review of wearable thermoelectric energy harvesting: From body temperature to electronic systems, Applied Energy 258 (2020) 114069.
[42] M. Cansiz, D. Altinel, G.K. Kurt, Efficiency in RF energy harvesting systems: A comprehensive review, Energy 174 (2019) 292-309.
[43] J.C. Kwan, A.O. Fapojuwo, Radio frequency energy harvesting and data rate optimization in wireless information and power transfer sensor networks, IEEE Sensors Journal 17(15) (2017) 4862-4874.

[44] J.C. Kwan, A.O. Fapojuwo, Sum-throughput maximization in wireless sensor networks with radio frequency energy harvesting and backscatter communication, IEEE Sensors Journal 18(17) (2018) 7325-7339.
[45] L. Xu, L. Xu, J. Luo, Y. Yan, B.E. Jia, X. Yang, Y. Gao, Z.L. Wang, Hybrid All‐in‐One Power Source Based on High‐Performance Spherical Triboelectric Nanogenerators for Harvesting Environmental Energy, Advanced Energy Materials 10(36) (2020) 2001669.
[46] M. Tayyab, J. Wang, J. Wang, M. Maksutoglu, H. Yu, G. Sun, F. Yildiz, M. Eginligil, W. Huang, Enhanced output in polyvinylidene fluoride nanofibers based triboelectric nanogenerator by using printer ink as nano-fillers, Nano Energy 77 (2020) 105178.
[47] Z.L. Wang, J. Chen, L. Lin, Progress in triboelectric nanogenerators as a new energy technology and self-powered sensors, Energy & Environmental Science 8(8) (2015) 2250-2282.
[48] Y. Su, X. Wen, G. Zhu, J. Yang, J. Chen, P. Bai, Z. Wu, Y. Jiang, Z.L. Wang, Hybrid triboelectric nanogenerator for harvesting water wave energy and as a self-powered distress signal emitter, Nano Energy 9 (2014) 186-195.
[49] K.Y. Lee, J. Chun, J.H. Lee, K.N. Kim, N.R. Kang, J.Y. Kim, M.H. Kim, K.S. Shin, M.K. Gupta, J.M. Baik, Hydrophobic sponge structure‐based triboelectric nanogenerator, Advanced Materials 26(29) (2014) 5037-5042.
[50] Y. Zhang, P.T.T. Phuong, E. Roake, H. Khanbareh, Y. Wang, S. Dunn, C. Bowen, Thermal energy harvesting using pyroelectric-electrochemical coupling in ferroelectric materials, Joule 4(2) (2020) 301-309.
[51] S. Patel, N. Novak, The pyroelectric energy harvesting and storage performance around the ferroelectric/antiferroelectric transition in PNZST, Journal of Materials Science 56(2) (2020) 1133-1146.
[52] A. Sultana, M.M. Alam, T.R. Middya, D. Mandal, A pyroelectric generator as a self-powered temperature sensor for sustainable thermal energy harvesting from waste heat and human body heat, Applied Energy 221 (2018) 299-307.
[53] S. Pandya, J. Wilbur, J. Kim, R. Gao, A. Dasgupta, C. Dames, L.W. Martin, Pyroelectric energy conversion with large energy and power density in relaxor ferroelectric thin films, Nature Materials 17(5) (2018) 432-438.
[54] G. Sebald, H. Kuwano, D. Guyomar, B. Ducharne, Experimental Duffing oscillator for broadband piezoelectric energy harvesting, Smart Materials and Structures 20(10) (2011) 102001.
[55] B.K. Panigrahi, D. Sitikantha, A. Bhuyan, H. Panda, K. Mohanta, Dielectric and ferroelectric properties of PVDF thin film for biomechanical energy harvesting, Materials Today: Proceedings 41 (2021) 335-339.
[56] Y. Liu, H. Zhang, J. Yu, Z. Huang, C. Wang, Y. Sun, Ferroelectric P (VDF-TrFE)/POSS nanocomposite films: Compatibility, piezoelectricity, energy harvesting performance, and mechanical and atomic oxygen erosion, RSC advances 10(29) (2020) 17377-17386.

[57] M.A. Abdelkareem, L. Xu, M.K.A. Ali, A. Elagouz, J. Mi, S. Guo, Y. Liu, L. Zuo, Vibration energy harvesting in automotive suspension system: A detailed review, Applied Energy 229 (2018) 672-699.
[58] S.P. Beeby, M.J. Tudor, N.M. White, Energy harvesting vibration sources for microsystems applications, Measurement Science and Technology 17(12) (2006) R175.
[59] A. Brenes, A. Morel, D. Gibus, C.S. Yoo, P. Gasnier, E. Lefeuvre, A. Badel, Large-bandwidth piezoelectric energy harvesting with frequency-tuning synchronized electric charge extraction, Sensors and Actuators A: Physical 302 (2020) 111759.
[60] S.D. Moss, O.R. Payne, G.A. Hart, C. Ung, Scaling and power density metrics of electromagnetic vibration energy harvesting devices, Smart Materials and Structures 24(2) (2015) 023001.
[61] Y. Zhang, T. Wang, A. Luo, Y. Hu, X. Li, F. Wang, Micro electrostatic energy harvester with both broad bandwidth and high normalized power density, Applied Energy 212 (2018) 362-371.
[62] Y. Zhang, T. Wang, A. Zhang, Z. Peng, D. Luo, R. Chen, F. Wang, Electrostatic energy harvesting device with dual resonant structure for wideband random vibration sources at low frequency, Review of Scientific Instruments 87(12) (2016) 125001.
[63] D. Wang, R. Melnik, L. Wang, Material influence in newly proposed ferroelectric energy harvesters, Journal of Intelligent Material Systems and Structures 29(16) (2018) 3305-3316.
[64] Y. Jia, Review of nonlinear vibration energy harvesting: Duffing, bistability, parametric, stochastic and others, Journal of Intelligent Material Systems and Structures 31(7) (2020) 921-944.
[65] H.X. Zou, L.C. Zhao, Q.H. Gao, L. Zuo, F.R. Liu, T. Tan, K.X. Wei, W.M. Zhang, Mechanical modulations for enhancing energy harvesting: Principles, methods and applications, Applied Energy 255 (2019) 113871.
[66] X. Zhang, S. Gao, D. Li, L. Jin, Q. Wu, F. Liu, Frequency up-converted piezoelectric energy harvester for ultralow-frequency and ultrawide-frequency-range operation, Applied Physics Letters 112(16) (2018) 163902.
[67] Y. Kuang, M. Zhu, Design study of a mechanically plucked piezoelectric energy harvester using validated finite element modelling, Sensors and Actuators A: Physical 263 (2017) 510-520.
[68] H. Fu, E.M. Yeatman, A methodology for low-speed broadband rotational energy harvesting using piezoelectric transduction and frequency up-conversion, Energy 125 (2017) 152-161.
[69] B. Andò, S. Baglio, A.R. Bulsara, V. Marletta, A. Pistorio, Investigation of a nonlinear energy harvester, IEEE Transactions on Instrumentation and Measurement 66(5) (2017) 1067-1075.
[70] J. Zhao, Z. You, A shoe-embedded piezoelectric energy harvester for wearable sensors, Sensors 14(7) (2014) 12497-12510.

[71] S. Leadenham, A. Erturk, Nonlinear M-shaped broadband piezoelectric energy harvester for very low base accelerations: primary and secondary resonances, Smart Materials and Structures 24(5) (2015) 055021.
[72] M. Guan, W.-H. Liao, Design and analysis of a piezoelectric energy harvester for rotational motion system, Energy Conversion and Management 111 (2016) 239-244.
[73] Y. Zhang, X. Song, Z. Zhang, D. Fu, R. Xiong, Piezoelectric energy harvesting based on multiaxial ferroelectrics by precise molecular design, Matter 2(3) (2020) 697-710.
[74] F. Qian, T.B. Xu, L. Zuo, Piezoelectric energy harvesting from human walking using a two-stage amplification mechanism, Energy 189 (2019) 116140.
[75] Y. Xu, Ferroelectric materials and their applications, Elsevier, Amsterdam, Netherlands, 2013.
[76] Z.-G. Ye, Handbook of advanced dielectric, piezoelectric and ferroelectric materials: Synthesis, properties and applications, Elsevier2008.
[77] Q. Liu, Electromechanical creep in ferroelectrics, University of Cambridge, 2007.
[78] N.-T. Tsou, Compatible domain structures in ferroelectric single crystals, Oxford University, UK, 2011.
[79] A. Renuka-Balakrishna, Application of a phase-field model to ferroelectrics, University of Oxford, 2016.
[80] J. Valasek, Piezo-electric and allied phenomena in Rochelle salt, Physical review 17(4) (1921) 475.
[81] S. Roberts, Dielectric and piezoelectric properties of barium titanate, Physical Review 71(12) (1947) 890.
[82] G.H. Haertling, C.E. Land, Hot‐pressed (Pb, La)(Zr, Ti) O3 ferroelectric ceramics for electrooptic applications, Journal of the American Ceramic Society 54(1) (1971) 1-11.
[83] P. Panda, B. Sahoo, PZT to lead free piezo ceramics: a review, Ferroelectrics 474(1) (2015) 128-143.
[84] Q. Li, W. Pan, L. Cross, Polarization reversal in PLZT 8/65/35 under hydrostatic pressures, Materials Letters 5(1-2) (1986) 51-53.
[85] C.S. Lynch, The effect of uniaxial stress on the electro-mechanical response of 8/65/35 PLZT, Acta Materialia 44(10) (1996) 4137-4148.
[86] S.-E. Park, T.R. Shrout, Ultrahigh strain and piezoelectric behavior in relaxor based ferroelectric single crystals, Journal of Applied Physics 82(4) (1997) 1804-1811.
[87] C.M. Landis, Non-linear constitutive modeling of ferroelectrics, Current Opinion in Solid State and Materials Science 8(1) (2004) 59-69.
[88] J. Huber, Micromechanical modelling of ferroelectrics, Current Opinion in Solid State and Materials Science 9(3) (2005) 100-106.
[89] R.C. Naber, C. Tanase, P.W. Blom, G.H. Gelinck, A.W. Marsman, F.J. Touwslager, S. Setayesh, D.M. De Leeuw, High-performance solution-processed polymer ferroelectric field-effect transistors, Nature Materials 4(3) (2005) 243-248.

[90] H. Ohigashi, K. Koga, M. Suzuki, T. Nakanishi, K. Kimura, N. Hashimoto, Piezoelectric and ferroelectric properties of P (VDF-TrFE) copolymers and their application to ultrasonic transducers, Ferroelectrics 60(1) (1984) 263-276.
[91] W. Gao, Y. Zhu, Y. Wang, G. Yuan, J.-M. Liu, A review of flexible perovskite oxide ferroelectric films and their application, Journal of Materiomics 6(1) (2020) 1-16.
[92] S. Mueller, S. Slesazeck, T. Mikolajick, J. Müller, P. Polakowski, S. Flachowsky, Next-generation ferroelectric memories based on FE-HfO 2, 2015 Joint IEEE International Symposium on the Applications of Ferroelectric (ISAF), International Symposium on Integrated Functionalities (ISIF), and Piezoelectric Force Microscopy Workshop (PFM), IEEE, 2015, 233-236.
[93] G.H. Haertling, Ferroelectric ceramics: history and technology, Journal of the American Ceramic Society 82(4) (1999) 797-818.
[94] Y. Shu, K. Bhattacharya, Domain patterns and macroscopic behaviour of ferroelectric materials, Philosophical Magazine B 81(12) (2001) 2021-2054.
[95] T. Ogawa, T. Ikegaya, Elastic constants measured from acoustic wave velocities in barium titanate piezoelectric ceramics, Japanese Journal of Applied Physics 54(1) (2014) 011501.
[96] L.D. Filip, N. Plugaru, L. Pintilie, Polarization branches and optimization calculation strategy applied to ABO3 ferroelectrics, Modelling and Simulation in Materials Science and Engineering 27(4) (2019) 045008.
[97] B. Luo, X. Wang, E. Tian, L. Wu, L. Li, First-principles effective Hamiltonian simulation of ABO3-type perovskite ferroelectrics for energy storage application, Journal of Applied Physics 120(7) (2016) 074106.
[98] W. Kinase, K. Harada, Ferroelectricity of Perovskite (ABO 3) Type Crystals, Ferroelectrics 283(1) (2003) 39-47.
[99] B. Mihailova, B.J. Maier, T. Steilmann, E. Dul'kin, M. Roth, Electric-field-induced local structural phenomena in Pb-based ABO 3-type relaxor ferroelectrics, IEEE transactions on ultrasonics, ferroelectrics, and frequency control 62(1) (2015) 7-17.
[100] I.A. Sergienko, C. Şen, E. Dagotto, Ferroelectricity in the magnetic E-phase of orthorhombic perovskites, Physical Review Letters 97(22) (2006) 227204.
[101] A. Hewat, Cubic-tetragonal-orthorhombic-rhombohedral ferroelectric transitions in perovskite potassium niobate: neutron powder profile refinement of the structures, Journal of Physics C: Solid State Physics 6(16) (1973) 2559.
[102] Z. Feng, X. Ren, Striking similarity of ferroelectric aging effect in tetragonal, orthorhombic and rhombohedral crystal structures, Physical Review B 77(13) (2008) 134115.
[103] X. Cheng, Q. Gou, J. Wu, X. Wang, B. Zhang, D. Xiao, J. Zhu, X. Wang, X. Lou, Dielectric, ferroelectric, and piezoelectric properties in potassium sodium niobate ceramics with rhombohedral–orthorhombic and orthorhombic–tetragonal phase boundaries, Ceramics International 40(4) (2014) 5771-5779.

[104] V. Khomchenko, D. Karpinsky, A. Kholkin, N. Sobolev, G. Kakazei, J. Araujo, I. Troyanchuk, B. Costa, J. Paixao, Rhombohedral-to-orthorhombic transition and multiferroic properties of Dy-substituted BiFeO 3, Journal of Applied Physics 108(7) (2010) 074109.
[105] M.E. Lines, A.M. Glass, Principles and applications of ferroelectrics and related materials, Oxford university press2001.
[106] C. Qiu, B. Wang, N. Zhang, S. Zhang, J. Liu, D. Walker, Y. Wang, H. Tian, T.R. Shrout, Z. Xu, Transparent ferroelectric crystals with ultrahigh piezoelectricity, Nature 577(7790) (2020) 350-354.
[107] F. Li, D. Lin, Z. Chen, Z. Cheng, J. Wang, C. Li, Z. Xu, Q. Huang, X. Liao, L.-Q. Chen, Ultrahigh piezoelectricity in ferroelectric ceramics by design, Nature Materials 17(4) (2018) 349-354.
[108] A. Von Hippel, Piezoelectricity, ferroelectricity, and crystal structure, Zeitschrift für Physik A Hadrons and nuclei 133(1-2) (1952) 158-173.
[109] J. Wang, S. Ju, Z. Li, The converse piezoelectric effect on electron tunnelling across a junction with a ferroelectric–ferromagnetic composite barrier, Journal of Physics D: Applied Physics 43(13) (2010) 135003.
[110] E. Fukada, T. Furukawa, Piezoelectricity and ferroelectricity in polyvinylidene fluoride, Ultrasonics 19(1) (1981) 31-39.
[111] P. Ueberschlag, PVDF piezoelectric polymer, Sensor review (2001).
[112] N. Murayama, K. Nakamura, H. Obara, M. Segawa, The strong piezoelectricity in polyvinylidene fluroide (PVDF), Ultrasonics 14(1) (1976) 15-24.
[113] K.M. Ok, E.O. Chi, P.S. Halasyamani, Bulk characterization methods for non-centrosymmetric materials: second-harmonic generation, piezoelectricity, pyroelectricity, and ferroelectricity, Chemical Society Reviews 35(8) (2006) 710-717.
[114] A. Sharma, Z.-G. Ban, S. Alpay, J. Mantese, Pyroelectric response of ferroelectric thin films, Journal of Applied Physics 95(7) (2004) 3618-3625.
[115] F.Y. Lee, S. Goljahi, I.M. McKinley, C.S. Lynch, L. Pilon, Pyroelectric waste heat energy harvesting using relaxor ferroelectric 8/65/35 PLZT and the Olsen cycle, Smart Materials and Structures 21(2) (2012) 025021.
[116] Q. Zhang, R. Whatmore, Improved ferroelectric and pyroelectric properties in Mn-doped lead zirconate titanate thin films, Journal of Applied Physics 94(8) (2003) 5228-5233.
[117] M. Shen, W. Li, M.-Y. Li, H. Liu, J. Xu, S. Qiu, G. Zhang, Z. Lu, H. Li, S. Jiang, High room-temperature pyroelectric property in lead-free BNT-BZT ferroelectric ceramics for thermal energy harvesting, Journal of the European Ceramic Society 39(5) (2019) 1810-1818.
[118] Y. Bai, T. Siponkoski, J. Peräntie, H. Jantunen, J. Juuti, Ferroelectric, pyroelectric, and piezoelectric properties of a photovoltaic perovskite oxide, Applied Physics Letters 110(6) (2017) 063903.

[119] F.Y. Lee, H.R. Jo, C.S. Lynch, L. Pilon, Pyroelectric energy conversion using PLZT ceramics and the ferroelectric–ergodic relaxor phase transition, Smart Materials and Structures 22(2) (2013) 025038.
[120] K. Uchida, S. Takahashi, K. Harii, J. Ieda, W. Koshibae, K. Ando, S. Maekawa, E. Saitoh, Observation of the spin Seebeck effect, Nature 455(7214) (2008) 778-781.
[121] T. Geballe, G. Hull, Seebeck effect in silicon, Physical Review 98(4) (1955) 940.
[122] H. Adachi, K.-i. Uchida, E. Saitoh, S. Maekawa, Theory of the spin Seebeck effect, Reports on Progress in Physics 76(3) (2013) 036501.
[123] M. Walter, J. Walowski, V. Zbarsky, M. Münzenberg, M. Schäfers, D. Ebke, G. Reiss, A. Thomas, P. Peretzki, M. Seibt, Seebeck effect in magnetic tunnel junctions, Nature Materials 10(10) (2011) 742-746.
[124] C. Jaworski, J. Yang, S. Mack, D. Awschalom, J. Heremans, R. Myers, Observation of the spin-Seebeck effect in a ferromagnetic semiconductor, Nature Materials 9(11) (2010) 898-903.
[125] C.R. Bowen, J. Taylor, E. LeBoulbar, D. Zabek, A. Chauhan, R. Vaish, Pyroelectric materials and devices for energy harvesting applications, Energy & Environmental Science 7(12) (2014) 3836-3856.
[126] Q. Hao, F. Hu, Y. Xiao, Multiple human tracking and identification with wireless distributed pyroelectric sensor systems, IEEE Systems Journal 3(4) (2009) 428-439.
[127] H. Xue, Q. Yang, D. Wang, W. Luo, W. Wang, M. Lin, D. Liang, Q. Luo, A wearable pyroelectric nanogenerator and self-powered breathing sensor, Nano Energy 38 (2017) 147-154.
[128] B. Naranjo, J.K. Gimzewski, S. Putterman, Observation of nuclear fusion driven by a pyroelectric crystal, Nature 434(7037) (2005) 1115-1117.
[129] D. Fang, C. Li, Nonlinear electric-mechanical behavior of a soft PZT-51 ferroelectric ceramic, Journal of Materials Science 34(16) (1999) 4001-4010.
[130] E. Soergel, Visualization of ferroelectric domains in bulk single crystals, Applied Physics B 81(6) (2005) 729-751.
[131] O. Kolosov, A. Gruverman, J. Hatano, K. Takahashi, H. Tokumoto, Nanoscale visualization and control of ferroelectric domains by atomic force microscopy, Physical Review Letters 74(21) (1995) 4309.
[132] H. Röhm, T. Leonhard, M.J. Hoffmann, A. Colsmann, Ferroelectric domains in methylammonium lead iodide perovskite thin-films, Energy & Environmental Science 10(4) (2017) 950-955.
[133] B. Casals, G.F. Nataf, D. Pesquera, E.K. Salje, Avalanches from charged domain wall motion in BaTiO3 during ferroelectric switching, APL Materials 8(1) (2020) 011105.
[134] X. Li, Q. Yang, J. Cao, L. Sun, Q. Peng, Y. Zhou, R. Zhang, Domain wall motion in perovskite ferroelectrics studied by the nudged elastic band method, The Journal of Physical Chemistry C 122(5) (2018) 3091-3100.
[135] R. Qin, H. Bhadeshia, Phase field method, Materials Science and Technology 26(7) (2010) 803-811.

[136] S.C. Hwang, C.S. Lynch, R.M. McMeeking, Ferroelectric/ferroelastic interactions and a polarization switching model, Acta Metallurgica et Materialia 43(5) (1995) 2073-2084.
[137] S.C. Hwang, J.E. Huber, R.M. McMeeking, N.A. Fleck, The simulation of switching in polycrystalline ferroelectric ceramics, Journal of Applied Physics 84(3) (1998) 1530-1540.
[138] F. Li, R. Rajapakse, A constrained domain-switching model for polycrystalline ferroelectric ceramics. Part I: Model formulation and application to tetragonal materials, Acta Materialia 55(19) (2007) 6472-6480.
[139] T. Michelitsch, W. Kreher, A simple model for the nonlinear material behavior of ferroelectrics, Acta Materialia 46(14) (1998) 5085-5094.
[140] W. Lu, D.-N. Fang, C. Li, K.-C. Hwang, Nonlinear electric–mechanical behavior and micromechanics modelling of ferroelectric domain evolution, Acta Materialia 47(10) (1999) 2913-2926.
[141] W. Chen, C. Lynch, A micro-electro-mechanical model for polarization switching of ferroelectric materials, Acta Materialia 46(15) (1998) 5303-5311.
[142] G. Arlt, A physical model for hysteresis curves of ferroelectric ceramics, Ferroelectrics 189(1) (1996) 103-119.
[143] R. McMeeking, S. Hwang, On the potential energy of a piezoelectric inclusion and the criterion for ferroelectric switching, Ferroelectrics 200(1) (1997) 151-173.
[144] J. Huber, N. Fleck, C. Landis, R. McMeeking, A constitutive model for ferroelectric polycrystals, Journal of the Mechanics and Physics of Solids 47(8) (1999) 1663-1697.
[145] A. Pathak, R.M. McMeeking, Three-dimensional finite element simulations of ferroelectric polycrystals under electrical and mechanical loading, Journal of the Mechanics and Physics of Solids 56(2) (2008) 663-683.
[146] X. Chen, D. Fang, K.-C. Hwang, Micromechanics simulation of ferroelectric polarization switching, Acta Materialia 45(8) (1997) 3181-3189.
[147] J. Rödel, W.S. Kreher, Self-consistent modelling of non-linear effective properties of polycrystalline ferroelectric ceramics, Computational materials science 19(1-4) (2000) 123-132.
[148] J. Rödel, W.S. Kreher, Modelling linear and nonlinear behavior of polycrystalline ferroelectric ceramics, Journal of the European Ceramic Society 23(13) (2003) 2297-2306.
[149] J. Li, G. Weng, A theory of domain switch for the nonlinear behaviour of ferroelectrics, Proceedings of the Royal Society of London. Series A: Mathematical, Physical and Engineering Sciences 455(1989) (1999) 3493-3511.
[150] W. Li, G. Weng, A theory of ferroelectric hysteresis with a superimposed stress, Journal of Applied Physics 91(6) (2002) 3806-3815.
[151] W. Li, G. Weng, A micromechanics-based thermodynamic model for the domain switch in ferroelectric crystals, Acta Materialia 52(8) (2004) 2489-2496.

[152] W. Lu, D. Fang, K. Hwang, Micromechanics of ferroelectric domain switching behavior: Part I: Coupled electromechanical field of domain inclusions, Theoretical and applied fracture mechanics 37(1-3) (2001) 29-38.
[153] W. Lu, D. Fang, K. Hwang, Micromechanics of ferroelectric domain switching behavior: Part II: Constitutive relations and hysteresis, Theoretical and applied fracture mechanics 37(1-3) (2001) 39-47.
[154] J.E. Huber, N. Fleck, Multi-axial electrical switching of a ferroelectric: theory versus experiment, Journal of the Mechanics and Physics of Solids 49(4) (2001) 785-811.
[155] J. Huber, N. Fleck, Ferroelectric switching: a micromechanics model versus measured behaviour, European Journal of Mechanics-A/Solids 23(2) (2004) 203-217.
[156] A.Y. Belov, W. Kreher, Viscoplastic models for ferroelectric ceramics, Journal of the European Ceramic Society 25(12) (2005) 2567-2571.
[157] M. Elhadrouz, T.B. Zineb, E. Patoor, Constitutive law for ferroelectric and ferroelastic single crystals: a micromechanical approach, Computational materials science 32(3-4) (2005) 355-359.
[158] S. Wan, K. Bowman, Modeling of electric field induced texture in lead zirconate titanate ceramics, Journal of Materials Research 16(8) (2001) 2306-2313.
[159] C.M. Landis, R.M. McMeeking, A self-consistent constitutive model for switching in polycrystalline barium titanate, Ferroelectrics 255(1) (2001) 13-34.
[160] J. Huber, N. Fleck, R. McMeeking, A crystal plasticity model for ferroelectrics, Ferroelectrics 228(1) (1999) 39-52.
[161] M. Kamlah, A.C. Liskowsky, R.M. McMeeking, H. Balke, Finite element simulation of a polycrystalline ferroelectric based on a multidomain single crystal switching model, International Journal of Solids and Structures 42(9-10) (2005) 2949-2964.
[162] I. Pane, N. Fleck, J. Huber, D. Chu, Effect of geometry upon the performance of a thin film ferroelectric capacitor, International Journal of Solids and Structures 45(7-8) (2008) 2024-2041.
[163] D. Zhou, Experimental investigation of non-linear constitutive behavior of PZT piezoceramics, FZKA Bunia 2003.
[164] S.-J. Kim, Q. Jiang, A finite element model for rate-dependent behavior of ferroelectric ceramics, International Journal of Solids and Structures 39(4) (2002) 1015-1030.
[165] S.-J. Kim, J. Choi, M. Kwak, A finite element prediction of ferroelectric switching behavior using a regular dodecahedron RVE, Computational mechanics 31(6) (2003) 469-478.
[166] S.C. Hwang, R.M. McMeeking, A finite element model of ferroelastic polycrystals, International Journal of Solids and Structures 36(10) (1999) 1541-1556.
[167] F. Li, D. Fang, Simulations of domain switching in ferroelectrics by a three-dimensional finite element model, Mechanics of Materials 36(10) (2004) 959-973.

[168] A. Warkentin, A. Ricoeur, A semi-analytical scale bridging approach towards polycrystalline ferroelectrics with mutual nonlinear caloric-electromechanical couplings, International Journal of Solids and Structures 200 (2020) 286-296.
[169] A. Ricoeur, S. Lange, Constitutive modeling of polycrystalline multiconstituent and multiphase ferroic materials based on a condensed approach, Archive of Applied Mechanics 89(6) (2019) 973-994.
[170] S. Lange, A. Ricoeur, A condensed microelectromechanical approach for modeling tetragonal ferroelectrics, International Journal of Solids and Structures 54 (2015) 100-110.
[171] L. Behlen, A. Warkentin, A. Ricoeur, Exploiting ferroelectric and ferroelastic effects in piezoelectric energy harvesting: theoretical studies and parameter optimization, Smart Materials and Structures 30(3) (2021) 035031.
[172] S. Lange, A. Ricoeur, High cycle fatigue damage and life time prediction for tetragonal ferroelectrics under electromechanical loading, International Journal of Solids and Structures 80 (2016) 181-192.
[173] A.F. Devonshire, XCVI. Theory of barium titanate: Part I, The London, Edinburgh, and Dublin Philosophical Magazine and Journal of Science 40(309) (1949) 1040-1063.
[174] P. Chen, P. Peercy, One dimensional dynamic electromechanical constitutive relations of ferroelectric materials, Acta Mechanica 31(3-4) (1979) 231-241.
[175] P. Chen, M.M. Madsen, One dimensional polar responses of the electrooptic ceramic PLZT 7/65/35 due to domain switching, Acta Mechanica 41(3-4) (1981) 255-264.
[176] E. Bassiouny, A. Ghaleb, G. Maugin, Thermodynamical formulation for coupled electromechanical hysteresis effects—I. Basic equations, International Journal of Engineering Science 26(12) (1988) 1279-1295.
[177] E. Bassiouny, A. Ghaleb, G. Maugin, Thermodynamical formulation for coupled electromechanical hysteresis effects—II. Poling of ceramics, International journal of engineering science 26(12) (1988) 1297-1306.
[178] E. Bassiouny, G. Maugin, Thermodynamical formulation for coupled electromechanical hysteresis effects—III. Parameter identification, International Journal of Engineering Science 27(8) (1989) 975-987.
[179] A.C. Cocks, R.M. Mcmeeking, A phenomenological constitutive law for the behaviour of ferroelectric ceramics, Ferroelectrics 228(1) (1999) 219-228.
[180] C.M. Landis, Fully coupled, multi-axial, symmetric constitutive laws for polycrystalline ferroelectric ceramics, Journal of the Mechanics and Physics of Solids 50(1) (2002) 127-152.
[181] R.M. McMeeking, C.M. Landis, A phenomenological multi-axial constitutive law for switching in polycrystalline ferroelectric ceramics, International Journal of Engineering Science 40(14) (2002) 1553-1577.
[182] J. Shieh, J. Huber, N. Fleck, An evaluation of switching criteria for ferroelectrics under stress and electric field, Acta Materialia 51(20) (2003) 6123-6137.

[183] M. Kamlah, C. Tsakmakis, Phenomenological modeling of the non-linear electro-mechanical coupling in ferroelectrics, International Journal of Solids and Structures 36(5) (1999) 669-695.
[184] M. Kamlah, U. Böhle, Finite element analysis of piezoceramic components taking into account ferroelectric hysteresis behavior, International Journal of Solids and Structures 38(4) (2001) 605-633.
[185] S. Klinkel, A phenomenological constitutive model for ferroelastic and ferroelectric hysteresis effects in ferroelectric ceramics, International Journal of Solids and Structures 43(22-23) (2006) 7197-7222.
[186] L.V. Laxman, S. Maniprakash, A. Arockiarajan, A phenomenological model for nonlinear hysteresis and creep behaviour of ferroelectric materials, Acta Mechanica 229(9) (2018) 3853-3867.
[187] M. Kamlah, Q. Jiang, A constitutive model for ferroelectric PZT ceramics under uniaxial loading, Smart Materials and Structures 8(4) (1999) 441.
[188] A. Gruverman, A. Kholkin, Nanoscale ferroelectrics: processing, characterization and future trends, Reports on Progress in Physics 69(8) (2005) 2443.
[189] J. Gregg, Ferroelectrics at the nanoscale, physica status solidi (a) 206(4) (2009) 577-587.
[190] I. Ponomareva, I. Naumov, I. Kornev, H. Fu, L. Bellaiche, Modelling of nanoscale ferroelectrics from atomistic simulations, Current Opinion in Solid State and Materials Science 9(3) (2005) 114-121.
[191] C. Ahn, K. Rabe, J.-M. Triscone, Ferroelectricity at the nanoscale: local polarization in oxide thin films and heterostructures, Science 303(5657) (2004) 488-491.
[192] M. Algueró, J.M. Gregg, L. Mitoseriu, Nanoscale Ferroelectrics and Multiferroics: Key Processing and Characterization Issues, and Nanoscale Effects, 2 Volumes, John Wiley & Sons 2016.
[193] Y. Cao, Q. Li, L.-Q. Chen, S.V. Kalinin, Coupling of electrical and mechanical switching in nanoscale ferroelectrics, Applied Physics Letters 107(20) (2015) 202905.
[194] J. Li, D. Liu, On ferroelectric crystals with engineered domain configurations, Journal of the Mechanics and Physics of Solids 52(8) (2004) 1719-1742.
[195] J.M. Ball, R.D. James, Fine phase mixtures as minimizers of energy, Analysis and Continuum Mechanics, Springer1989, 647-686.
[196] A. Renuka Balakrishna, I. Muench, J.E. Huber, Study of periodic domain patterns in tetragonal ferroelectrics using phase-field methods, Smart Materials, Adaptive Structures and Intelligent Systems, American Society of Mechanical Engineers, 2015, V001T02A001.
[197] A.R. Balakrishna, J.E. Huber, I. Münch, Nanoscale periodic domain patterns in tetragonal ferroelectrics: A phase-field study, Physical Review B 93(17) (2016) 174120.
[198] A. Kontsos, C.M. Landis, Phase-field modeling of domain structure energetics and evolution in ferroelectric thin films, Journal of applied mechanics 77(4) (2010).

[199] W. Zhang, K. Bhattacharya, A computational model of ferroelectric domains. Part I: model formulation and domain switching, Acta Materialia 53(1) (2005) 185-198.
[200] W. Zhang, K. Bhattacharya, A computational model of ferroelectric domains. Part II: grain boundaries and defect pinning, Acta Materialia 53(1) (2005) 199-209.
[201] K. Dayal, K. Bhattacharya, A real-space non-local phase-field model of ferroelectric domain patterns in complex geometries, Acta Materialia 55(6) (2007) 1907-1917.
[202] J. Zhang, R. Wu, S. Choudhury, Y. Li, S.Y. Hu, L. Chen, Three-dimensional phase-field simulation of domain structures in ferroelectric islands, Applied Physics Letters 92(12) (2008) 122906.
[203] I. Steinbach, Phase-field models in materials science, Modelling and Simulation in Materials Science and Engineering 17(7) (2009) 073001.
[204] G.J. Weng, The Prager Medal Lecture: micromechanics and some aspects of phase fields in ferroelectric crystals, Acta Mechanica 225(4-5) (2014) 979-998.
[205] B. Völker, P. Marton, C. Elsässer, M. Kamlah, Multiscale modeling for ferroelectric materials: a transition from the atomic level to phase-field modeling, Continuum Mechanics and Thermodynamics 23(5) (2011) 435-451.
[206] Y. Gu, M. Li, A.N. Morozovska, Y. Wang, E.A. Eliseev, V. Gopalan, L.-Q. Chen, Flexoelectricity and ferroelectric domain wall structures: Phase-field modeling and DFT calculations, Physical Review B 89(17) (2014) 174111.
[207] U.V. Waghmare, First-principles theory, coarse-grained models, and simulations of ferroelectrics, Accounts of Chemical Research 47(11) (2014) 3242-3249.
[208] S. Ahmed, S. Pichardo, L. Curiel, O. Rubel, First-principle modelling of the ferroelectric switching in BaTiO3: concurrent switching versus domain wall motion, Modelling and Simulation in Materials Science and Engineering 22(5) (2014) 055014.
[209] V. Boddu, F. Endres, P. Steinmann, Molecular dynamics study of ferroelectric domain nucleation and domain switching dynamics, Scientific reports 7(1) (2017) 1-10.
[210] P. Fan, Y. Zhang, Q. Yang, J. Jiang, L. Jiang, M. Liao, Y. Zhou, Origin of the Intrinsic Ferroelectricity of HfO2 from ab Initio Molecular Dynamics, The Journal of Physical Chemistry C 123(35) (2019) 21743-21750.
[211] M.G. Shahraki, S. Ghorbanali, The temperature and oxygen vacancy effects on the diffusion coefficient and ionic conductivity in ferroelectric BaTiO3 nanowires; A molecular dynamics study, Microelectronics Reliability 82 (2018) 153-158.
[212] F. Lu, H. Lee, S. Lim, Modeling and analysis of micro piezoelectric power generators for micro-electromechanical-systems applications, Smart Materials and Structures 13(1) (2003) 57.
[213] C. Bowen, H. Kim, P. Weaver, S. Dunn, Piezoelectric and ferroelectric materials and structures for energy harvesting applications, Energy & Environmental Science 7(1) (2014) 25-44.

[214] D. Damjanovic, Ferroelectric, dielectric and piezoelectric properties of ferroelectric thin films and ceramics, Reports on Progress in Physics 61(9) (1998) 1267.
[215] Z. Yang, J. Zu, Comparison of PZN-PT, PMN-PT single crystals and PZT ceramic for vibration energy harvesting, Energy Conversion and Management 122 (2016) 321-329.
[216] B. Lee, S. Lin, W. Wu, X. Wang, P. Chang, C. Lee, Piezoelectric MEMS generators fabricated with an aerosol deposition PZT thin film, Journal of Micromechanics and Microengineering 19(6) (2009) 065014.
[217] S.B. Kim, H. Park, S.H. Kim, H.C. Wikle, J.H. Park, D.J. Kim, Comparison of MEMS PZT cantilevers based on d31 and d33 modes for vibration energy harvesting, Journal of microelectromechanical systems 22(1) (2012) 26-33.
[218] J. Ghazanfarian, M.M. Mohammadi, Piezoelectric Energy Harvesting: a Systematic Review of Reviews, arXiv preprint arXiv:2101.09312 (2021).
[219] C. Covaci, A. Gontean, Piezoelectric energy harvesting solutions: A review, Sensors 20(12) (2020) 3512.
[220] M.R. Sarker, S. Julai, M.F.M. Sabri, S.M. Said, M.M. Islam, M. Tahir, Review of piezoelectric energy harvesting system and application of optimization techniques to enhance the performance of the harvesting system, Sensors and Actuators A: Physical 300 (2019) 111634.
[221] M. Safaei, H.A. Sodano, S.R. Anton, A review of energy harvesting using piezoelectric materials: state-of-the-art a decade later (2008–2018), Smart Materials and Structures 28(11) (2019) 113001.
[222] S. Priya, H.C. Song, Y. Zhou, R. Varghese, A. Chopra, S.G. Kim, I. Kanno, L. Wu, D.S. Ha, J. Ryu, A review on piezoelectric energy harvesting: materials, methods, and circuits, Energy Harvesting and Systems 4(1) (2019) 3-39.
[223] F. Narita, M. Fox, A review on piezoelectric, magnetostrictive, and magnetoelectric materials and device technologies for energy harvesting applications, Advanced Engineering Materials 20(5) (2018) 1700743.
[224] Y. Tan, Y. Dong, X. Wang, Review of MEMS electromagnetic vibration energy harvester, Journal of microelectromechanical systems 26(1) (2016) 1-16.
[225] A.R.M. Siddique, S. Mahmud, B. Van Heyst, A comprehensive review on vibration based micro power generators using electromagnetic and piezoelectric transducer mechanisms, Energy Conversion and Management 106 (2015) 728-747.
[226] E.S. Leland, P.K. Wright, Resonance tuning of piezoelectric vibration energy scavenging generators using compressive axial preload, Smart Materials and Structures 15(5) (2006) 1413.
[227] J. Liu, H. Fang, Z. Xu, X. Mao, X. Shen, D. Chen, H. Liao, B. Cai, A MEMS-based piezoelectric power generator array for vibration energy harvesting, Microelectronics Journal 39(5) (2008) 802-806.
[228] L. Staaf, A. Smith, E. Köhler, P. Lundgren, P. Folkow, P. Enoksson, Achieving increased bandwidth for 4 degree of freedom self-tuning energy harvester, Journal of Sound and Vibration 420 (2018) 165-173.

[229] S. Dhote, Z. Yang, J. Zu, Modeling and experimental parametric study of a tri-leg compliant orthoplanar spring based multi-mode piezoelectric energy harvester, Mechanical Systems and Signal Processing 98 (2018) 268-280.
[230] J. Iannacci, G. Sordo, E. Serra, U. Schmid, The MEMS four-leaf clover wideband vibration energy harvesting device: design concept and experimental verification, Microsystem Technologies 22(7) (2016) 1865-1881.
[231] Z. Wang, R. Elfrink, R. Vullers, V. Van Acht, M. Tutelaers, S. Matova, J. Oudenhoven, R. Van Schaijk, Large power amplification of a piezoelectric energy harvester excited by random vibrations, 2013 IEEE 26th International Conference on Micro Electro Mechanical Systems (MEMS), IEEE, 2013, 106-109.
[232] JX Liu, Analysis of Load Voltage and Output Power for Rainbow Shape Piezoelectric
Monomorph Energy Transferring Elements., Acta Aeronautica et Astronautica Sinica 32 (2011).
[233] J.C. Park, J.Y. Park, Asymmetric PZT bimorph cantilever for multi-dimensional ambient vibration harvesting, Ceramics International 39 (2013) S653-S657.
[234] H. Wang, F. Hu, K. Wang, Y. Liu, W. Zhao, Three-dimensional piezoelectric energy harvester with spring and magnetic coupling, Applied Physics Letters 110(16) (2017) 163905.
[235] R. Chen, L. Ren, H. Xia, X. Yuan, X. Liu, Energy harvesting performance of a dandelion-like multi-directional piezoelectric vibration energy harvester, Sensors and Actuators A: Physical 230 (2015) 1-8.
[236] K. Fan, F. Chao, J. Zhang, W. Wang, X. Che, Design and experimental verification of a bi-directional nonlinear piezoelectric energy harvester, Energy Conversion and Management 86 (2014) 561-567.
[237] S. Vasilev, P. Zelenovskiy, D. Vasileva, A. Nuraeva, V.Y. Shur, A.L. Kholkin, Piezoelectric properties of diphenylalanine microtubes prepared from the solution, Journal of Physics and Chemistry of Solids 93 (2016) 68-72.
[238] S.K. Ghosh, D. Mandal, Efficient natural piezoelectric nanogenerator: electricity generation from fish swim bladder, Nano Energy 28 (2016) 356-365.
[239] S. Lee, S.H. Bae, L. Lin, Y. Yang, C. Park, S.W. Kim, S.N. Cha, H. Kim, Y.J. Park, Z.L. Wang, Super‐flexible nanogenerator for energy harvesting from gentle wind and as an active deformation sensor, Advanced Functional Materials 23(19) (2013) 2445-2449.
[240] B.Y. Lee, J. Zhang, C. Zueger, W.-J. Chung, S.Y. Yoo, E. Wang, J. Meyer, R. Ramesh, S.-W. Lee, Virus-based piezoelectric energy generation, Nature Nanotechnology 7(6) (2012) 351-356.
[241] K.-A.N. Duerloo, M.T. Ong, E.J. Reed, Intrinsic piezoelectricity in two-dimensional materials, The Journal of Physical Chemistry Letters 3(19) (2012) 2871-2876.
[242] Y. Qi, M.C. McAlpine, Nanotechnology-enabled flexible and biocompatible energy harvesting, Energy & Environmental Science 3(9) (2010) 1275-1285.

[243] D. Vasilescu, R. Cornillon, G. Mallet, Piezoelectric resonances in amino-acids, Nature 225(5233) (1970) 635-635.
[244] M.A. Karami, B. Yardimoglu, D.J. Inman, Coupled out of plane vibrations of spiral beams for micro-scale applications, Journal of Sound and Vibration 329(26) (2010) 5584-5599.
[245] M.A. Karami, D.J. Inman, Analytical modeling and experimental verification of the vibrations of the zigzag microstructure for energy harvesting, Journal of Vibration and Acoustics 133(1) (2011).
[246] H. Fang, J. Liu, Z. Xu, L. Dong, L. Wang, D. Chen, B. Cai, Y. Liu, Fabrication and performance of MEMS-based piezoelectric power generator for vibration energy harvesting, Microelectronics Journal 37(11) (2006) 1280-1284.
[247] N. Zhao, J. Yang, Q. Yu, J. Zhao, J. Liu, Y. Wen, P. Li, Three-dimensional piezoelectric vibration energy harvester using spiral-shaped beam with triple operating frequencies, Review of Scientific Instruments 87(1) (2016) 015003.
[248] N. Sharpes, A. Abdelkefi, S. Priya, Two-dimensional concentrated-stress low-frequency piezoelectric vibration energy harvesters, Applied Physics Letters 107(9) (2015) 093901.
[249] A. Massaro, S. De Guido, I. Ingrosso, R. Cingolani, M. De Vittorio, M. Cori, A. Bertacchini, L. Larcher, A. Passaseo, Freestanding piezoelectric rings for high efficiency energy harvesting at low frequency, Applied Physics Letters 98(5) (2011) 053502.
[250] M. Rezaeisaray, M. El Gowini, D. Sameoto, D. Raboud, W. Moussa, Low frequency piezoelectric energy harvesting at multi vibration mode shapes, Sensors and Actuators A: Physical 228 (2015) 104-111.
[251] M. Song, Y. Zhang, M. Peng, J. Zhai, Low frequency wideband nano generators for energy harvesting from natural environment, Nano Energy 6 (2014) 66-72.
[252] A. Erturk, J.M. Renno, D.J. Inman, Modeling of piezoelectric energy harvesting from an L-shaped beam-mass structure with an application to UAVs, Journal of Intelligent Material Systems and Structures 20(5) (2009) 529-544.
[253] H. Li, D. Liu, J. Wang, X. Shang, M.R. Hajj, Broadband bimorph piezoelectric energy harvesting by exploiting bending-torsion of L-shaped structure, Energy Conversion and Management 206 (2020) 112503.
[254] Z. Chen, Y. Yang, Z. Lu, Y. Luo, Broadband characteristics of vibration energy harvesting using one-dimensional phononic piezoelectric cantilever beams, Physica B: Condensed Matter 410 (2013) 5-12.
[255] M. Ferrari, V. Ferrari, M. Guizzetti, D. Marioli, A. Taroni, Piezoelectric multifrequency energy converter for power harvesting in autonomous microsystems, Sensors and Actuators A: Physical 142(1) (2008) 329-335.
[256] H. Yu, J. Zhou, L. Deng, Z. Wen, A vibration-based MEMS piezoelectric energy harvester and power conditioning circuit, Sensors 14(2) (2014) 3323-3341.

[257] L. Deng, Z. Wen, X. Zhao, C. Yuan, G. Luo, J. Mo, High Voltage Output MEMS Vibration Energy Harvester in d_{31} Mode With PZT Thin Film, Journal of microelectromechanical systems 23(4) (2014) 855-861.
[258] M.F. Daqaq, R. Masana, A. Erturk, D. Dane Quinn, On the role of nonlinearities in vibratory energy harvesting: a critical review and discussion, Applied Mechanics Reviews 66(4) (2014).
[259] L. Tang, Y. Yang, A nonlinear piezoelectric energy harvester with magnetic oscillator, Applied Physics Letters 101(9) (2012) 094102.
[260] R. Harne, M. Thota, K. Wang, Concise and high-fidelity predictive criteria for maximizing performance and robustness of bistable energy harvesters, Applied Physics Letters 102(5) (2013) 053903.
[261] A. Erturk, J. Hoffmann, D.J. Inman, A piezomagnetoelastic structure for broadband vibration energy harvesting, Applied Physics Letters 94(25) (2009) 254102.
[262] X. Li, M. Guo, S. Dong, A flex-compressive-mode piezoelectric transducer for mechanical vibration/strain energy harvesting, IEEE transactions on ultrasonics, ferroelectrics, and frequency control 58(4) (2011) 698-703.
[263] L. Wang, S. Chen, W. Zhou, T.-B. Xu, L. Zuo, Piezoelectric vibration energy harvester with two-stage force amplification, Journal of Intelligent Material Systems and Structures 28(9) (2017) 1175-1187.
[264] E. Tufekcioglu, A. Dogan, A flextensional piezo-composite structure for energy harvesting applications, Sensors and Actuators A: Physical 216 (2014) 355-363.
[265] R. Esmaeeli, H. Aliniagerdroudbari, S.R. Hashemi, A. Nazari, M. Alhadri, W. Zakri, A.H. Mohammed, C. Batur, S. Farhad, A rainbow piezoelectric energy harvesting system for intelligent tire monitoring applications, Journal of Energy Resources Technology 141(6) (2019).
[266] H.S. Yoon, G. Washington, A. Danak, Modeling, optimization, and design of efficient initially curved piezoceramic unimorphs for energy harvesting applications, Journal of Intelligent Material Systems and Structures 16(10) (2005) 877-888.
[267] W. Wang, T. Yang, X. Chen, X. Yao, Vibration energy harvesting using a piezoelectric circular diaphragm array, IEEE transactions on ultrasonics, ferroelectrics, and frequency control 59(9) (2012) 2022-2026.
[268] S. Kim, W.W. Clark, Q. Wang, Piezoelectric energy harvesting with a clamped circular plate: analysis, Journal of Intelligent Material Systems and Structures 16(10) (2005) 847-854.
[269] M. Deterre, E. Lefeuvre, E. Dufour-Gergam, An active piezoelectric energy extraction method for pressure energy harvesting, Smart Materials and Structures 21(8) (2012) 085004.
[270] S.B. Horowitz, M. Sheplak, L. Cattafesta, T. Nishida, A MEMS acoustic energy harvester, Journal of Micromechanics and Microengineering 16(9) (2006) S174.
[271] F. Huet, F. Formosa, A. Badel, J.-F. Capsal, M. Lallart, Vibration energy harvesting device using P (VDF-TrFE) hybrid fluid diaphragm, Sensors and Actuators A: Physical 247 (2016) 12-23.

[272] S. Roundy, E.S. Leland, J. Baker, E. Carleton, E. Reilly, E. Lai, B. Otis, J.M. Rabaey, P.K. Wright, V. Sundararajan, Improving power output for vibration-based energy scavengers, IEEE Pervasive computing 4(1) (2005) 28-36.
[273] M. Khazaee, A. Rezaniakolaie, L. Rosendahl, A broadband macro-fiber-composite piezoelectric energy harvester for higher energy conversion from practical wideband vibrations, Nano Energy 76 (2020) 104978.
[274] B. Ren, S.W. Or, Y. Zhang, Q. Zhang, X. Li, J. Jiao, W. Wang, D.a. Liu, X. Zhao, H. Luo, Piezoelectric energy harvesting using shear mode 0.71 Pb (Mg 1/3 Nb 2/3) O 3–0.29 PbTiO 3 single crystal cantilever, Applied Physics Letters 96(8) (2010) 083502.
[275] D.J. Shin, S.J. Jeong, C.E. Seo, K.H. Cho, J.H. Koh, Multi-layered piezoelectric energy harvesters based on PZT ceramic actuators, Ceramics International 41 (2015) S686-S690.
[276] X. Gao, J. Wu, Y. Yu, Z. Chu, H. Shi, S. Dong, Giant piezoelectric coefficients in relaxor piezoelectric ceramic PNN‐PZT for vibration energy harvesting, Advanced Functional Materials 28(30) (2018) 1706895.
[277] Y. Yue, Y. Hou, M. Zheng, X. Yan, J. Fu, M. Zhu, High power density in a piezoelectric energy harvesting ceramic by optimizing the sintering temperature of nanocrystalline powders, Journal of the European Ceramic Society 37(15) (2017) 4625-4630.
[278] S. Banerjee, S. Bairagi, S.W. Ali, A critical review on lead-free hybrid materials for next generation piezoelectric energy harvesting and conversion, Ceramics International (2021).
[279] X. Yan, M. Zheng, X. Gao, M. Zhu, Y. Hou, High-performance lead-free ferroelectric BZT–BCT and its application in energy fields, Journal of Materials Chemistry C 8(39) (2020) 13530-13556.
[280] J. Kim, J.H. Koh, (Na, K) NbO3–(Bi, Na) TiO3 piezoelectric ceramics for energy-harvesting applications, Journal of the European Ceramic Society 35(14) (2015) 3819-3825.
[281] W.S. Kang, J.H. Koh, (1− x) Bi0. 5Na0. 5TiO3–xBaTiO3 lead-free piezoelectric ceramics for energy-harvesting applications, Journal of the European Ceramic Society 35(7) (2015) 2057-2064.
[282] M. Zheng, Y. Hou, X. Yan, L. Zhang, M. Zhu, A highly dense structure boosts energy harvesting and cycling reliabilities of a high-performance lead-free energy harvester, Journal of Materials Chemistry C 5(31) (2017) 7862-7870.
[283] D.J. Shin, J. Kim, J.H. Koh, Piezoelectric properties of (1-x) BZT-xBCT system for energy harvesting applications, Journal of the European Ceramic Society 38(13) (2018) 4395-4403.
[284] X. Yan, M. Zheng, Y. Hou, M. Zhu, H. Yan, High energy conversion efficiency in Mn‐modified Ba0. 9Ca0. 1Ti0. 93Zr0. 07O3 lead‐free energy harvester, Journal of the American Ceramic Society 101(6) (2018) 2330-2338.
[285] M. Wu, T. Zheng, H. Zheng, J. Li, W. Wang, M. Zhu, F. Li, G. Yue, Y. Gu, J. Wu, High-performance piezoelectric-energy-harvester and self-powered

mechanosensing using lead-free potassium–sodium niobate flexible piezoelectric composites, Journal of Materials Chemistry A 6(34) (2018) 16439-16449.
[286] A. Erturk, O. Bilgen, D. Inman, Power generation and shunt damping performance of a single crystal lead magnesium niobate-lead zirconate titanate unimorph: Analysis and experiment, Applied Physics Letters 93(22) (2008) 224102.
[287] A. Mathers, K.S. Moon, J. Yi, A vibration-based PMN-PT energy harvester, IEEE Sensors Journal 9(7) (2009) 731-739.
[288] S.E. Moon, S.Q. Lee, S.k. Lee, Y.G. Lee, Y.S. Yang, K.H. Park, J. Kim, Sustainable vibration energy harvesting based on Zr‐doped PMN‐PT piezoelectric single crystal cantilevers, ETRI journal 31(6) (2009) 688-694.
[289] C. Xu, B. Ren, W. Di, Z. Liang, J. Jiao, L. Li, L. Li, X. Zhao, H. Luo, D. Wang, Cantilever driving low frequency piezoelectric energy harvester using single crystal material 0.71 Pb (Mg1/3Nb2/3) O3-0.29 PbTiO3, Applied Physics Letters 101(3) (2012) 033502.
[290] S. Shahab, S. Zhao, A. Erturk, Soft and hard piezoelectric ceramics and single crystals for random vibration energy harvesting, Energy Technology 6(5) (2018) 935-942.
[291] S.K. Karan, S. Maiti, A.K. Agrawal, A.K. Das, A. Maitra, S. Paria, A. Bera, R. Bera, L. Halder, A.K. Mishra, Designing high energy conversion efficient bio-inspired vitamin assisted single-structured based self-powered piezoelectric/wind/acoustic multi-energy harvester with remarkable power density, Nano Energy 59 (2019) 169-183.
[292] C. Shuai, G. Liu, Y. Yang, F. Qi, S. Peng, W. Yang, C. He, G. Wang, G. Qian, A strawberry-like Ag-decorated barium titanate enhances piezoelectric and antibacterial activities of polymer scaffold, Nano Energy 74 (2020) 104825.
[293] C. Shuai, G. Liu, Y. Yang, W. Yang, C. He, G. Wang, Z. Liu, F. Qi, S. Peng, Functionalized BaTiO3 enhances piezoelectric effect towards cell response of bone scaffold, Colloids and Surfaces B: Biointerfaces 185 (2020) 110587.
[294] S. Harstad, N. D'Souza, N. Soin, A.A. El Gendy, S. Gupta, V.K. Pecharsky, T. Shah, E. Siores, R.L. Hadimani, Enhancement of β-phase in PVDF films embedded with ferromagnetic Gd5Si4 nanoparticles for piezoelectric energy harvesting, AIP Advances 7(5) (2017) 056411.
[295] J.H. Lee, K.Y. Lee, B. Kumar, N.T. Tien, N.E. Lee, S.W. Kim, Highly sensitive stretchable transparent piezoelectric nanogenerators, Energy & Environmental Science 6(1) (2013) 169-175.
[296] L. Jin, S. Ma, W. Deng, C. Yan, T. Yang, X. Chu, G. Tian, D. Xiong, J. Lu, W. Yang, Polarization-free high-crystallization β-PVDF piezoelectric nanogenerator toward self-powered 3D acceleration sensor, Nano Energy 50 (2018) 632-638.
[297] X. Liu, J. Ma, X. Wu, L. Lin, X. Wang, Polymeric nanofibers with ultrahigh piezoelectricity via self-orientation of nanocrystals, ACS Nano 11(2) (2017) 1901-1910.

[298] V. Bhavanasi, D.Y. Kusuma, P.S. Lee, Polarization Orientation, Piezoelectricity, and Energy Harvesting Performance of Ferroelectric PVDF‐TrFE Nanotubes Synthesized by Nanoconfinement, Advanced Energy Materials 4(16) (2014) 1400723.
[299] J.H. Jung, M. Lee, J.I. Hong, Y. Ding, C.Y. Chen, L.J. Chou, Z.L. Wang, Lead-free NaNbO3 nanowires for a high output piezoelectric nanogenerator, ACS Nano 5(12) (2011) 10041-10046.
[300] K.I. Park, M. Lee, Y. Liu, S. Moon, G.T. Hwang, G. Zhu, J.E. Kim, S.O. Kim, D.K. Kim, Z.L. Wang, Flexible nanocomposite generator made of BaTiO3 nanoparticles and graphitic carbons, Advanced Materials 24(22) (2012) 2999-3004.
[301] H. Yu, T. Huang, M. Lu, M. Mao, Q. Zhang, H. Wang, Enhanced power output of an electrospun PVDF/MWCNTs-based nanogenerator by tuning its conductivity, Nanotechnology 24(40) (2013) 405401.
[302] S. Xu, Y.w. Yeh, G. Poirier, M.C. McAlpine, R.A. Register, N. Yao, Flexible piezoelectric PMN–PT nanowire-based nanocomposite and device, Nano Letters 13(6) (2013) 2393-2398.
[303] S. Siddiqui, D.I. Kim, M.T. Nguyen, S. Muhammad, W.S. Yoon, N.E. Lee, High-performance flexible lead-free nanocomposite piezoelectric nanogenerator for biomechanical energy harvesting and storage, Nano Energy 15 (2015) 177-185.
[304] S. Siddiqui, D.I. Kim, E. Roh, T.Q. Trung, M.T. Nguyen, N.E. Lee, A durable and stable piezoelectric nanogenerator with nanocomposite nanofibers embedded in an elastomer under high loading for a self-powered sensor system, Nano Energy 30 (2016) 434-442.
[305] Y.K. Fuh, C.C. Kuo, Z.M. Huang, S.C. Li, E.R. Liu, A transparent and flexible graphene‐piezoelectric fiber generator, Small 12(14) (2016) 1875-1881.
[306] J. Fu, Y. Hou, X. Gao, M. Zheng, M. Zhu, Highly durable piezoelectric energy harvester based on a PVDF flexible nanocomposite filled with oriented BaTi2O5 nanorods with high power density, Nano Energy 52 (2018) 391-401.
[307] Y. Zhang, C.K. Jeong, T. Yang, H. Sun, L.-Q. Chen, S. Zhang, W. Chen, Q. Wang, Bioinspired elastic piezoelectric composites for high-performance mechanical energy harvesting, Journal of Materials Chemistry A 6(30) (2018) 14546-14552.
[308] D. Singh, A. Choudhary, A. Garg, Flexible and robust piezoelectric polymer nanocomposites based energy harvesters, ACS Applied Materials & Interfaces 10(3) (2018) 2793-2800.
[309] B. Dutta, E. Kar, N. Bose, S. Mukherjee, NiO@ SiO2/PVDF: A flexible polymer nanocomposite for a high performance human body motion-based energy harvester and tactile e-skin Mechanosensor, ACS Sustainable Chemistry & Engineering 6(8) (2018) 10505-10516.
[310] P. Thakur, A. Kool, N.A. Hoque, B. Bagchi, F. Khatun, P. Biswas, D. Brahma, S. Roy, S. Banerjee, S. Das, Superior performances of in situ synthesized ZnO/PVDF thin film based self-poled piezoelectric nanogenerator and self-charged photo-power bank with high durability, Nano Energy 44 (2018) 456-467.

[311] S. Ye, C. Cheng, X. Chen, X. Chen, J. Shao, J. Zhang, H. Hu, H. Tian, X. Li, L. Ma, High-performance piezoelectric nanogenerator based on microstructured P (VDF-TrFE)/BNNTs composite for energy harvesting and radiation protection in space, Nano Energy 60 (2019) 701-714.
[312] X. Guan, B. Xu, J. Gong, Hierarchically architected polydopamine modified BaTiO3@ P (VDF-TrFE) nanocomposite fiber mats for flexible piezoelectric nanogenerators and self-powered sensors, Nano Energy 70 (2020) 104516.
[313] L. Yang, S. Chi, S. Dong, F. Yuan, Z. Wang, J. Lei, L. Bao, J. Xiang, J. Wang, Preparation and characterization of a novel piezoelectric nanogenerator based on soluble and meltable copolyimide for harvesting mechanical energy, Nano Energy 67 (2020) 104220.
[314] Y. Ahn, J.Y. Lim, S.M. Hong, J. Lee, J. Ha, H.J. Choi, Y. Seo, Enhanced piezoelectric properties of electrospun poly (vinylidene fluoride)/multiwalled carbon nanotube composites due to high β-phase formation in poly (vinylidene fluoride), The Journal of Physical Chemistry C 117(22) (2013) 11791-11799.
[315] Y. Hu, Y. Zhang, C. Xu, G. Zhu, Z.L. Wang, High-output nanogenerator by rational unipolar assembly of conical nanowires and its application for driving a small liquid crystal display, Nano Letters 10(12) (2010) 5025-5031.
[316] M. Choi, G. Murillo, S. Hwang, J.W. Kim, J.H. Jung, C.-Y. Chen, M. Lee, Mechanical and electrical characterization of PVDF-ZnO hybrid structure for application to nanogenerator, Nano Energy 33 (2017) 462-468.
[317] M.M. Alam, A. Sultana, D. Mandal, Biomechanical and acoustic energy harvesting from TiO2 nanoparticle modulated PVDF nanofiber made high performance nanogenerator, ACS Applied Energy Materials 1(7) (2018) 3103-3112.
[318] Z.L. Wang, J. Song, Piezoelectric nanogenerators based on zinc oxide nanowire arrays, Science 312(5771) (2006) 242-246.
[319] Y. Qin, X. Wang, Z.L. Wang, Microfibre–nanowire hybrid structure for energy scavenging, Nature 451(7180) (2008) 809-813.
[320] R. Yang, Y. Qin, L. Dai, Z.L. Wang, Power generation with laterally packaged piezoelectric fine wires, Nature Nanotechnology 4(1) (2009) 34-39.
[321] Y. Lin, Y. Liu, H.A. Sodano, Hydrothermal synthesis of vertically aligned lead zirconate titanate nanowire arrays, Applied Physics Letters 95(12) (2009) 122901.
[322] S. Xu, Y. Qin, C. Xu, Y. Wei, R. Yang, Z.L. Wang, Self-powered nanowire devices, Nature Nanotechnology 5(5) (2010) 366-373.
[323] S. Xu, B.J. Hansen, Z.L. Wang, Piezoelectric-nanowire-enabled power source for driving wireless microelectronics, Nature Communications 1(1) (2010) 1-5.
[324] J. Briscoe, M. Stewart, M. Vopson, M. Cain, P.M. Weaver, S. Dunn, Nanostructured p‐n junctions for kinetic‐to‐electrical energy conversion, Advanced Energy Materials 2(10) (2012) 1261-1268.
[325] J.I. Sohn, S.N. Cha, B.G. Song, S. Lee, S.M. Kim, J. Ku, H.J. Kim, Y.J. Park, B.L. Choi, Z.L. Wang, Engineering of efficiency limiting free carriers and an interfacial

energy barrier for an enhancing piezoelectric generation, Energy & Environmental Science 6(1) (2013) 97-104.
[326] S.H. Shin, Y.H. Kim, M.H. Lee, J.Y. Jung, J.H. Seol, J. Nah, Lithium-doped zinc oxide nanowires–polymer composite for high performance flexible piezoelectric nanogenerator, ACS Nano 8(10) (2014) 10844-10850.
[327] B. Moorthy, C. Baek, J.E. Wang, C.K. Jeong, S. Moon, K.-I. Park, D.K. Kim, Piezoelectric energy harvesting from a PMN–PT single nanowire, RSC advances 7(1) (2017) 260-265.
[328] A. Koka, Z. Zhou, H.A. Sodano, Vertically aligned BaTiO 3 nanowire arrays for energy harvesting, Energy & Environmental Science 7(1) (2014) 288-296.
[329] A. Koka, H.A. Sodano, A low ‐ frequency energy harvester from ultralong, vertically aligned BaTiO3 nanowire arrays, Advanced Energy Materials 4(11) (2014) 1301660.
[330] Z. Zhou, H. Tang, H.A. Sodano, Scalable synthesis of morphotropic phase boundary lead zirconium titanate nanowires for energy harvesting, Advanced Materials 26(45) (2014) 7547-7554.
[331] R.A. Whiter, V. Narayan, S. Kar Narayan, A scalable nanogenerator based on self ‐ poled piezoelectric polymer nanowires with high energy conversion efficiency, Advanced Energy Materials 4(18) (2014) 1400519.
[332] Z. Zhou, C.C. Bowland, M.H. Malakooti, H. Tang, H.A. Sodano, Lead-free 0.5 Ba (Zr 0.2 Ti 0.8) O 3–0.5 (Ba 0.7 Ca 0.3) TiO 3 nanowires for energy harvesting, Nanoscale 8(9) (2016) 5098-5105.
[333] M.H. Seo, J.Y. Yoo, S.Y. Choi, J.S. Lee, K.W. Choi, C.K. Jeong, K.J. Lee, J.B. Yoon, Versatile transfer of an ultralong and seamless nanowire array crystallized at high temperature for use in high-performance flexible devices, ACS Nano 11(2) (2017) 1520-1529.
[334] Y. Chen, Y. Zhang, L. Zhang, F. Ding, O.G. Schmidt, Scalable single crystalline PMN-PT nanobelts sculpted from bulk for energy harvesting, Nano Energy 31 (2017) 239-246.
[335] A. Nafari, C.C. Bowland, H.A. Sodano, Ultra-long vertically aligned lead titanate nanowire arrays for energy harvesting in extreme environments, Nano Energy 31 (2017) 168-173.
[336] W. Jin, Z. Wang, H. Huang, X. Hu, Y. He, M. Li, L. Li, Y. Gao, Y. Hu, H. Gu, High-performance piezoelectric energy harvesting of vertically aligned Pb (Zr, Ti) O 3 nanorod arrays, RSC advances 8(14) (2018) 7422-7427.
[337] A. Nafari, C.C. Bowland, H.A. Sodano, Vertically aligned lead titanate nanowire arrays for high temperature energy harvesting, Smart Materials, Adaptive Structures and Intelligent Systems, American Society of Mechanical Engineers, 2015, V002T07A018.
[338] A. Koka, Z. Zhou, H.A. Sodano, Vertically aligned BaTiO3 nanowire arrays for energy harvesting, Energy & Environmental Science 7(1) (2014) 288-296.

[339] C. Dagdeviren, B.D. Yang, Y. Su, P.L. Tran, P. Joe, E. Anderson, J. Xia, V. Doraiswamy, B. Dehdashti, X. Feng, Conformal piezoelectric energy harvesting and storage from motions of the heart, lung, and diaphragm, Proceedings of the National Academy of Sciences 111(5) (2014) 1927-1932.
[340] A. Khan, Z. Abas, H.S. Kim, I.-K. Oh, Piezoelectric thin films: an integrated review of transducers and energy harvesting, Smart Materials and Structures 25(5) (2016) 053002.
[341] K.I. Park, S. Xu, Y. Liu, G.T. Hwang, S.J.L. Kang, Z.L. Wang, K.J. Lee, Piezoelectric BaTiO3 thin film nanogenerator on plastic substrates, Nano Letters 10(12) (2010) 4939-4943.
[342] K.I. Park, J.H. Son, G.T. Hwang, C.K. Jeong, J. Ryu, M. Koo, I. Choi, S.H. Lee, M. Byun, Z.L. Wang, Highly ‐ efficient, flexible piezoelectric PZT thin film nanogenerator on plastic substrates, Advanced Materials 26(16) (2014) 2514-2520.
[343] Z. Pi, J. Zhang, C. Wen, Z.-b. Zhang, D. Wu, Flexible piezoelectric nanogenerator made of poly (vinylidenefluoride-co-trifluoroethylene)(PVDF-TrFE) thin film, Nano Energy 7 (2014) 33-41.
[344] G.T. Hwang, H. Park, J.H. Lee, S. Oh, K.I. Park, M. Byun, H. Park, G. Ahn, C.K. Jeong, K. No, Self ‐ powered cardiac pacemaker enabled by flexible single crystalline PMN ‐ PT piezoelectric energy harvester, Advanced Materials 26(28) (2014) 4880-4887.
[345] S.H. Shin, Y.H. Kim, M.H. Lee, J.Y. Jung, J. Nah, Hemispherically aggregated BaTiO3 nanoparticle composite thin film for high-performance flexible piezoelectric nanogenerator, ACS Nano 8(3) (2014) 2766-2773.
[346] M.M. Abolhasani, M. Naebe, K. Shirvanimoghaddam, H. Fashandi, H. Khayyam, M. Joordens, A. Pipertzis, S. Anwar, R. Berger, G. Floudas, Thermodynamic approach to tailor porosity in piezoelectric polymer fibers for application in nanogenerators, Nano Energy 62 (2019) 594-600.
[347] J. Roscow, J. Taylor, C. Bowen, Manufacture and characterization of porous ferroelectrics for piezoelectric energy harvesting applications, Ferroelectrics 498(1) (2016) 40-46.
[348] Q. Zheng, H. Zhang, H. Mi, Z. Cai, Z. Ma, S. Gong, High-performance flexible piezoelectric nanogenerators consisting of porous cellulose nanofibril (CNF)/poly (dimethylsiloxane)(PDMS) aerogel films, Nano Energy 26 (2016) 504-512.
[349] F.R. Fan, Z.Q. Tian, Z.L. Wang, Flexible triboelectric generator, Nano Energy 1(2) (2012) 328-334.
[350] W.G. Kim, D.W. Kim, I.W. Tcho, J.K. Kim, M.S. Kim, Y.K. Choi, Triboelectric Nanogenerator: Structure, Mechanism, and Applications, ACS Nano 15(1) (2021) 258-287.
[351] B. Mahapatra, K.K. Patel, P.K. Patel, A review on recent advancement in materials for piezoelectric/triboelectric nanogenerators, Materials Today: Proceedings (2020).

[352] D.A. Barkas, C. Psomopoulos, P. Papageorgas, K. Kalkanis, D. Piromalis, A. Mouratidis, Sustainable Energy Harvesting through Triboelectric Nano–Generators: A Review of current status and applications, Energy Procedia 157 (2019) 999-1010.
[353] Q. Shi, T. He, C. Lee, More than energy harvesting–Combining triboelectric nanogenerator and flexible electronics technology for enabling novel micro-/nano-systems, Nano Energy 57 (2019) 851-871.
[354] J.M. Baik, J.P. Lee, Strategies for ultrahigh outputs generation in triboelectric energy harvesting technologies: from fundamentals to devices, Science and Technology of Advanced Materials 20(1) (2019) 927-936.
[355] G. Khandelwal, N.P.M.J. Raj, S.-J. Kim, Triboelectric nanogenerator for healthcare and biomedical applications, Nano Today 33 (2020) 100882.
[356] J. Luo, W. Gao, Z.L. Wang, The Triboelectric Nanogenerator as an Innovative Technology toward Intelligent Sports, Advanced Materials 33(17) (2021) 2004178.
[357] Z.L. Wang, Triboelectric nanogenerator (TENG)—sparking an energy and sensor revolution, Advanced Energy Materials 10(17) (2020) 2000137.
[358] G. Zhu, C. Pan, W. Guo, C.-Y. Chen, Y. Zhou, R. Yu, Z.L. Wang, Triboelectric-generator-driven pulse electrodeposition for micropatterning, Nano Letters 12(9) (2012) 4960-4965.
[359] S. Wang, L. Lin, Z.L. Wang, Nanoscale triboelectric-effect-enabled energy conversion for sustainably powering portable electronics, Nano Letters 12(12) (2012) 6339-6346.
[360] S. Niu, S. Wang, L. Lin, Y. Liu, Y.S. Zhou, Y. Hu, Z.L. Wang, Theoretical study of contact-mode triboelectric nanogenerators as an effective power source, Energy & Environmental Science 6(12) (2013) 3576-3583.
[361] B. Ghatak, S. Banerjee, S.B. Ali, R. Bandyopadhyay, N. Das, D. Mandal, B. Tudu, Design of a self-powered triboelectric face mask, Nano Energy 79 (2021) 105387.
[362] C. Hou, J. Geng, Z. Yang, T. Tang, Y. Sun, F. Wang, H. Liu, T. Chen, L. Sun, A Delta‐Parallel‐Inspired Human Machine Interface by Using Self‐Powered Triboelectric Nanogenerator Toward 3D and VR/AR Manipulations, Advanced Materials Technologies 6(1) (2021) 2000912.
[363] S. Li, D. Liu, Z. Zhao, L. Zhou, X. Yin, X. Li, Y. Gao, C. Zhang, Q. Zhang, J. Wang, A fully self-powered vibration monitoring system driven by dual-mode triboelectric nanogenerators, ACS Nano 14(2) (2020) 2475-2482.
[364] C. Bu, F. Li, K. Yin, J. Pang, L. Wang, K. Wang, Research progress and prospect of triboelectric nanogenerators as self-powered human body sensors, ACS Applied Electronic Materials 2(4) (2020) 863-878.
[365] C. Zhang, L. Liu, L. Zhou, X. Yin, X. Wei, Y. Hu, Y. Liu, S. Chen, J. Wang, Z.L. Wang, Self-Powered Sensor for Quantifying Ocean Surface Water Waves Based on Triboelectric Nanogenerator, ACS Nano 14(6) (2020) 7092-7100.

[366] Y. Song, N. Wang, C. Hu, Z.L. Wang, Y. Yang, Soft triboelectric nanogenerators for mechanical energy scavenging and self-powered sensors, Nano Energy (2021) 105919.
[367] Z.L. Wang, From contact-electrification to triboelectric nanogenerators, Reports on Progress in Physics (2021).
[368] C. Wu, A.C. Wang, W. Ding, H. Guo, Z.L. Wang, Triboelectric nanogenerator: a foundation of the energy for the new era, Advanced Energy Materials 9(1) (2019) 1802906.
[369] Z. Lin, B. Zhang, H. Zou, Z. Wu, H. Guo, Y. Zhang, J. Yang, Z.L. Wang, Rationally designed rotation triboelectric nanogenerators with much extended lifetime and durability, Nano Energy 68 (2020) 104378.
[370] S. Wang, L. Lin, Y. Xie, Q. Jing, S. Niu, Z.L. Wang, Sliding-triboelectric nanogenerators based on in-plane charge-separation mechanism, Nano Letters 13(5) (2013) 2226-2233.
[371] S. Niu, Y. Liu, S. Wang, L. Lin, Y.S. Zhou, Y. Hu, Z.L. Wang, Theory of sliding - mode triboelectric nanogenerators, Advanced Materials 25(43) (2013) 6184-6193.
[372] G. Zhu, J. Chen, Y. Liu, P. Bai, Y.S. Zhou, Q. Jing, C. Pan, Z.L. Wang, Linear-grating triboelectric generator based on sliding electrification, Nano Letters 13(5) (2013) 2282-2289.
[373] Y. Yang, H. Zhang, J. Chen, Q. Jing, Y.S. Zhou, X. Wen, Z.L. Wang, Single-electrode-based sliding triboelectric nanogenerator for self-powered displacement vector sensor system, ACS Nano 7(8) (2013) 7342-7351.
[374] Y. Yang, Y.S. Zhou, H. Zhang, Y. Liu, S. Lee, Z.L. Wang, A single - electrode based triboelectric nanogenerator as self - powered tracking system, Advanced Materials 25(45) (2013) 6594-6601.
[375] H. Zhang, Y. Yang, X. Zhong, Y. Su, Y. Zhou, C. Hu, Z.L. Wang, Single-electrode-based rotating triboelectric nanogenerator for harvesting energy from tires, ACS Nano 8(1) (2014) 680-689.
[376] Z. Lin, J. Chen, J. Yang, Recent progress in triboelectric nanogenerators as a renewable and sustainable power source, Journal of Nanomaterials 2016 (2016).
[377] Z.L. Wang, On Maxwell's displacement current for energy and sensors: the origin of nanogenerators, Materials Today 20(2) (2017) 74-82.
[378] S. Wang, Y. Xie, S. Niu, L. Lin, Z.L. Wang, Freestanding triboelectric - layer - based nanogenerators for harvesting energy from a moving object or human motion in contact and non - contact modes, Advanced Materials 26(18) (2014) 2818-2824.
[379] H. Guo, X. Jia, L. Liu, X. Cao, N. Wang, Z.L. Wang, Freestanding triboelectric nanogenerator enables noncontact motion-tracking and positioning, ACS Nano 12(4) (2018) 3461-3467.
[380] S. Niu, Y. Liu, X. Chen, S. Wang, Y.S. Zhou, L. Lin, Y. Xie, Z.L. Wang, Theory of freestanding triboelectric-layer-based nanogenerators, Nano Energy 12 (2015) 760-774.

[381] J. Yang, J. Chen, Y. Yang, H. Zhang, W. Yang, P. Bai, Y. Su, Z.L. Wang, Broadband vibrational energy harvesting based on a triboelectric nanogenerator, Advanced Energy Materials 4(6) (2014) 1301322.
[382] J. Chen, H. Guo, C. Hu, Z.L. Wang, Robust triboelectric nanogenerator achieved by centrifugal force induced automatic working mode transition, Advanced Energy Materials 10(23) (2020) 2000886.
[383] Y. Xie, S. Wang, S. Niu, L. Lin, Q. Jing, J. Yang, Z. Wu, Z.L. Wang, Grating‐structured freestanding triboelectric‐layer nanogenerator for harvesting mechanical energy at 85% total conversion efficiency, Advanced Materials 26(38) (2014) 6599-6607.
[384] V. Nguyen, S. Kelly, R. Yang, Piezoelectric peptide-based nanogenerator enhanced by single-electrode triboelectric nanogenerator, APL Materials 5(7) (2017) 074108.
[385] C. Jirayupat, W. Wongwiriyapan, P. Kasamechonchung, T. Wutikhun, K. Tantisantisom, Y. Rayanasukha, T. Jiemsakul, C. Tansarawiput, M. Liangruksa, P. Khanchaitit, Piezoelectric-induced triboelectric hybrid nanogenerators based on the ZnO nanowire layer decorated on the Au/polydimethylsiloxane–Al structure for enhanced triboelectric performance, ACS Applied Materials & Interfaces 10(7) (2018) 6433-6440.
[386] Y. Guo, X.-S. Zhang, Y. Wang, W. Gong, Q. Zhang, H. Wang, J. Brugger, All-fiber hybrid piezoelectric-enhanced triboelectric nanogenerator for wearable gesture monitoring, Nano Energy 48 (2018) 152-160.
[387] Z.H. Lin, G. Cheng, S. Lee, K.C. Pradel, Z.L. Wang, Harvesting water drop energy by a sequential contact‐electrification and electrostatic‐induction process, Advanced Materials 26(27) (2014) 4690-4696.
[388] G. Zhu, Y. Su, P. Bai, J. Chen, Q. Jing, W. Yang, Z.L. Wang, Harvesting water wave energy by asymmetric screening of electrostatic charges on a nanostructured hydrophobic thin-film surface, ACS Nano 8(6) (2014) 6031-6037.
[389] A. Ahmed, Z. Saadatnia, I. Hassan, Y. Zi, Y. Xi, X. He, J. Zu, Z.L. Wang, Self‐powered wireless sensor node enabled by a duck‐shaped triboelectric nanogenerator for harvesting water wave energy, Advanced Energy Materials 7(7) (2017) 1601705.
[390] Y. Mao, D. Geng, E. Liang, X. Wang, Single-electrode triboelectric nanogenerator for scavenging friction energy from rolling tires, Nano Energy 15 (2015) 227-234.
[391] G. Zhu, Y.S. Zhou, P. Bai, X.S. Meng, Q. Jing, J. Chen, Z.L. Wang, A shape‐adaptive thin‐film‐based approach for 50% high‐efficiency energy generation through micro‐grating sliding electrification, Advanced Materials 26(23) (2014) 3788-3796.
[392] C. Han, C. Zhang, W. Tang, X. Li, Z.L. Wang, High power triboelectric nanogenerator based on printed circuit board (PCB) technology, Nano Research 8(3) (2015) 722-730.

[393] B.D. Chen, W. Tang, C. He, C.R. Deng, L.J. Yang, L.P. Zhu, J. Chen, J.J. Shao, L. Liu, Z.L. Wang, Water wave energy harvesting and self-powered liquid-surface fluctuation sensing based on bionic-jellyfish triboelectric nanogenerator, Materials Today 21(1) (2018) 88-97.
[394] S.S.K. Mallineni, Y. Dong, H. Behlow, A.M. Rao, R. Podila, A wireless triboelectric nanogenerator, Advanced Energy Materials 8(10) (2018) 1702736.
[395] X. Cao, M. Zhang, J. Huang, T. Jiang, J. Zou, N. Wang, Z.L. Wang, Inductor‐free wireless energy delivery via Maxwell's displacement current from an electrodeless triboelectric nanogenerator, Advanced Materials 30(6) (2018) 1704077.
[396] I. Münch, M. Krauß, C.M. Landis, J.E. Huber, Domain engineered ferroelectric energy harvesters on a substrate, Journal of Applied Physics 109(10) (2011) 104106.
[397] I. Muench, M. Krauss, W. Wagner, M. Kamlah, Ferroelectric nanogenerators coupled to an electric circuit for energy harvesting, Smart Materials and Structures 21(11) (2012) 115026.
[398] S. Patel, A. Chauhan, R. Vaish, A technique for giant mechanical energy harvesting using ferroelectric/antiferroelectric materials, Journal of Applied Physics 115(8) (2014) 084908.
[399] A. Chauhan, S. Patel, R. Vaish, Enhanced mechanical energy conversion potential in ferroelectric single crystals, Materials Technology 31(5) (2016) 274-280.
[400] A.N. Bakshi, A.A.B. Moghal, N.A. Madhar, S. Patel, R. Vaish, Effect of stress on energy conversion and storage characteristics of (1-xy) PIN-xPMN-yPT single crystals, Ferroelectrics Letters Section 42(4-6) (2015) 107-114.
[401] W.D. Dong, J.A. Gallagher, C.S. Lynch, Ideal energy harvesting cycle using a phase transformation in ferroelectric crystals, Smart Materials and Structures 23(12) (2014) 125026.
[402] W.D. Dong, P. Finkel, A. Amin, K.A. Cunefare, C.S. Lynch, Energy harvesting using the FER–FEO phase transformation in [011] cut single crystal PIN-PMN-PT, Journal of Intelligent Material Systems and Structures 25(14) (2014) 1786-1799.
[403] W. Dong, P. Finkel, A. Amin, C.S. Lynch, Mechanical energy harvesting utilizing phase transition in 32 mode relaxor-ferroelectric PIN-PMN-PT single crystals, Industrial and Commercial Applications of Smart Structures Technologies 2012, International Society for Optics and Photonics, 2012, 834308.
[404] A.R. Balakrishna, J.E. Huber, Nanoscale domain patterns and a concept for an energy harvester, Smart Materials and Structures 25(10) (2016) 104001.
[405] W. Kang, J.E. Huber, Prospects for energy harvesting using ferroelectric/ferroelastic switching, Smart Materials and Structures 28(2) (2019) 024002.
[406] W. Kang, J.E. Huber, Energy harvesting based on compressive stress-induced ferroelectric/ferroelastic switching in polycrystalline ferroelectric materials, Cell Reports Physical Science (2021) 100707.
[407] W. Kang, L. Chang, J. Huber, Investigation of mechanical energy harvesting cycles using ferroelectric/ferroelastic switching, Nano Energy (2021) 106862.

[408] S. Hwang, C. Lynch, R. McMeeking, Ferroelectric/ferroelastic interactions and a polarization switching model, Acta Metallurgica et Materialia 43(5) (1995) 2073-2084.
[409] G.A. Schneider, Influence of electric field and mechanical stresses on the fracture of ferroelectrics, Annual Review of Materials Research 37 (2007) 491-538.
[410] S. Kamba, V. Bovtun, J. Petzelt, I. Rychetsky, R. Mizaras, A. Brilingas, J. Banys, J. Grigas, M. Kosec, Dielectric dispersion of the relaxor PLZT ceramics in the frequency range 20 Hz-100 THz, Journal of Physics: Condensed Matter 12(4) (2000) 497.
[411] A. Masys, W. Ren, G. Yang, B. Mukherjee, Piezoelectric strain in lead zirconate titante ceramics as a function of electric field, frequency, and dc bias, Journal of Applied Physics 94(2) (2003) 1155-1162.
[412] R. Thomas, S. Mochizuki, T. Mihara, T. Ishida, PZT (65/35) and PLZT (8/65/35) thin films by sol–gel process: a comparative study on the structural, microstructural and electrical properties, Thin Solid Films 443(1-2) (2003) 14-22.
[413] M. Lente, A. Picinin, J. Rino, J. Eiras, 90° domain wall relaxation and frequency dependence of the coercive field in the ferroelectric switching process, Journal of Applied Physics 95(5) (2004) 2646-2653.
[414] A. Bokov, Z.-G. Ye, Recent progress in relaxor ferroelectrics with perovskite structure, Progress in Advanced Dielectrics (2020) 105-164.
[415] J. Huber, F. Hofmann, S. Barhli, T. Marrow, C. Hildersley, Observation of crack growth in a polycrystalline ferroelectric by synchrotron X-ray diffraction, Scripta Materialia 140 (2017) 23-26.
[416] H.-B. Fang, J.-Q. Liu, Z.-Y. Xu, L. Dong, L. Wang, D. Chen, B.-C. Cai, Y. Liu, Fabrication and performance of MEMS-based piezoelectric power generator for vibration energy harvesting, Microelectronics Journal 37(11) (2006) 1280-1284.
[417] T. Tanimoto, K. Yamamoto, T. Morii, Nonlinear stress-strain behavior of piezoelectric ceramics under tensile loading, Applications of Ferroelectrics, 1994. ISAF'94., Proceedings of the Ninth IEEE International Symposium on, IEEE, 1991, 394-397.
[418] Z. Yang, A. Erturk, J. Zu, On the efficiency of piezoelectric energy harvesters, Extreme Mechanics Letters 15 (2017) 26-37.
[419] L.W. Martin, A.M. Rappe, Thin-film ferroelectric materials and their applications, Nature Reviews Materials 2(2) (2016) 1-14.
[420] L.E. Cross, Ferroelectric materials for electromechanical transducer applications, Materials Chemistry and Physics 43(2) (1996) 108-115.
[421] W. Ma, L.E. Cross, Flexoelectricity of barium titanate, Applied Physics Letters 88(23) (2006) 232902.
[422] R. Zhu, Z. Wang, H. Ma, G. Yuan, F. Wang, Z. Cheng, H. Kimura, Poling-free energy harvesters based on robust self-poled ferroelectric fibers, Nano Energy 50 (2018) 97-105.

[423] C.D.M. Junior, A. Erturk, D.J. Inman, An electromechanical finite element model for piezoelectric energy harvester plates, Journal of Sound and Vibration 327(1-2) (2009) 9-25.
[424] Z. Yi, B. Yang, G. Li, J. Liu, X. Chen, X. Wang, C. Yang, High performance bimorph piezoelectric MEMS harvester via bulk PZT thick films on thin beryllium-bronze substrate, Applied Physics Letters 111(1) (2017) 013902.
[425] K. Najafi, T. Galchev, E.E. Aktakka, R.L. Peterson, J. McCullagh, Microsystems for energy harvesting, 2011 16th International Solid-State Sensors, Actuators and Microsystems Conference, IEEE, Beijing, China, 2011, 1845-1850.
[426] S.S. Won, H. Seo, M. Kawahara, S. Glinsek, J. Lee, Y. Kim, C.K. Jeong, A.I. Kingon, S.H. Kim, Flexible vibrational energy harvesting devices using strain-engineered perovskite piezoelectric thin films, Nano Energy 55 (2019) 182-192.
[427] M. Salauddin, R. Toyabur, J. Park, A free motion driven electromagnetic and triboelectric hybridized nanogenerator for scavenging low frequency vibrations, 2018 IEEE Micro Electro Mechanical Systems (MEMS), IEEE, Belfast, UK, 2018, 233-236.
[428] W. Jin, Z. Wang, H. Huang, X. Hu, Y. He, M. Li, L. Li, Y. Gao, Y. Hu, H. Gu, High-performance piezoelectric energy harvesting of vertically aligned $Pb(Zr,Ti)O_3$ nanorod arrays, RSC advances 8(14) (2018) 7422-7427.
[429] W. He, W. Liu, J. Chen, Z. Wang, Y. Liu, X. Pu, H. Yang, Q. Tang, H. Yang, H. Guo, Boosting output performance of sliding mode triboelectric nanogenerator by charge space-accumulation effect, Nature Communications 11(1) (2020) 1-8.
[430] S.W. Ma, Y.J. Fan, H.Y. Li, L. Su, Z.L. Wang, G. Zhu, Flexible porous polydimethylsiloxane/lead zirconate titanate-based nanogenerator enabled by the dual effect of ferroelectricity and piezoelectricity, ACS Applied Materials & Interfaces 10(39) (2018) 33105-33111.
[431] D. Tantraviwat, P. Buarin, S. Suntalelat, W. Sripumkhai, P. Pattamang, G. Rujijanagul, B. Inceesungvorn, Highly dispersed porous polydimethylsiloxane for boosting power-generating performance of triboelectric nanogenerators, Nano Energy 67 (2020) 104214.
[432] J. Wang, C. Wu, Y. Dai, Z. Zhao, A. Wang, T. Zhang, Z.L. Wang, Achieving ultrahigh triboelectric charge density for efficient energy harvesting, Nature Communications 8(1) (2017) 1-8.
[433] Y. Park, Y.E. Shin, J. Park, Y. Lee, M.P. Kim, Y.R. Kim, S. Na, S.K. Ghosh, H. Ko, Ferroelectric multilayer nanocomposites with polarization and stress concentration structures for enhanced triboelectric performances, ACS Nano 14(6) (2020) 7101-7110.
[434] L. Xu, T.Z. Bu, X.D. Yang, C. Zhang, Z.L. Wang, Ultrahigh charge density realized by charge pumping at ambient conditions for triboelectric nanogenerators, Nano Energy 49 (2018) 625-633.
[435] W. Liu, Z. Wang, G. Wang, G. Liu, J. Chen, X. Pu, Y. Xi, X. Wang, H. Guo, C. Hu, Integrated charge excitation triboelectric nanogenerator, Nature Communications 10(1) (2019) 1-9.

[436] Y. Bai, L. Xu, S. Lin, J. Luo, H. Qin, K. Han, Z.L. Wang, Charge pumping strategy for rotation and sliding type triboelectric nanogenerators, Advanced Energy Materials 10(21) (2020) 2000605.
[437] H. Wang, L. Xu, Y. Bai, Z.L. Wang, Pumping up the charge density of a triboelectric nanogenerator by charge-shuttling, Nature Communications 11(1) (2020) 1-9.
[438] Y. Liu, W. Liu, Z. Wang, W. He, Q. Tang, Y. Xi, X. Wang, H. Guo, C. Hu, Quantifying contact status and the air-breakdown model of charge-excitation triboelectric nanogenerators to maximize charge density, Nature Communications 11(1) (2020) 1-8.
[439] H. Zumbahlen, Linear circuit design handbook, Newnes2011.